Frontiers in low temperature plasma diagnostics IV : papers, Rolduc Conference Centre, The Netherlands, 25.03.2001-29.03.2001

Frontiers in Low Temperature Plasma Diagnostics IV

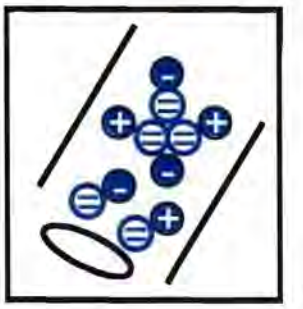

Papers

Rolduc Conference Centre
The Netherlands
25.03.2001-29.03.2001

Department of Applied Physics
Eindhoven University of Technology
The Netherlands

Proceedings of:

Frontiers in Low Temperature Plasma Diagnostics IV

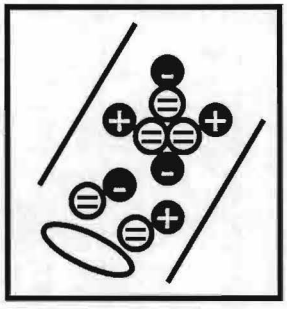

Rolduc Conference Centre
The Netherlands
25.03.2001-29.03.2001

Edited by W.W. Stoffels

Published by the Organizing Committee of
Frontiers in Low Temperature Plasmas IV

Scientific Committee:

Prof. N. Sadeghi, Grenoble (France)
Prof. H.F. Döbele, Essen (Germany)
Prof. D.C. Schram, Eindhoven (The Netherlands)
Prof. S. de Benedictis, Bari (Italy)
Prof. G. Hancock, Oxford (England)
Prof. B. Graham, Belfast (Northern Ireland)
Dr. Ch. Hollenstein, Lausanne (Switzerland)
Prof. G. Kroesen, Eindhoven (The Netherlands)

Organizing Committee:

Prof. M.C.M. van de Sanden,
Dr. R. Engeln
Dr. W.W. Stoffels

Sponsors

Centre for Plasma Physics and Radiation Technology (CPS)
Foundation for Fundamental Research on Matter (FOM).

CPS
CENTRUM
VOOR PLASMAFYSICA EN
STRALINGSTECHNOLOGIE

FOM

Correspondence

Eindhoven University of Technology
Department of Applied Physics
PO box 513
5600 MB Eindhoven
The Netherlands
webpage: http://www.phys.tue.nl/FLTPD/LTPD4.html
e-mail: fltpd.phys@tue.nl

Invited presentations

Short oral presentations

Poster session 1:
Monday March 26, 20:00-22:00

Poster session 2:
Wednesday March 28 20:00-22:00

INVITED PAPERS

VUV Laser Spectroscopy of High Vibrational and Rotational H_2-States

Thomas Mosbach and H.F. Döbele
Institut für Laser- und Plasmaphysik, Universität-GH Essen, D-45117 Essen Germany

Introduction

Negative hydrogen ions extracted from plasma sources are widely applied to generate high-current charged and neutral particle beams for accelerator systems. H^- ions in the MeV energy range are considered as primary charged particles for neutral beam heating of fusion devices [1-2]. Magnetic multipole plasma sources have been found to have a high content of H^- ions [8-9], and magnetic field configurations have been developed for optimization and efficient extraction [1-4]. There has been, however, a discussion extending over years on the underlying generation mechanisms of H^- ions [11-19]. Dissociative attachment (DA) of low energy electrons (~1eV) to highly rovibrationally excited electronic-ground-state molecules - excited through collisons by fast energy electrons (E~10eV)[8-11] - is considered an important generation mechanism [5-7].

$$e + H_2(X^1\Sigma_g^+(v'',J'')) \rightarrow H_2^-(^2\Sigma_{g/u}^+) \rightarrow H^- + H$$

It is well known that molecular reaction rates in low temperature plasmas are critically dependent on vibrational and rotational excitation. The cross-section for the DA-process increases e.g. by five orders of magnitude with increasing rovibrational excitation [5-7]. The DA cross-sections are characterized by a sharp maximum near threshold. In addition, the energy threshold decreases with increasing excitation, thus involving to a larger portion of the low energy part of the EEDF. From this it is clear that the corresponding increase in the dissociative attachment rates with increasing excitation is even more dramatic.
An alternative channel for the formation of H^- is dissociative attachment of electrons to electronically excited states of molecular hydrogen. High-lying Rydberg states have been discussed recently because of the large value of the attachment rate coefficient [18-20].
Calculations of the vibrational population include a multitude of processes. Some of the cross-sections involved can be considered as well established, whereas others are only known by order of magnitude [21].
An experimental verification of the results of the models is still lacking since suitable diagnostic techniques to determine populations of highly excited states of hydrogen (and deuterium) molecules in their electronic-ground-state were not available so far. Emission spectroscopy does not yield information, because these homonuclear electronic-ground-state molecules do not have rotation or rotation-vibration spectra. Several groups attempted to diagnose rovibrational state populations using CARS, REMPI and VUV absorption spectroscopy [22-27]. These contributions concentrated, however, on the low rovibrational states due to lack of sensitivity of these laser spectroscopic methods.
We have applied laser induced fluorescence diagnostics in the VUV to determine rovibrational state populations for two reasons: Firstly, the metastable character of these states provides a simple means to overcome the well known plasma background light problem by fast interruption of the discharge current and, secondly, our method of generation of VUV

radiation - stimulated anti-Stokes Raman scattering (SARS) in liquid nitrogen cooled molecular hydrogen [28] - allows us to excite all molecular Lyman-transitions down to the transmission limit of the optical components.

Theory

Assume that a particle with differential scattering cross-section $\frac{d\sigma}{d\Omega}$ is irradiated with pulsed laser light of intensity $I=\frac{d\phi}{dA}$. $\phi=\frac{dW}{dt}$ is the radiation power of the laser pulse of energy W; dA is the effective scattering area. The radiation intensity scattered into the solid angle $d\Omega$ by the particle is then: $J_S=\frac{d\sigma}{d\Omega}I$. The total scattered radiation intensity of many particles described by their number density n is given by

$$J_{tot}=\int\int \frac{d\sigma}{d\Omega} I_\nu d\nu\, n dV,$$

whereby $I_\nu d\nu$ takes care of the spectral distribution of the laser light. The total energy ΔW_{tot} scattered per laser pulse into $\Delta\Omega$ is obtained by integration over the the solid angle and the laser pulse duration. Under the assumptions that the differential scattering cross-section can be regarded as constant over $\Delta\Omega$ and that the particle density is non-varying over the volume of observation $V = A\,L$, one obtains:

$$\Delta W_{tot}=\Delta\Omega\, nL\int \frac{d\sigma}{d\Omega}\frac{dW}{d\nu}d\nu \qquad (1)$$

A. LIF signal in the linear case

We assume in the following that the medium is transparent in the spectral range of excitation and observation, i.e. absorption or reabsorption should be neglectable, and that the scattered signal depends linearly on the irradiated laser pulse energy, i.e. we neglect saturation effects. Furthermore, quenching is neglected for the time scales under consideration. The spectral distribution of the laser light is assumed to be Gaussian with the spectral width Δ_L:

$$W_\nu = W\, G_{Laser}(\nu-\nu_L;\Delta_L)$$

The differential scattering cross-section can be factorized by means of an angular factor $K(\theta)$ with $\int K(\theta)d\Omega=1$ and the total scattering cross-section σ defined by:

$$\frac{d\sigma}{d\Omega}=K(\theta)\sigma$$

The total scattering cross-section can be expressed by the absorption cross-section [29]. The inhomogeneously broadened spectral line profile due to the Doppler effect can be described by a convolution integral of a Gaussian profile and Lorentzian natural line profile:

$$\sigma(\nu)=\pi r_0 \lambda_{pq}^2 f_{qp} G_{Doppler}\left(\frac{k\nu_k}{2\pi};\Delta_D\right)*L_{Line}\left(\nu-\nu_{pq}-\frac{k\nu_k}{2\pi};\Delta_{pq}\right)$$

(r_0 : classical electron radius, ν_{pq} : central line frequency, f_{qp} : oscillator strength).
Therefore, the calculation of the integral in eq. (1) is reduced to a convolution problem. In general, the spectral width of the natural line is small in comparision with the Doppler width. Thus equation (1) becomes:

$$\Delta W_{tot}=\Delta\Omega nL\pi r_0 \lambda_{qp}^2 f_{qp} W G\left(\nu_{pq}-\nu_L;\sqrt{\Delta_{pq}^2+\Delta_L^2}\right)K(\theta)$$

If the detection system has the quantum efficiency $\eta(\nu_L)$ at laser frequency ν_L, the photon density gathered by the photodetector per pulse is given by:

$$\phi_F=\eta(\nu_L)h\nu_L\Delta W_{tot}=\eta(\nu_L)\Delta\Omega nL\pi r_0 \lambda_{qp}^2 f_{qp} h\nu_L W G\left(\nu_{pq}-\nu_L;\sqrt{\Delta_{pq}^2+\Delta_L^2}\right)K(\theta)$$

B. Calibration of the LIF-signals by Rayleigh-scattering

In order to obtain quantitative densities, it is necessary to eliminate the unknown quantities like quantum efficiency of the detection system and detection geometry (solid angle, length of scattering volume). This can be performed by a comparision with Rayleigh scattering from a gas with known Rayleigh scattering cross-section and under identical imaging conditions. Especially in the case of low saturation of the LIF-signals this calibration technique is very useful, since the radiation power dependence cancels out. Under the assumption that the differential cross-section for Rayleigh scattering is constant over the spectral width of the laser pulse, which is fulfilled far from resonances of the Rayleigh scattering gas, equation (1) can be rewritten as:

$$\Delta W_{R,tot}=\Delta\Omega nL\frac{d\sigma}{d\Omega}W_R$$

If the detection system has the quantum efficiency $\eta(\nu_L)$ at laser frequency ν_L, the photon density gathered by the photodetector per pulse is given by:

$$\phi_R=\eta(\nu_L)h\nu_L\Delta W_{R,tot}=\eta(\nu_L)\Delta\Omega nL\frac{d\sigma}{d\Omega}h\nu_L W_R$$

For an ideal gas of isotropic particles, small enough to be treated in the dipole approximation, the differential cross-section for Rayleigh scattering is described by [30]:

$$\frac{d\sigma_R}{d\Omega}=\frac{9\pi^2\lambda^4}{n_{R,0}^2}\left(\frac{\kappa_R^2(\lambda)-1}{\kappa_R^2(\lambda)+2}\right)^2\sin^2(\theta)$$

Where $n_{R,0}$ and κ_R are the number density and the refractive index of the Rayleigh scattering gas (Ar,Kr,Xe,...) at known reference conditions. For molecular scattering gases (N_2, O_2, ...)

an additional correction factor is introduced, which describes the effect of depolarization resulting from the scattering process [30]:

$$K_{\Delta}=3\frac{(1-\Delta)\sin^2(\theta)+\Delta}{3-4\Delta}$$

Where Δ is a measure for the degree of depolarization (e.g. $\Delta_{N_2}=0.030, \Delta_{O_2}=0.054$ [31])

C. Correction factor due to polarization of the fluorescence

The observed laser induced fluorescence signal for a given rotational-vibrational transition contains all Zeeman π - and $\sigma_{\pm}$ - components that are possible subsequent to the laser excitation according to the selection rules for dipole radiation. In the case of excitation of an isotropic medium by linearly polarized laser light, the electric field vector of the laser light defines the quantization axis in absence of an external magnetic field. As the electromagnetic field of linearly polarized light do not have an angular momentum, only certain definite transitions, in which the magnetic quantum number remains constant ($\Delta M=0$), will take place in atoms or molecules (conservation of the angular momentum of the particle-field system). As a result, the excited particles will be at definite magnetic sublevels, that means the upper magnetic sublevels are not uniformly populated and therefore the fluoresence light will be polarized partially [32].
The spatial intensity and polarization distribution of the π -components ($\Delta M=0$) correspond to an electric dipole which is orientated parallel to the electric field of the laser light; the $\sigma_{\pm}$ - components ($\Delta M\pm 0$) correspond to an electric dipole executing uniform rotation in a plane perpendicular to the electric field of the laser light (rotor) [32]. The spatial intensity distribution due to a dipole and due to a rotor is proportional to $sin^2(\theta)$ and $1+\cos^2(\theta)$, respectively, where θ is the angle between the direction of observation and the exciting electric field. The light emitted by a dipole in any direction is completely linear polarized along the laser field. In general, the radiation due to a rotor is elliptically polarized. When $\theta=\frac{\pi}{2}$, linearly polarized radiation with the electric vector parallel to the plane of the rotor is observed, while when $\theta=0$ the polarization is circular.
If the total intensity of all π -components and of all σ -components for perpendicular observation is denoted by I_{π} and I_{σ}, then the overall intensity observed at an angle θ is given by:

$$I(\theta)=I_{\pi}\sin^2(\theta)+I_{\sigma}\left(1+\cos^2(\theta)\right)$$

Using the following relations

$$I(\theta)=:K(\theta)I_{tot}\ ;\ I_{tot}=\int I(\theta)d\Omega\ ;\ \int K(\theta)d\Omega=1$$

and the degree of polarization for perpendicular observation: $P_{\perp}:=\frac{I_{\pi}-I_{\sigma}}{I_{\pi}+I_{\sigma}}$

The correction factor due to the radiation field may be obtained from $P_\perp$ by

$$K(\theta)=\frac{1}{4\pi}\frac{3}{3-P_\perp}\left(1-P_\perp\cos^2(\theta)\right).$$

In the case $P_\perp=1$ the field corresponds to an electric dipole, $P_\perp=0$ corresponds to isotropic emission and $P_\perp=-1$ characterizes the radiation field due to an electric rotor. The degree of polarization $P_\perp$ for the lines of a singlet bandsystem are calculated for linearly polarized incident light by [32-33]. The correction factors for the line series are shown graphically in fig.{1} for perpendicular observation. It must be emphasized that the theoretical value for the degree of polarization holds only at sufficiently low pressure when the molecule is free to radiate without the interference of collisions. Conversely the study of the depolarization brought about by collisions may be used for an investigation of the nature of such collisions. This field of research is called plasma polarization spectroscopy - see [34].

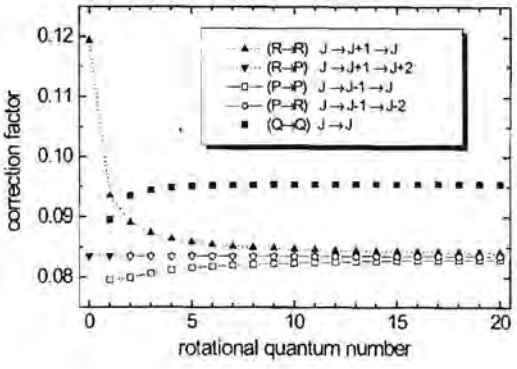

Fig. 1: *LIF correction factor for the line series of singlet bandsystems for linearly polarized exciting light*

Experiment

The plasma is generated in a magnetic multipole source. Two tungsten loops act as cathodes; the body of the chamber is the anode. $SmCo_5$ magnets, positioned on the outer surface of the cylindrical stainless steel chamber, provide efficient confinement of the charged particles, especially of the fast electrons. The source can be operated in the pulsed mode with the option to control "on" and "off" intervals independently. Discharge parameters for the measurements reported are: I=0.5-8A, U=100V and P=1.5Pa; the "on"-interval lasts for ~2ms. For these parameters, the plasma radiation disappears typically within microseconds after current shut-off.

The spatial structure of the plasma is investigated by a standard Langmuir probe system (SmartProbe Scientific Instruments). Fig.{2} shows the electron energy distribution function (EEDF) measured in a plane between the filaments. The central section which is essentially field-free has a diameter of ~6cm. The central part is the section where the highly excited molecules are predominantly formed through collisions by electrons of energies in excess of 10eV, the so-called E-V process [8-11]. Fast electrons with energies in excess of 20eV could not be identified in our discharge with this Langmuir probe system.

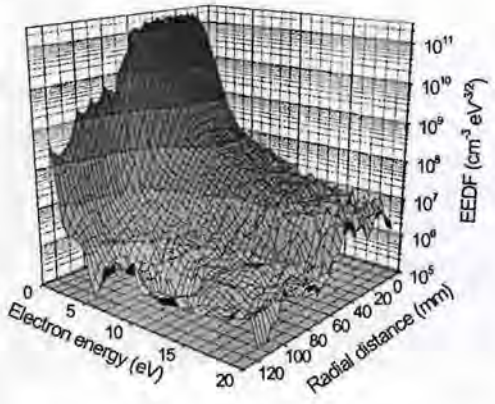

Fig. 2: *EEDF as a function of the radial distance from the chamber axis.*

For probing the different discrete Lyman-transitions it is necessary to generate coherent narrow-bandwidth, broadly tunable VUV-radiation in the wavelength range between 115 and

165 nm (without a gap). Our laser system consists of an excimer laser-pumped dye laser with pulse energies of 30-60mJ in the spectral range 410-500nm, pulse duration 15ns, bandwidth ~0.2cm^{-1}. After frequency doubling in a BBO-crystal we obtain UV-radiation in the wavelength range 205-250nm with pulse energies of 4-8mJ. The UV-radiation is focussed into the Raman cell, in which the LIF pump radiation is generated by SARS. The essentials of the Raman cell are described in [28]. With this scheme of VUV generation all Raman orders (together with the depleted pump radiation) leave the Raman cell simultaneously. We use a ruled grating (R=1m) to single-out the required anti-Stokes order.

Fig.{3} shows the experimental setup. The suitable VUV-radiation propagates through the plasma to a VUV monochromator whose exit slit is equipped with a solar blind VUV PMT. The laser induced fluorescence light is collected perpendicular to the beam with a mirror system. The fluorescence light is spectrally resolved by a monochromator and detected by a gated solar blind VUV PMT (gate duration approximately 1μs). The fluorescence light is recorded within the discharge „off" intervals. Pulse delay units allow us to trigger the laser pulse and the detection electronics at any time within this time window.

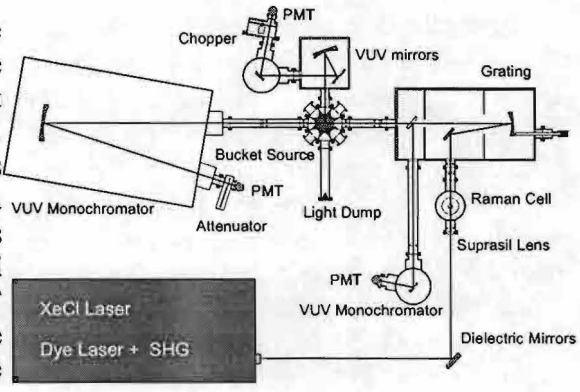

Fig. 3: *Experimental arrangement*

Fluorescence lines are recorded by scanning the wavelength (by tuning the dye laser) over the absorption lines in typically 50 spectral steps. 200 signal pulses are summed up at each spectral position. The translational temperatures, inferred from the Gaussian line profiles, are close to room temperature for I=0.5A and show an increase up to 700 K for I=8A. Note that our laser spectroscopic method allows us in particular to probe the high rovibrational states - up to the dissociation limit of molecular hydrogen - with very good SNR. Limitations towards probing lower energy states are given through the reabsorption of the fluorescence light in the plasma (v"<4) and through the limited transmission of the window material in the VUV (v"<2). The SNR also decreases with the generation of higher anti-Stokes orders (shorter wavelength), because firstly SARS is a non-linear process and secondly the generation of the next anti-Stokes order needs previous anti-Stokes orders. In consequence the pulse to pulse fluctuations increase with increasing anti-Stokes order.

Measurements

Fig.{4} shows the measured decay times (1/e) for J"=1, v">4 states. We are concentrating on high energy states and will not consider states with v" below 4 where absorption would represent a complication. The vibrational states 6 to 11 exhibit comparable decay times of the order of 100μs, whereas the highest levels decay much faster.

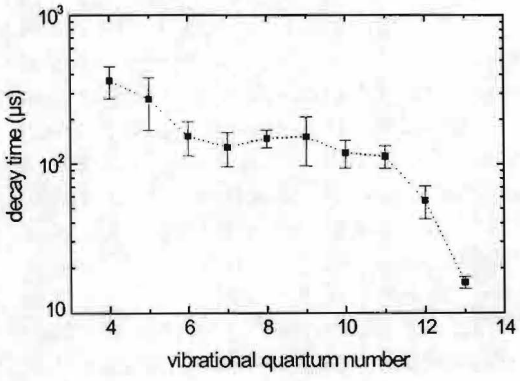

Fig. 4: *Measured decay times of the X(v", J"=1) populations*

The decay time as a function of the rotational excitation was measured for the v"-states 4, 12 and 13. Higher rotational states decay slightly faster (factor 2-4). The dependence of the decay times on the discharge current is only weak.

The rotational population (fig.{5}) turns out, in agreement with earlier results [24-27], to be Boltzmann distributed for the first 4 to 5 rotational states and to exhibit a significant relative overpopulation for higher states. The rotational temperatures related to the Boltzmann distributed states corresponds well with the translational temperatures deduced from the Doppler-broadening of the individual line profiles. The vibrational state v"=13 represents an exception: The rotational state populations turn out to be underthermal with a "quasi temperature" of 150 K (at a translational temperature from the line profile of 310K).

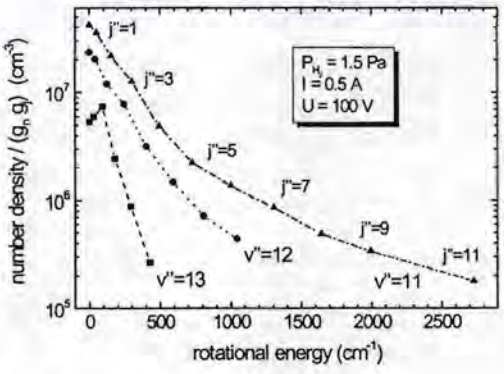

Fig. 5: *Measured populations of the rotational substates of v"-states, divided by statistical weights*

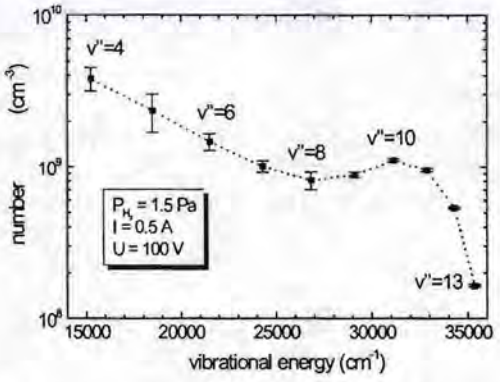

Fig. 6: *Measured vibrational population distribution including rotational levels*

Fig.{6} shows the vibrational population distribution after summation over the rotational states. The theoretically predicted suprathermal behaviour for high vibrational states is obvious. Note that the relative shape is in good agreement with calculations by Fukumasa [15]; even our measured hump around v"=10 is present. According to this work three different excitation processes generate the plateau-like suprathermal distribution for the vibrational population, namly: Collisional excitation of $H_2(v")$ by fast electrons, neutralization of molecular ions, and wall recombination.

Our measurements of the vibrational and rotational distributions and the EEDF allow us to calculate the stationary H^- density in the central section from theoretical rovibrational state dependent cross-sections for dissociative attachment and theoretical cross-sections for the main loss mechanisms in our plasma.
We have measured the H^- density using the photodetachment technique [35] in connection with a Langmuir probe. The value of the H^- density obtained from this measurement is in excellent agreement with our calculated value. For details see [36]. We conclude that our measurements of populations of vibrational and rotational levels and negative ions lead, for our discharge and the selected parameters, to a consistent picture, if we consider

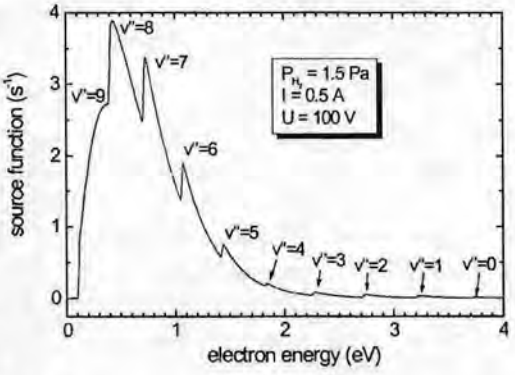

Fig. 7: *Energy dependence of the electron contribution to the dissociative attachment rate*

dissociative attachment of electrons to rovibrationally excited electronic-ground-state molecules as the dominant mechanism.
Figure {7} shows the energy dependence of the electron contribution to the dissociative attachment rate. We calculated this using the measured vibrational population at I=0.5A, the measured EEDF at I=0.5A and theoretical cross-sections for the dissociative attachment [7]. It is easily seen that the most important hydrogen states are the states around v"=8 and the most important electrons for the dissocative attachment have energies around 0.5eV.

Figure {8} shows the populations of vibrational states as a function of the discharge current. The population densities increase in general with current, and the increase depends on the vibrational state. Higher states show a saturation behaviour. It seems that the suprathermal population will change to a thermal population at higher discharge currents. This behaviour is easily seen in figure {9} that simply gives another illustration of the information in figure {8}. The dependence of the vibrational population distribution on the discharge current is an important information due to the fact that the population distribution is strongly connected with the high energy part (E>10eV) of the EEDF. Note that the dissociative attachment process is only sensitive to the low energy part of the EEDF (E<10eV) due to the sharp maximum of the DA cross-section and the exponentielly decreasing slope for higher electron energies. It is therefore possible to separate the EEDF into independent parts.

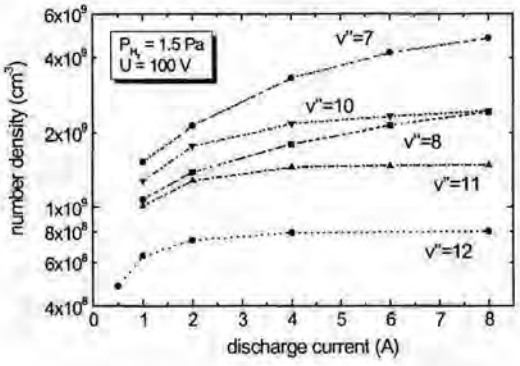

Fig. 8: *Measured populations of vibrational states as a function of discharge current*

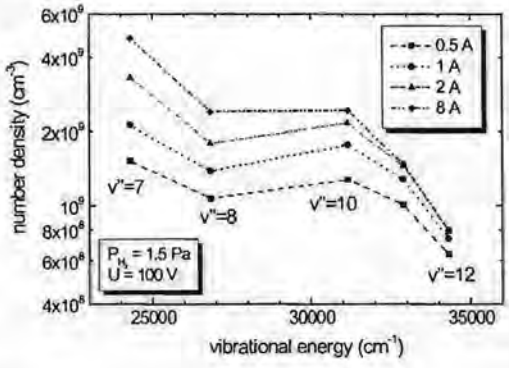

Fig. 9: *Measured vibrational population distributions as a function of discharge current*

The figures {10} - {13} show some results on the effect of the addition of noble gases on the vibrational population. The addition of argon and xenon to a hydrogen base pressure of 1.5Pa causes a decrease of the vibrational population. The slope of the population change increases with the vibrational number of the hydrogen state. An example is shown in fig. {11}. Note the logarithmic scales.

The addition of xenon to a hydrogen base pressure of 0.2Pa also causes a decrease of the vibrational population (fig.{13}). We have done these measurements at this low pressure to have the possibility to compare our results with H^- measurements of other groups [37-38]. They found in this pressure range an increase in the H^- density. At this point we can not decide, whether the production of negative ions via dissociative attachment will be dominated by the low energy part of the EEDF or by the vibrational population distribution. We plan to measure the H^- density and the EEDF in near future. If we will find an increase in the H^- density, then it is definitively not due to an increase of the vibrational population. In this case we expect that the measurements of the EEDF will clarify this basic question.

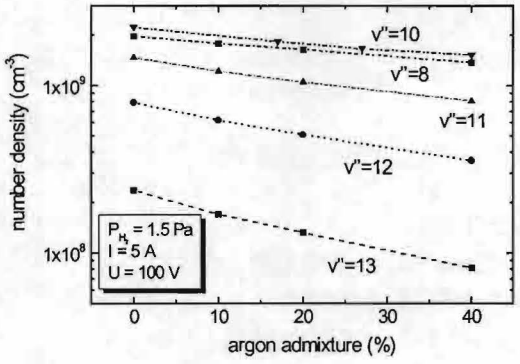

Fig.10: *Vibrational population as a function of added partial pressures of argon. Hydrogen base pressure: 1.5Pa*

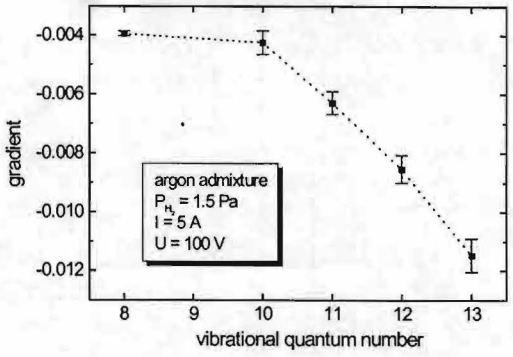

Fig.11: *Slope of population change with pressure as a function of vibrational number.*

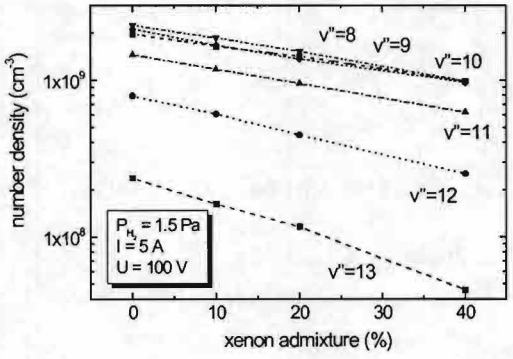

Fig. 12: *Vibrational population as a function of added partial pressures of xenon. Hydrogen base pressure: 1.5 Pa*

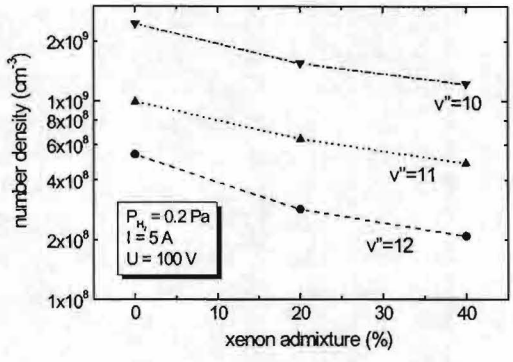

Fig. 13: *Vibrational population as a function of added partial pressures of xenon. Hydrogen base pressure: 0.2 Pa*

Summary

We report on measurements of vibrational and rotational excited electronic-ground-state hydrogen molecules in a magnetic multipole plasma source by LIF with VUV radiation. The measurements are taken after rapid shut-off of the discharge current. Absolute level populations are obtained using Rayleigh scattering calibration with krypton. The theoretically predicted suprathermal population of the vibrational distribution is clearly identified. We found also non-Boltzmann rotational distributions for the high vibrational states. The addition of noble gases (argon and xenon) to hydrogen leads to a decrease of the vibrational population.

We plan to extend our measurements to other parameter regions and to include deuterium. Furthermore, measurements of the branching ratios of different molecular Lyman-transitions from an upper level to the 15(30) possible lower levels are currently under work.

Acknowledgments

Thanks are due to Carola Fischer and Jürgen Leistikow for expert technical assistance. This work was funded by the "Deutsche Forschungsgemeinschaft" in the frame of the Sfb191.

References

[1] K.W. Ehlers, J. Vac. Sci. Technol. A1, 974 (1983)
[2] A.J.T. Holmes, Plasma Phys. Controlled Fusion 34, 653 (1992)
[3] K.N. Leung, K.W. Ehlers, Rev. Sci. Instrum. 55, 342 (1984)
[4] A.J.T. Holmes, L.M. Lea, A.F. Newman and M.P.S. Nightingale, Rev. Sci. Instrum. 58, 223 (1987)
[5] J.M. Wadehra and J.N. Bardsley, Phys. Rev. Lett. 41, 1795 (1978)
[6] J.P. Gauyacq, J. Phys. B 18, 1859 (1985)
[7] A.P. Hickman, Phys. Rev. A 43, 3495 (1991)
[8] M. Bacal and D.A. Skinner, Comments At. Mol. Phys. 23, 283 (1990)
[9] J.R. Hiskes, Comments At. Mol. Phys. 19, 59 (1987)
[10] J.R. Hiskes, J. Appl. Phys. 70, 3409 (1991)
[11] C. Gorse et al., Chem. Phys. 161, 211 (1992)
[12] M. Bacal, C. Michaut, L.I. Elizarov and F. El. Balghiti, Rev. Sci. Instrum. 67, 1138 (1996)
[13] P. Berlemont, D.A. Skinner and M. Bacal, Rev. Sci. Instrum. 64, 2721 (1993)
[14] O. Fukumasa, J. Phys. D 22, 1668 (1989)
[15] O. Fukumasa, K. Mutou, H. Naitou, Rev. Sci. Instrum. 63, 2693 (1992)
[16] D.A. Skinner et al., Phys. Rev. E 48, 2122 (1993)
[17] J.R. Hiskes, Appl. Phys. Lett. 57, 231 (1990)
[18] J.R. Hiskes, Appl. Phys. Lett. 69, 755 (1996)
[19] K. Hassouni, A. Gicquel and M. Capitelli, Chem. Phys. Lett. 290, 502 (1998)
[20] P.G. Datskos, L.A. Pinnaduwage and J.F. Kielkopf, Phys. Rev. A 55, 4131 (1997)
[21] W.G. Graham, Plasma Sources Sci. Technol. 4, 281 (1995)
[22] M. Pealat, J-P.E. Taran, M. Bacal and F. Hillion, J. Chem. Phys. 82, 4943 (1985)
[23] P.J. Eenshuistra, A.W. Kleyn and H.J. Hopman, Europhys. Lett. 8, 423 (1989)
[24] J.H.M. Bonnie, P.J. Eenshuistra and H.J. Hopman, Phys. Rev. A 37, 1121 (1988)
[25] G.C. Stutzin et al., Chem. Phys. Lett. 155, 475 (1989)
[26] G.C. Stutzin et al., Rev. Sci. Instrum. 61, 619 (1990)
[27] D. Wagner, B. Dikmen and H.F. Döbele, Plasma Sources Sci. Technol. 7, 462 (1998)
[28] M. Spaan, A. Goehlich, V. Schulz-von der Gathen and H.F. Döbele, Appl. Opt. 33, 3865 (1994)
[29] K. Shimoda: Introduction to Laser Physics, Springer (1986)
[30] C.M. Penney, J. Opt. Soc. Am. 59, 34 (1969)
[31] R.Penndorf, J. Opt. Soc. Am. 47, 176 (1957)
[32] P.P. Feofilov: The Physical Basis of Polarized Emission authorized translation from Russian consultants bureau, New York (1961)
[33] A. Omont, Prog. Quantum Electronics 5, 69, Pergamon Press (1977)
[34] T. Fujimoto, S.A. Kazantsev, Plasma Phys. Control. Fusion 39, 1267 (1997)
[35] M. Bacal, Rev. Sci. Instrum. 71, 3981 (2000)
[36] T. Mosbach, H.-M. Katsch and H.F. Döbele, Phys. Rev. Lett. 85, 3420 (2000)
[37] K.N. Leung, K.W. Ehlers and R.V. Pyle, Rev. Sci. Instrum. 56, 2097 (1985)
[38] N.P. Curran, M.B. Hopkins, D. Vender and B.W. James, Plasma Sources Sci. Technol. 9, 169 (2000)

Laser diagnostics in a diamond depositing oxy-acetylene flame

R.J.H. Klein-Douwel, R.L. Stolk and J.J. ter Meulen
AppliedPhysics, University of Nijmegen
Toernooiveld, 6525 ED Nijmegen, The Netherlands
email: robertkd@sci.kun.nl

1. Introduction

An efficient and relatively simple method in chemical vapour deposition (CVD) of diamond is the use of highly exothermic reactions which take place in flames. Hydrocarbon flames of various structures and compositions can be used. In 1988 Hirose and Kondo were the first to successfully apply an oxy-acetylene combustion flame for the deposition of diamond on a cooled substrate under atmospheric conditions.[1] This method was soon picked up by several other groups, and the technique is now well developed to deposit polycrystalline diamond on non-diamond substrates and single crystalline diamond layers on a diamond seed crystal.[2-5]

In flame deposition of diamond the high velocity gas flow of the flame impinges at normal incidence on the cooled substrate. This creates a stagnation-point flow at the surface where the gas stream is deflected radially. The exact shape of the gas stream profile depends on the flow velocity beyond the flame front and on the distance between flame front and substrate. Recently Okkerse *et al.* have reported a two-dimensional numerical simulation of an oxy-acetylene torch reactor for diamond CVD at atmospheric pressure.[6] Both gas phase and surface chemistry were taken into account. From these calculations it was obtained that CO, H_2, H, OH and C_2H_2 are the major species beyond the flame front. The temperature profile and the transport of important radical species like atomic hydrogen and CH_3 towards the substrate were calculated, taking hydrodynamic gas phase properties like convection and diffusion into account.[7] Also the diamond growth rate has been calculated for various conditions in the oxyacetylene flame, agreeing reasonably well to experimental results.[7]

The mechanism of the diamond growth process is believed to be based on etching by atomic hydrogen. The carbon atoms of the top layer are connected to the diamond bulk below and their remaining bonds are either dangling or terminated by hydrogen atoms. The adsorbed hydrogen atoms can be etched away by gas phase atomic hydrogen, forming gas phase H_2, which leaves a free site on the surface. At such a site CH_3, which is thought to be an important growth species, may stick to one surface carbon atom and, after one or more of its hydrogen atoms have been desorbed, to a neighbouring one as well. Aside of H atoms other free radicals might be important for hydrogen abstraction from the surface as well. Apart from CH_3, the growth species may include CH, C_2, and CN, molecules often present in flames.

The exact deposition mechanism, however, is not well known and laser diagnostic techniques can be used to shed light on the flame processes and to obtain relations between the gas phase and the diamond layer characteristics, such as growth rate, morphology, and nitrogen incorporation. Two different techniques have been applied: two-dimensional Laser Induced Fluorescence (2D-LIF) and Cavity Ring Down Spectroscopy (CRDS). Both techniques are non-intrusive and species selective. The 2D-LIF method is applied because of its high spatial resolution and high sensitivity. The CRDS method yields absolute densities. The obtained information elucidates the role of flame species and their importance (or unimportance) for diamond growth. The relations between diamond growth and flame characteristics can be used as a monitor in the growth process, enabling fast feedback to obtain diamond layers with

properties closer to desired for industrial applications, and reveal which parameters are important for upscaling of the deposition area.

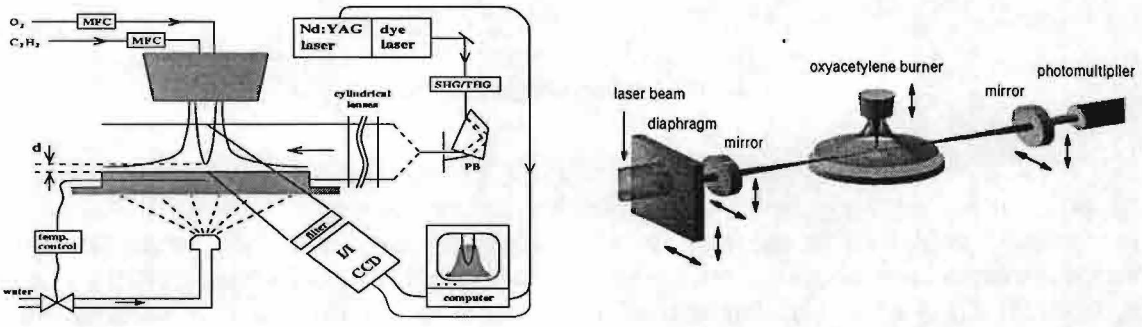

Figure 1 (left) Schematic representation of the diamond growth and LIF detection setup. MFC = mass flow controllers, SHG/THG = second/third harmonic generation (if applicable), PB = Pellin-Broca prism, I/I = image intensifier, CCD = charge coupled device camera. The distance d between the substrate and the tip of the flame front is indicated. Figure 2 (right) Schematic representation of the Cavity Ring Down setup; arrows denote directions of adjustment.

2. Experimental setup

The experimental setup for diamond growth combined with 2D-LIF or CRDS detection is schematically shown in Fig. 1 and 2, respectively. The setup has been described extensively elsewhere,[8,9] but the main details are given here. The deposition process is critically dependent on the acetylene supersaturation S_{ac}, which is why both the oxygen and acetylene flows are regulated by mass flow controllers. In addition to O_2 and C_2H_2 also controlled addition of nitrogen is possible. The burner orifice diameter is 1.4 mm and the oxygen flow is 3.0 standard liters per minute. Diamond growth can take place on a molybdenum substrate, positioned in the acetylene feather, for $0 < S_{ac} \leq 9\%$. For $S_{ac} > 9\%$ the deposit will not contain diamond anymore, but mostly amorphous carbon. In most experiments $S_{ac} = 5\%$ is used, resulting in an acetylene flow of ≈2.5 SLM. The substrate is cooled from below by a pulsed water nozzle, which is regulated by a thermocouple located 2.5 mm beneath the centre of the substrate surface. The temperature T_s at the substrate surface is kept at 1050 ± 20 °C. Prior to deposition the molybdenum substrate is scratched with micrometre sized diamond powder to enhance nucleation and adhesion to the substrate of the diamond layer to be grown.

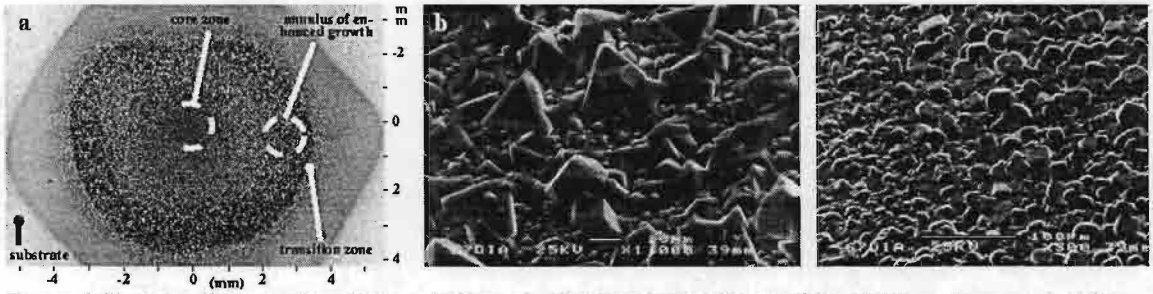

Figure 3 Photographs revealing the morphology of a diamond layer, deposited by a laminar flame at d=4.04 mm. (a) Normal photograph, showing the entire layer; various regions are indicated. The slight spherical asymmetry is caused by an irregularity in the burner tip. (b) SEM photograph of the core zone, *showing normal-sized crystallites embedded in many much smaller ones. The scale bar is 10 μm long. (c) Transition zone, revealing a highly {100} textured region, beyond the annulus of enhanced growth (which is located outside the upper right-hand corner of the image). At the left-hand side the small crystallites of the diamond layer edge become visible. The scale bar is 100 μm long.*

Apart from S_{ac} and T_s, the distance d between the tip of the flame front and the substrate is a main parameter in determining the growth process. Typical values of d are between 0.5 and 3 mm, where short distances result in a high central maximum in the diamond growth rate v_d (which can be more than 100 μm/h) and larger distances yield a central valley surrounded by an annulus of enhanced growth. Diamond layers deposited at a distance d of 1 to 2 mm reveal in their centre a continuous area of uniform thickness and well connected randomly oriented {111} and {100} facets. The diameter of this region is 4 - 5 mm. A photograph showing an entire diamond layer, deposited with a laminar flame at the somewhat larger distance d = 4.04 mm, is given in Fig. 3a. At distances d larger than about 3 mm a so called core zone of 2 mm in diameter is developed in the centre. In this core zone the crystallites mainly reveal {111} facets and also show a large amount of secondary nucleation, as can be seen in Fig. 3b, which gives a scanning electron microscope (SEM) photograph of the core zone. The large crystallites in this photograph, which are of normal size, are interspersed with many much smaller ones. Outside the centre an annular region of enhanced growth is observed, where the morphology is markedly different. This annulus typically exhibits large columnar crystallites, separated by voids or embedded in an amorphous layer, which frequently have {100} top facets almost parallel to the substrate. In Fig. 3a it appears darker than the centre due to a lower density of reflecting facets. Outside the annulus of enhanced growth a sharp transition zone is generally found, which is only 0.1 - 0.2 mm wide and can exhibit a continuous, highly {100} textured morphology. A SEM photograph of this zone is shown in Fig. 3c. Beyond this transition zone the morphology resembles that of the central area, with the size of the crystallites rapidly diminishing towards the edge of the diamond layer.

After growth the deposited diamond layers are characterized by optical microscopy, scanning electron microscopy (SEM), Raman spectroscopy, and cathodoluminescence topography (CL), which technique reveals information about the incorporation of nitrogen into the diamond layer. The diamond layer thickness is determined by focusing the optical microscope with an accuracy of ±2 μm at various locations of the layer.

3. Laser diagnostics

The application of the LIF technique is schematically shown in Fig. 1. The radiation of a Nd:YAG laser pumped dye laser (Quantel YG 781C10 + TDL-50, 7 ns pulses, repetition frequency 10 Hz, bandwidth 0.3 cm^{-1}, frequency doubled if needed) is shaped into a thin sheet by a cylindrical telescope, which traverses a vertical cross section of the flame. Fluorescence from the excited molecules is collected by a charge coupled device (CCD) camera equipped with an image intensifier, with an appropriate filter in front of it, and the signals are digitized by and can be further processed on a personal computer.

The LIF signal is proportional to the population density in the lower state of the species of interest. Determining this proportionality constant, *i.e.* quantification of the LIF signal, suffers from several problems. Due to collisions of the excited species with neighbouring species in the flame, part of the fluorescence is quenched. This quenching strongly depends on the local gas composition and temperature, which are unknown. Consequently the absolute determination of molecular densities by LIF is in general not possible in atmospheric flames. Most of the present LIF measurements concern relative densities in a layer parallel and close to the substrate, where the temperature is not expected to vary much. Hence the conclusions drawn from these results will not be affected much by neglecting temperature effects. However, it should be realized that the variation of the gas composition may have some influence on the results.

A schematic view of the CRDS setup is shown in Fig. 2. The CRDS technique is based upon the decay of a laser pulse inside an optically stable cavity formed by two plano-concave highly reflecting mirrors. After coupling in the cavity, the pulse is reflected many times between the mirrors. The intensity of the signal coupled out of the cavity shows an exponential decay in time. This decay is characterized by the 1/e ring down time τ, which depends on the reflectivity R of the mirrors, the distance L between the mirrors and the presence inside the cavity of species that reduce the intensity of the laser pulse *e.g.* by absorbing or scattering light [10]:

$$\tau(\nu)=\frac{L}{c}\left[\left|ln(R(\nu))\right|+\sum_i \sigma_i(\nu)\cdot\int_0^L N_i(x)dx+\sum_j S_j\right]^{-1} \qquad (1)$$

where c is the speed of light and ν the frequency of the laser light; the first summation is over all absorbing species i with absorption cross sections σ_i, with the integration over the entire length of the cavity; the second summation is over all losses other than the ones described by the first summation. It is important to note that τ does not depend on the intensity of the laser beam, meaning that the measurement of concentrations is not hampered by fluctuations in the laser power, which is a major advantage of CRDS over direct laser absorption. By determining the ring down times at an absorption peak of a certain species and at the baseline (on and off resonance, respectively), the absorption by the species can be obtained.

The same laser system was used as in the LIF measurements. The reflectivity of the plano-concave cavity mirrors (Laser Optik, radius of curvature 25 cm) was determined to be 0.997 at 430 nm. Together with the cavity length of 40 cm, this resulted in a ring down time of the empty cavity of 400 ns. A horizontal or vertical scan of the laser beam through the flame is made by selecting a 1.1 mm narrow beam out of the total laser beam by means of an extracavity diaphragm which can be positioned accurately in horizontal and vertical direction. In this way, a scan can be made over 4 mm from the axis without the need of changing the position of the incident laser beam. The alignment of the cavity is retained by adjusting the position of the mirrors each time the diaphragm has been moved. In every experiment, the laser beam transmitted through the diaphragm is aligned as close to the substrate as possible, in order to measure concentrations close to where the diamond formation takes place. Acquisition of the signal is performed using a fast photomultiplier tube (Thorn-EMI 9863 QA/350) coupled to an 8 bits 250 Msamples/s oscilloscope (LeCroy 9361). The oscilloscope is read out by a PC equipped with specially designed software to determine ring down times.

The measurements of the decrease of the ring down time τ yield a column density of a particular species in a specific energy state. In order to deduce the absolute density distribution, measurements are performed in a horizontal plane with steps of 0.5 mm up to 4 mm from the axis, whereafter an Abel transformation is performed on the obtained column density profiles. Hereto, the non-normalized data are fitted with third-order polynomials, which are transformed to yield the local molecular density N(r) by numerically solving:

$$N(r)=\pi^{-1}\int_r^R\left(dC/dy\right)\left(y^2-r^2\right)^{-1/2}dy \qquad (2)$$

where C is the fitted polynomial, y the distance with respect to the flame axis and R a cut-off radius defining an area outside which the species concentration is taken to be zero. When approaching r = 0, the obtained concentration goes to infinity due to the factor $(y^2-r^2)^{-1/2}$, so close to the flame axis the transformation does not yield reliable results.

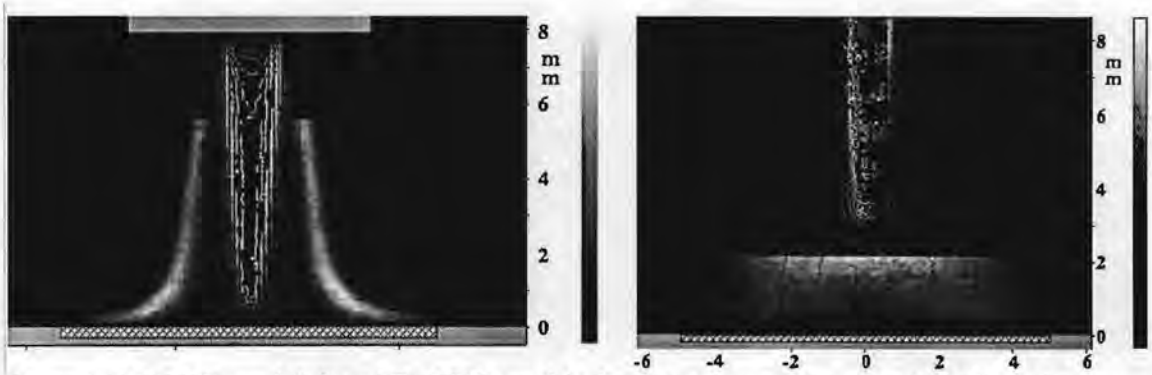

Figure 4 (a) CN LIF signal (left) and (b) H LIF signal (right) during diamond deposition in the flame (linear gray scale in arbitrary units, ranging from black (zero) to white (maximum)). Natural emission of the flame is superimposed (isophotes, representing equal intensity difference steps). The distance between flame front and substrate is d=0.55 mm (a) and d=3.05 mm (b). The images are corrected for the vertical intensity distribution of the laser beam (the noisy uppermost part is removed for reasons of clarity). The substrate and the burner tip are indicated in gray, the crosshatched area depicts the diamond deposition region, and dimensions are in mm.

4. Results and discussion

An example of a CN LIF signal is given in Fig. 4a. As can be seen CN is located at the edge of the acetylene feather and is not found at or close to the flame front. This may be explained by a mechanism in which the CN is formed from carbon containing species from inside the flame and nitrogen containing species from outside the flame. Because the flame is fuel-rich, the acetylene combustion is incomplete and species containing one or more carbon atoms are ubiquitous at and beyond the flame front. N_2 from the ambient air is entrained by the gas flow of the flame and diffuses into the acetylene feather, where it may be decomposed by thermal dissociation or reactions with radicals in the acetylene feather.

In Fig. 4b an LIF result is presented of atomic hydrogen in the first two millimetres above the substrate, which reveals H to be present inside as well as outside the acetylene feather. Measurements at various heights of the laser beam in the flame show that H LIF signal is also found at the flame front, where it is created. Atomic hydrogen diffuses rapidly throughout the flame and is consumed outside the acetylene feather by reactions with ambient air.

In order to study the species distribution close to the substrate in more detail, horizontal profiles are taken from LIF images obtained at various distances d. Figure 5 shows horizontal profiles of the C_2, CN, and H LIF signals, for each species, one at a relatively small distance d and one at a relatively large distance. Also shown in this figure is the lateral variation of the growth rate v_d of the corresponding diamond layers, which is measured along the path of the laser beam. The behaviour of the H and C_2 profiles is similar: for small distances d a clear central maximum is found and the LIF signal decreases more or less linearly with radial distance, whereas for large distances the central maximum is substituted by a central minimum. The presence of atomic hydrogen, however, extends radially further than that of C_2. For CN, however, a completely different behaviour is observed, showing a maximum at the position of the annulus of enhanced growth.

In Fig. 5 the annulus of enhanced growth is clearly visible in the variation of v_d. When v_d is compared to the radial distribution of the H LIF signal close to the substrate, it is striking that

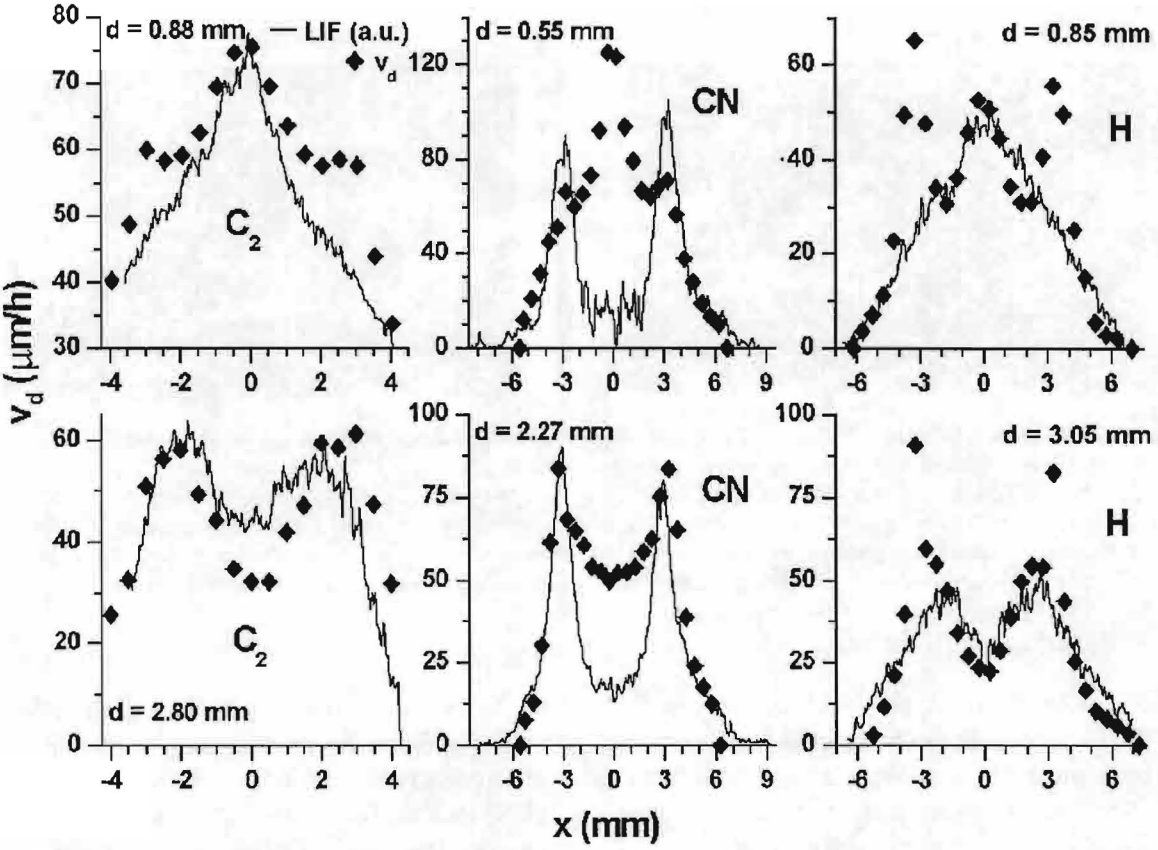

Figure 5 Horizontal profiles of the C_2 (left), CN (centre), and H (right) LIF signals (solid lines) compared to the variation of the growth rate v_d (diamonds) of the corresponding diamond layer, as measured along the path of the laser beam.

both show a very similar radial behaviour from the centre all the way to the edge of the diamond layer, if the annulus of enhanced growth is not taken into account. The good agreement between the H distribution close to the substrate and v_d (apart from the annulus of enhanced growth) indicates the importance of atomic hydrogen to the deposition rate of the diamond layer, which has already been studied elaborately in theory.[11-16] At the edge of the diamond layer atomic hydrogen is still found in measurable quantities, but diamond growth here is limited by the lack of carbon containing species. The correspondence between the C_2 profiles and v_d is similar to that of atomic hydrogen, although it is limited to a smaller area. The resemblance indicates that C_2 may be important for the diamond growth rate in the centre of the deposited layer, [8] which agrees to the role of C_2 as a diamond precursor, as put forward by Gruen and co-workers. [17-21]

Inspection of Fig. 5 shows that v_d drops much less rapidly with increasing distance d in the annulus of enhanced growth than in the centre of the diamond layer. In addition to this, the annulus of enhanced growth and the transition zone just outside it reveal a large fraction of {100} facets parallel to the substrate, compared to the centre and the outer edge of the diamond layer. These observations are strong indications that the growth mechanism in the annulus is different from elsewhere in the deposited diamond layer. This was investigated by measurements with controlled addition of nitrogen to the combustion gases.[22] It was found that the CN LIF signal in the central area is linearly proportional to the added nitrogen flow for nitrogen flows ranging from 0 to 100 sccm. As in the case of zero nitrogen addition, maxima are present at the annulus of enhanced growth for flows up to 25 sccm. The fact that

the maxima in the horizontal CN profiles coincide with the annulus of enhanced growth therefore indicates that CN or a closely related species (only one or two reaction steps away) may be important in the diamond growth process in the annulus, regarding both the morphology and the local growth rate. The influence of CN (or a closely related species) on the growth rate may be explained by the possibilities of CN and HCN to abstract adsorbed hydrogen from the growing diamond surface [23, 24], which creates free growth sites and may increase the local growth rate. The preferential formation of {100} facets parallel to the substrate in and close to the annulus of enhanced growth may also be related to the presence of CN or a closely related species, since similar morphologies have been observed upon nitrogen addition to flame and other diamond growing CVD systems [23, 25-28], in which studies also the positive effect of nitrogen addition to the diamond growth rate is described.

After growth the diamond layers are examined by cathodoluminescence to study the incorporation of nitrogen as nitrogen-vacancy pairs into the diamond lattice. Depending on the distance d between flame front and substrate and the exact composition of the acetylene and oxygen source gases, the nitrogen incorporation in the centre of the diamond layer is medium to completely absent, but in the annulus of enhanced growth always a maximum nitrogen incorporation is found. This can be explained by diffusion and subsequent thermal decomposition of ambient N_2 in the flame: outside the acetylene feather the temperature is too low for N_2 decomposition and close to the flame axis the diffusion of nitrogen decreases, resulting in a maximum amount of reactive nitrogen at the location where CN is found, *i.e.* above the annulus of enhanced growth. The CN LIF signal can therefore be used as an indicator for nitrogen incorporation into the diamond layer during the flame growth process.

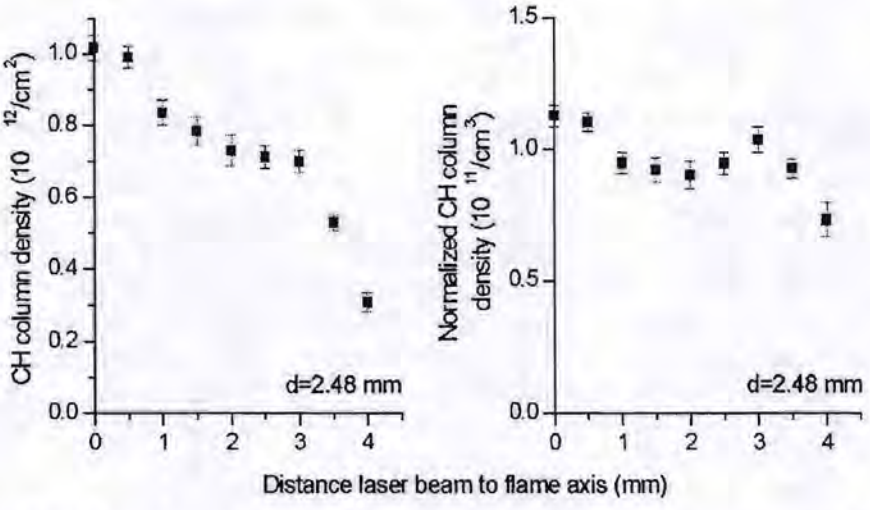

Figure 6 (a) CH column density as a function of the distance between the laser beam and the flame axis, measured by cavity ring down spectroscopy at a distance d = 2.48 mm between the conical flame front and the substrate, (b) CH density of (a) normalized with respect to the laser path length through the flame.

As an example of absolute density determinations the results of CRD measurements on CH are presented in Fig. 6. Here a profile of the CH column densities are given as a function of the distance from the flame axis for d = 2.48 mm, measured during diamond deposition. On the flame axis at an average height of 0.44 mm above the substrate, the CH column density is $1.0 \cdot 10^{12}$ cm^{-2}. The decrease of the column density with increasing distance from the flame

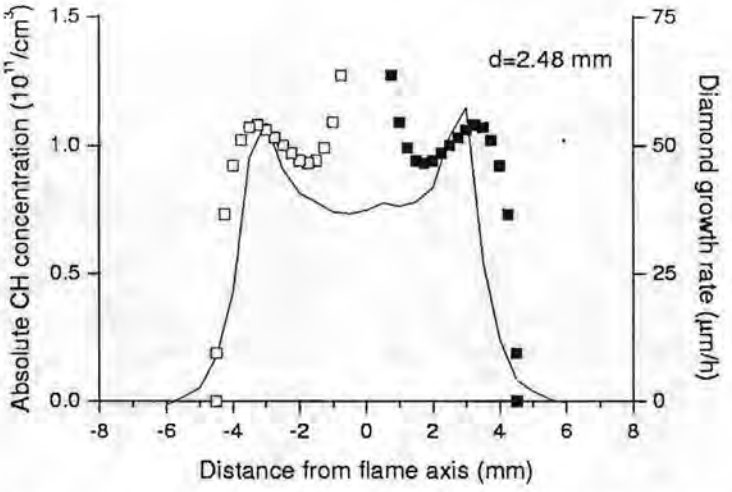

Figure 7 Absolute CH concentration profile (left ordinate), obtained from the profile of figure 6a by Abel transformation, and diamond growth rate profile of the deposited diamond layers (right ordinate); the solid line indicates the growth profile, filled squares indicate absolute CH concentration obtained via the transformation, open squares are mirror images of the filled ones with respect to the flame-axis.

axis is partly caused by the path length of the laser beam through the flame, which decreases as $(R^2-r^2)^{1/2}$, where R is a cut-off radius defining an area outside which the CH concentration is taken to be zero and r is the (radial) distance from the flame axis. Figure 6b shows the profile of Fig. 6a, corrected for this difference in path length, yielding normalized column densities. In the case of a homogeneous CH distribution, these profiles should be constant, which is clearly not the case. An Abel transformation was performed on the column density profile of Fig. 6a, resulting in the distribution which is shown in Fig. 7, together with the growth rate profile of the diamond layer deposited during the measurements. Similar to CN the CH distribution shows a maximum at the position of the annulus of enhanced growth.

Klein-Douwel *et alii* reported equal winglike features in 2D-LIF profiles of CH measured in the same experimental system under similar experimental conditions. One such LIF profile is shown in Fig. 8a.[8] In order to compare this profile, taken during diamond deposition at 1.20 mm, to CH column density profiles, a path integrated distribution profile was derived from the LIF profile. This was done by fitting a nine-term polynomial to it and transforming the obtained smooth curve to a path integrated signal. The result is shown in Fig. 8b, showing a CRDS profile measured during diamond deposition at d=1.37 mm with a height of the laser beam above the substrate of 0.73 mm, as well as the signal derived from the LIF measurements, which was scaled to the CRDS profile at y = 0 mm. The LIF based curve in Fig. 8b shows a good agreement with the CRDS data, which leads to the conclusion that the LIF measurements yield reliable relative CH concentrations which can be calibrated by a comparison with the CRDS results.

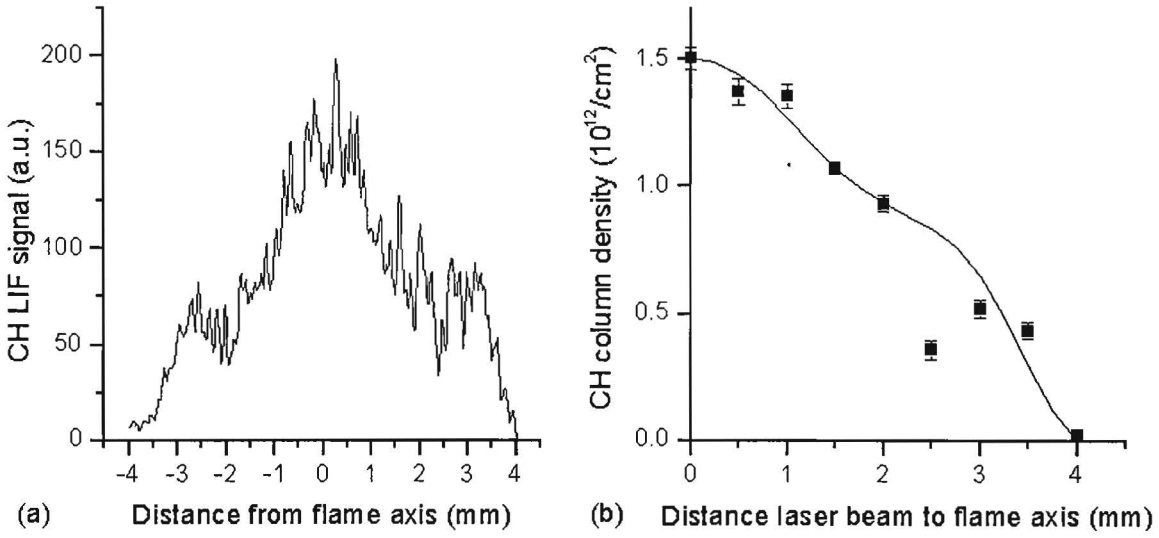

Figure 8 (a) CH LIF profile, recorded during diamond deposition at d=1.20 mm by Klein-Douwel et al. [8], (b) comparison of a path integrated LIF signal, derived from (a), and the CRDS profile measured during diamond deposition at d=1.37 mm at a height of 0.73 mm between the laser beam and the substrate.

The similarity between the distributions of CN and CH gives rise to the suggestion that CH, like CN, may play some role in the formation of the annulus as well. A possible reason for the similarity of the CH and CN distributions could be a reaction or reaction scheme in which CH is a precursor of CN. One reaction scheme in which this may be the case is the prompt NO mechanism, which is one of the pathways for NO_x formation in hydrocarbon combustion.[30, 31] In the first step of this mechanism, CH reacts with atmospheric nitrogen to give HCN [31]:

$$CH + N_2 \rightarrow HCN + N \qquad (3)$$

HCN reacts further to NO or N_2 in a number of steps, in which CN is one of the possible intermediate species. Another possibility to link the CH distribution to that of CN is the reaction [31]:

$$CH + N \rightarrow CN + H \qquad (4)$$

in which CN is formed directly from CH. The question whether CH is actually of importance in the formation mechanism of the annulus of enhanced growth and, if so, what its exact role in this mechanism is, should await further research.

5. Conclusions

Flame deposition of diamond by the oxy-acetylene flame is a relatively simple and fast technique to grow diamond layers. Yet the exact growth mechanism is not well known and therefore molecule specific laser diagnostic techniques were applied to the flame during diamond growth. It was demonstrated that 2D-LIF is a powerful and highly sensitive technique to obtain information about molecular density distributions. Although quantification of the LIF signal is hampered by collisional quenching, the obtained signals of H, C_2, and CN reveal much information about the diamond growth process. Relations are observed between the distributions of these three species in the flame and the growth rate, morphology, and nitrogen incorporation of the diamond layers.

As a complementary technique Cavity Ring Down Spectroscopy can be used to determine absolute molecular densities. Absolute CH concentration profiles were deduced from column density profiles by applying Abel transformation processing, showing annular structures of enhanced concentration, that have a position similar to that of the annulus of enhanced growth. This may indicate a role of CH in the formation mechanism of enhanced growth areas, which makes closer investigation of the CH radical in relation to flame CVD relevant. The obtained concentration profiles are in agreement with previous LIF measurements on CH, thus offering a calibration method for the LIF results.

References

1. Y. Hirose and N. Kondo, Extended Abstracts, 35th Jpn. Appl. Phys. Spring Meeting, March 1988, p. 434
2. Y. Matsui, A. Yuuki, M. Sahara, and Y. Hirose, Jpn. J. Appl. Phys. 28 (1989) 1718
3. G. Janssen, W.J.P. van Enckevort, J.J.D. Schaminee, W. Vollenberg, L.J. Giling, and M. Seal, J. Cryst. Growth 104 (1990) 752 (1990)
4. L.M. Hanssen, K.A. Snail, W.A. Carrington, J.E. Butler, S. Kellogg, and D.B. Oakes, Thin Solid Films 196 (1991) 271
5. J.J. Schermer, J.E.M. Hogenkamp, G.C.J. Otter, G. Janssen, W.J.P. van Enckevort, and L.J. Giling, Diamond Relat. Mater. 2 (1993) 1149
6. M. Okkerse, C.R. Kleijn, M.H.J.M. deCroon, H.E.A. van de Akker and G.B. Marin, J. Appl. Phys. 88 (2000) 4417
7. M. Okkerse, Thesis, Technical University Delft (2000)
8. R.J.H. Klein-Douwel, J.J.L. Spaanjaars, and J.J. ter Meulen, J. Appl. Phys. 78 (1995) 2086
9. R.L. Stolk and J.J. ter Meulen, Diamond Relat. Mater. 8 (1999) 1251
10. R.T. Jongma, M.G.H. Boogaarts, I. Holleman, G. Meijer, Rev. Sci. Instrum. 66 (1995) 2821
11. G. Janssen, W.J.P. van Enckevort, and L.J. Giling, Proc. First Int. Symp. on Diamond and Diamond-like Films, J.P. Dismukes (ed.), The Electrochemical Soc., Pennington, 508 (1989)
12. M. Frenklach and K.E. Spear, J. Mater. Res. 3 (1988) 133
13. M. Frenklach, J. Appl. Phys. 65 (1989) 5142
14. M. Frenklach and H. Wang, Phys. Rev. B 43 (1991) 1520
15. S.J. Harris and D.G. Goodwin, J. Phys. Chem. 97 (1993) 23
16. A. Ohl, J. Röpcke, and W. Schleinitz, Diamond Relat. Mater. 2 (1993) 298
17. D.M. Gruen, S. Liu, A.R. Krauss, and X. Pan, J. Appl. Phys. 75 (1994) 1758
18. D.M. Gruen, S. Liu, A.R. Krauss, J. Luo, and X. Pan, Appl. Phys. Lett. 64 (1994) 1502
19. D.M. Gruen, C.D. Zuiker, A.R. Krauss, and X. Pan, J. Vac. Sci. Technol. A 13 (1995) 1628
20. D.A. Horner, L.A. Curtiss, and D.M. Gruen, Chem. Phys. Lett. 233 (1995) 243
21. P.C. Redfern, D.A. Horner, L.A. Curtiss, and D.M. Gruen, J. Phys. Chem. 100 (1996) 11654
22. R.L. Stolk, M.M.J.W. van Herpen, J.J. Schermer and J.J. ter Meulen, to be published
23. S. Bohr, R. Haubner, and B. Lux, Appl. Phys. Lett. 68 (1996) 1075
24. A. Badzian, T. Badzian, and S.-T. Lee, Appl. Phys. Lett. 62 (1993) 3432
25. R. Locher, C. Wild, N. Herres, D. Behr, and P. Koidl, Appl. Phys. Lett. 65 (1994) 34
26. W. Muller-Sebert, E. Worner, F. Fuchs, C. Wild, and P. Koidl, Appl. Phys. Lett. 68 (1996) 759
27. S. Jin and T.D. Moustakas, Appl. Phys. Lett. 65 (1994) 403
28. G.Z. Cao, J.J. Schermer, W.J.P. van Enckevort, W.A.L.M. Elst, and L.J. Giling, J. Appl. Phys. 79 (1996) 1357
29. R.J.H. Klein-Douwel and J.J. ter Meulen, J. Appl. Phys. 83 (1998) 4734
30. C.P. Fenimore, 17th Symp. (Int.) Comb., The Combustion Institute, Pittsburgh, 1979, p. 661.
31. J. Warnatz, U. Maas, R.W. Dibble, Combustion, Springer-Verlag, Berlin Heidelberg, 1996, ch. 17.

A new self-calibrated method for precise quantitative analysis by laser induced breakdown spectroscopy

Dunja Bulajic, Michela Corsi, Gabriele Cristoforetti, Stefano Legnaioli, Vincenzo Palleschi, Azenio Salvetti and Elisabetta Tognoni

Istituto di Fisica Atomica e Molecolare del CNR
Area della Ricerca del CNR
Via Alfieri, 1 – 56010 S.Giuliano Terme (Pisa) ITALY
http://www.ifam.pi.cnr.it
e-mail: vince@ifam.pi.cnr.it

Introduction

The LIBS (Laser Induced Breakdown Spectroscopy) technique is a fast and essentially non-destructive diagnostic method, based on the analysis of the spectral emission of the plasma produced by focusing an intense laser beam on the sample to be investigated. Typical temperatures and electron densities in the induced plasma can reach several eV and 10^{18} electrons/cm^3. After irradiation, the de-excitation of the atoms and ions in the focal spot produces characteristic emission lines; the spectral region of interest for LIBS analysis is typically in the 200-800nm range.

The LIBS technique doesn't require sample preparation and can be applied on samples of arbitrary shapes in solid, liquid or gaseous status. The measuring time is very short (seconds); moreover, with the use of new spectral detection systems (Echelle spectrometers) a fast mapping of the sample surface can be performed in a short time. However, LIBS applications to diagnostic systems were limited, up to now, to qualitative or semi-quantitative information on material composition [1]. In particular cases, the LIBS signal due to an atomic element shows a linear response vs. the element concentration into the sample, allowing to perform quantitative analysis using calibration curves obtained from reference samples of known composition. This is usually verified for trace elements. However, the concentration of major components is more difficult to measure, because of the so-called 'matrix effect': the differences in electronegativity and ionisation potential between the atomic components of the sample usually lead to competition phenomena that induce non-linearities in the spectral line intensity as a function of element concentration. In order to perform quantitative measurement of the major components, calibration curves are needed in a range of composition the closest possible to that of the unknown sample. Since the aim of a measure is often to analyse unknown samples, such a requirement leads to a logical loop in the measurement procedure.

With the aim of overcoming the matrix effect and its adverse influence in LIBS quantitative analysis, the Istituto di Fisica Atomica e Molecolare in Pisa has developed and patented an innovative algorithm for LIBS quantitative analysis without calibration curves. Assuming that some simple conditions are verified, this new self-calibrated LIBS method (CF-LIBS) allows obtaining quantitative information by interpreting the experimental results using the equations describing the plasma [2].

The dynamic range of CF-LIBS technique is remarkably wide: the technique gives simultaneously quantitative information about concentrations ranging from 90% down to parts per million.

The new CF-LIBS method developed at IFAM could become a viable alternative to the traditional analytical procedures (AAS, ICP, etc.). A number of applications have been

suggested: as an example, automatic control in industrial processes or monitoring of polluted soils can be mentioned. The technique has already been tested at IFAM laboratories for the analysis of metallic alloys, yielding excellent results with respect to measurement quickness (a few seconds), sensitivity (1 ppm), precision (better than 1 %), possibility of in situ operation, cheapness. The technique has also been applied in the field of Cultural Heritage conservation for determining analytical composition of pigments, ancient bronze objects, and ceramic glazes.

Experimental set-up

The CF-LIBS experimental set-up is analogous to the apparatus required for traditional LIBS measurements. The experimental prototype for LIBS analysis, operating since several years at IFAM-CNR Institute in Pisa [3-6], is sketched in fig.(1).

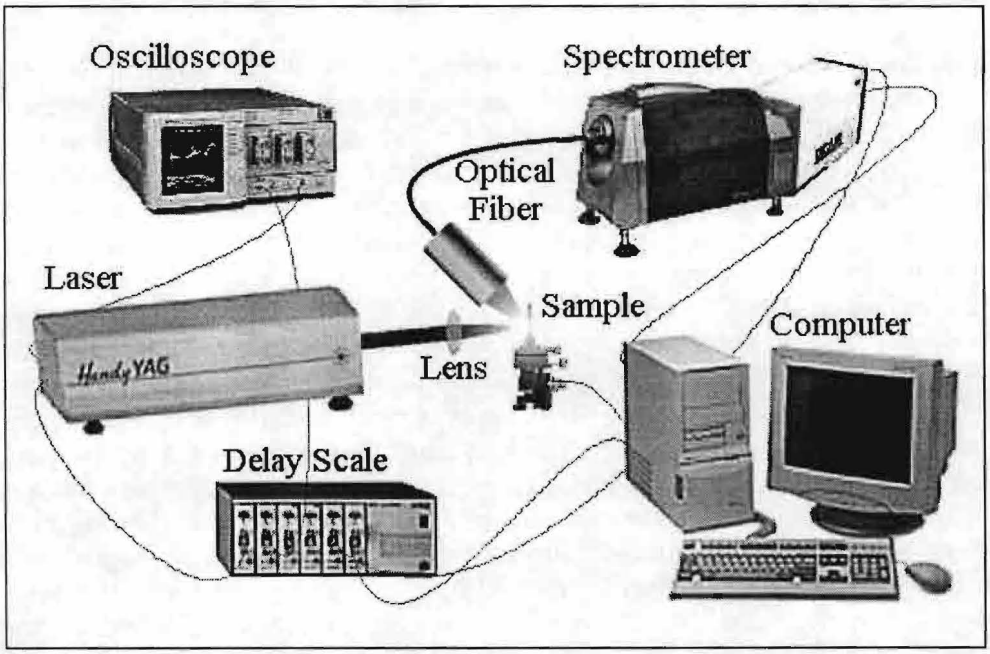

Figure 1: *Experimental LIBS setup*

The prototype uses a Q-switched Nd-Yag laser, delivering about 600 mJ at 1064 nm in 7ns pulses, at a maximum repetition rate of 10Hz, for generating a micro-plasma at the sample surface. The laser beam is focused on the sample by means of a lens of 20 cm focal length. The light emitted by the sample is collected using an optical system and then sent through an optical fibre to an Echelle type spectrometer (Mechelle 7500 by Multichannel Instruments, Sweden) coupled with an intensified CCD camera (PCO). The use of an Echelle spectrometer allows acquiring a whole spectrum (from 200 to 900 nm) in a single laser shot, thus greatly reducing the time needed for the measurement. The importance of using Echelle spectrometers in LIBS measurements has been discussed in ref. [7]. The resulting spectrum is analysed by computer using specialised software developed at IFAM. A typical spectrum is reported in fig. (2). Using a suitable delay scale the CCD camera is triggered 10 μs after the laser pulse, in order to reduce the contribution of the continuum *Brehmsstrahlung* radiation to the LIBS signal. A gate width of about 5 μs is used, which allows obtaining a good LIBS

signal in a regime where space and time variations of plasma parameters are almost negligible [8]. Under these conditions, the LIBS spectra are obtained by averaging over about 10 laser shots. The sample is placed on a motorised translation stage for changing the measurement point after a few laser shots, in order to avoid the formation of deep craters on the sample surface that might change the laser-sample coupling efficiency.

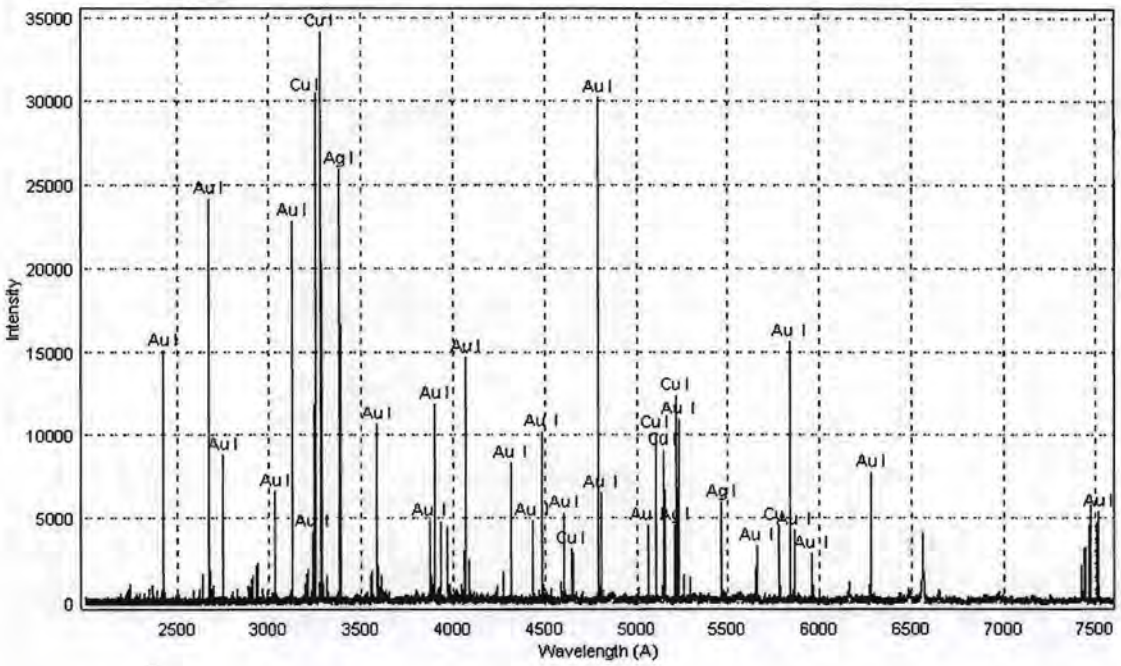

Figure 2: *LIBS spectral signal collected during the analysis of a Au-Ag-Cu alloy. Specific lines emitted by different species are marked.*

The CF-LIBS algorithm

The method used for the analysis of LIBS spectra has been described in detail elsewhere [7-9], therefore we will just present here the basic characteristics of our approach. As starting hypotheses of the procedure we assume that the plasma in Local Thermodynamic Equilibrium (LTE) and is thin for the radiation. The validity of the LTE approximation in our experimental conditions seems confirmed *a posteriori* by the Boltzmann-like distribution of atomic levels obtained and by some simulation models of LIBS plasma expansion [11]. The second hypothesis is certainly verified for lines emitted by trace elements but can become unreliable for the resonant lines that come from major elements with higher concentration in the plasma; so, in order to obtain a reliable estimate for the material composition, we must apply a correction to the results which accounts for this non linear effect. This problem will be treated theoretically more in detail in a forthcoming paper; here we limit ourselves to a discussion of the fundamental results of this procedure.

According to the initial hypotheses, the LIBS line integral intensity corresponding to the transition between two levels E_k and E_i can be expressed as:

$$(1) \qquad I_\lambda^{ki} = \mathrm{FCA}_{ki} \frac{g_k \exp(-E_k/kT)}{U(T)}$$

where λ, C, A_{ki}, g_k and F are the wavelength of the transition, the concentration of the emitting atomic specie, the transition probability for the given line, the k level degeneracy and a constant to be determined after normalisation of the specie concentrations, respectively. U(T) is the partition function for the emitting specie defined as: ·

$$U(T) = \sum_k g_k \exp(-E_k/kT) \tag{2}$$

Taking the logarithm of eq. (1) and substituting the following definitions:

$$\begin{aligned} y &= ln\ \frac{I_\lambda^{ki}}{g_k A_{ki}} \\ m &= -\frac{1}{kT} \\ x &= E_k \\ q &= ln\ \frac{CF}{U(T)} \end{aligned} \tag{3}$$

we obtain a linear relationship between the y and x parameters

$$y = m\,x + q \tag{4}$$

which can be graphically represented as a 'Boltzmann plot' (see an example in fig.3). According to eq. (3), the slope of the plot is related to the species temperature. In the framework of the LTE model, this temperature is the same for all the species. Thus, it is possible measuring the temperature of one or several species (for example AuI, CuI and AgI in fig.3) and using the same temperature for the other species (AgII in fig.3) , for which the slope of the plot is not obtainable with sufficient precision..

The dispersion of the experimental points is due both to the experimental uncertainties and to the uncertainties existing on the A_{ki} parameters in the literature. The overall error in the Boltzman plot can be estimated as the standard deviation of the points with respect to the best linear fit.

The q parameter in eq. (4) is proportional to the logarithm of the species concentration via the F constant factor. The F factor can be determined by normalising the species concentrations as

$$\sum_k C_k = 1 \tag{5}$$

The application of the above-described method to, for example, metallic alloys allows to obtain the concentration of all the components of the alloys, including the trace elements in concentrations down to the detection limit of the technique (typically 1 ppm), without the need of calibration. The minimum error in alloy composition determination is of the order of the concentration of the undetected elements.

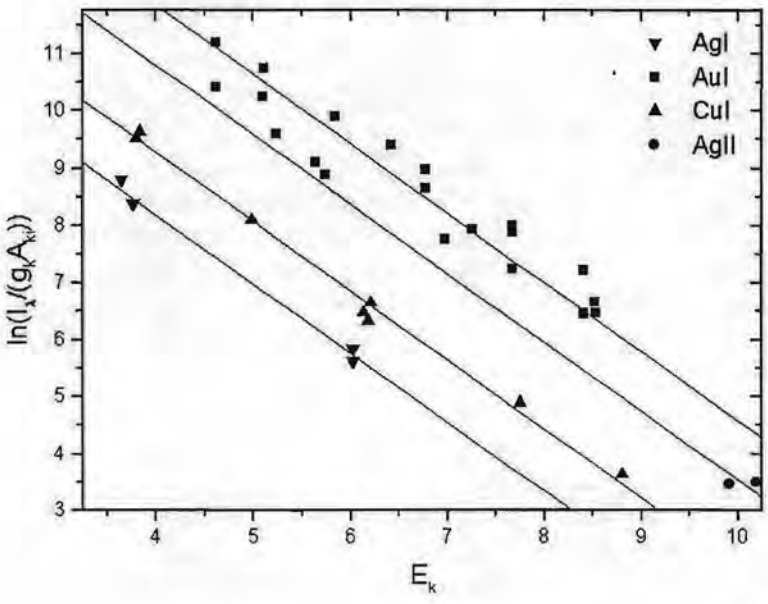

Figure 3 : *Boltzmann plot for a Au-Ag-Cu alloy. Continuous lines represent the result of a linear best fit. Note that the best fit lines corresponding to different species are practically parallel, i.e. the temperature of all the species in the sample is the same (within the experimental errors), according to the predictions of LTE.*

Applications

The procedure here proposed can be applied for the analysis of solid, liquid and gaseous samples. A few results are described in the following as an example of different fields of application that could get benefits from the features of CF-LIBS technique.

Gold caratage in precious alloys and analysis of steel samples

In order to test the accuracy of the LIBS prototype and the reliability of the above-described method, we performed a CF-LIBS analysis on three steel NIST certified samples (NIST 1155, NIST 1171 and NIST 1172) and three ternary precious alloys (Au200, Au750 and Au917) of know composition.

The LIBS analysis was performed using a 2 μs delay and 5 μs gate; the results were averaged over 50 laser shots. The point of analysis was moved on the sample surface in order to avoid the formation of a large crater. In both cases the self absorption correction algorithm was applied.

The precious alloys were ternary (Au, Ag and Cu) in the form of irregular foils of about 10mm x 10mm x 0.5mm, corresponding to gold concentrations of 200/1000, 750/1000 and 917/1000 in weight [10].

The results are reported in figure 4; it's interesting to note the improvement due to self absorption correction. The standard deviation of the CF-LIBS determined caratage from the 'perfect correlation' line is about 0.1%; the accuracy of the CF-LIBS measurements thus lies in the same range as that of cupellation (fire assay) technique.

It would be interesting to compare the accuracy of the CF-LIBS results with the ones that could be obtained from exactly the same experimental data by using conventional calibration techniques. In this case one should build one calibration curve by plotting the intensity of one (or more) Au lines versus the nominal Au concentration. Unfortunately, because of the unavoidable fluctuations in laser energy and laser-sample coupling, the scattering of the experimental data with respect to a hypothetical calibration line is very high. This error would greatly affect the precision of LIBS measurements based on the standard calibration techniques, since the calibration curve should be obtained with exactly the same experimental configuration used in the measurements (laser energy, laser-sample coupling,...). Moreover one should build different calibration curves for the different possible compositions of the precious alloy to be analysed in order to avoid the problems deriving from the "matrix effect". These results reinforce our considerations on the difficulty of obtaining precise determination of the material composition, with conventional LIBS techniques based on calibration curves, on unknown samples.

The analysis of metallic samples is also very important in industry, usually for monitoring the production process and the quality of products.
The results obtained for the three steel samples are reported in fig. 5.
It is evident that the self-absorption correction leads to a more accurate determination of the material composition with respect to the standard CF-LIBS approach, with an improvement in precision of about one order of magnitude.
Moreover, it should be noted that the absolute error in the concentration determination is greater for steel measurements (about 1% after correction) than gold alloys (about 0.2%); this is due in part to the high complexity of the steel spectra and to the fact that the lines of the major element in steel (Fe) are in general more self-absorbed that the major elements (Au, Ag, Cu and, eventually, Pd) of the precious alloys.

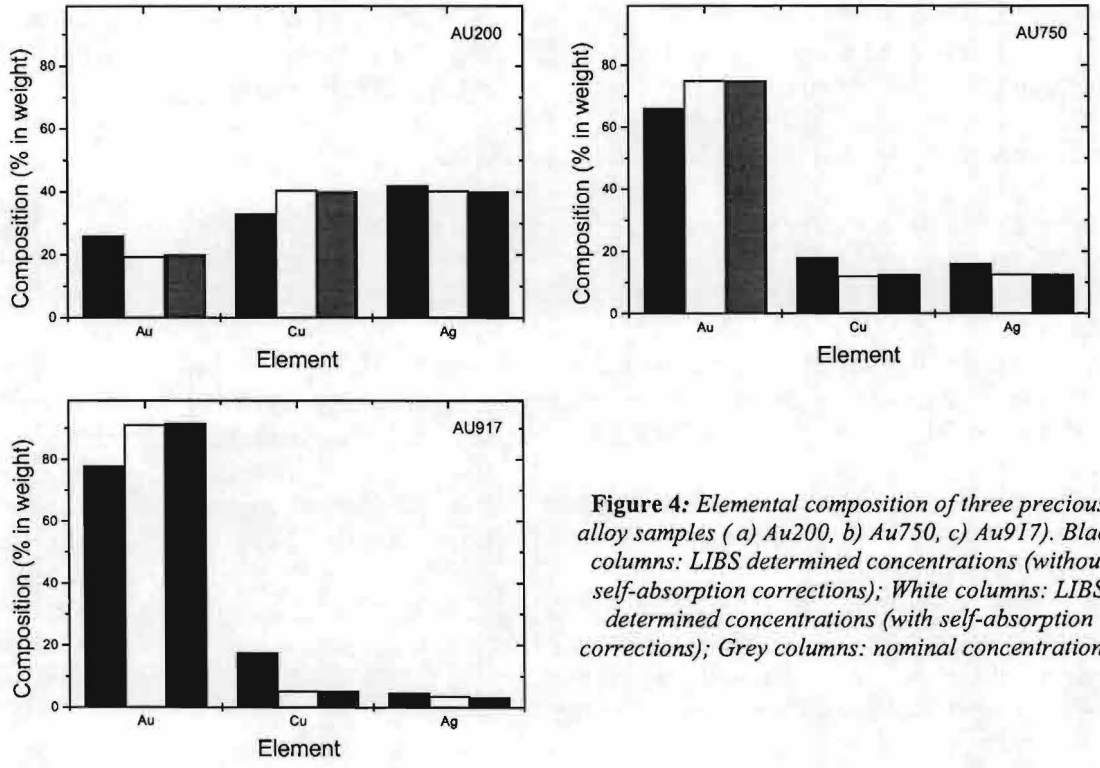

Figure 4: *Elemental composition of three precious alloy samples (a) Au200, b) Au750, c) Au917). Black columns: LIBS determined concentrations (without self-absorption corrections); White columns: LIBS determined concentrations (with self-absorption corrections); Grey columns: nominal concentrations.*

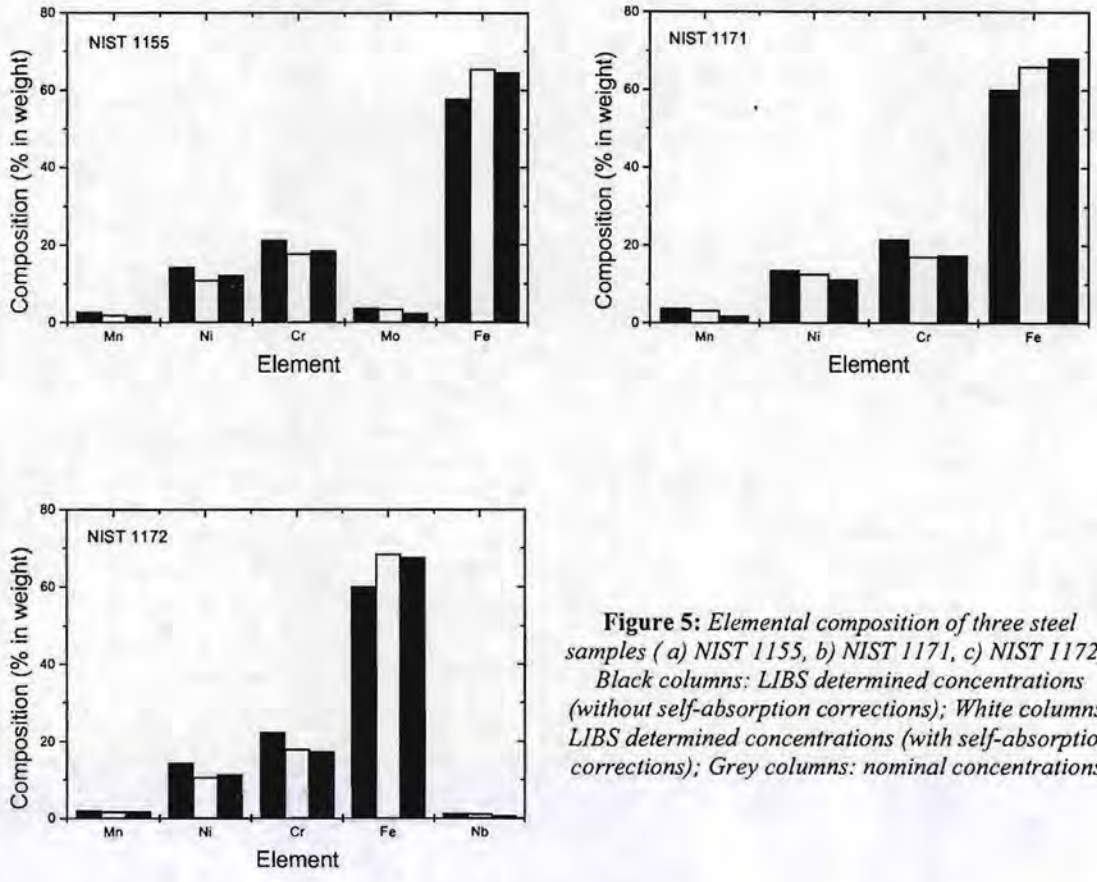

Figure 5: *Elemental composition of three steel samples (a) NIST 1155, b) NIST 1171, c) NIST 1172). Black columns: LIBS determined concentrations (without self-absorption corrections); White columns: LIBS determined concentrations (with self-absorption corrections); Grey columns: nominal concentrations.*

Quantitative analysis of pigments used in Art conservation

In recent years, a great deal of interest has been devoted to laser applications to Cultural Heritage study, both in the fields of artwork conservation and analysis. Among them, Laser Induced Breakdown Spectroscopy seems to be one of the most promising approach because it can be performed *in situ* and is essentially micro-destructive (optimising the experimental set-up the hole left on the sample can be reduced down to a few microns in diameter); a number of applications have been suggested, ranging from automatic control of the laser cleaning process to paintings analysis for study and authentication. Thanks to new approach developed at IFAM, it's now possible to obtain precise quantitative information on composition of materials of interest in Cultural Heritage conservation, without need for reference samples or calibration curves.

In order to demonstrate the application of CF-LIBS method to paintings analysis, we determined the elemental composition of five artificial pigments (Titanium white, Zinc white, Cadmium Yellow, Cadmium Red, and Ultramarine Blue). A typical section of spectrum is shown in fig.6 for the five samples; the emission lines of the characteristic components are well recognisable, making simple the qualitative identification of the different pigments. The results of quantitative analysis are reported in fig.7.

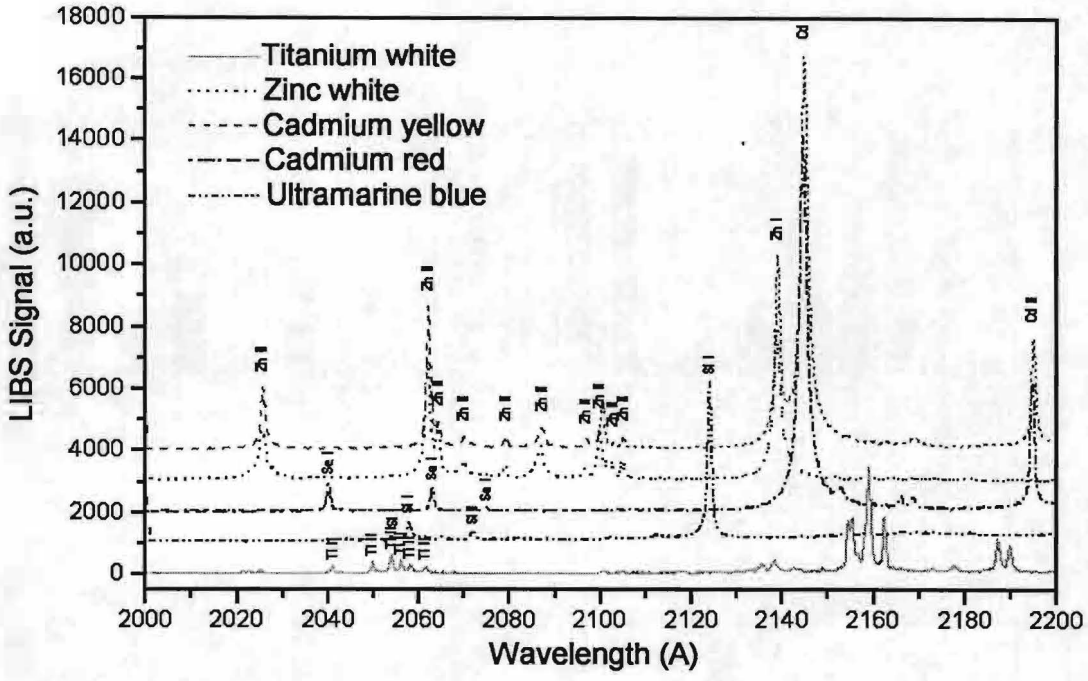

Figure 6: *A section of the spectrum of the five pigments considered.*

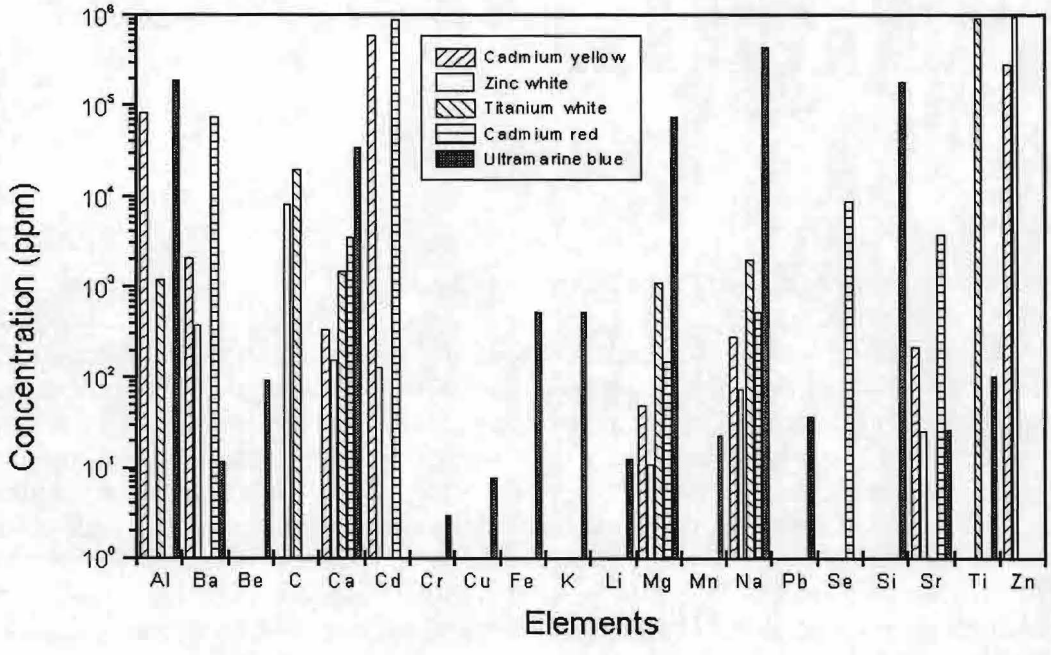

Figure 7: *Composition of the pigments obtained by CF-LIBS*

Conclusions

LIBS is a fast and essentially non-destructive diagnostic method which can be used directly *in situ*. The samples don't need to be prepared and can be solid, liquid or gaseous.
Using the proposed calibration-free procedure developed and patented at IFAM-CNR in Pisa, precise quantitative results can be obtained in a few minutes without need of reference samples. Both major components and trace elements (down to concentrations of order of 1 ppm) can be simultaneously measured. The accuracy of the measurements is strong improved with the new algorithm, which accounts for the self absorption effect.
The application of CF-LIPS allows to overcome the so called 'matrix effect', which has been up to now the major obstacle to practical LIBS applications to multi-elemental quantitative analysis.

References

[1] A.S.Eppler, D.A.Cremers, D.D.Hickmott, M.J.Ferris and A.C.Koskelo, *Appl. Spectrosc.*, **50** (9) (1996) 1175-1181
[2] A. Ciucci, M. Corsi, V. Palleschi, S. Rastelli, A.Salvetti and E. Tognoni, *Appl. Spectrosc.*, **53** (8) (1999) 960
[3] Lazzari C., De Rosa M., Rastelli S., Ciucci A., Palleschi V. and Salvetti A., *Laser and Particle Beams* **12** (3) (1994) 525.
[4] Ciucci A., Rastelli S., Palleschi V., Barbini R., Colao F., Fantoni R., Palucci A., Ribezzo S., and Van Der Steen H. J. L., *Appl. Phys. B* **63** (1996) 185.
[5] Arca G., Ciucci A., Palleschi V., Rastelli S. and Tognoni E., *Detection of pollutants in liquids by Laser Induced Breakdown Spectroscopy Technique, Proceedings of IGARSS*, 27-31 May 1996, Lincoln, Nebraska, pp. 520-522.
[6] Arca G., Ciucci A., Palleschi V., Rastelli S. and Tognoni E., *Appl. Spectrosc.* **51** (8) (1997) 1102.
[7] Ciucci A., Palleschi V., Rastelli S., Salvetti A. and Tognoni E., *Appl. Spectrosc.*, 53 (1999) 960.
[8] Capitelli M., Capitelli F., Eletskii A. *Spectrochimica Acta Part B* **55** (2000) 559
[9] Corsi M., Palleschi V., Salvetti A. And Tognoni E., *Research Advances in Applied Spectroscopy* **1** (2000) 41
[10] Corsi M., Cristoforetti G., Palleschi V., Salvetti A., Tognoni E., *The European Physical Journal D*,**13** (3) (2001) 373
[11] Vidal et al., private comunication

Pulsed and continuous wave cavity ring-down spectroscopy probes of chemical vapour deposition plasmas

Andrew J. Orr-Ewing
School of Chemistry, University of Bristol
United Kingdom.

1. Introduction

The prospect of being able to synthesise diamond films suitable for many different applications ensures continued effort towards understanding the precise nature of the chemical physics that underlies diamond chemical vapour deposition (CVD). The process involves activation of an appropriate gaseous mixture in the vicinity of a substrate upon which polycrystalline diamond will deposit. Most laboratory research to date has been centred on hot filament (HF) or low power (a few kW) microwave (MW) activation, using comparatively simple benchtop reactors, though most industrial production now involves high power microwave systems or the use of dc plasma jets. The gas mixture used most commonly consists of small amounts (~1%) of a hydrocarbon (usually methane) in hydrogen. Commonly used substrates for supporting diamond film growth include Si, Mo and W, all of which show the necessary tendency for interfacial carbide formation at the optimum growth temperature (~900 °C). Any thorough understanding of diamond CVD requires knowledge of the chemical environment in the vicinity of the diamond film during growth. Thus we need information on factors such as the gas phase species present, the sources, interconversion and sinks of the key reactive (radical) species, their spatial distribution and their transport through the gas, the chemistry occurring at the gas-surface interface, and the way in which all of these factors vary with, for example, temperature, pressure and the extent of activation (*i.e.* filament temperature or applied microwave power). Much of this potential complexity is illustrated schematically in fig. 1.

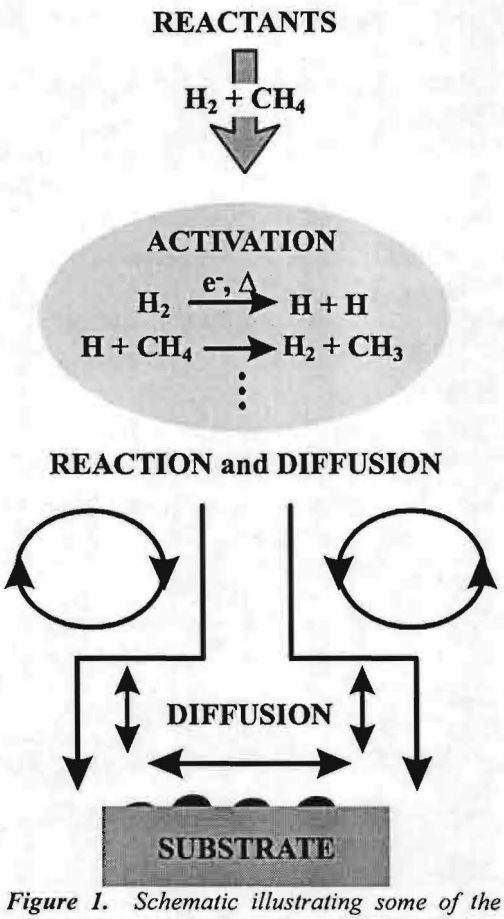

Figure 1. *Schematic illustrating some of the more important processes occurring during diamond CVD*

The central differences in the various deposition methods are the way in which the precursors are activated and how they are transported to the growth surface. However, common to nearly all methods is the production of atomic hydrogen, which is the driving force behind both the gas phase and many of the gas-surface reactions. The parent H_2 molecule may be dissociated on the surface of a heated filament (HFCVD), by electron bombardment in microwave plasma assisted reactors (MW-PACVD) or in the arc jet of a plasma torch. The resulting H atoms begin a series of abstraction reactions in the gas phase and many species can result from the host of reactions

facilitated by the large amounts of atomic hydrogen. The local steady state gas phase composition and the resulting CVD diamond film qualities and growth rates are largely independent of the source hydrocarbon. Stable species that have been monitored in diamond CVD reactors include H_2, CH_4, C_2H_2 and C_2H_4 using techniques such as coherent anti-Stokes Raman spectroscopy (CARS), vacuum ultraviolet (VUV) absorption, mass spectrometry (MS) and infrared (IR) absorption. Laser techniques are attractive in that they offer an unobtrusive, spatially localised measure both of the local gas temperature and of the concentration of the particular species being probed.

Radical chemistry governs the majority of CVD diamond growth with the methyl radical, CH_3, being most favoured as the key growth species in low power (*e.g.* HF or MW-PACVD) reactors. Optical diagnostics applied to the measurement of CH_3 radicals in diamond CVD environments include IR, UV and VUV absorption spectroscopy, resonance enhanced multiphoton ionisation (REMPI) spectroscopy and, most recently, cavity ring down spectroscopy (CRDS). C atom concentrations have also been monitored using VUV absorption, while C_2 and CH radicals have been monitored via their spontaneous emission, by laser induced fluorescence (LIF), degenerate four wave mixing (DFWM), CRDS, and absorption spectroscopy.

Given the presence of reactive radical species in diamond CVD, it is necessary to consider both gas phase and gas-surface reactions for any comprehensive understanding of the growth mechanism. Models that include both gas-phase and gas-surface reactions have made significant recent advances, particularly for hot filament systems where the chemistries at the filament, substrate and the intermediate area can be treated by assuming them to be separable. and the most sophisticated models treat the full three dimensionality of the heat and species flux transfer processes in the vicinity of the hot filament and substrate. Accurate profiling of atom and radical concentrations is now all the more important for the purpose of validating these models.

2. Previous optical diagnostic experiments at Bristol

A hot filament CVD reactor has been used as a model system for developing optical probes and understanding the chemistry of the CVD environment. Some of the previous work on laser detection of H and CH_3 used to characterise the chemistry of the reactor is summarised briefly here.

(a) REMPI detection of H atoms

The concentration of atomic H in the vicinity of the growing diamond surface is a critical factor determining film quality and growth rates. H atoms initiate most of the gas phase chemistry in low power CVD reactors. They continuously create (by abstraction of surface terminating hydrogen atoms) and re-terminate (thereby preventing the reconstruction to non-diamond forms) the reactive surface sites necessary for the propagation of the diamond lattice. H atoms also preferentially etch much of the non-diamond carbon deposited. The slow homogeneous recombination rate of atomic hydrogen at typical reactor pressures and temperatures is such that a super-equilibrium concentration exists in the vicinity of the substrate surface even though this is often remote from the point at which H atoms are produced.

We previously investigated and validated H atom detection by REMPI at the excitation wavelength of 243.1 nm, resonant at the two photon energy with the n=2←n=1 transition, where unintentional photochemistry of molecular species present in the gas mixture is unlikely. H^+ ions formed in the probe volume were collected on a 750 μm diameter Pt wire probe maintained at –48.5 V, the end of which was positioned ~1.5 mm from the laser focus.

Figure 2 shows representative lineshapes of the 2s←1s two photon transition of atomic H recorded by 2+1 REMPI. The lineshape of the frequency doubled probe laser makes minimal contribution to the measured linewidth and, after deconvoluting this contribution, the remaining linewidth is ascribed to Doppler broadening, with $\Delta\nu_D$, the FWHM linewidth, providing a measure of the local translational temperature:

$$\Delta\nu_D = \frac{\nu_0}{c}\sqrt{\frac{8kTln2}{M}} \qquad (1)$$

where ν_0 is the line centre transition frequency, c is the speed of light and M is the mass.

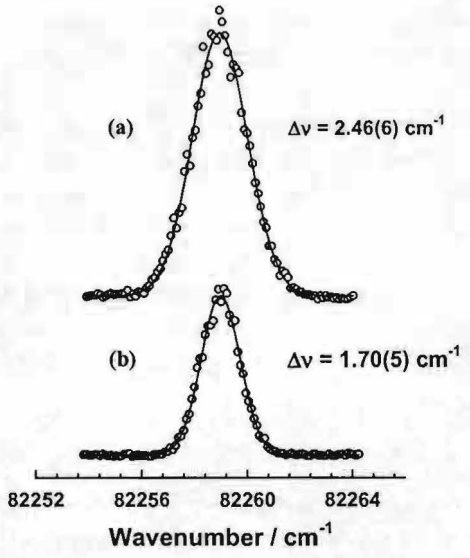

Figure 2. Doppler lineshapes of the H atom 2s←1s two photon transition recorded in 20 Torr of pure H_2 at (a) d = 0 and (b) d = 10 mm from a Ta filament held at T_{fil} = 2375 K. The FWHMs of fitted Gaussian functions yield the local temperature, while the integrated areas provide a measure of the relative H atom number density.

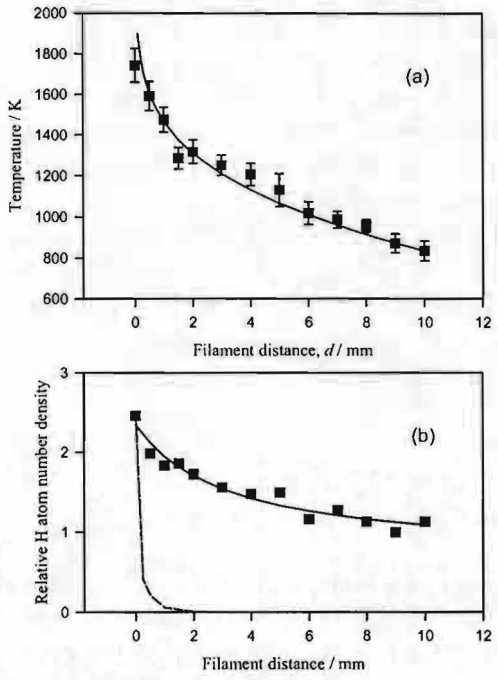

Figure 3. Variation of (a) the local gas temperature and (b) [H] in 20 Torr of pure H_2 with T_{fil} = 2360 K, as deduced from analysis of the H atom 2s←1s two photon lineshapes, plotted as a function of d. The dashed curve shows the relative H atom number density expected for thermal equilibrium at the measured local gas temperature.

Figures 3(a) and (b) show, respectively, the H atom translational temperature and the relative number density profile measured in 20 Torr of pure H_2 (100 sccm flow rate), each plotted as a function of the distance from the filament, *d*. The results are consistent with the view that H atoms in HFCVD reactors are produced at the hot filament surface, and diffuse into the bulk. The H atom recombination rate at typical reactor pressures and temperatures is so slow that a 'super-equilibrium' concentration of H atoms exists throughout much the reactor (see dashed line in fig. 3) including, most importantly, in the vicinity of the substrate surface.

(b) REMPI detection of CH_3

The CH_3 radical is the dominant carbon containing radical species in HF and MW-CVD environments, appearing with a mole fraction ~10% that of CH_4 under standard growth

conditions. We have used laser wavelengths of ~333 nm to detect CH_3 radicals via the origin band of the $3p_z; {}^2A_2'' \leftarrow \tilde{X}\ {}^2A_2''$ transition using 2+1 REMPI. Two correction factors must be applied to convert a REMPI signal measured at one wavelength within the CH_3 ($3p_z \leftarrow \tilde{X}$) origin band into a relative number density of CH_3 radicals. The first recognises that the origin band contour is itself a temperature dependent function, and that measurements made at any one REMPI probe laser wavelength will thus sample a temperature dependent fraction of the total REMPI signal. The second, more substantial, correction recognises the temperature dependence of the vibrational partition function of the CH_3 radical. Thus the measured CH_3 REMPI signals must be scaled to reflect the trend in populations of the v"=0 level in order to obtain *total* CH_3 relative number densities. Figure 4 shows the radial dependence of the measured CH_3 REMPI signals obtained using gas mixtures comprising (a) 1% CH_4 in H_2 and (b) 0.5% C_2H_2 in H_2, both at total pressures of 20 Torr, a gas flow rate of 100 sccm and T_{fil} = 2200 K, together with best estimates of the d dependence of the *total* CH_3 number density after inclusion of the temperature dependent corrections described above.

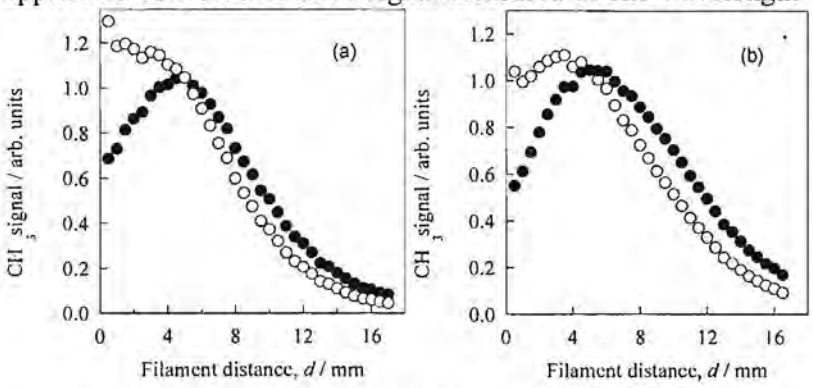

Figure 4: *radial dependence of the CH_3 REMPI signal for (a) 1% CH_4 in H_2 and (b) 1% C_2H_2 in H_2. ● experiment; O corrected data.*

3. Cavity ring-down spectroscopy

(a) Methods

CRDS is an ultrasensitive absorption spectroscopy technique that is relatively simple to implement experimentally. It is based on injecting a laser pulse into a cavity bounded by two ultra-high reflectivity mirrors, as shown schematically in figure 5. The laser pulse is trapped within the cavity (retro-reflecting from both mirrors) for many thousands of round trips (if R > 99.9 %) and thus a pathlength of many kilometres can be established within a benchtop apparatus. The technique has numerous applications in spectroscopy, kinetics, analytical and atmospheric chemistry. It has also been applied as a probe of a variety of plasmas, with detection of, for example, CF, SiF_2, AlF and CF_2 in etching plasmas generated by RF discharge in fluorocarbon gases,[1] and H(n=2) atoms[2] and CH radicals[3] in an Ar/C_2H_2 plasma.

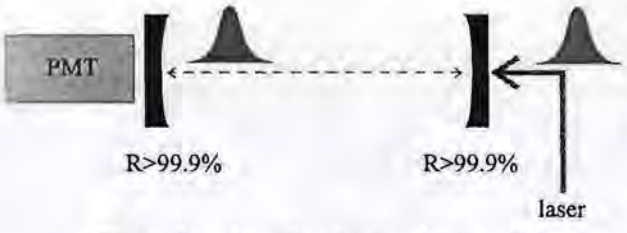

Figure 5: *schematic of a ring-down cavity.*

The simplest treatment of pulsed laser CRDS approximates that a light pulse trapped within the cavity bounces back and forth between two ultra-high reflectivity mirrors. For each reflection of the light pulse at a mirror of reflectivity R, a small fraction (1-R) of the light leaks through the mirror. Thus, for an empty cavity, the light intensity decays gradually to zero. A sensitive light detector placed behind one mirror would, if fast enough, detect a series of pulses. More usually the detector response time will smooth out the individual

pulses to give an exponential decay of detected intensity with time. The time dependence of the intensity for a cavity of length ℓ is given by:

$$I(t) = I_0 \exp\{-t/\tau\} \tag{2}$$

where

$$\tau = \frac{\ell}{c|\ln R|} \approx \frac{\ell}{c(1-R)} \tag{3}$$

is the empty-cavity ring-down time, the time for the intensity to decay to 1/e of its original value. For a cavity bounded by two mirrors of reflectivity R, the number of round trips, N, performed in the time taken for the intensity to fall to 1/e of its initial value is obtained as

$$R^{2N} = \frac{1}{e} \quad \text{or} \quad N = \frac{-1}{2\ln R}. \tag{4}$$

Thus, for example, for a mirror reflectivity of 0.999, N=500 whereas for R=0.99999, N=50000, giving a pathlength in a 1-m cavity of 100 km. Such high reflectivities are feasible with modern mirror coatings.

If an absorbing species is introduced into the cavity, and the laser is scanned in wavelength, then when the frequency of the laser matches an absorption of the sample gas, the resultant additional loss mechanism for light from the cavity speeds up the decay of the trapped light intensity. For absorption conditions corresponding to Beer-Lambert law behaviour, the decay of light intensity will still be exponential with time dependence given by:

$$I(t) = I_0 \exp\left\{-\frac{t}{\tau} - \alpha c t\right\} \tag{5}$$

where α is the molecular absorption coefficient (with dimensions of length^{-1}, generally quoted in cm^{-1}), and c is the speed of light. The product of c and t is the pathlength, L, over which the absorption is measured. The decay rate is now given by

$$\frac{1}{\tau'} = \frac{1}{\tau} + c\alpha. \tag{6}$$

This equation can also be written in terms of the change in decay rate of the ring-down signal,

$$\Delta k = \frac{1}{\tau'} - \frac{1}{\tau} = c\alpha. \tag{7}$$

The measurement of Δk thus gives α directly at any particular frequency. If the absorption cross section, σ, is known at the wavelength of the experiment, then the concentration of the absorbing species, [X], can be determined using $\alpha = [X]\sigma$.

CRDS has been used as a probe of HF-CVD reactors using the $\tilde{B} - \tilde{X}$ electronic transition of the CH_3 radical.[4] Knowing the absorption coefficient of CH_3 radicals at 213.9 nm, and making an educated guess as to the absorption length over which they are likely to be present in a HFCVD reactor (~ the length of the hot filament), Zare and co-workers estimated CH_3 number densities, as a function of distance from the filament, and as a function of both filament and substrate temperature, and found the CH_3 number density to peak ~4 mm from the hot filament rather than at the filament itself.

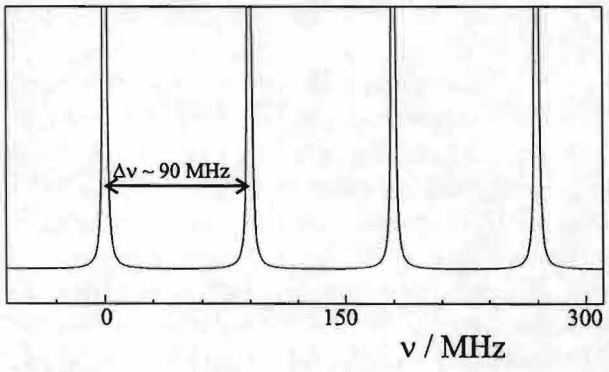

Figure 6: *mode structure of a high finesse cavity*

The simplified picture of CRDS presented above assumes that all frequencies of the laser pulse can be

injected into the cavity. The typical longitudinal mode structure of a high finesse ring down cavity is shown in figure 6, and the spacing of the modes (which depends upon the mirror separation, and in this instance is ~0.003 cm^{-1}) is generally much smaller than the bandwidth of a pulsed laser (~0.1 cm^{-1}), permitting coupling of laser light into the cavity regardless of the nominal wavelength of the laser. Likewise, the widths of spectral lines will usually exceed the cavity mode spacing under room temperature or hotter conditions, so spectral features will not be missed. The use of cw lasers (such as external cavity diode lasers (ECDLs)) for CRDS, however, presents additional complications because of their much narrower bandwidths (~ 1 MHz). The frequency of the laser must be matched to the frequency of a cavity mode for build-up of light intensity within the cavity to occur. If this can be arranged, however, a rapid switch-off of the laser beam following cavity excitation causes a ring-down with single-exponential decay character because only a single cavity mode is excited. Several methods exist for matching the laser and cavity frequencies including cavity locking, or modulation of either the cavity length or the laser frequency. Alternatively, the cavity mode structure can be made so dense that the likelihood of excitation is greatly enhanced. Figure 7 shows a diagram of a diode laser CRD spectrometer incorporating modulation of the cavity length or the laser frequency.

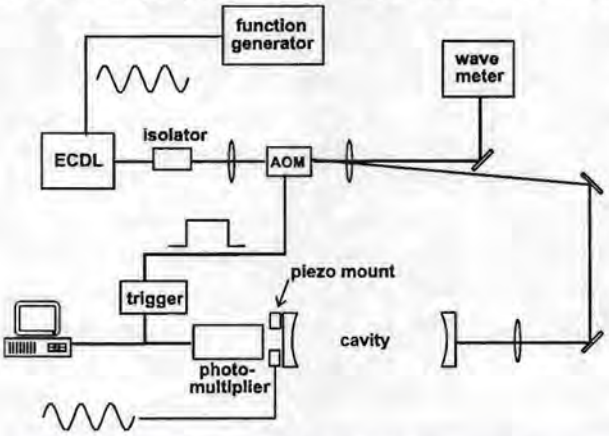

Figure 7: schematic of a cw CRDS experiment.

(b) Advantages of CRDS

CRDS has numerous advantages over competing techniques: REMPI is restricted to non-ionized environments whereas LIF signal can be hard to differentiate from a radiant background. Moreover, fluorescence time-scales can be ns to μs, so competitive collisional quenching or excited state dissociation can destroy the LIF signal. CRDS can be used against a brightly radiant background, and at a variety of pressures, without concern for collisional quenching of the excited state. The change in the ring-down time when tuned to an absorption can be directly related to the concentration of absorbers if the absorption cross section is known. Excitation can occur to discretely structured or continuous excited states, and absorption can be measured in ionised environments such as plasmas, with sensitivity greatly in excess of CARS or DFWM. Its primary disadvantages are that overlapping absorptions by different species are not distinguished unless a spectrum is scanned, and absorption is averaged over a column defined by the laser beam, so is not specific to a single point in the plasma.

4. Description of the experimental apparatus

(a) HF-CVD reactor

Figure 8 shows a schematic of the Bristol CVD reactor incorporating a CRDS probe. The chamber comprises a six-way cross. Two side ports are equipped with flange mounted quartz windows to allow entry and exit of the probe laser beam, and high reflectivity mirrors are mounted inside the windows. The mirror and window assemblies are connected to the main chamber by edge-welded bellows and can be adjusted by micrometers to align the ring-down cavity. The reactor part of the apparatus is designed so that it can be translated vertically by ≤ 25 mm relative to the fixed ring-down axis to enable spatially resolved profiling of key

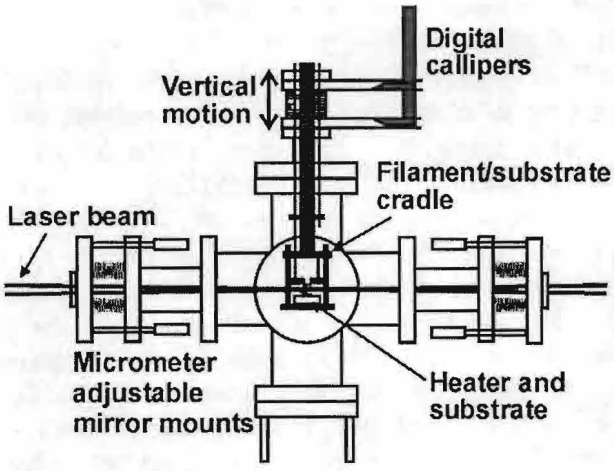

Figure 8: schematic diagram of the modified HF-CVD reactor.

species. This is achieved by suspending a cradle beneath a linear transfer mechanism attached to the top flange on which are located filament mounting posts, substrate heater plate and electrical feed-throughs. Attached to the mechanism is a pair of digital callipers, which permit positioning of the cradle with sub-millimetre precision. The cradle can also be rotated through any angle to allow measurements to be carried out along, or perpendicular to, the filament axis. Power is supplied to the filament and substrate heater by two separate DC power supplies operating in constant current mode. The 7-turn filament is wound from 250 m diameter tantalum wire and has a coil diameter of ~3 mm. Typically, in pure H_2, the filament draws 6.5 A at ~12.5 V, maintaining a colour temperature of ~2100 °C as measured by a two-colour optical pyrometer. The substrate, when in place, is mounted on a purpose designed heated copper block, and the substrate temperature monitored by a type K thermocouple tip embedded in the top surface of this block.

Prior to growth, the chamber is evacuated to a base pressure of ~10^{-2} Torr. A typical growth run employs 0.5 % CH_4 in H_2, which is pre-mixed in a manifold and then fed into the reactor through a port located above the cradle assembly. Mass flow controllers (MFCs), in series with a needle valve are used to maintain a total flow of 100 sccm at a chamber pressure of 20 Torr. When diamond is to be grown, a substrate (normally a 1 cm^2 piece of silicon wafer, pre-abraded with fine diamond grit) is attached to the heater plate and the filament–substrate separation chosen (normally in the range 4-6 mm). Scanning electron microscopy (SEM) and laser Raman spectroscopy are used to verify successful CVD diamond growth.

(b) DC arc jet

DC-arc jet plasmas operating with hydrocarbon/H_2/Ar gas mixtures enable chemical vapour deposition (CVD) of high quality diamond films at growth rates unobtainable using the more traditional hot filament or microwave reactors. The DC-arc jet therefore provides an excellent environment in which to study the mechanism of diamond CVD. The DC-arc plasma jet thus far has been monitored by spatially resolved optical emission spectroscopy (OES) only, with particular reference to emissions from electronically excited H atoms, and C_2 and CN radicals both along the length of, and transverse to, the arc jet axis. We hope to present the results of first CRDS probing of the arc jet environment at the meeting.

Figure 9 provides a schematic illustration of the experimental apparatus used for film deposition and for optical probing of the plasma. The DC-arc jet plasma is generated using a twin torch head arrangement (Aeroplasma Corp.) designed to operate at up to 10 kW discharge power. Twin torch arrangements such as this provide improved plasma stability over single torch systems. The N-torch is designed to propagate a stable plasma flow by incorporating a secondary spiral jet stream of pre-mixed Ar and H_2 into the primary Ar plasma prior to the converging-diverging nozzle orifice. Methane and, when required, N_2 are introduced into the Ar/H_2 plasma through an annular injection ring (I in fig. 9) positioned 100 mm downstream from the nozzle. All gas flows are metered using appropriate mass flow

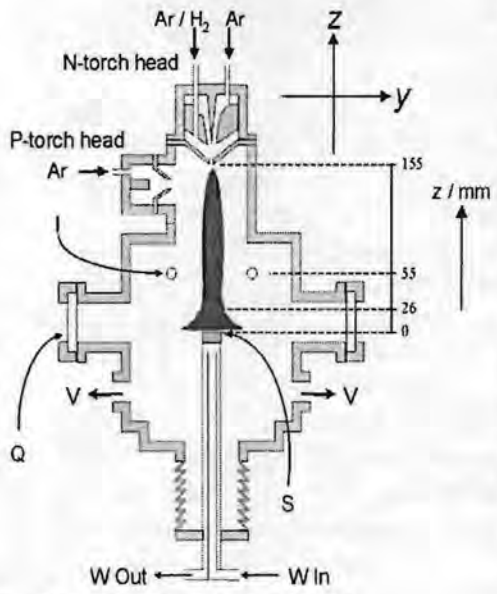

Figure 9: schematic of the dc arc jet.

controllers. The plasma impinges normal to the surface of a water-cooled polished molybdenum substrate (16 mm diameter), positioned 155 mm from the nozzle exit, on which the polycrystalline diamond film condenses. The pressure in the reaction chamber is monitored continually and controlled at 50 Torr. The chamber is water-cooled and evacuated to a base pressure of 50 mTorr. Input powers to the arc jet are 5.9 kW (78 V, 76 A). The diamond films delaminate on cooling and are analysed as free-standing. Growth rate and surface topology are revealed by SEM, while laser Raman spectroscopy provides an indication of film quality.

(c) Lasers

For detection of CH_3 radicals, 213.9 nm radiation is generated by frequency doubling the fundamental output of a dye laser pumped by the third harmonic of an Nd:YAG laser. The frequency doubled laser beam is focussed through a spatial filter prior to injection into the ring-down cavity. Typical ring-down times are 400 ns, and a single exponential fit to the ring-down decay is used to determine the ring-down rate, k. Care is taken to ensure that the logarithm of the decay trace is a linear function over the range of decay times fitted. Individual ring-down events are fitted, and the resultant k values averaged over 1000 laser shots. The ring-down time in the absence of methyl absorption is determined by turning off the flow of CH_4 to the HF-CVD reactor.

Continuous wave near IR radiation is generated by a external cavity diode laser (Newport), tuneable over the range ~ 1.29 - 1.32 μm. The laser beam shape is circularised using a pair of anamorphic prisms, and is focussed through an acousto-optic modulator prior to injection into the ring-down cavity, with mode matching achieved by an f=500 mm lens. The light exciting the cavity is detected by an InGaAs photodiode and amplified by a high gain fast amplifier. When the transmitted signal exceeds a user-selected threshold, the AOM is switched on a 10-ns timescale and ring-down of the light intensity that has built up in the cavity is observed. The first experiments using this laser will probe the methane absorption on an overtone band at 1.31 μm. The diode laser wavelength is scanned by ramping a voltage to a piezo mount supporting the laser cavity mirror, and is modulated about the ramp voltage to ensure mode matching to the cavity. Ring-down traces are recorded either on an 8-bit digital oscilloscope or a 12-bit DAQ card (National Instruments) and are analysed using custom programs within LabView.

5. What do these measurements tell us about the chemistry of hot filament reactors ?

The REMPI studies demonstrate that the concentration of H atoms is almost invariant to the pressure of H_2, and its concentration decreases monatonically with distance from the filament, consistent with the assumption that, at the prevailing pressures and temperatures, the dominant H atom formation mechanism is H_2 bond fission on the surface of the hot filament. Diffusion is the dominant transport mechanism in low pressure (*e.g.* HFCVD) reactors. The

local gas temperature as determined from Doppler lineshape analysis of H atoms increases approximately linearly with increasing T_{fil}, but even 1 mm from the filament is ~700 K cooler than the filament surface as measured by optical pyrometry.

Addition of even trace amounts of CH_4 leads to carburisation of the filament and complicates the chemistry prevailing in a HFCVD reactor considerably, by introducing a wider variety of surface sites and offering new and efficient reactive loss mechanisms (both heterogeneous and homogeneous) for H atoms. The observation, that the CH_3 signal maximises at $d > 0$, *i.e.* away from the filament, is in marked contrast to the measured H atom number density. Nonetheless, the qualitative form of the radial profile of the CH_3 signal is readily explicable once it is recognised that the CH_3 number density is largely determined by the gas phase equilibrium

$$H + CH_4 \rightleftharpoons CH_3 + H_2 \qquad (8)$$

and that, although the H atom number density decreases monotonically with increasing d, the *total* gas number density (and thus the CH_4 number density) increases with d due to the inverse dependence between number density and T_{gas} (at constant pressure). These deductions are verified by 3-D numerical simulations of a representative HFCVD reactor which include a full set of heat and mass transport equations and include detailed gas phase reaction mechanisms, diffusion, H atom production at the filament, and gas-surface chemistry at the substrate.

The present data suggest that the apparently excellent agreement between the CRDS data and theory may be somewhat fortuitous, however. The CRDS measurements return column densities, along which there is inevitably a marked temperature variation. Just as in the CH_3 REMPI study, the absorbances measured by CRDS will necessarily be sensitive to any temperature dependence in the spectrum and ground state partition function, but the monitoring wavelength was chosen because of the reported temperature invariance of the CH_3 absorption cross-section of 213.9 nm. Absorption measurements at this wavelength may also be contaminated by overlapping contributions from hot bands of C_2H_2, which arise whenever CH_4/H_2 gas mixtures are used for diamond CVD. Both the total C_2H_2 number density and the fraction of the population contributing to long wavelength hot band absorption will depend on T_{gas}, and thus vary along the column length.

Other C_1 species such as C atoms and CH radicals have concentrations that depend upon the various equilibria

$$CH_x + H \rightleftharpoons CH_{x-1} + H_2, \qquad (9)$$

where x = 1-4. Each reaction involves at most a small activation barrier in either direction, so equilibration is rapid. Numerical simulations confirm CH_3 to be the dominant C_1 radical species in HF or low power MWCVD reactors (*i.e.* at low H/H_2 ratios), but in highly activated environments (*e.g.* a plasma torch reactor) C atoms will dominate.

C_2 radicals themselves will be present both in their ground ($X^1\Sigma_g^+$) and low lying excited ($a^3\Pi_u$) electronic states in any diamond CVD reactor. Since the singlet radicals, in particular, react very rapidly with H_2, and collision induced singlet-triplet interconversion will be efficient at typical process pressures, we should anticipate low (*c.f.* $[CH_3]$) steady state C_2 concentrations. Such accords with experiment. H atom abstraction from C_2H_2 is an endothermic process, implying that the C_2H radical number density should also be low. Such an expectation is borne out by MBMS studies which failed to identify C_2H amongst the gas phase species present during diamond CVD.

For C_2H_2/H_2 feedstock gas mixtures, the current understanding regarding CH_3 radical formation when using hot filament activated C_2H_2/H_2 gas mixtures is not clear cut. Numerous

studies have demonstrated that CVD diamond may be grown, with comparable quality and efficiency, using either CH_4 or C_2H_2 as the carbon precursor. A variety of *in situ* studies have demonstrated C_2H_2 conversion into CH_4, that the C_2H_2/CH_4 mixing ratio at typical process temperatures is essentially independent of the hydrocarbon feedstock gas used, and the presence of CH_3 radicals. Possible gas phase and surface catalysed routes for converting C_2H_2 to CH_3 have been proposed but which, if either, is the dominant contributor to the measured CH_3 concentrations remains uncertain. Most simulations suggest no conversion from C_2H_2 to any other hydrocarbon via gas phase chemistry, in marked contradiction to the experimental observation and it has therefore been concluded, almost by default, that C–C bond breaking must involve adsorption, hydrogenation and subsequent desorption on hot surfaces within the reactor. Recent 3-D modelling studies, however, challenge this assertion by proposing a gas phase mechanism for CH_3 formation from C_2H_2 in the cooler regions of the reactor.

6. Work in progress

We are currently exploring the use of CRDS for detection and concentration profiling of several different radical and molecular species in hot-filament and DC arc-jet reactors. In particular, we are using pulsed visible and UV CRDS to probe C_2 and CH_3 in hydrocarbon / H_2 gas mixtures, and are exploring the formation of CH_3 radicals from C_2H_2/Ar feedstock gas mixtures. Moreover, we are using UV CRDS to study the role of radicals such as NH and CN in reactors seeded with small amounts of NH_3 or N_2. Also under development is the use of cw CRDS in the near IR using an ECDL to measure concentrations and temperatures of hydrocarbons via their C-H stretching vibrational overtones and combination bands. Early results from these studies will be presented at the conference.

7. Acknowledgements

This article draws upon the work of several colleagues at the University of Bristol, and I am particularly grateful for the contributions from Professor M.N.R. Ashfold, J.A. Smith, J.B. Wills and H. Moores.

8. References

[1] J.P. Booth, G. Cunge, L. Biennier, D. Romanini and A. Kachanov, Chem. Phys. Lett. **317**, 631 (2000)
[2] M.C.M. van de Sanden, M.F.A.M. van Hest, A. de Graaf, A.H.M. Smets, K.G.Y. Letourneur, M.G.H. Boogaarts and D.C. Schram, Diamond Relat. Mater. **8**, 677 (1999).
[3] R. Engeln, K.G.Y. Letourneur, M.G.H. Boogaarts, M.C.M. van de Sanden, and D.C. Schram, Chem. Phys. Lett. **310**, 405 (1999).
[4] P. Zalicki, Y. Ma, R.N. Zare, E.H. Wahl, T.G. Owano, and C.H. Kruger, Appl. Phys. Lett. **67**, 144 (1995); E.H. Wahl, T.G. Owano, C.H. Kruger, P. Zalicki, Y. Ma, and R.N. Zare, Diamond Relat. Mater. **5**, 373 (1996).

Corona discharges: fundamentals and diagnostics

E.M. van Veldhuizen, W.R. Rutgers
Faculty of Applied Physics, Technische Universiteit Eindhoven
PO Box 513, 5600 MB Eindhoven, The Netherlands

Introduction

Corona discharges are discussed in this paper as one example of pulsed atmospheric discharges. Other configurations used are the dielectric barrier and the packed bed reactor. Here only the volume discharge will be discussed and not the surface discharge that also plays a role in these last two cases.
The paper is divided in two parts. Fundamental processes that are important in corona discharges are treated in the first section. The characteristic properties of the corona will show up clearly here, its fast development in time and space being a dominating feature. It will also be indicated where knowledge of the processes involved is still marginal or even missing.
The second part gives an overview of experimental diagnostics that are in use to obtain data of the propagating discharge. Commonly used methods are treated as well as state-of-the-art developments.

General aspects of discharges at atmospheric pressure

Discharges at a pressure of 1 bar have several appearances. Lightning is one of them and although it is known with most people it is difficult to describe the lightning discharge in detail. In terms of discharges it is an arc with rather short duration and high power density. Arcs are also used in a more controlled way for instance for welding, high voltage circuit breakers or certain types of lamps. Arcs with duration in the microsecond range are usually called sparks and they are often observed at switching contacts. In case of high voltage applications breakdown can cause severe damage. Even shorter discharges can be created which in fact stop before they are completed in to arcs. These are sometimes called transient discharges and have typical time duration in the range of nanoseconds. There are two ways to create these discharges. A dielectric layer can cover one or two of the electrodes in the discharge gap. At a sufficiently high voltage between the electrodes the discharge starts in the gas volume. It spreads out until it reaches the electrodes but at the dielectric it builds up a space charge that cancel the applied electric field. At that moment the discharge stops. This discharge is usually called dielectric barrier discharge. The second method is to use an asymmetric electrode pair. Then the discharge develops in the high field region near the sharp electrode and it spreads out towards the cathode. In this case there are two possibilities to avoid the transition in to an arc. First the voltage can be made low enough to stop the spreading of the discharge somewhere before the cathode is reached. Second one can stop or lower the voltage when the cathode is reached. In the second way more energy can be put on to the discharge but it is more difficult to make the power supply. This type of discharge is called corona. It is a positive corona when the electrode with the strongest curvature is connected to the positive output of the power supply and a negative corona when this electrode is connected to the negative terminal of the power supply. In corona discharges at relatively low voltages the discharge stops itself due to the build up of space charge near the sharp electrode. This space charge then disappears due to diffusion and recombination and a new discharge pulse appears. This is the self-repetitive corona and it occurs in the positive and in the negative case.

Atmospheric discharges are under investigation since two decades for many environmental purposes [1]. The corona discharge and the barrier discharge are both good candidates in these applications. It is still an open question which type of discharge has the highest efficiency in plasmachemical applications. It appears that the barrier discharge can achieve higher electrical power densities but the corona discharge may be easier scalable to large gas flows. The barrier discharge is more complicated since it is a combination of a gas discharge and a surface discharge along the dielectric. This article is restricted from now on to the corona discharge. Only the positive corona will be discussed in detail since it was shown in many cases to be more effective than the negative case.

Development steps

The growing of the (positive) corona discharge will now be treated in more detail. Several steps are part of this process:

1. An asymmetric electrode configuration must be made
2. A high voltage must be applied
3. Some free electric charge must be present
4. An avalanche must build up and leave behind a space charge area
5. Photons from the avalanche create new charge carriers outside the space charge area
6. New avalanches develop closer to the cathode

Ad. 1: Field enhancement near one electrode is required. The most common methods used in practice for this purpose are point-to-plane and wire-in-cylinder geometries. The point-to-plane is convenient for comparisons with model calculations and the wire-in-cylinder is most suitable for gas treatment where the residence time in the cylinder is an important parameter especially for the plasmachemical processes. Surface roughness can be expected to be important for field enhancement. Recent photographs taken at TUE show that the streamer is connected to the anode on a spot with a dimension in the order of one pixel of the CCD camera used, i.e. ~20 μm. The corona current is ~1 A, so this leads to a current density of ~3 10^9 A/m^2. Erosion (or sputtering) of the anode can be expected in such a case. In laboratory experiments this is not a problem and these aspects have not been studied in detail. For large-scale, long-term application it may become an important factor in maintenance cost.

Ad. 2: The breakdown field strength in a uniform gap with atmospheric air is in the order of 3 kV/mm. This implies that a free electron gains on average several eV of energy from the field in-between collisions. The ionization energy of air molecules is roughly 10 eV. Nevertheless there will be electrons in the tail of the electron energy distribution function that have enough energy to cause ionization. Near a surface roughness much higher field strengths are readily obtained. Field emission cannot occur, however, because the electrons are drawn towards the anode.

Ad. 3: The first electron, which should start the discharge, can be provided in two ways. Cosmic radiation produces them at a rate of ~1 el/mm^{3}s. This leads to rather low background electron densities of 10^3-10^6 el/cm^3. This can imply that it takes some time for an electron to be at the right place, i.e. a region where the electric field is high enough. This time is called inception time lag and in practice it varies from about 1 ns to many microseconds. Another process that can provide electrons is field detachment from negative ions. This effect can be important when ions of a previous discharge are still present. It occurs in the self-repetitive DC corona and it causes the streamer to choose the path of its predecessor. In most applications of pulsed corona it does not occur due to the low repetition rate (~100 Hz).

Ad. 4: When the first electron has caused an ionization there are two electrons left that again start moving in the electric field and ionize again etc. In this way the so-called avalanche builds up. This process continues until the space charge of the slow ions that are left behind cancels the applied electric field. The avalanche can also stop at the anode before it is complete. In such a case the avalanche extinguishes. The length required to build up a complete avalanche is called the critical length; at 1 bar it is in the order of 1 mm [2].

Ad. 5: The space charge region cancels the field between itself and the anode, but it enhances the field in the direction towards the cathode. A free electron at the right position in this area can start a new avalanche. However, the background electron has by now disappeared from the gap due to drift. A process that can provide new electrons is photoionization. This is caused by VUV resonance photons of N_2 that are absorbed by O_2. Only the photons that originate in the tail of the lineprofile of N_2 can travel far enough, but in principle one electron is sufficient. This explanation cannot be used for discharges in e.g. pure N_2 or noble gases. Unfortunately however, data on photoionization in theses cases is unavailable. In case of N_2-O_2 mixtures only one paper is known which gives quantitative data [3]. Computer models of streamer propagation are also made without photoionization. An artificial background electron density is then required for starting new avalanches. Although such a background is not realistic, the results are very similar to models that do include photoionization.

Ad. 6: The electrons of the new avalanche cancel the previous space charge but they create a new one closer to the cathode. It is found that a so-called stability field of 5 kV/cm is sufficient to continue the propagation of the streamer channel. A cathode sheath builds up when the avalanche reaches the cathode [4]. This process is usually not considered in streamer propagation models. If the power supply can continue to deliver current the temperature of the channel will increase due to Joule heating, then its resistance will drop and the discharge may develop in to an arc.

In this paper the situation is considered that the corona current stops after the streamer head reaches the cathode. Many processes continue to occur in the gap after the discharge has stopped. The ones that are often important for further physical and chemical processes are:

1. Attachment
2. Recombination
3. Diffusion
4. Vibrational relaxation
5. Metastable quenching
6. Radical reactions

Ad. 1: Attachment is the formation of negative ions when low energy electrons combine with atoms or molecules. Not all particles form negative ions, examples are the noble gases and also nitrogen molecules. Some molecules that easily form negative ions are O_2, H_2O and CO_2. The conductivity of a plasma is strongly influenced by the capturing of low energy electrons: the light and mobile electrons are replaced by heavy ions. Therefore the field strength for sustaining a certain current is much higher in an electronegative gas. This effect partly explains e.g. why a small amount of water can have a big impact on a noble gas discharge or the difference between dry air and flue gas.

Ad. 2: Recombination of positive ions and electrons (or negative ions) leads back to the neutral gas as before the discharge pulse. It can cause some additional effects such as the

emission of recombination radiation which can be used to determine the electron energy if its intensity is sufficient. In case of a corona discharge this is not to be expected. Further it can lead to the formation of excited states that have high chemical activity. The recombination time in the atmospheric corona discharge is estimated to be in the order of 1 μs. It has not been measured up to now. The time interval required for a corona pulse in order not to notice its predecessor is found in experiments to be in the order of 1 ms. This is probably due to negative ions and/or metastables that have much longer lifetimes than electrons.

Ad. 3: The active particles in a corona discharge are formed in a thin channel (diameter ~200 μm). It is often the intention to treat the whole gas volume, so one may wonder if diffusion is able to spread the radicals significantly. From Schlieren pictures (see next section) it is seen that the streamer diameter increases to ~2 mm in 200 μs. So, this increases the treated volume but still a single discharge pulse treats only a volume fraction in the order of 10^{-3}. This explains why in practice a residence time of several seconds is usually required for a complete treatment. The turbulence created by the corona pulses probably helps to mix the gas but this effect has not been studied in detail up to now.

Ad. 4: The high-energy electrons in the streamer head cause ionization and excitation to higher electronic states. The most important example is the $N_2(C)$-state because it leads to the UV emission of the so-called Second Positive System. The excitation also leads to high vibrational relaxation by which these states decay through collisions to rotational and translational excitation. This is the same as saying that the gas is heated. Emission spectroscopy can give quantitative results about these processes (see next section).

Ad. 5: Excited metastable states cannot lose their energy by emission of a photon. Another process to take away energy from them is by collisional quenching. Metastables are often close to resonant levels, so a collision with a low energy electron can cause them to become resonant, lose the energy within ~1 μs by emitting a VUV photon and become a ground state. It is also possible that they transfer all their energy to a different molecule. In this way quenching of a N_2 metastable can cause dissociation of a water molecule. This process is considered to give an important contribution to the formation of OH radicals in humid air or flue gas. No quantitative studies are available at present, however.

Ad. 6: Radicals are formed by electron impact dissociation of molecules in the streamer head region. The dissociation energy is usually somewhat lower than the ionization energy. Primary radicals are the ones created directly by these collisions, e.g. O, H, OH and N. They may react rapidly with molecules to form secondary radicals such as HO_2 or O_3. If contaminations such as SO_2 or NO are present O, HO2 and O3 can oxidize them to acids. The N radical can reduce NO to N_2. How much this happens depends on the gas composition. This is one of the major application areas of corona discharges [1].

Diagnostics

1. Cloud chamber tracks

The first recordings of avalanches have been made by Raether [5]. He used a cloud chamber to grow droplets around the ions that are left behind. These droplets are photographed through light scattering. Such pictures are extremely sensitive but have, however, no time resolution. Fig. 1 is obtained from the original paper by Raether from 1939. He used a plan parallel gap with N_2 at 150 Torr. The length of the avalanche is of the order of 1 cm.

Fig. 1: Cloud track picture of a single avalanche, cathode at the left (by H. Raether, [5]).

2. Streak pictures

The next method, used by Wagner, is streak photography using an image-intensified camera [6]. The pictures obtained with such a system show one spatial dimension versus time. Figure 2 gives an example.

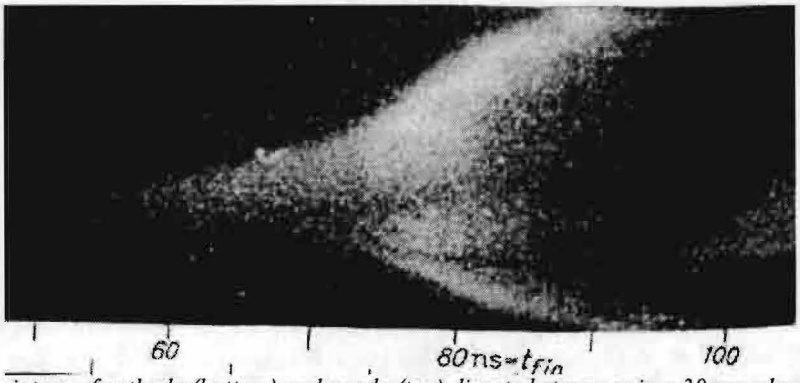

Fig. 2: Streak picture of cathode (bottom) and anode (top) directed streamer in a 30 mm plane gap with 378 Torr N_2 (by K.H. Wagner, [6]).

In fig. 2 it can be seen that in the case of plane electrodes the streamer starts in the middle of the gap and it develops towards cathode and anode. Two phases of developments are distinguished: from 60 to 70 ns with a propagation velocity of ~2-3 10^5 m/s and from 70 to 80 the speed becomes ~10^6 m/s.

3. Photography

The streamer discharge is difficult to access by experiments due to its transient nature. Its total duration is in the order of 10 ns and the streamer head moves along its own thickness in 0.1 ns. This resolution is still not obtained with state-of-the-art cameras. Present day intensified CCD camera's can be gated down to about 1 ns. The sensitivity of these cameras is becoming close to that of photomultipliers, this is quite sufficient to allow single shot exposures. An example is given in fig. 3, which is a photograph of a point-plane corona discharge in a 25 mm gap in ambient air using a voltage pulse of 25 kV with a rise time of 30 ns. The camera used here is an Andor Technology ICCD-452 having the following specifications:

- 1024 x 1024 pixels
- pixel size 13 μm x 13μm

- sensitivity 180-850 nm
- minimum optical gate 0.8 ns
- full width at half maximum 21 μm
- gain up to 3600

Fig. 3: Pictures of streamer propagation in a point-to-plate gap using a 0.8 ns intensifier gate, real size per frame ~3x3 cm² (picture by A.H.F.M. Baede)

Figure 3 shows three pictures at different trigger moments. The time lap between the left and the right pictures is ~40 ns. This value cannot be determined very accurate in the present set-up used because of jitter in the power supply and the corona initiation. The dark spots of the streamer heads are overexposed in these pictures; therefore they look larger than they are. An analysis of their full width at half maximum shows a value of 150 μm for all streamers observed under this condition [7]. Figure 4 shows similar pictures in a wire-cylinder gap with a cylinder having an inner diameter of 290 mm. A voltage pulse of 100 kV is used here having a rise time of 20 ns.

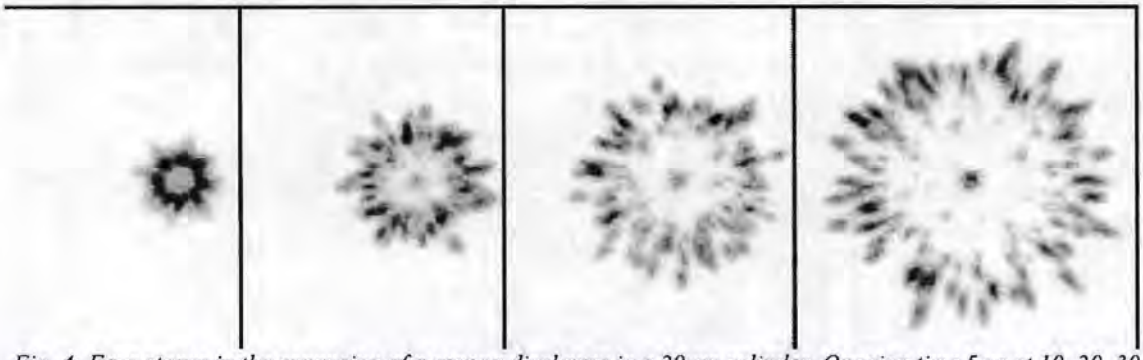

Fig. 4: Four stages in the expansion of a corona discharge in a 29 cm cylinder. Opening time 5 ns at 10, 20, 30 and 40 ns after the initial rise of the voltage pulse of 200 kV with 20 ns rise time, real size last frame ~30x30 cm² (by P.P.M. Blom, [8])

Figures 3 and 4 show similarities in the way the streamer heads move from anode to cathode but in the streamer diameters are quite different, in fig. 3 they are ~0.2 mm and in fig. 4 ~1 cm. Comparing these figures to 2-D modeling of streamer propagation one finds that the results of fig. 3 are close to those obtained by simulations. The situation of fig. 4 is different due to the extreme rate of rise of the voltage. It resembles the fast ionization wave (FIW) where electron energies are higher than in the corona discharge [9]. This FIW is the transition region to runaway electrons that can have keV's of energy as has been measured by detection of X-rays [10].

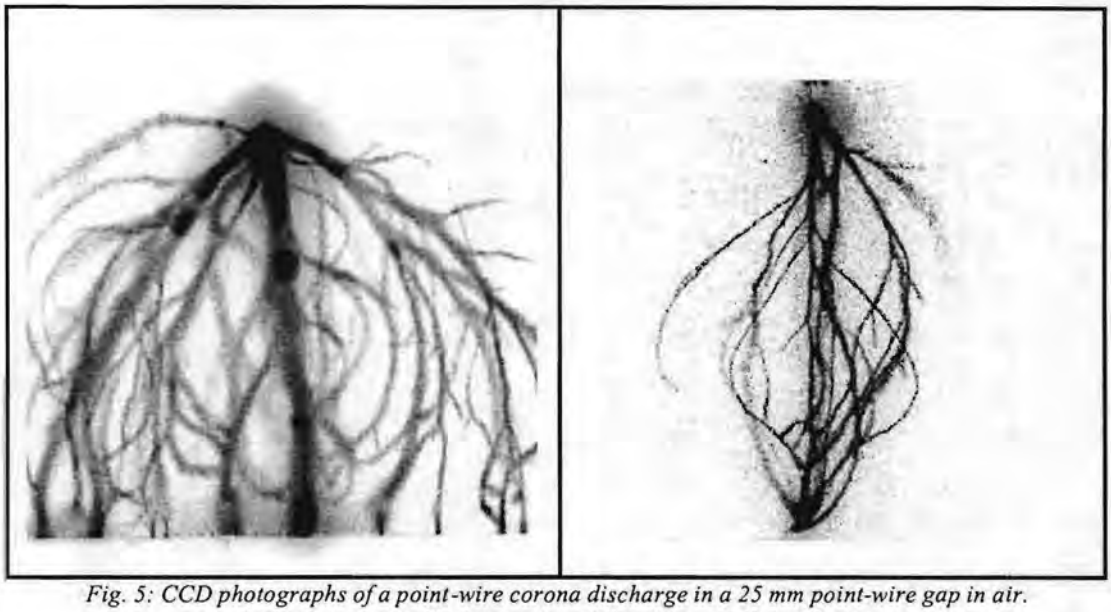

Fig. 5: CCD photographs of a point-wire corona discharge in a 25 mm point-wire gap in air. Left: view perpendicular to wire, right: view parallel with wire

Figure 5 shows two examples of pictures taken with exposure times of 100 ns, i.e. a time integrated picture of the discharge crossing the gap. In the left part one sees that the streamers spread out to a width that is larger than the point-wire distance. The right figure shows how the streamers bend out in the middle of the gap but they redirect towards the wire.

4. Schlieren photography

The path created by the corona streamer has a composition that is different from the surrounding gas. It can also have an enhanced temperature. Therefore its refractive index differs from its background. Such a difference can be visualized by Schlieren photography. This can be performed in three ways: 1. standard Schlieren methods are sensitive to the gradient in the refractive index, dn/dx, 2. interferometry, which is related directly to the refractive index n and 3. shadowgraphy which is proportional to d^2n/dx^2 [2, 11]. Figure 6 is obtained by a standard knife-edge method.

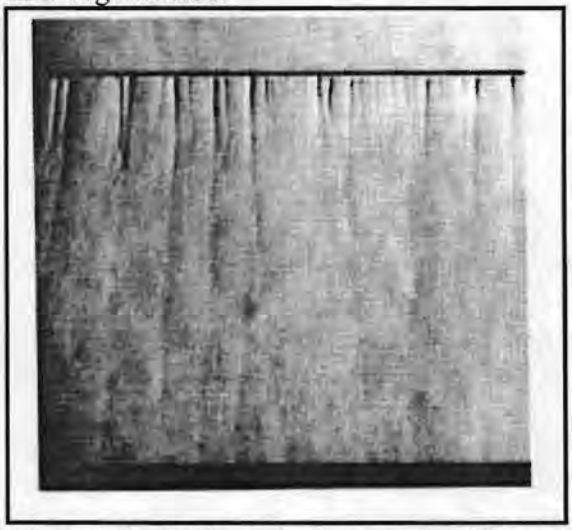

Fig. 6: Schlieren photograph of wire-plane pulsed corona taken 100 μs after the voltage pulse (by Y.L.M. Creyghton, [2])

The remarkable result of Schlieren pictures of a corona discharge is that its appearance is most clearly 50 to 100 μs after the voltage pulse. Within 1 μs the streamer paths are not observed. The explanation for this is that the fast electrons first cause ionization and vibrational excitation that does not affect n. After vibrational de-excitation to rotations and translations the streamer channel gets heated and shows up more clearly. A time constant of 100 μs for this process is reasonable.

5. Emission spectroscopy

The optical emission of the corona streamer can be analyzed by spectroscopic techniques. Monochromators have sufficient resolution for a discharge at 1 bar but main problems are the low intensity and the short duration. A technique that is well suited in this case is the time-correlated single-photon counting method. It uses an optical trigger to determine the timing of the photon to be counted. A time-to-amplitude converter can be included to obtain a time resolution down to 0.1 ns. Several slightly different version of this method are in use, not only for the pulsed corona [2, 12] but also for the self-repetitive discharge [13-15].

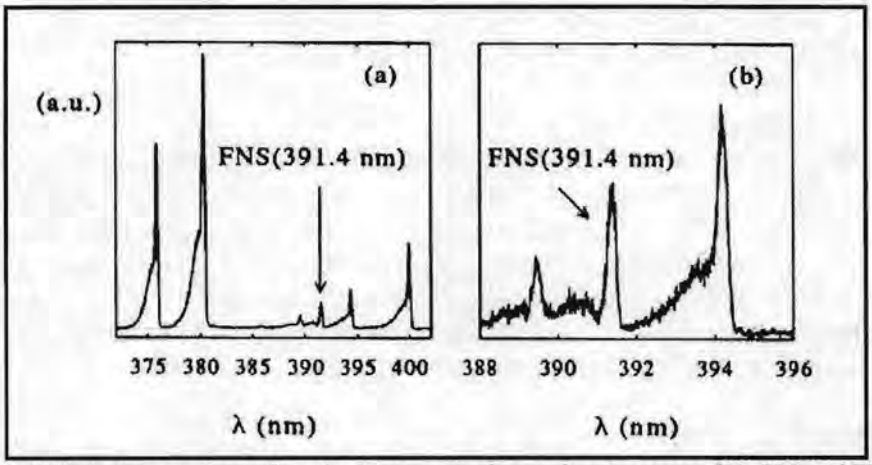

Fig. 7: Emission spectrum of a pulsed corona discharge showing parts of N_2 SPS and FNS (by Y.L.M. Creyghton, [2]).

Figure 7 gives an example of a part of the nitrogen spectrum in the near UV. It shows part of the Second Positive System of N_2 and the First Negative System of N_2^+. Because these systems have very different excitation levels the ratio of their intensities is a measure of the electron energy. Using this effect one obtains ~10 eV for electrons in the streamer head [2].

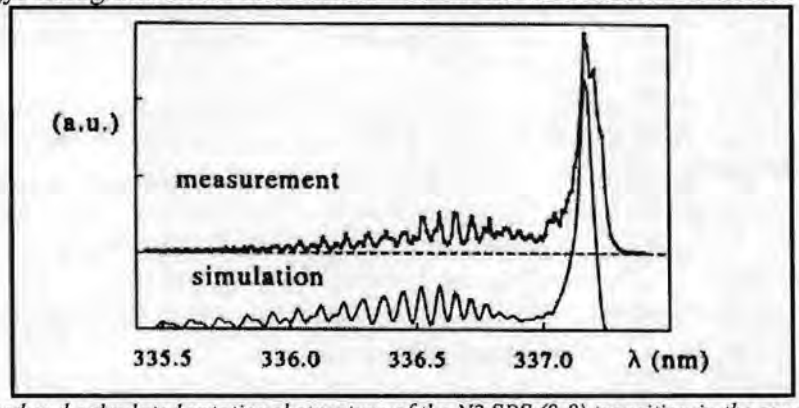

Fig. 8: Measured and calculated rotational structure of the N2 SPS (0-0) transition in the secondary streamer phase of a pulsed corona (by Y.L.M. Creyghton, [2])

In figure 8 the rotational structure of the SPS (0-0) transition is resolved. It is compared with a calculated spectrum with a rotational temperature of 350 K. The spectrum shown here is recorded in a time interval of 50-200 ns after rise of the voltage pulse, so the secondary streamer is observed [2]. It shows that the gas is still hardly heated at this instant.
The width of the measured spectral line can also be used. A nice example of it is given in [16] where the Stark broadening of the H-β line is used to determine the electron density. The result of 10^{15} cm^{-3} is, however, one order of magnitude higher than values obtained from simulations [1].

6. Absorption spectroscopy
Atoms and molecules can absorb light of specific wavelengths. The advantage of absorption is that it easily gives quantitative information on the lower level of the transition involved. Calibration is usually straightforward from known cross sections or gas mixtures. This method can be used to detect all kinds of species in a discharge (or any other gaseous system). Ozone is a well-known example but also NO, NO_2, SO_2 and NH_3 are easily determined [1, 17]. Short living excited states and radicals, created by the discharge can also be measured. A nice example is the OH ground state density in a tandem barrier discharge [18]. Absorption spectra can also be used to determine rotational temperatures [19].

7. Laser induced fluorescence
Although absorption spectroscopy is relatively easy it cannot be used in many cases because the absorption of low-density species is weak. The molecule that has absorbed radiation can emit this in other directions and also at other wavelengths, the so-called fluorescence. In that case using a strong source, e.g. a laser, can increase the signal. The sensitivity of this method is many orders of magnitude higher than the classical absorption technique. The first example of its use in a barrier discharge is the detection of OH radicals [20, 21]. Other examples are N_2^+ [22], $N_2(A)$ [23], NO [24], N [25].

Final remarks
The corona discharge at atmospheric pressure is in use and under investigation already for a long time. Its use with a pulsed power supply is of more recent date. From all information given above one may get the idea that the situation is well known. This is, however, not the case. Many processes are only estimated or assumed, e.g. field emission, photoionization, diffusion, recombination, and collisional de-excitation. The fact arising from this situation is that for e.g. values found for the electron density range from 3 10^{13} to 2 10^{15} cm^{-3}. For OH radicals very few measurements are available. In [18] a volume-averaged value of 10^{15} cm^{-3} is obtained. This implies a density inside the streamer that is much higher than values obtained from simulations [1].
So the problem that is faced is to make the results more quantitative. This must be done from theory and experiment since not all details can be measured using present day equipment. All methods mentioned above can be used for this purpose with detection possibilities that have only recently become available, e.g. generation-IV CCD-camera's. New techniques can probably be added. On can think of Coherent Anti-Stokes Raman Scattering to be used in rough environments. It is already being tested in barrier discharges [26]. Another possibility is Cavity Ringdown Spectroscopy, which is an extremely sensitive absorption technique that could be used to determine short living intermediate species.
The final aim should be to develop sufficient understanding of the discharge in order to predict and develop applications.

References

[1] E.M. van Veldhuizen (editor), *Electrical Discharges for Environmental Purposes: Fundamentals and Applications,* Nova Science Publishers, New York, 1999, ISBN 1-56072-743-8, 420 pages.

[2] Y.L.M. Creyghton, *Pulsed Positive Corona Discharges: Fundamental Study and Application to Flue Gas Treatment*, Ph.D. thesis TUE, Eindhoven, September 1994.

[3] G.W. Penney, G.T. Hummert, *Photoionization measurements in air, oxygen and nitrogen*, J. Appl. Phys. **41**(1970)572-577.

[4] I. Odrobina, M. Cernak, *Numerical simulation of streamer–cathode interaction*, J. Appl. Phys. **78**(1995)3635.

[5] H. Raether, *The development of electron avalanche in a spark channel (from observations in a cloud chamber)*, Zeitschrift fur Physik **112**(1939)464. (Reproduced in: *Electric Breakdown in gases,* J.A. Rees, The Macmillan Press, London, 1973).

[6] K.H. Wagner, *Vorstadium des Funken, untersucht mit dem Bildverstaerker*, Zeitschrift fur Physik **204**(1967)177.

[7] E.M. van Veldhuizen, A.H.F.M. Baede, D. Hayashi, W.R. Rutgers, *Fast imaging of streamer propagation*, APP Spring Meeting, Bad Honnef, 2001, p. 231-234.

[8] P.P.M. Blom, *High-Power Pulsed Corona*, Ph.D. thesis, Eindhoven University of Technology, ISBN 90-386-0250-2, 1997.

[9] S.M. Starikovskaia, A.Yu. Starikovskii, D.V. Zatsepin, *The development of a spatially uniform fast ionization wave in a large discharge volume*, J. Phys. D: Appl. Phys. **31**(1998)1118-1125.

[10] G.A. Mesyats, Yu.I. Bychkov, V.V. Kremnev, *Pulsed nanosecond electric discharges in gases*, Sov. Phys. Uspekhi **15**(1972)282-297.

[11] Y.L.M. Creyghton, E.M. van Veldhuizen, W.R. Rutgers, *Electrical and optical study of pulsed positive corona*, in: *Non-Thermal Plasmas for Pollution Control*, ed. by B.M. Penetrante and S.E. Schultheis, NATO ASI Series, subseries G, vol. 34, Springer, 1993, part A, p. 205.

[12] O. Motret, C. Hibert, S. Pellerin, J.M. Pouvesle, *Rotational temperature measurements in atmospheric pulsed dielectric barrier discharge – gas temperature and molecular fraction effects*, J. Phys. D: Appl. Phys. **33**(2000)1493-1498.

[13] K. Kondo, N. Ikuta, *Highly resolved observation of the primary wave emission in atmospheric positive-streamer corona*, J. Phys. D: Appl. Phys. **13**(1980)L33.

[14] F. Tochikubo, T.H. Teich, *Optical emission from a pulsed corona discharge and its associated reactions*, Jpn. J. Appl. Phys. **39**(2000)1343-1350.

[15] R. Brandenburg, K.V. Kozlov, P. Michel, H.-E. Wagner, *Diagnostics of the single filament barrier discharge in air by cross-correlation spectroscopy*, HAKONE VII, Greifswald, Germany, sept. 2000, p.189-193.

[16] E. Gerova, S. Muller, *Measurements of electron density in dielectric barrier discharges*, XXIII ICPIG, Toulouse, France, 1997, p. IV-120.

[17] I.P. Vinogradov, K. Wiesemann, *Classical absorption and emission spectroscopy of barrier discharges in N_2/NO and O_2/NO_x mixtures*, Plasma Sources Sci. Technol. **6**(19997)307.

[18] C. Hibert, I. Gaurand, O. Motret, J.M. Pouvesle, *[OH(X)] measurements by resonant absorption spectroscopy in a pulsed dielectric barrier discharge*, J. Appl. Phys. **85**(1999)7070-7075.

[19] M. Spaan, J. Leistikow, V. Schultz-von der Gatten, H.F. Döbele, *Dielectric barrier discharges with steep voltage rise: laser absorption spectroscopy of NO concentrations and temperatures*, Plasma Sources Sci. Technol. **9**(2000)146-151.

[20] J.J. Coogan, A.D. Sappey, *Distribution of OH within silent discharge plasma reactors*, IEEE Trans. Plasma Sci. **24**(1996)91-92.

[21] R. Sankaranarayanan, B. Pashaie, S.K. Dhali, *Laser-induced fluorescence of OH radicals in a dielectric barrier discharge*, Appl. Phys. Lett. 77(2000)2970-2972.

[22] R. Siegel, N. Abramzon, K. Becker, *Electron-impact dissociation and ionization of molecules studied by laser-induced fluorescence techniques*, XXIII ICPIG, Toulouse, France, July 1997, p. I-62-63.

[23] G. Dilecce, S. de Benedictis, *Experimental studies on elementary kinetics in N_2-O_2 pulsed discharges*, Plasma Sources Sci. Technol. **8**(1999)266-278.

[24] G.J. Roth, M.A. Gundersen, *Laser-induced fluorescence images of NO distribution after needle plane pulsed negative corona discharge*, IEEE Trans. Plasma Sci. **27**(1999)28-29.

[25] V. Schultz-von der Gatten, M. Thomson, Ch. Lukas, M. Spaan, H.F. Döbele, *Time and space resolved TALIF-spectroscopy of N-atoms in a dielectric barrier discharge with steep voltage rise*, HAKONE VII, Greifswald, Germany, September 2000, p. 194-198.

[26] A. Pott, T. Doerk, J. Uhlenbusch, J. Ehlbeck, J. Höschele, J. Steinwandel, *Polarization-sensitive coherent anti-Stokes Raman scattering applied to the detection of NO in a microwave discharge for reduction of NO,* J. Phys. D: Appl. Phys. **31**(1998) 2485-2498.

The Hook Method - Interferometric Diagnostics of Gas Discharges

E. Kindel, F. Adler

Institut für Niedertemperatur-Plasmaphysik, 17489 Greifswald, F.-L.-Jahn-Str. 19

Germany

1 Introduction

The hook method is a classical interferometric method which was introduced by ROZHDESTVENSKI in 1912 [1]. It was first established to measure oscillator strengths of absorption lines in various gases and vapours with known particle number densities. For this reason the spectral behaviour of the refractive index in vicinity of an absorption line (anomalous dispersion) has been investigated. On the other hand, this method has been used to determine number densities for systems with known oscillator strengths [2 - 4].

The main features of the hook method are its insensitivity to the line shape and its large dynamic range as well as its applicability to optically thick lines.

We used this method for the absolute determination of the density of excited atoms and atoms in ground state in low and medium pressure discharges as well as in high pressure mercury discharge lamps.

In this paper results which were received from hook experiments will be presented with two examples (the positive column of a pulsed xenon medium pressure discharge and the arc of a high pressure mercury discharge lamp).

2 Theoretical Background

The theory of the hook method is based on the anomalous dispersion in the proximity of an absorption line, where sharp changes of the refractive index occur. Near an isolated absorption line at λ_0 but far from the line center the dispersion function for the refractive index is expressed as [5]

$$n-1=\frac{r_0 N_i f_{ik} \lambda_0^3}{4\pi(\lambda-\lambda_0)}\left[1-\frac{g_i N_k}{g_k N_i}\right]. \qquad (1)$$

$N_{i,k}$ are the lower and upper state densities for the transition, respectively, $g_{i,k}$ are the lower and upper statistical weights, $r_0 = e^2/(mc^2)$ is the classical electron radius, λ_0 is the wavelength of the transition and f_{ik} is the absorption oscillator's strength.

The main part in the experimental setup of the hook method is a combination of an interferometer and a spectrometer (see Figure 1a). A backlight source is used for the illumination of the interferometer. Horizontal fringes will appear in the focal plane of the spectrometer for a properly adjusted interferometer (see Figure 1b). If in one arm of the interferometer a dispersive medium with an optical transition at λ_0 is situated, typical distortions in the fringes will appear (see Figure 1b). By changing the interference order the fringes can be made oblique so that the so called hooks occur (see Figure 1c). From the wavelength distance Δ of the hooks the density of the lower level of the transition at λ_0 can be calculated.

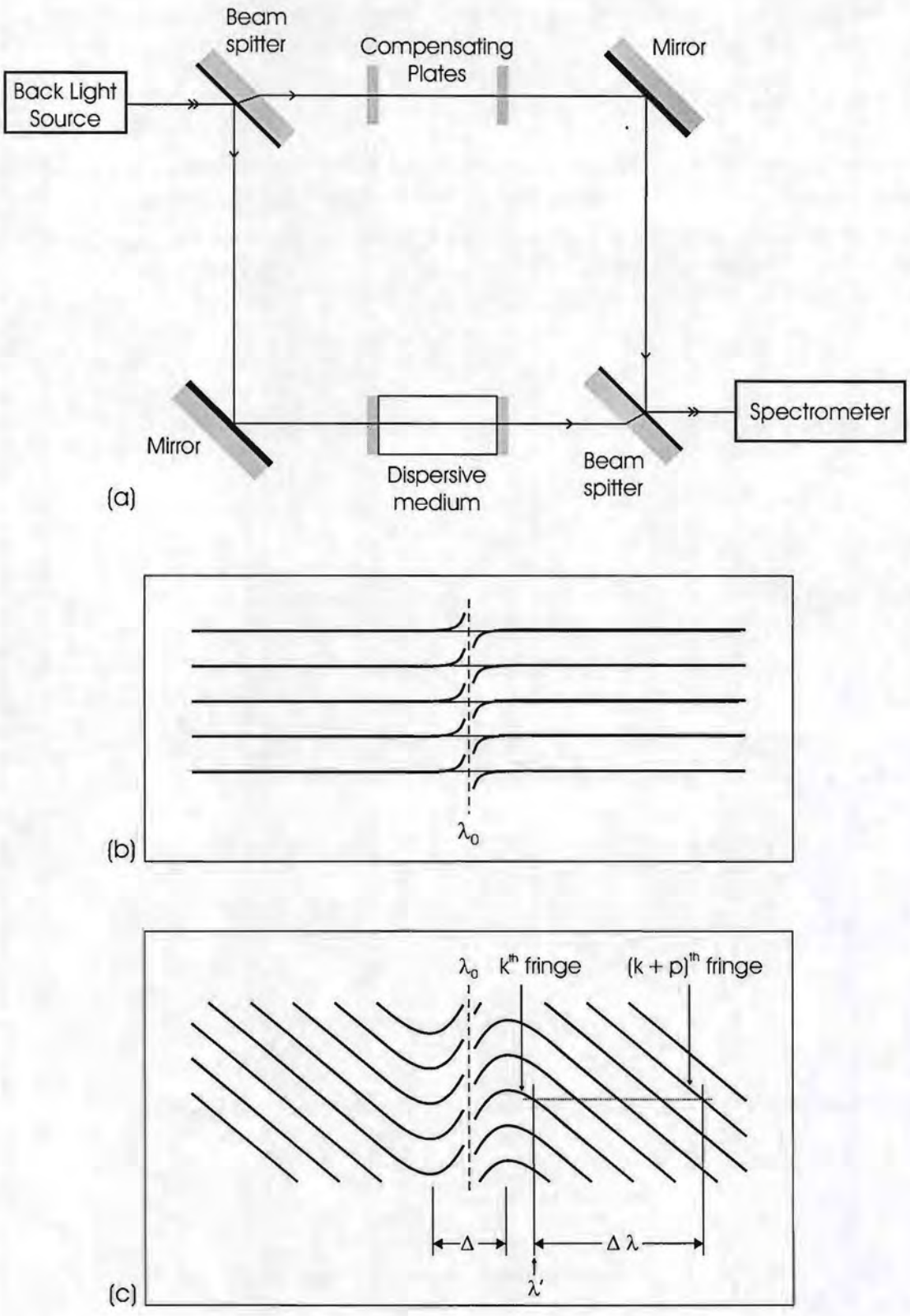

Figure 1: *(a): MACH – ZEHNDER Interferometer, (b) – (c) : schematic fringe profiles from an interferometer – spectrometer set-up.*

The relation between the order m of an interference fringe and its height in the focal plane is given by the fringe equation

$$ay + (n-1)l + \Delta l = m\lambda,\ m = 0, \pm 1, \pm 2, \ldots, \tag{2}$$

where a is the angle between the two interfering beams in the interferometer, l is the length of the dispersive medium and Δl is the difference in the optical path length of both beams.

The rise of an interfering fringe is given by $\mathrm{d}y/\mathrm{d}\lambda$. In the region of normal dispersion $\mathrm{d}n/\mathrm{d}\lambda = 0$ the differentiation of equation (2) yields

$$\left(\frac{\mathrm{d}\,y}{\mathrm{d}\,\lambda}\right)_{n=\text{constant}} = \frac{m}{a} \tag{3}$$

At the position of the hooks, i.e. at λ_{max} and λ_{min} (see Figure 1c) the condition

$$\left(\frac{\mathrm{d}\,y}{\mathrm{d}\,\lambda}\right)_{\lambda_{max}} = \left(\frac{\mathrm{d}\,y}{\mathrm{d}\,\lambda}\right)_{\lambda_{min}} = 0 \tag{4}$$

is valid. The differentiation of equation (2) at λ_{max} and λ_{min} leads to

$$l\frac{\mathrm{d}\,n}{\mathrm{d}\,\lambda} = -K \tag{5}$$

with K as hook constant. Combining the SELLMEIER formula (1) with equation (5) and assuming that $g_i N_k / g_k N_i$ can be neglected, we get

$$l\left(\frac{\mathrm{d}\,n}{\mathrm{d}\,\lambda}\right) = -\frac{r_0}{4\pi}\frac{N_i f_{ik} l \lambda_0^3}{(\lambda - \lambda_0)^2} = -K\,. \tag{6}$$

The solution of this equation results in

$$\lambda_{max,min} = \lambda_0 \pm \sqrt{\frac{r_0 N_i f_{ik} l \lambda_0^3}{4\pi K}}\,. \tag{7}$$

With the hook distance $\Delta = \lambda_{max} - \lambda_{min}$ the particle density N_i is then obtained by

$$N_i = \frac{\pi K}{r_0 f_{ik} l \lambda_0^3}\Delta^2 \tag{8}$$

The hook constant K needs to be determined by counting fringes in a line-free wavelength region (see Figure 1c) using

$$K = \frac{p\lambda'}{\Delta\lambda} \tag{9}$$

where p is the number of fringes.

HUBER [5], MARLOW [6] and HUBER and SANDEMANN [7] give an extensive review of the hook method. More sensitive than the hook technique are the hook vernier [8] and phase methods [9] where the vertical spacing of the hooks or phase shift is measured, respectively.

3 Practical Application

3.1 Hook Measurements in the Positive Column of a Pulsed Xe Medium Pressure Gas Discharge

Introduction

Motivated by the use of VUV radiation in numerous industrial applications, investigations of pulsed rare-gas discharges at medium pressure have become the subject of interest recently. In order to get a deeper understanding of the main processes in such discharges, theoretical and experimental studies of the positive column plasma of a pulsed xenon discharge have been performed [10-12].

For such kind of discharges it is well known that especially two effects in the afterglow play an important role in the generation of radiation. Due to the high formation rate of molecular ions by three-body collisions between atomic ions and atoms in the ground state the dissociative recombination between molecular ions and electrons becomes the main channel of deionisation of the plasma. This process is connected with the population of the levels lying below the ground state of Xe_2^+ and leads to the emission of atom lines [13,14].

On the other hand excited atoms in the states $1s_4$ (resonance) and $1s_5$ (metastable) are the precursors leading to the formation of excimers $Xe_2^*(^1\Sigma_u^+)$ and $Xe_2^*(^3\Sigma_u^+)$ by three-body collisions with ground state atoms. The radiative decomposition of these excited rare gas molecules to the dissociative van-der- WAALS ground state $^1\Sigma_g^+$ leads to the radiation of the so- called first and second continuum at 150 nm and 170 nm, respectively [15].

In [9] we presented time resolved measurements of absolute densities of $1s_4$ and $1s_5$ states and the flux of VUV radiation in the positive column of pulsed xenon discharges at pressures between 1 and 40 Torr and in the current range of 100-300 mA.

Experimental Set-up

The experimental set-up is shown in Figure 2. As a background light source we used a dye laser (FLGR-2, Carl Zeiss Jena) with a grating and a beam expanding telescope in the oscillator. The resultant band width is 0.02 nm. The dye laser is pumped by a N_2- pulse laser of about 600 kW peak power with a pulse duration of 8-10 ns. Thus, time resolved measurements down to this time are possible.

The laser beam traverses a MACH-ZEHNDER-interferometer. The discharge tube is situated in one branch and two glass plates in the other one, in order to compensate the windows of the discharge tube. By inserting a third compensating plate in the latter branch the fringes are shifted to a higher order and appear oblique so that typical hooks are formed near the absorption line. Instead of a spectrograph we used, similar to van de WEIJER et al. [16], a combination of a beam expander, a grating with 1200 lines/mm and a CCD-camera. By a proper adjustment we got a sharp interference picture at a distance of 5 m from the grating with a typical dispersion of 60 mm/nm. We applied an OMA in connection with a light guide to determine the dispersion in the plane of the camera .

The interference pattern was stored and analysed using a computer. For the analysis we applied the so-called hook vernier method processed by our specially designated software, including a fast Fourier transform (FFT). This method, which utilizes the vertical shift of the fringes, is about ten times more sensitive than the normal hook technique.

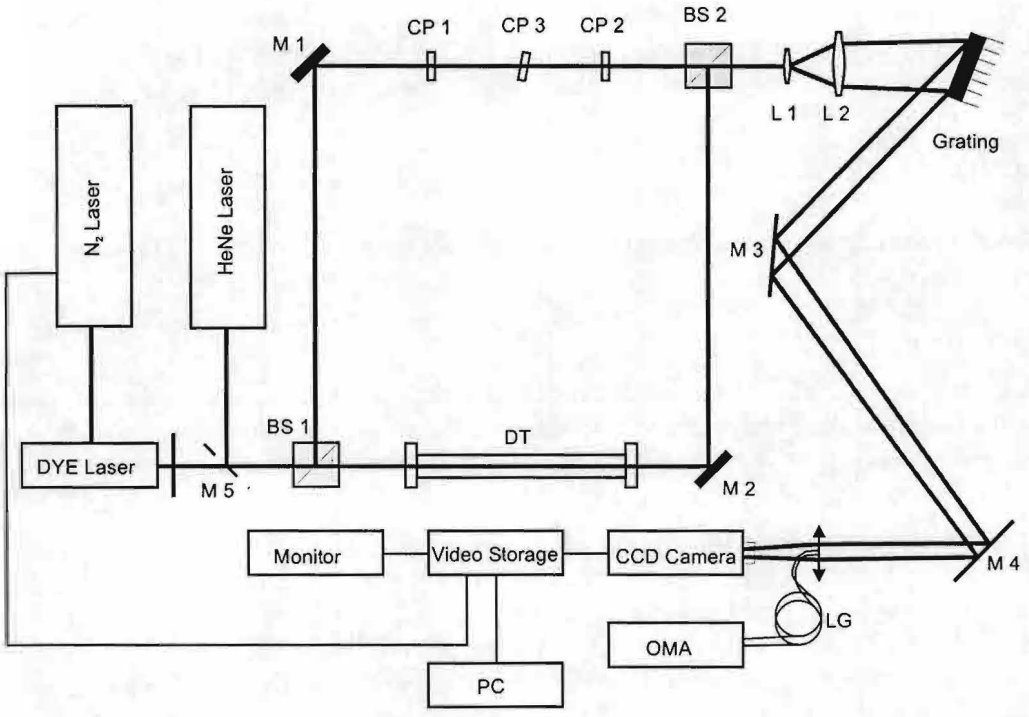

Figure 2: *Experimental set-up for measuring hook distances at a plasma (M: mirror, BS: beam splitter, CP: compensating plate, L: lens, DT: discharge tube).*

For the adjustment of the MACH-ZEHNDER-interferometer we applied the dye laser as a monochromatic light source. Due to the high coherence length the adjustment is relatively simple. Afterwards we removed the expanding telescope from the oscillator of the dye laser. Thus, we obtained a broadband light source (about 1nm) so that the hook separation is always in this wavelength range.

For the determination of the densities in the $1s_5$ and $1s_4$ levels we used the transitions of $2p_6$ - $1s_5$ at 823.16 nm and $2p_5$ - $1s_4$ at 828.01 nm, respectively (cf. Figure 3). A typical interference pattern is to be seen in Figure 4.

Results

The time behaviour of the densities $1s_4$ and $1s_5$ and the maximum VUV- radiation in dependence of the Xe-pressure for a peak current of 130 mA and a frequency of 6 kHz is shown in Figure 5. It has been found that the effect of a higher density as well as a higher maximum VUV- radiation in the afterglow appears at pressures of $p \geq 10$ Torr. The measured densities are in the range of 1×10^{11} - $5\times10^{12}cm^{-3}$, whereby in most cases the metastable density are four to five times higher than the resonance density (see Figure 8). Moreover we can see that with higher pressure the densities increase and in the temporal afterglow they become up to ten times larger than in the active phase of the discharge.

The time to reach the maximum density in the afterglow is shortened with increasing pressure. For example, the maximum density at 10 Torr for the metastable is reached after about 40 s, whereas at 40 Torr only 15 s are needed. This effect, observed by MICHEL [17] too, can be explained by the dependence of the recombination coefficient on electron temperature. With higher pressure the temperature decays more quickly. This is connected with an increasing recombination coefficient. For more detailed explanations see [10, 12].

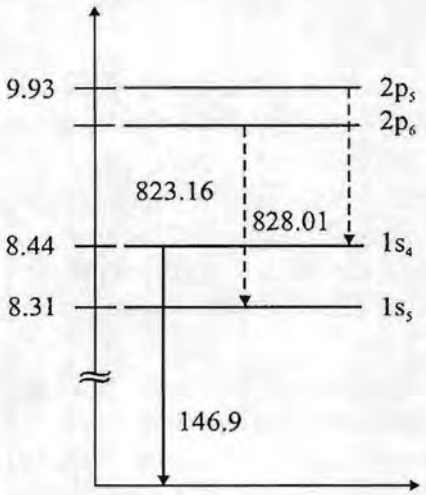

Figure 3: *Simple term scheme from Xenon including relevant radiation transitions.*

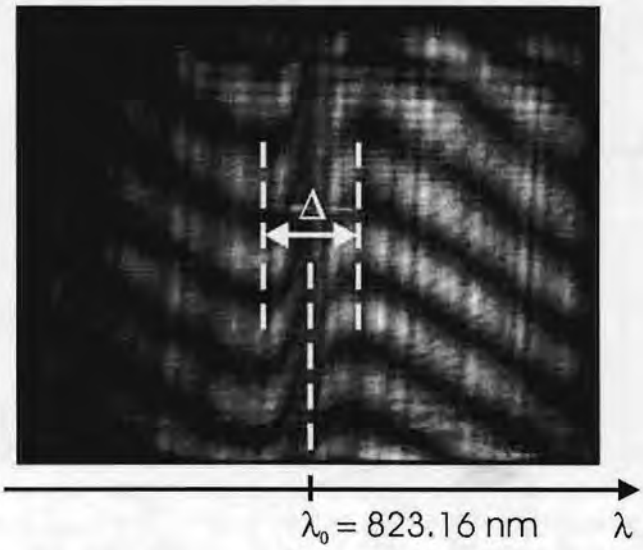

Figure 4: *Typical measured interference pattern (Xenon), Δ = 0.176 nm).*

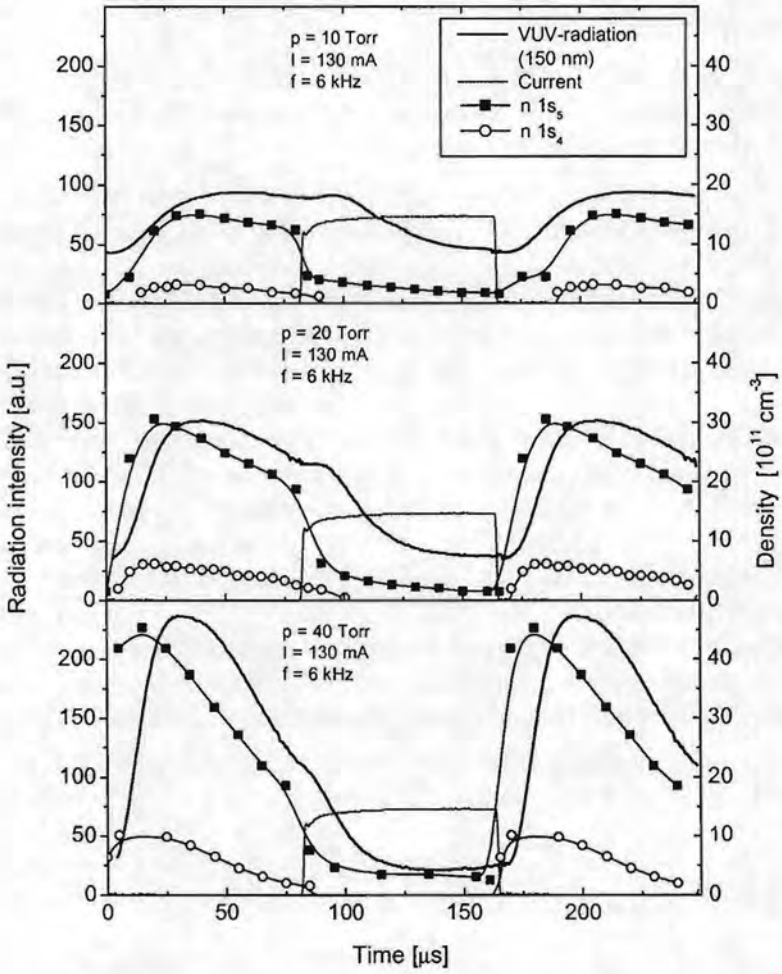

Figure 5: *Measured VUV – radiation and excited state density ($1s_4$, $1s_5$) over the time in comparison with the discharge current.*

3.2 Hook Measurements in the Arc of a High- Pressure Mercury Discharge Lamp

Introduction

Concerning the understanding of high-pressure mercury discharges it is necessary to know the particle densities and the radial temperature distribution. The knowledge about that densities is the basis for the description of the plasma state and the calculation of relevant properties.

Our first paper [18] dealing with this subject was intended to study the possibility of using this method for high-pressure mercury and mercury iodide lamps. By measuring the radial behaviour of absolute densities of excited atoms in mercury we were able to calculate the radial temperature profile by applying the BOLTZMANN law. These results agree well with those determined by emission spectroscopy.

Later on we used this method for investigations in mercury discharges with deviations from the local thermodynamic equilibrium [19]. With an improved experimental set-up [20] we could measure the radial density profile of the ground state $6^2P_{1/2}$ and the metastable level $6^2P_{3/2}$ of thallium up to a relative radius of 96% in a Hg-TlI high- pressure discharge. This is considerable because such lamps with their cylindrical tubes act as lenses and make the adjustment of the used interferometer very difficult.

Below we present select results that were received in a high-pressure mercury discharge.

Experimental set-up

To measure the densities in the mercury triplet states 6^3P_0, 6^3P_1 and 6^3P_2 and the ground state 6^1S_0 we used the transitions at 404.7, 435.8, 546.1 and 253.7 nm [see Figure 6], respectively. All these transitions are optically thick [21,22].

The used experimental set-up compares to the one that was used for the investigations in the pulsed medium pressure discharge [see Figure 2]. In one arm of the interferometer the mercury discharge lamp is placed in vertical position so that the laser beam traverses the lamp side-on. In the other arm of the interferometer a similar discharge tube and a compensating plate are situated to compensate the path length differences and shift the fringes to a higher order to get typical hooks. To investigate the radial profile of the densities the discharge lamp was moved via a translation stage with a step width of 0.5 mm. For an high spatial resolution the laser beam was reduced to 0.3 mm in diameter. The spectral bandwidth of the dye laser is about 1 nm. Therefore, hook separations in the order of tenth of an angström unit can be registered by only one laser shot. For the determination of absolute densities in the ground state the transition at 253.7 nm is used. To generate this UV radiation a BBO I crystal (210-340 nm) is applied. The generation of the second harmonic leads to a further limitation of the laser bandwidth. Therefore, the line profile has to be scanned by adjusting the laser frequency to get the whole interferogram. This was done in steps of 0.2 nm width [see Figure 7]. For these measurements in the UV–region all beam splitters, compensating plates and lenses in the MACH-ZEHNDER interferometer are of synthetic quartz. Furthermore, the commonly used CCD camera is replaced by a UV-sensitive tube camera (Hamamatsu C 2400-05).

For the experiments a conventionally 250 W high-pressure mercury lamp was used operating at 50 Hz. It has an inner diameter of 1.6 cm, an inter electrode distance of 2.75 cm, a total volume of 5.2 cm^3 containing 27 mg Hg.

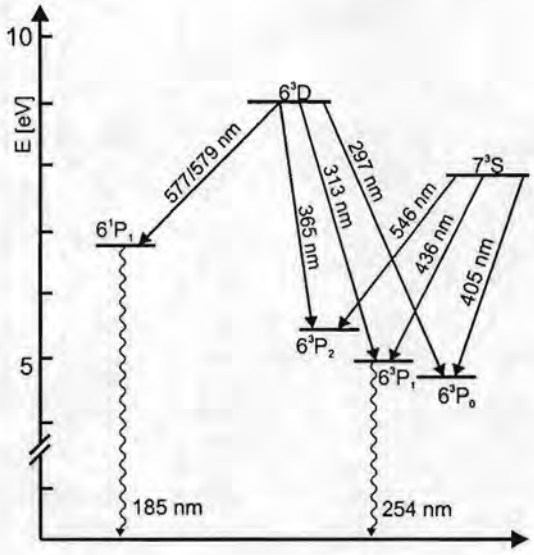

Figure 6: *Simplified energy level diagram of atomic mercury.*

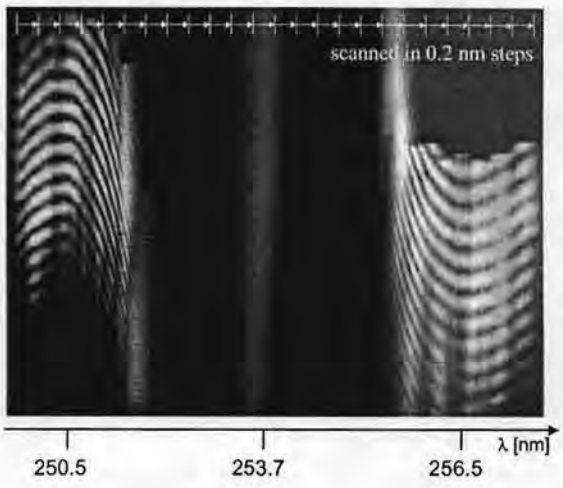

Figure 7: *Interferogram of the Hg–line at 253.7 nm, $N_0 = 6.1 \times 10^{24}$ cm^{-3}.*

Results

Figure 8 shows the radial behavior of the measured product $N\,l$ (density times absorption length) for the three excited states. It can be seen that with this experimental arrangement the densities are measurable up to 5 mm out of the axis. (With a new laser system and modifications in the beam leading measurements are possible up to a relative radius of 96% [20].)

Furthermore, in the axis the densities of the 6^3P_1 level exhibit the highest value followed by the 6^3P_2 and the 6^3P_0 levels, respectively. The 6^3P_0 radial profile shows a flatter distribution than the 6^3P_2 level which is in accordance with BOLTZMANN's law for a given temperature profile. Because it is difficult to determine the absorption length l accurately the quantity $N\,l$ is indicated. All measured values are integrated over the line of sight. In order to get the densities N over the radius, an ABEL inversion needed to be applied.

In Figure 9 the absolute densities for the triplet in dependence on the radial position are shown. With these data and the measured ground state density the temperature profile is calculated using the BOLTZMANN law [see Figure 10]. Within the failure limitations (± 15% for the density measurements, leading to $\Delta T = \pm 240$ K) the curves show the same temperature behavior.

The comparison of the temperature distributions obtained using the hook method and emission spectroscopy [18] is shown in Figure 11. The arc temperature on the axis is about 6150 ± 330 K for the emissions measurements. The hook results for the axis temperature of 6390 K are a little higher. Both temperature distributions agree well with each other concerning the shape and the absolute values within their failure limitations.

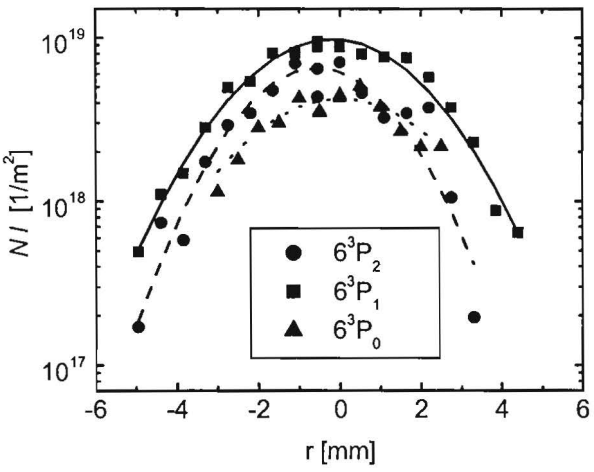

Figure 8: *Measured values of* N I *of the* 6^3P_0, 6^3P_1 *and* 6^3P_2 *levels over the radius* r *for 240 W lamp power.*

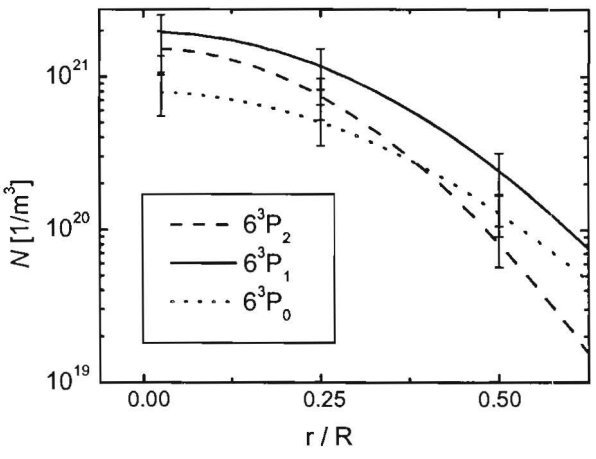

Figure 9: *Population densities of different levels over the reduced radius, same power as in Figure 8.*

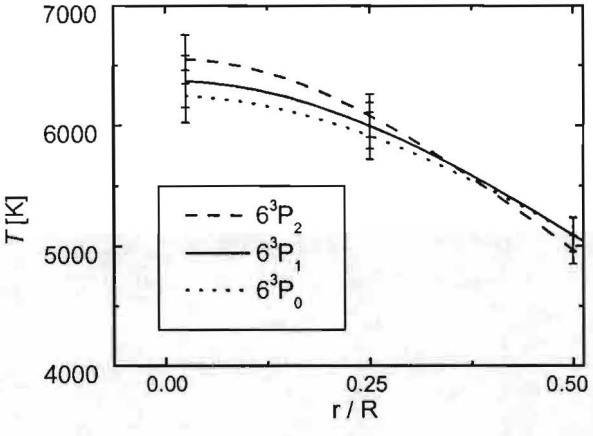

Figure 10: *Calculated temperatures evaluated from the population density of different levels, same power as in Figure 8.*

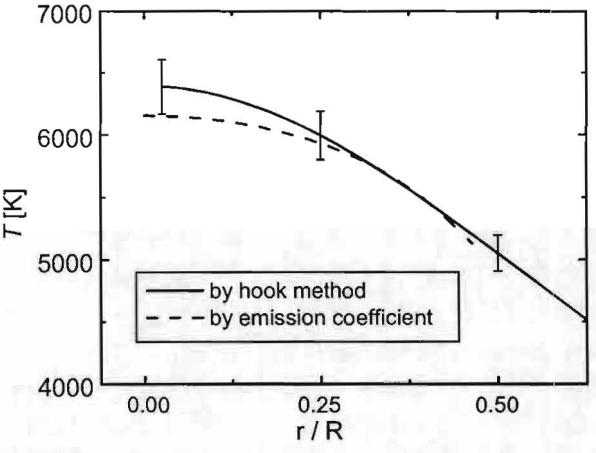

Figure 11: *Comparison of temperature distributions obtained using hook method or emission spectroscopy, respectively. Same power as in Figure 8.*

3.3 References

[1] ROZHDESTVENSKI D S 1912 *Ann. Phys.* **39** 307.
[2] KOPFERMANN H and LADENBURG R 1928 *Z. Phys.* **48** 15.
[3] KOCK M and KÜHNE M 1977 *J. Phys. B: At. Mol. Phys.* **10** 3421.
[4] SPERGER R and NEGER T 1991 *Opt. Commun.* **80** 401.
[5] HUBER M C E 1971 *Modern Optical Methods in Gas Dynamics Research* (New York: Plenum) p 85.
[6] MARLOW W C 1967 *Appl. Opt.* **6** 1715.
[7] HUBER M C E and SANDEMANN R J 1986 *Rep. Prog. Phys.* **49** 397.
[8] SANDEMANN R J 1979 *Appl. Opt.* **18** 3873.
[9] BACHOR H A and KOCK M 1980a *J. Phys. B: At. Mol. Phys.* **13** 2497.
[10] KINDEL E and SCHIMKE C 1996 *Contrib. Plasma Phys.* **36** 711.
[11] KINDEL E and SCHIMKE C 1996 *Journal of Light & Visual Environment* **9** 34.

[12] LOFFHAGEN D Kindel E and SCHIMKE C 1997 *Proc. 12th International Conference on Gas Discharges & Their Applications* **II** 715.
[13] PFAU S and RUTSCHER A 1972 *Beitr. Plasmaphys.* **12** 53.
[14] CONNOR T R and BIONDI M A 1965 *Phys. Rev.* **140** 778.
[15] MILLET P, BIROT A, BRUNET H, GALY J, PONS-GERMAN B and TEYSSER J L 1978 *Chem. Phys.* **69** 92.
[16] van de WEIJER P and CREMERS R M M 1982 *J. Appl. Phys.* **53** 1401.
[17] MICHEL P 1972 *Beitr. Plasmaphys.* **12** 301.
[18] KINDEL E, KETTLITZ M, SCHIMKE C and SCHÖPP H 1998 *J. Phys. D: Appl. Phys.* **31** 1352.
[19] ELLOUMI H, KINDEL E, SCHIMKE C and Zissis G 1999 *J.Appl. Phys.* **86** 4134.
[20] KLOSS A, KINDEL E and SCHÖPP H 2000 *Proc.13th International Conference on Gas Discharges & Their Applications,* Glasgow Vol. **II** 504.
[21] DAMELINCOURT J J, AUBES M, FRAGNAC P and KARABOURNIOTIS D 1983 *J. Appl. Phys.* **54** 3087.
[22] STORMBERG H P and SCHÄFER R 1983 *J. Appl. Phys.* **54** 4338.

Chemical topography analysis using XPS during plasma etching in Si processing

L. Vallier, O. Joubert , G. Cunge, J. Foucher
Laboratoire des Technologies de la Microélectronique, UMR CNRS-UJF, 17 rue des Martyrs (CEA-LETI), 38054 Grenoble Cedex 9, France.

We have used x-ray photoelectron spectroscopy (XPS) to investigate the nature and composition of surfaces exposed to the plasma during the patterning of sub-μm structures in a high-density plasma (HDP) source, as a function of plasma operating conditions for front-end processing (namely silicon gate etching), and back-end processing, (namely aluminum interconnect lines etching). The chemical topography analysis using XPS clearly reveal the build-up of passivation layers on the features sidewalls, which drive the anisotropy control of the etch process. The formation mechanisms of such layers are discussed and their consequences in terms of critical dimension (CD) control or corrosion control are examined; as a conclusion, a gate etch process involving the engineering of those sidewall passivation layers is presented.

I- Introduction

Etch requirements depend on materials and process schemes used to construct transistors, DRAM memory cells and interconnects that comprise Silicon integrated circuits (IC). In semiconductor manufacturing, this concerns three basic categories of materials: polysilicon, dielectrics, and metals. In general, the requirements for each of these materials are well defined and predictable for each new IC generation.
In polysilicon etching, the main application is the transistor gate region, which requires etching through a gate stack to stop on a very thin gate oxide. Selectivity with respect to the oxide is critical and requires the development of complicated recipes to minimize oxide loss while maintaining critical dimension (CD) control.
Dielectric etch applications represent another challenging process due to the combination of the complexity of structures to be etched (self-aligned contact and dual damascene applications) and the trade-off between opening high aspect ratio structures and obtaining high selectivities between the dielectric, silicon and silicon nitride. In addition to the complexity added by the new structures, a new category of materials with low dielectric constants need to be integrated into standard processes opening a new field of investigation in plasma etching.
In metal etching, the dominant application is interconnect line formation. Challenges in metal etch arise from the chemical and structural complexity of the films to be etched. One key issue is to obtain anisotropy by resist etch by-products redeposition on the metal sidewalls and efficiently removing these chlorine rich films during subsequent anticorrosion treatment.
As device dimensions are getting smaller and smaller, information on the etched surfaces exposed to the plasma is becoming essential to understand and to control the involved etch mechanisms, as well as to develop new etching recipes. X-ray photoelectron spectroscopy is a very surface sensitive analysis technique providing elemental quantification and chemical information; however it is not straightforward to implement for sub-micron features analysis on multi-layer stacks as encountered in IC fabrication; photoelectron shadowing effect in conjunction with the differential charging of insulating *vs.* conductive materials under a low energy electron gun have to be used to extract the data on dedicated samples, therefore achieving spatial resolution enabling chemical topography analysis. As useful information have to be obtained on actual patterned substrates without air exposure after the plasma

treatment, we have designed a customized chamber to perform chemical topography analysis using XPS on 200 mm wafers etched in a commercial high density plasma (HDP) etcher. Several processes listed above have been analyzed with emphasis on the features sidewall composition linked to the anisotropy of the process. A good control of the sidewall layer formation through a good plasma parameters control has led to the development of the passivation layers engineering illustrated with the tailoring of polysilicium gates for ultimate CMOS applications.

II- Experimental procedure

This study has been carried out in a cluster tool platform dedicated to the etching of 200 mm diameter wafers.[1] The experimental apparatus is composed of a load-lock chamber located in a class 10 clean room, a robotized vacuum transfer chamber, a silicon plasma etching chamber equipped with a HDP helicon source operating at a RF frequency of 13.56 MHz, an aluminum plasma etching chamber equipped with a HDP inductive source operating at a RF frequency of 13.56 MHz, and an ultra high vacuum surface analysis chamber. In all silicon and aluminum etch experiments, the RF source power is set to provide a high-density plasma (higher than 10^{11} cm^{-3}) and ensuring the best etching uniformity (10 % at 3σ). In both plasma chambers, the sample can be independently biased using a 600 W maximum power supplied at 13.56 MHz; thermal contact between the chuck and the sample is achieved by Helium backside cooling at 10 Torr and the wafer platen temperature is maintained at 25°C.
After etching, wafers are immediately transferred under vacuum in the surface analysis chamber dedicated to X-ray photoelectron spectroscopy studies. The XPS analysis chamber is equipped with an X-ray photoelectron spectrometer (ESCALAB 220 I) from VG Scientific, a single electrostatic lens flood gun (VG model LEG 41) and a mass spectrometer (Micromass 386). The analysis chamber is equipped with two X-ray sources: a non-monochromatized X-ray source consisting of a water cooled standard twin anode (Al K_α @ 1486.6 eV, Mg K_α @ 1253.6 eV) and a monochromatized Al K_α small spot size source. The energy resolution is defined as the full width at half maximum (FWHM) of the $Ag3d_{5/2}$ peak and exceeds 0.8 eV with a sensitivity larger than 350 000 counts per second (cps) for the twin source. The energy resolution of the $Ag3d_{5/2}$ peak using the monochromatized Al K_α source is less than 0.47 eV with a sensitivity of 25 000 cps. The ultra high vacuum (UHV) chamber is pumped with a 300 l/s ion pump (MECA 2000) and a water cooled titanium sublimator (MECA 2000). An additional ion pump (Varian 8l/s) is located between the monochromatized Al K_α source and the X-ray monochromator.
The electron energy analyzer is a 150 mm mean radius, 180° spherical sector with a multi-element electrostatic input lens. The analysis area is adjustable from 3 mm to less than 100 µm depending on the lens operation mode and the selected spot size for the monochromatized source. A multi-channeltron array (6 channels) detects photoelectrons in the spectroscopic mode. Two irises of the electron input lens system can be manually tuned to adjust the acceptance angle (± 6° max). The electron flood gun used for charging surfaces provides electrons with low kinetic energy ranging between 0 and 80 eV. The angle between the optical axis of the input lens and the normal of the wafer is fixed at 45°.
XPS is the most appropriate quasi *in situ* technique to analyze the layers formed during plasma etching. Indeed, the chemical composition of reactive layers formed under plasma exposure on any surface of a wafer presenting some topography can be determined using the chemical topography analysis technique.[2,3] In order to perform the chemical topography analysis using XPS, a dedicated optical lithographic mask has to be set first; then, it can be used to pattern with a photoresist mask or a hard mask, either polysilicium gate stacks, or

aluminum interconnect stacks as well as interlayer dielectric stacks. An unmasked area has been left at the center of the 200 mm wafer to perform endpoint detection of the stack etching by real-time ellipsometry at 1.96 eV photon energy. The mask design used in this study allows XPS analysis of the tops, sidewalls and bottoms of the features using the method of geometrical shadowing of photoelectrons. The patterned areas are composed of regular arrays of lines and spaces, blanket substrate and unpatterned mask material. Each area has a size of at least 4 mm^2, therefore larger than the probed surface by XPS. For each array, a 90° rotation of the wafer allows both parallel and perpendicular lines to the incidence plane made by the optical axis of the spectrometer and the normal of the wafer to be analyzed. In the parallel mode, the photoelectrons entering the spectrometer lens are those coming from the top and the bottom of the features, while in the perpendicular mode only unshadowed photoelectrons coming from the top, the sidewall, and depending on the aspect ratio of the selected array, the bottom of the features, can enter the lens. Chemical topography analysis is reinforced with the use of a low energy electron gun to charge insulating materials; the photoelectrons escaping such a negatively charged surface are shifted to lower binding energy in the detected spectrum, making easier the peaks attribution and the subsequent surface quantification of the analyzed surfaces. The following example is for a silicon gate stack patterned with an oxide hard mask and etched with an HBr, Cl_2, and O_2 plasma based chemistry. When the lines are in the perpendicular orientation, the analyzed areas are both the top and the side of the SiO_2 hard mask and the side of the a-Si lines. The flood gun is intentionally set to negatively charge the insulating hard mask surfaces in order to differentiate, for each energy region, unshifted contributions originating from the conducting a-Si sidewalls and shifted ones originating from the insulating hard mask surfaces. As an example, the Si *2p* doublet at 99.6 eV binding energy is easily observable in the Si *2p* energy region and can be unambiguously affected to the silicon bulk material of the gate; therefore, all XPS peaks at a binding energy slightly higher than that of the Si *2p* doublet are attributed to Si atoms on the gate sidewall exhibiting a chemical shift induced by chemical bonding to O, Cl and Br atoms, while peaks at a lower binding energy are unambiguously attributed to silicon atoms located on the mask (charging of the mask shifts the Si *2p* peak by approximately 9 eV). Performing data processing on the peaks areas originating from the a-Si gate sidewalls allows its quantification by computing the atomic concentration of non oxidized silicon (Si^{0+}, hereafter called Si-Si) and oxidized silicon (ΣSi^{n+}, n = 1 to 4, hereafter called SiO_x), as well as oxygen, chlorine and bromine extracted from the Si *2p*, O *1s*, Cl *2p* and Br *3d* core level energy regions. Actually, the Si-Si concentration corresponds to the Si *2p* doublet contribution, while the SiO_x concentration is the contribution of several species that form a broad peak on the high binding energy side of the doublet, such as $SiBr_x$, $SiCl_x$, SiO_x and their mixture, most of them having unknown binding energies. Peak areas are determined after spectral deconvolution based on an iterative numerical fitting procedure. Individual line shapes are simulated with the combination of Lorentzian and Gaussian functions. A Shirley function is used to perform background subtraction. Each element concentration is obtained by dividing the peak areas by the corresponding Scofield cross section (Si *2p*: 0.82; O *1s*: 2.93; Br *3d*: *2.84*; Cl *2p*: 2.29).[4]
Using such a powerful technique, chemical topography analysis was performed on several plasma processes to investigate the build-up of sidewall passivation layers linked with the process anisotropy.

III- Polysilicon gate etching

In polysilicon etching the main application is the formation of the transistor gate region, which requires etching of a silicide/polysilicon sandwich and the stopping on a very thin gate

oxide. Selectivity to the gate oxide is critical since only minimal amounts of oxide loss can be tolerated. The development of etch recipes preserving the integrity of thin gate oxides, is achievable using an HBr rich, Cl_2 plasma added with O_2, with an accurate end-point detection system to trigger a "landing step" which uses ion bombardment energies similar to those used for the overetch step and which are below the sputtering threshold of silicon dioxide.[5] For the first 3/4 of the polysilicon layer thickness, the etching proceeds using the high energy ion bombardment of the main etching step and the remaining thickness is etched using the landing step. Introducing the landing step reduces the magnitude of the trenching and allows the gate oxide to be reached with a very high polysilicon/SiO_2 selectivity. Using such recipes, polysilicon gates can be developed on gate oxides thinner than 3 nm. Nowadays, as gate dimensions are entering the sub 0.1μm region, the main issue is the critical dimension (CD) control of the gate throughout the etch process. Several studies, based on x-ray photoelectron spectroscopy analyses on 0.25 μm gate technology processes, have already shown that when using $HBr/Cl_2/O_2$, HBr/O_2, Cl_2/O_2 chemistries, the passivation film formed on the sidewalls of resist or oxide masked polysilicon gates is a halogen rich silicon dioxide layer.[3,6,7] The only difference between the chemical composition of the passivation layer is that it contains a low carbon concentration (less than 10%) when resist is used as a mask, which shows that carbon etch products are not essential in the passivation film formation. On the other hand, the oxygen concentration added to the gas phase has a strong influence on the oxide film thickness formed on the polysilicon sidewalls.[6] Depending on the process parameters, the cumulated thickness on the sidewalls can exceed the CD deviation budget (+/- 10% of the nominal CD) bearable in sub 0.1 μm gate fabrication. We have performed chemical topography analyses using XPS to investigate the composition of sidewall passivation films formed during the plasma patterning of 0.1 μm silicon gates in the high-density plasma (HDP) source, as a function of plasma operating conditions for HBr, Cl_2 and O_2 based chemistry. Results clearly show that sidewall passivation films are SiX_xO_y based material (X= Br, Cl, with $x+2y \leq 4$) and that they are formed during the main step of the gate etch process; finally they become more oxidized as the overetch step proceeds, leading to an oxide like layer after halogen desorption. A plausible hypothesis to explain the oxide like layer formation on the sidewalls of the polysilicon features, is that the silicon based etch products generated from the reactive layer at the bottom of the trenches, either after line of sight deposition or after recycling in the plasma gas phase, may react on the sidewalls where the absence of ion bombardment favours the oxide layer formation.[3] The experimental results presented in Fig. 1 shows that in a HBr/O_2 plasma, the passivation layer is a SiO_xBr_y layer. It also shows that the SiO_x area originating from the passivation layer remains almost unchanged with the overetch time. Since most of the a-Si layer is etched during the main etch step of the process (the a-Si etch rate is only 5% lower in dense features than in open areas), the passivation layer essentially forms during the main etch step. The non-variation of the SiO_x percentage with the overetch time clearly confirms the link between silicon based etch by-products and passivation layer build-up. It also shows that the a-Si sidewall is not oxidized by the oxygen atoms present in the gas phase during the overetch step. We also observe in Fig. 1 that oxygen concentration in the passivation layer increases as a function of the overetch time, while bromine concentration decreases, showing that during the overetch step, bromine atoms are substituted by oxygen atoms. Moreover the Si-Si percentage (originating from the a-Si sidewalls) decreases as a function of the overetch time, showing that photoelectrons are screened more efficiently by the passivation layer, even if the amount of oxidized Si in this passivation layer is unchanged as a function of time (as shown by the constant SiO_x percentage). We can conclude from all these observations that the substitution of bromine by

oxygen and the increase in the oxygen concentration in the passivation layer as a function of the overetch time, leads to its densification. This conclusion is supported by the Si *2p* spectra presented in Fig. 2 showing the evolution of the broad SiO_x peak of the main etch into a more pronounced peak attributed to the fully oxidized state of silicon while, at the same time, the overall SiO_x area remains almost unchanged.

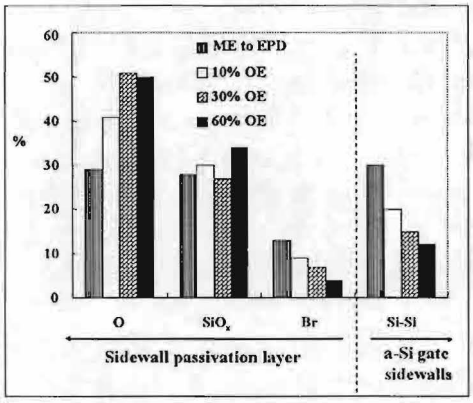

Fig.1: Quantitative chemical composition of a-Si gate sidewall passivation films formed after the main etch (ME) step up to the end point detection (EPD), and different overetch (OE) steps of a gate etch process using HBr/O_2 chemistry.

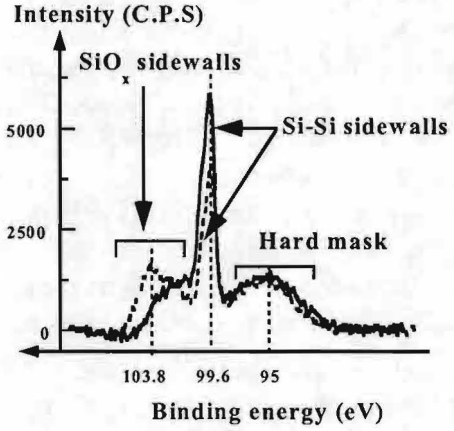

Fig.2: Si *2p* energy region recorded by XPS with the low energy electron gun on, in a dense (line= space= 125 nm) array after a gate etch process using HBr/O_2 chemistry. The plain line corresponds to the spectrum recorded after the main etch step, and the dotted line after the whole process (main etch + overetch).

Other experimental results, not reported here, obtained by chemical topography analysis using XPS, have shown the strong sensitivity of the sidewall passivation film formation with respect to the plasma operating conditions and the process parameters, like the oxygen dilution, the bias power and the Cl_2/HBr ratio in the gas phase. All of them confirm the same behavior of the passivation layer when it is present. As a conclusion, we can say that the silicon gate sidewall passivation layer is highly desirable to work with (but not always necessary) in order to ensure anisotropic profiles. Indeed, this film prevents lateral etching, therefore protecting the silicon sidewalls throughout the process, including the overetch step. However, it is formed at the early beginning of the gate etch process both on the mask and silicon gate sidewalls. With feature dimensions shrinking below 100 nm, and below, the induced CD deviation can be larger than the allowed CD budget fixed at ±10% of the nominal CD. Therefore a good control of the layer formation conditions has to be implemented into the process.

III- Metal etching

Challenges in metal etch arise from the chemical and structural complexity of the film to be etched which is made of a thin TiN/Ti barrier under the Al metal layer, covered with a thin TiN ARC needed to pattern the stack with photoresist in the previous lithographic step. The difficulty of the process is to vertically etch the metal stack and to minimize the underneath silicon dioxide loss during the overetch. Nowadays, mixtures of chlorine and BCl_3 are state of the art for plasma Al etching. As the etching mechanism of Al with chlorine is purely chemical, a protective layer on the Al sidewall is mandatory to obtain anisotropic profile; it is now well established that this layer relies on the deposition on the sidewall of Al etching and

carbon based photoresist by-products as the etching proceeds. All the chlorine based-approaches suffer from lack of photoresist selectivity, which is in a range of usually less than 2.5. Moreover, the shrinking of geometries (associated with shorter wavelengths to expose the resist) strongly reduces the focus budget of the lithographic step prior to the etching process. To compensate for this effect and to obtain the resolution required, thinner photoresist films have to be used which reinforces even more the need for developing etching recipes with greater Al/resist selectivities, but keeping a good protective capping of the Al line sidewall.

One key issue of interconnection definition is that after dry etching, and exposure of interconnects to atmospheric moisture, rapid corrosion of the etched structures may occur, leading to Integrated Circuit (IC) failure and yield degradation. Addressing all the issues related to corrosion is critical and post-etch anticorrosion treatments have to be efficient at removing all chlorine-based compounds from all surfaces of the metal stacks. Modern anticorrosion treatments consist in many cases of high pressure H_2O/O_2 based plasmas followed by a wet chemistry removing polymers. The role of the water-based plasma treatment is to strip the photoresist (which after being exposed to chlorine-rich plasmas contains a large amount of chlorine) and lower the chlorine content on surfaces by forming volatile HCl. The role of the wet depolymerizing chemistry is to remove the chlorine-rich aluminum species left on the metal surfaces after anticorrosion plasma treatments. After this process, no chlorine should remain on any metal surface of the stack. Chemical topography analyses by XPS combined with wide dispersive x-ray fluorescence (WDXRF) have been used to evaluate the efficiency of the metal stack anticorrosion treatments [8] after the etch in the Inductively Coupled Plasma reactor (ICP) using the common Cl_2/BCl_3 chemistries. Analyses performed prior to anti-corrosion treatment have shown that a chlorine rich carbon film is formed on the sidewalls of the aluminium features during the etching process and that the thickness of this film increases during the overetch time. The passivation film enhances anisotropic etching by providing a thin protective layer against the spontaneous etch reaction of chlorine with aluminium. The film results from the high resist sputtering rate, which induces a high partial pressure of carbon etching products in the gas phase, which products are redeposited on the sidewalls and bottoms of the features. Chemical topography analyses by XPS have shown that, after anticorrosion treatment, residual chlorine species are still present on the aluminium sidewalls of the features. Combining the results obtained by WDXRF and XPS has led to a better understanding of the action of both the high pressure water-based plasmas and wet depolymerizers. The high pressure plasma treatment lowers the chlorine concentration at the near surface of the aluminium sidewall, but not throughout the chlorinated aluminium layer. The wet depolymerizer partially or totally removes the layer which has been depleted in chlorine by water based plasma but is not efficient enough to remove all the chlorine-containing metal layer.[8]

For the next ULSI generations, a great research effort is focused on the dual damascene approach for the interconnect layer formation where metal etching issues are replaced by new challenges in dielectric etching to open high aspect ratio with a good selectivity between PECVD oxide dielectric, PECVD nitride on large areas (flat selectivity) and PECVD nitride on top of the holes (corner selectivity). In addition to the complexity added by those new structures, a key requirement is the lowering of the dielectric constant mandatory for 0.13 μm processes and below, introducing new carbon containing dielectric materials to replace silicon oxide, therefore requiring new mask and new chemistries. As in front-end processes, chemical topography analysis using XPS will be very useful when addressing the patterning and the integration of those new materials.

IV- Application to the sidewall passivation layer engineering

Let us come back to front-end processing, namely to silicon gate patterning, to examine the consequences that can be drawn on the sidewall passivation layer formation. All the XPS analysis, when compared with the etched profile shapes observed by SEM, have shown that the anisotropic etching of silicon lines relies on the formation of a $SiO_XBr_YCl_Z$ passivation layer on the trenches sidewalls, and that the thicker this layer is, the better the chemical lateral etching (or undercut) was prevented. In particular, it was shown [9] that the SiO-like passivation layer is very thick in HBr/O_2 (up to 9 nm) and that their thickness increases markedly with the O_2 flux in the chamber. On the other hand, pure Cl_2 plasmas do not lead to the formation of a thick passivation layer,[2,10] and only a reactive $SiCl_X$ layer is find on the sidewalls. In such a case, anisotropic etching is more difficult to perform because the sidewalls are not efficiently protected, and etching directionality relies on the fact that silicon etching by Cl atoms is strongly ion assisted.[10] It was also shown that during an overetch step in HBr/O_2 (where no more etching products are release in the gas phase), O atoms can substitute to Br atoms thus re-enforcing the passivation layer formed during the main etch step by transforming it into SiO_2.

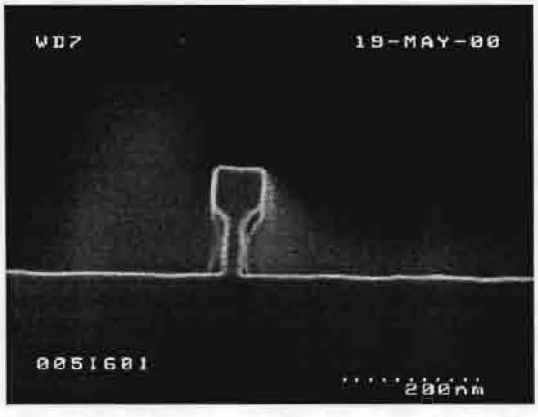

Fig. 3: SEM view of a notched profile gate etched with the process flow described in the text. The CD at the bottom of the gate is 30 nm while the CD after the E-beam lithography was 70 nm.

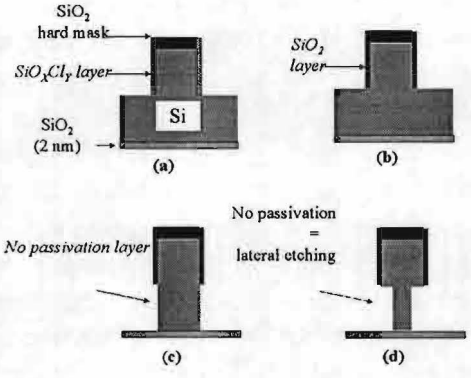

Fig. 4: Engineering of the passivation layer. (a) anisotropic etching of one half of the gate in $HBr/Cl_2/O_2$. (b) Reinforcement (oxidation) of the passivation layer. (c) anisotropic and selective etching of the rest of the gate in Cl_2 (no passivation layer formation). (d) overetch and lateral erosion.

On the basis of those observations, we have performed the engineering of the passivation layers in order to design notched gates in silicon. As shown in Fig.3, a notched gate is a gate in which the bottom of the gate (which length defines the speed of the device) is smaller than its upper part which size is defined by lithography. However, it shall be underlined that the term "notched" that usually refers to a marked undercutting at the Si/SiO_2 interface and that is attributed to ion deflection due to charging of the gate, is not appropriate here where the lateral etching of the bottom of the gate is purely chemical. In order to realise such a gate, we have used a multi-step process summarised in Fig.4 in which we have tuned the thickness and composition of the passivation layer formed on the silicon sidewalls. The principle is to etch the gate anisotropically but within two steps, the first one forming a thick passivation layer while on the contrary the second one avoid the formation of such a layer. As a result, during the last step (after reaching the gate oxide) that also serves as an overetch, lateral erosion of the silicon sidewall is possible at the location where no passivation layer has been formed,

namely the bottom of the gate, resulting in a notched gate, the final CD being controlled by the time length of the overetch. As a result, a controlled etch in two dimensions has been performed to pattern a gate having a smaller dimension at the bottom than at the top, allowing the design of transistors whose final channel length is smaller than the one defined by lithography. This allows very small gates to be realized (less than 20 nm), and open the way to gain one stepper generation in IC circuits fabrication.

Acknowledgments

The prospective part of this work has been performed at the Center for Projects in Advanced Microelectronics (CPMA), Grenoble, France.
The CPMA is a multiproject institute operated by the Centre National de la Recherche Scientifique (CNRS), the Laboratoire d'Electronique, de Technologie et d'Instrumentation (LETI, CEA, Grenoble), the Institut National Polytechnique de Grenoble (INPG), and the Institut National des Sciences Appliquées (INSA, Lyon).

The authors would like to thank L. Desvoivres for the polysilicon gate etching experiments and P. Czuprynski for the metal etching studies.

References:

[1] F.H. Bell, O. Joubert, and L. Vallier, J. Vac. Sci. Technol. B 14, 96 (1996)
[2] F. H. Bell, and O. Joubert, J. Vac. Sci. Technol. B 14, 2493 (1996)
[3] K. V. Guinn, C. C. Cheng, and V. M. Donnelly, J. Vac. Sci. Technol. B 13, 214 (1995)
[4] J. H. Scofield, J. Electron. Spectrosc. Relat. Phenom. 8, 129 (1976)
[5] Y. H. Lee, J. Vac. Sci. Technol. A 10(4), 1318 (1992)
[6] F. H. Bell, and O. Joubert, J. Vac. Sci. Technol. B 15(1), 88 (1997)
[7] M. Haverlag, G. S. Oehrlein, and D. Vender, J. Vac. Sci. Technol. B 12(1), 96 (1994)
[8] P. Czuprynski, and O. Joubert, J. Vac. Sci. Technol. B 15, 1000 (1997)
[9] L. Desvoivres, L. Vallier, and O. Joubert, J. Vac. Sci. Technol. B 19(2), Mar. Apr. 2001 Issue
[10] K. H. A. Bogart, and V. M. Donnelly, J. Appl. Phys. 87,8351 (2000)

Measuring Current, Voltage and Impedance in RF Plasmas

D. Vender
PRL, NCPST, School of Physical Sciences, Dublin City University, Dublin 9, Ireland

Introduction

Since radiofrequency plasmas are generated electrically, the most basic and natural measurements that we can make on these plasmas are measurements of current and voltage. Additionally, since input power is one of the most important control

ese

measurements.

Although external, *global* measurements of total current and voltage are very useful in plasma control (especially in an industrial context), they provide limited insight into the discharge structure and other important aspects. In this paper we look at examples of *local* measurements. Local measurements can be relatively simple to make and yield information on the distribution of power deposition. They can also be used to examine the discharge maintenance mechanism and even the plasma composition.

After a brief discussion of global measurements in the first section, we look at magnetic probe measurements and how these can be combined with Langmuir probe data to obtain greater insight.

1 External Measurements

RF measurement techniques are well developed but plasmas do present some challenges. They are normally excited in resonant circuits and voltages are often just beyond the capabilities of commercially available probes. Simple voltage dividers can be used but care has to be taken because components are non-ideal at rf frequencies. Resistive dividers must be compensated as shown in Figure 1(a). Performance at very high frequency (~100 MHz) is usually limited. Purely capacitive dividers also have disadvantages and

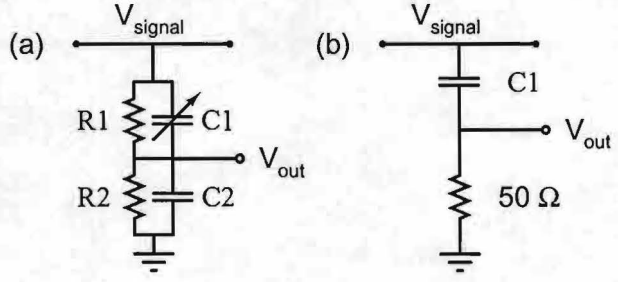

Figure 1: (a)*A compensated resistive voltage divider and* (b)*a differentiating voltage sensor.*

are complicated by the impedance of the measuring instrument. A useful trick is to use the circuit in Figure 1(b). The capacitor can be made quite small (~1 pF) by simply bringing the sensor wire close to the signal wire. The resistor represents the 50 Ω coaxial

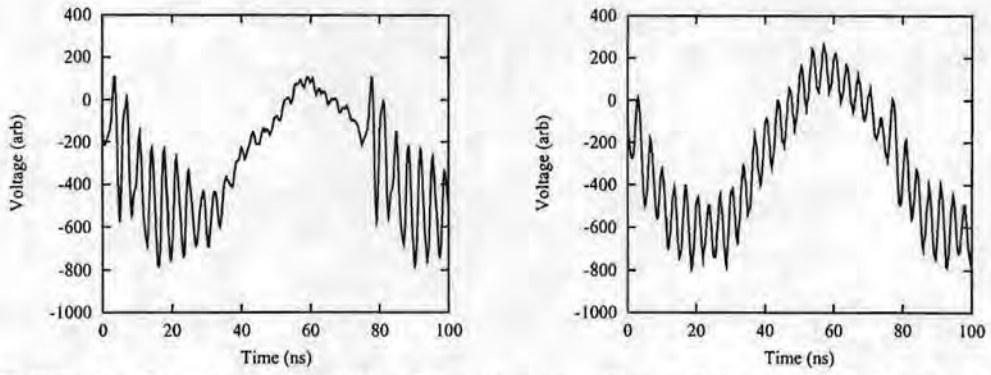

Figure 2: *The driven electrode voltage in a capacitive system for a 8.2 W, 20 mTorr argon plasma (left) and 10 W, 20 mTorr oxygen plasma with an electrode separation of 4 cm. The high harmonics are amplified by the capacitive pickup sensor.*

cable which is matched at the measuring device. RF quality cables and load resistors can have excellent frequency characteristics and the sensor capacitor can also be close to ideal. A small sensor capacitor does not load the circuit appreciably, an important factor in high Q resonant circuits.

The circuit in Figure 1(b) differentiates the signal but this is an important advantage. We are usually i rested in the higher harmonics and they are amplified. Since the signal is normally digitized with fast ADC's offering limited bit resolution, this amplification is a bonus. Figure 2 shows the (differentiated) voltage on the driven electrode of a 13.56 MHz capacitive rf plasma [1] with the 22nd harmonic clearly visible. It is interesting that the hf oscillation starts as the sheath begins expanding [2].

Currents can be measured with commercially available transformers or, alternatively, simple loop sensors can be used. In all cases it is important to shield the current sensor to minimize capacitive pickup. Differential loop sensors can be used to overcome problems caused by image currents and the exact placement of the rf conductors. If the actual plasma current is required it is crucial to measure the current return path. This is because electrode shields can conduct away a large fraction of the current measured at the driven electrode connection. These comments also apply to inductive antennas.

A good treatment of rf voltage and current measurements has recently been given by Sobolewski [3] who shows what can be determined from time resolved measurements of the sheath voltage and current. To obtain the true sheath voltage an internal measurement of the plasma potential is needed. Even if this is not possible, it may be important to make a measurement of the grounded electrode voltage in capacitive systems. Depending on the configuration, the grounded electrode can have a significant rf voltage on it!

2 Local Measurements

In view of the limitations of external measurements it is fortunate that internal, local measurements are possible. In this section we discuss magnetic field measurements. These can be used to measure current, electric field and the complex conductivity. Magnetic probes (or B-dot probes) have been used in inductive plasmas since the early days and their application and development continues [4–12].

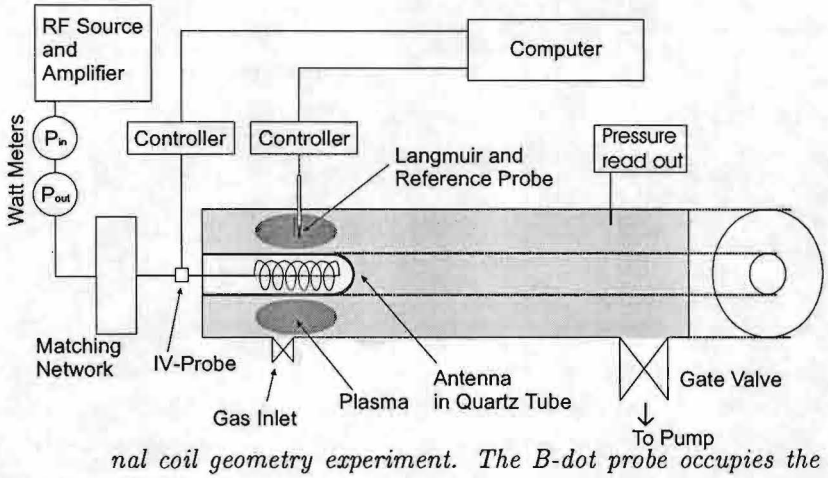

nal coil geometry experiment. The B-dot probe occupies the same position as the Langmuir probe.

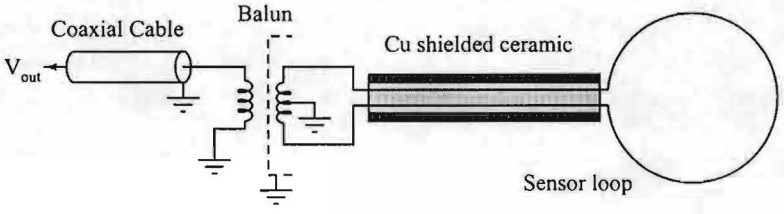

Figure 4: *B-dot probe showing only one Balun and the circular loop.*

One of the most interesting new developments is the use of bare double loop probes [9,10] to simultaneously measure dB_z/dt and dB_r/dt. The spatial coordinates refer to the cylindrical experimental system shown in Figure 3 which has an internal coil along the z axis. The coil current produces an oscillating B field in the z direction and induced E and plasma current in the azimuthal θ direction. The B-dot probe has one circular 3 mm diameter loop which measures $B_z(r)$ while the other loop is a figure of 8 (7 mm maximum dimension) which provides the spatial derivative of B_r with respect to z. The probe is sketched schematically in Figure 4. It is mounted on a computer driven bellows sealed translation stage so radial profiles of the signals are collected during each measurement.

The most difficult part of the experiment is undoubtedly the probe construction. In order to obtain good spatial resolution the loops are small and made of thin (0.15 mm) molybdenum wire. The probe shaft is a 0.8 mm OD ceramic tube with 4 bores to accommodate the wire. A 1.2 mm OD copper tube shields the probe shaft. Common mode (capacitive pickup) signal is reduced and impedance match to the measuring circuit improved by using an inline balun transformer as shown in Figure 4. The common mode is rejected by using the central earth point and further reduced by the copper foil electrostatic shield between the primary and secondary windings. The number of turns in the secondary is optimised for the measuring circuit which consists of a 50 Ω coaxial cable connected to a high speed oscilloscope.

It is customary to use a vector voltmeter [7] to obtain sufficient phase accuracy, but we have shown that an oscilloscope is adequate providing that it is fast (2 GHz sampling

frequency) and that the whole waveform is used by fitting the data to estimate the phase. The two loops of the figure-8 loop must have the same area. Even if this is the case some error creeps in since the wires cannot be collocated within the ceramic tube. Probe calibration is performed by immersing the circular loop in a known 13.56 MHz field generated in a solenoid for which the current is measured and the field calculated numerically. Since $\nabla \times \mathbf{B} = 0 = dB_z/dr - dB_r/dz$ in our geometry, the figure-8 loop can be calibrated against the circular loop by performing a vacuum measurement in the plasma chamber. The transmission and common mode rejection must be checked for the balun transformer to ensure that any resonances are sufficiently far from the signal frequency.

As the probe is swept through the plasma we obtain the radial profiles of B_z and dB_r/dz. Differentiating B_z with respect to r we then determine the profiles of the azimuthal electric field $E_\theta(r)$ and that of the current density $J_\theta(r)$ from the appropriate Maxwell's equations

$$E_\theta(r) = -10^{-8}\frac{i\omega}{r}\int_0^r r' B_z(r')dr', \tag{1}$$

$$J_\theta(r) = \frac{10}{4\pi}\left(\frac{dB_r}{dz} - \frac{dB_z}{dr}\right), \tag{2}$$

where r, z are in cm, B in Gauss, E in $V.\text{cm}^{-1}$ and J in A.cm^{-2}. The integral in Equation (1) is performed by assuming that $E = 0$ at the outer metallic wall of the vacuum chamber.

The main advantage of this small and delicate probe is the low level of perturbation of the plasma current. Using the shielded balun also greatly reduces the common mode and we estimate the signal to noise ratio to be greater than 60 dB. This means that it is possible to measure deep into the skin layer and observe the field behaviour associated with the anomalous skin effect [12–16].

Typical results [12] are illustrated in Figure 5. Note that there is a geometrical field dropoff associated with the cylindrical geometry. The phase reversal just beyond 4 cm from the antenna tube is characteristic of the anomalous skin effect. Under these circumstances the plasma conductivity is a nonlocal parameter.

3 Plasma Conductivity

The current and electric field in the plasma are related by Ohm's law

$$J = \sigma E \tag{3}$$

where σ is the complex conductivity which can be expressed [17] by

$$\sigma = \frac{e^2 n_e}{m_e\left(\nu_{en} + i\omega_{eff}\right)} \tag{4}$$

where both the effective collision frequency ν_{en} and the effective frequency ω_{eff} depend on the energy dependent collision cross section for momentum transfer and the eedf. The power density is given by

$$P(r) = J(r)E(r)\cos\Psi(r), \tag{5}$$

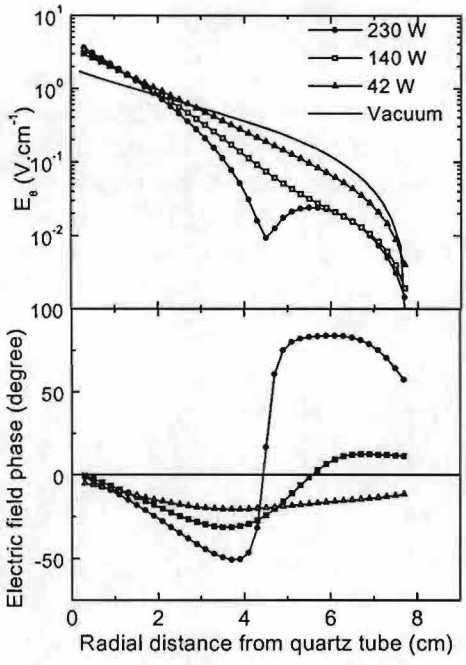

Figure 5: *The induced electric field amplitude (top) and phase relative to the phase in vacuum (bottom) at an argon pressure of 5 mTorr for 3 values of the power and in vacuum.*

with Ψ the measured phase angle. By comparing the actual power absorption with that expected from the conductivity, it is possible to separate the total power into an ohmic part and a collisionless part [12, 14]. Since the conductivity depends on the eedf, it is crucial to measure this and we have used a modified Scientific Systems Langmuir probe system to obtain measurements of the plasma parameters including the eedf.

We find that at 5 mTorr and 230 watts in argon about 50% of the power is dissipated in collisionless heating, whereas at 0.4 mTorr this is nearly 100% [12]. The B-dot probe in conjunction with a Langmuir probe can thus provide insight into the relative importance of various heating mechanisms in the rf plasma.

A complete set of data used to calculate the spatial dependence of the power density is shown in Figure 6 for a 100 W argon plasma at 100 mTorr. dB_r/dz and dB_z/dr are shown separately in the current plot and it is clear that just the first term is much smaller but it cannot be neglected. The system provides 'clean' and reproducible values of the power density over more than 5 orders of magnitude.

4 Plasma Production

Now that we know where the power is deposited we can get further insight by comparing this with where the plasma is actually made. The ionization source term can be obtained from Langmuir probe data [18,19]. At low pressure the plasma is non-local and the source term follows the density (with a correction for the variation of the plasma potential). At high pressure the source term should follow the power deposition which is governed by the skin effect (c.f. Figure 6).

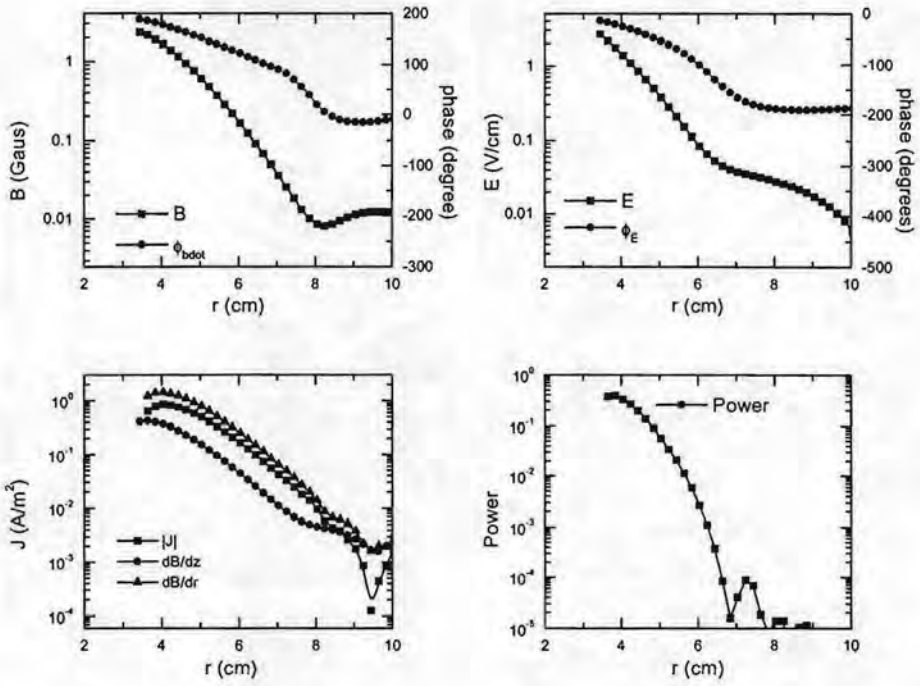

Figure 6: *Magnetic field amplitude and phase (upper left), electric field amplitude and phase (upper right), the current (lower left) and power (lower right) as a function of radial position from the centre of the chamber.*

Except at the lowest pressure the appropriate transport equation is

$$\nabla(D_a \nabla n_e(r,z)) = S(r,z) \tag{6}$$

with n_e the density and D_a the diffusion coefficient. We obtain the ionization source term $S(r,z)$ by inverting this transport equation, using D_a and density n_{exp} obtained from Langmuir probe measurements and standard data for collision cross sections.

The inversion is accomplished by an iterative procedure, where we begin with a guess for the source term S and solve the transport equation in the forward direction for n with a rapid elliptic solver. Then the source term is refined using Gold's ratio method:

$$S^{(i+1)} = \frac{n_{exp}}{n^{(i)}} S^{(i)} \tag{7}$$

where superscripts denote iteration number. Proof that this method uniquely converges is not available. However, we can show that it correctly recovers source terms when applied to model problems with known answers, such as results from computer simulations. There are some anomalies near boundaries in the results. These arise from finite-sized-probe effects, and can in principle be removed by an additional deconvolution step.

It is well known that metastable atoms can play an important role in argon plasmas by providing a two step ionization channel for plasma production. The existence of two step ionization can make the plasma more non-local at higher pressure, contrary to expectation. The density profile of metastables is not easy to determine without direct

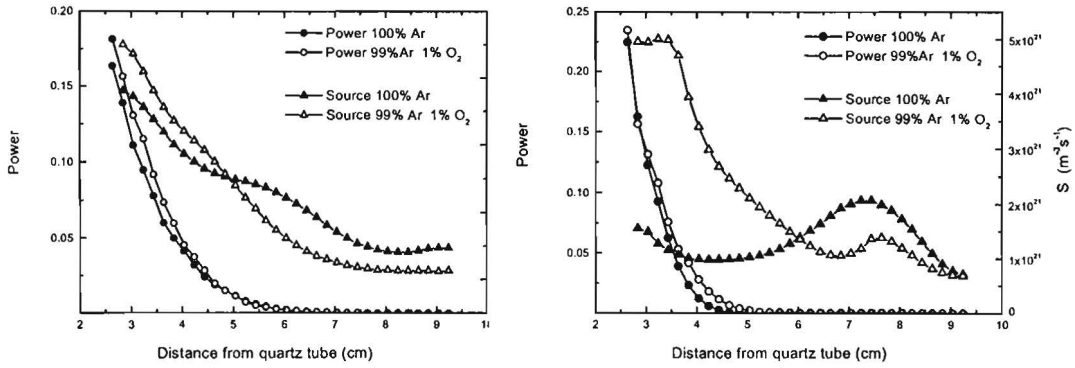

Figure 7: *Power deposition compared to the ionization source term for 100 W and 20 mTorr (left) and 100 mTorr (right).*

measurement. We have chosen to check the possible importance of metastables by introducing small amounts of a molecular gas (O_2) to efficiently quench the metastables [20] and reduce two step ionization.

An example of the results [21] is shown in Figure 7. At low pressure power deposition is almost unaffected by oxygen addition and the source terms are also very similar. There is some indication of increased non-locality in the pure argon plasma. At the higher pressure power deposition is still unaffected by oxygen addition but source terms are now quite different and there is a clear indication of non-locality in the pure argon plasma.

Metastable densities can of course be measured by LIF but it is perhaps worth noting that we are describing purely electrical measurements and in principle very little equipment is required. Using B-dot probes in combination with Langmuir probes, we can investigate the details of the electron heating mechanism as well as the plasma production mechanism. A fairly complete understanding of the rf plasma can be built up in this way.

5 Conclusion

One of the driving factors for the development of new probe techniques is the fact that Langmuir probes are actually quite difficult to interpret and do not perform well in the chemically active plasmas used in many applications. Alternatives which are better for measuring some one or other plasma parameter are under constant development [22–26]. With the continuing advance of electronic instrumentation, it is worth updating some of the older techniques (e.g. resonance probes—see Ref [27]), as well as using new ideas.

Acknowledgements

I would like to thank Bob Piejak for help with the B-dot probe design. Gilles Cunge and Brendan Crowley constructed the probe and performed the measurements. William Rullenraad carried out further measurements during his stage at DCU. Miles Turner devised and carried out the density profile inversion. This work was supported by Association EURATOM-DCU Contract No. ERB 50004 CT 960011.

References

[1] D. Vender, unpublished (1994).

[2] D. Vender and R. W. Boswell, J. Vac. Sci. Technol. A **10**, 1331 (1992).

[3] M. A. Sobolewski, Appl. Phys. Lett. **72**, 1146 (1998), M. A. Sobolewski, Phys. Rev. E **59**, 1059 (1999).

[4] V. A. Godyak and R. B. Piejak, J. de Physique IV **8**, 241 (1998).

[5] J. Hopwood, C. R. Guarnieri, S. J. Whitehair and J. J. Cuomo, J. Vac. Sci. Technol. A **11**, 147 (1993)

[6] A. R. Ellingboe, Phys. Plasmas **3**, 2797 (1996).

[7] R. Piejak, V. Godyak and B. Alexandrovich, J. Appl. Phys. **78**, 5296 (1995).

[8] J. A. Meyer, R. Mau and A. E. Wendt, J. Appl. Phys. **79**, 1298 (1996).

[9] R. Piejak, V. Godyak and B. Alexandrovich, J. Appl. Phys. **81**, 3416 (1997).

[10] G. Cunge, B. Crowley, D. Vender and M. M. Turner, *FLTPD III*, Saillon, Switzerland (1999).

[11] G. Cunge, B. Crowley, D. Vender and M. M. Turner, Plasma Sources. Sci. Technol. **8**, 1 (1999).

[12] G. Cunge, B. Crowley, D. Vender and M. M. Turner, *in press at* J. Appl. Phys. (2001).

[13] M. M. Turner, Phys. Rev. Lett. **71**, 1844 (1993).

[14] V. A. Godyak, R. B. Piejak, B. M. Alexandrovich, Phys. Rev. Lett. **80**, 3264 (1998).

[15] V. A. Godyak, R. B. Piejak, B. M. Alexandrovich and V. I. Kolobov, Phys. Plasmas **6**, 1804 (1999).

[16] S. Takechi and S. Shinohara, Jpn. J. Appl. Phys. **38**, L148 (1999).

[17] G. G. Lister, Y. M. Li and V. A. Godyak, J. Appl. Phys. **79**, 8993 (1996).

[18] C. Deegan, PhD thesis DCU (1999).

[19] B. Crowley, M. M. Turner, W. Rullenraad and D. Vender, 27th em IEEE ICOPS, New Orleans (2000).

[20] L.G. Piper, J.E. Velazco and D.W. Setser, J. Chem. Phys. **59**, 3323 (1973).

[21] W. Rullenraad, stage thesis, DCU/TUE (2000).

[22] R. L. Stenzel, Rev. Sci. Instrum. **62**, 130 (1991).

[23] S. Torven, H. Gunell and N. Brenning, J. Phys. D **28**, 595 (1995).

[24] N. StJ. Braithwaite, J. P. Booth and G. Cunge, Plasma Sources Sci. Technol. **5**, 677 (1996).

[25] M. Klick, W. Rehak and M. Kammeyer, Jpn. J. Appl. Phys. **36**, 4625 (1997).

[26] T. Shirakawa and H. Sugai, Jpn. J. Appl. Phys. **32**, 5129 (1993).

[27] P. E. Vandenplas, *Electron Waves and Resonances in Bounded Plasmas*, Wiley Interscience, London (1968).

X and XUV radiations: generation and applications opportunities for diagnostics

J.-M. Pouvesle
Université d'Orléans - France

ORAL CONTRIBUTIONS

Atom Oxygen Density and Sticking Coefficient Measurements in an Inductively Coupled Plasma.

S. Gomez, P.G. Steen and W.G. Graham,

Dept. of Pure and Applied Physics,
Queen's University of Belfast, BT7 INN,
Northern Ireland

1. Introduction

The interaction of reactive atomic species with surfaces is a key phenomenon in many plasma processes. Here oxygen dissociation fractions and atomic densities have been measured in an inductively coupled plasma system. In addition to the dependence of dissociation fractions on operating conditions, particular attention has been paid to spatially resolved measurements close to the lower electrode surface, which supported various sample materials. These spatially resolved atomic oxygen measurements allowed the atom sticking coefficients to be determined.

2. Experimental details

A GEC reference reactor, configured for operation in inductive mode, was used for the measurements. The antenna is a 5-turn water-cooled copper coil that couples power to the plasma through a quartz window. The coil is driven at 13.56 MHz through a close coupled, high power rf matching network. Powers ranging from 10 W to 300 W and gas pressures ranging from a few to 67 Pa were used. The grounded lower electrode diameter is 165.1 mm with an electrode-quartz window spacing of approximately 40.5 mm. This electrode was constructed of stainless steel and various sample materials were placed on the surface.

The atomic oxygen densities were obtained by using two photon laser induced fluorescence (LIF) The spatially resolved measurements were obtained by creating a sheet of laser light which illuminated the region between the quartz window and a bottom electrode. The main difficulties in using this technique for two photon LIF will be discussed.

3. Results and Discussion

The inductive GEC plasma system can operate in both inductive (H) and capacitive (E) mode. As can be seen from Figures 1 the atomic oxygen densities measured in the centre of the plasma in inductive mode are significantly higher than in capacitive mode.

The atomic oxygen density shows more pronounced power dependence in capacitive mode than in inductive mode. The dissociation fractions agree quite well with a simple kinetic model for the E mode.

Operation with and without sample materials such as textiles, silicon, aluminium and stainless on the lower, grounded electrode were contrasted. The axial profile of the atomic oxygen density close to the sample surfaces is used to determine the net sticking coefficient,α. The measured values of α were found to be pressure dependent. Typical values are 0.3±0.1 for stainless steel and 0.09±0.05 for aluminium at 50 mTorr and 100 W.

4. Acknowledgements

This work was supported by the EU BRITE programme under the Plasmatex project.

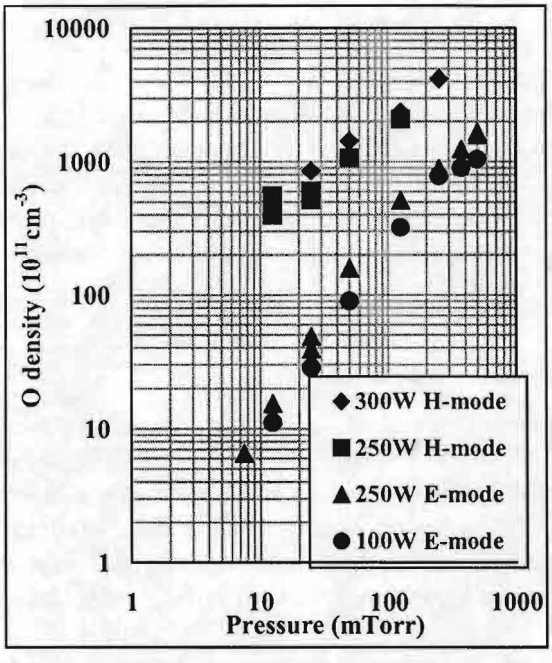

Figure 1. Measured atomic oxygen densities in the centre of the GEC reference reactor.

Diagnostics of N_2/O_2 pulsed rf plasma jet: TALIF measurements of N and O atoms and OES of the glow

A. Broc, G. Dilecce and S. De Benedictis
Centro di Studio per la Chimica dei Plasmi CNR
c/o Dept. of Chemistry, Univ. of Bari
Via Orabona 4, 70126 Bari, Italy

Introduction

Sources of O and N atoms are of great interest for aerospace testing facilities. Streams of supersonic or subsonic atoms are produced by plasma expanding through an axy-simmetric convergent-divergent nozzle. Depending on plasma condition the jet is composed of molecular and atomic neutrals and ions. The fluid dynamic characterization of the stream and particularly the atom density measurement is therefore an important task. Several laser techniques are employed to this purpose [1]. The detection of $O(^3P)$ and $N(^4S)$ in afterglows is efficiently operated by two photons laser induced fluorescence (TALIF) with UV photons [2, 3]. Despite the high sensitivity of TALIF for atom detection, the absolute density measurements require a calibrated TALIF. Actually in literature there are several measurements of O and N atoms carried out by TALIF using different calibration methods [4, 5]. However the application of TALIF to O and N atoms in a supersonic plasma jet is quite rare. The present work is focused on laser characterization of flow-field properties of the N_2 and O_2 plasma expansion and particularly on the main aspects of TALIF measurements of O and N atoms in supersonic *rf* plasma jet. The plasma is produced by a capacitive coupled discharge in co-axial electrode configuration stainless steel chamber. The apparatus is shown in Fig. 1

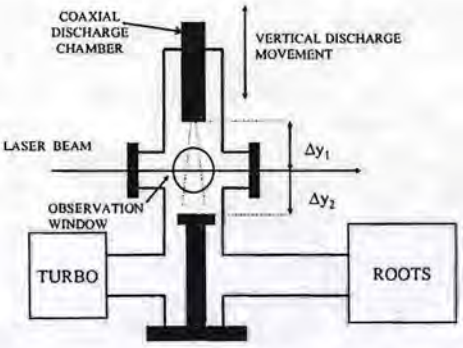

Figure 1: *Setup of plasma jet. The laser beam and detection axis are fixed while the discharge and whole jet are moveable.*

Characterization of N_2 plasma jet by LIF on sputtered Fe

In previous experiments we investigated the flow field temperature and density in N_2 and O_2 of supersonic expansions by using NO seeded in the main flow as a tracing specie [6]. NO is then monitored by LIF. The complex structures of the flow field patterns were clearly evidenced.

This approach has been then applied to supersonic plasma jets but several drawbacks have been evidenced. The dissociation of NO tracer, as well as the presence of a stray *rf* field in the expansion chamber that create a weak secondary discharge dominated by electron processes, impose limits to the power that can be delivered to the discharge. The increase of the background pressure in the expansion chamber reduces to some extent these effects. We have searched for a different fluid-dynamic tracer to employ at low pressure conditions. A good tracing is given by Fe atoms produced by sputtering of the *rf* electrode. They expand with the main flow in the low pressure chamber.

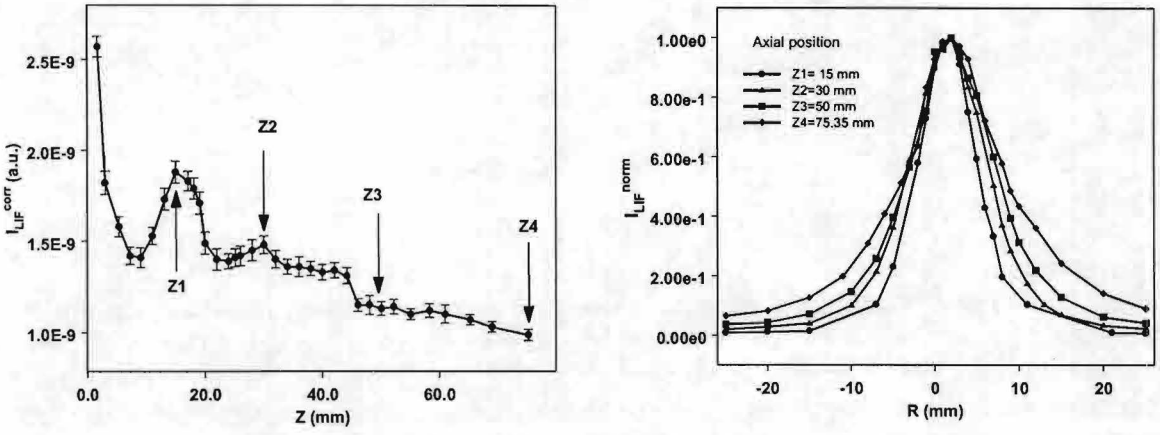

Figure 2: *Axial (a) and radial (b) profiles of Fe atoms in jet produced by sputtering in N_2 discahrge at 100 W P_1= 4.1 Torr and P_2= 0.2 Torr.*

Fe atoms are detected by LIF spectroscopy using the following atomic transitions:

$$Fe(\ a\ ^5D_{J=3} + h\nu_L \rightarrow v\ ^5P^o_{J=3} \rightarrow a\ ^5P_{J=3} + h\nu_E) \qquad (1)$$

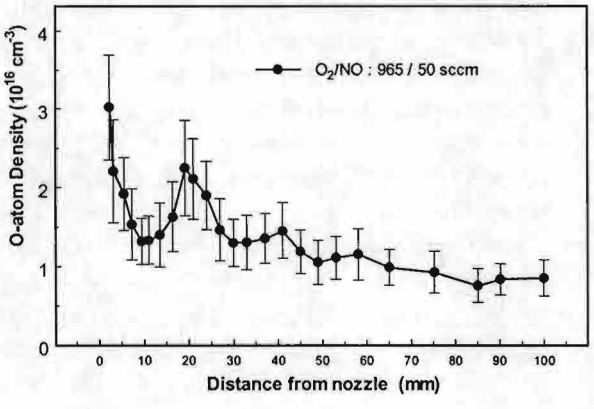

Figure 3: A *xial density profile of O atoms in NO/O_2 continuous plasma jet at P_1= 10 Torr, P_2= 0.5 Torr and 275 watt.*

The excitation takes place with laser photons at 208.41417 nm and the fluorescence is detected at 328.6754 nm. The axial and radial profiles of Fe in the N_2 plasma jet are shown in Fig.1a and b. The present density structures agree very well with those traced by LIF on NO seeded in N_2 plasma jet. in a condition previously investigated [7] very similar to the present one and not reported here for reasons of space. Fe tracing is very powerful whatever the discharge power and the background pressure in the expansion chamber.

O atom TALIF measurements in O_2 plasma jet

TALIF measurements of $O(^3P)$ have been carefully carried using the transition

$$O(\ 2p\ ^3P_2 + 2h\nu_L \rightarrow 3p\ ^3P_2 \rightarrow 3s\ ^3S_1 + h\nu_E) \qquad (2)$$

The excitation is by two laser photons at 225.582 nm and LIF detection at 844.6 nm. The axial profile of O-atoms in O_2 plasma jet has been reported in Fig. 3. In this case we have employed the calibration procedure developed in [8]. This calibration is based on the fact that the quenching rate coefficient of $3p^3P_2$ level by O_2 is much higher than by O. The quenching

rate can then be correlated to the O density. The calibration is operated *in situ* by LIF experiments carried out in the background region of O_2 plasma jet in which the discharge dissociation of O_2 can be significantly varied. Dissociation degrees larger than 20% have been achieved, and this makes the measurements almost straightforward. The error reported in the figure is mainly due to the calibration uncertainty.

N atom TALIF measurements in N_2 plasma jet

TALIF measurements of N(^{4}S) have been carried out using the two excitation pathways [3]

$$N(2p^3\ ^4S^0 + 2h\nu_L \rightarrow 3s\ ^4D^0_{J=7/2} \rightarrow 3s\ ^4P_{J=5/2} + h\nu_E) \qquad (3)$$

$$N(2p^3\ ^4S^0 + 2h\nu_L \rightarrow 3p\ ^4S^0_{J=3/2} \rightarrow 3s\ ^4P + h\nu_E) \qquad (4)$$

In the pathway (3) the laser excitation occurs with λ_L =210.7885 nm photons and the fluorescence is at λ_E = 868.027 nm while in (4) λ_L =206.718 nm and λ_E = 746.83 nm.

Contrary to the oxygen case, the measurements of N atom density by TALIF is particularly difficult since the dissociation of N_2 is not large. Then TALIF signal is not easily discriminated with respect to the N_2 (FPS) emission that cover the full red spectral region. This is particularly true for discharge conditions in which the *rf* field escapes through the nozzle into the expansion region so that the contribution of FPS emission by electron impact is large. On the other hand the attempt to increase N density by increasing the power delivered to the discharge is not advantageous because FPS also increases. The situation is similar whatever of the two excitation schemes is used and despite the use of a gated photomultiplier. In such condition the only possibility to detect N atom is to operate in pulsed discharge regime and detecting the atom in the very early afterglow time. To overcome this limit we have modified the relative surface of the discharge electrodes, enhancing the asymmetry of the discharge, so as to reduce the plasma potential and consequently the stray field in the expansion region also at high *rf* power. In such condition it was possible to detect N atoms in both continuous and pulsed discharge regime. In Fig.4 it is reported the axial profile of N atoms measured by TALIF at 207 nm in a pulsed jet with discharge time ON/OFF set at 30 ms and 70 ms respectively. The TALIF measurement was operated at 29 ms in the discharge period. The calibration of TALIF measurements has been operated *in situ* employing the NO titration technique, monitoring of N atom loss directly by TALIF, combined to local static pressure measurements by Pitot tube. Several types of injections have been tested and the fluid dynamic problems are very similar to those discussed in [9]. In the present condition a dissociation degree of about 0.3% has been measured by a titration operated with single orifice injector set at 2 cm from the nozzle. The titration gas is injected counter-flow.

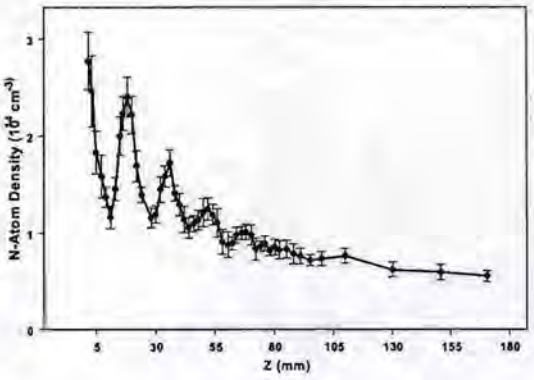

Figure 4: *Axial density profile of N atoms in N_2 pulsed plasma jet at P_1= 10 Torr, P_2= 0.5 Torr. and 500 watt,*

We have used also ring injector. Fig. 5 shows a typical N atom loss plot as function of NO flow rate obtained by TALIF measurements at 15 cm from the injection point. The *ring*

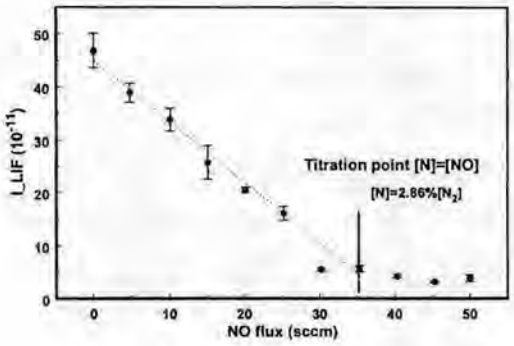

Figure 5: *Titration of N atoms by NO in the jet P_1= 18 Torr, P_2= 1.5 Torr and 500 watt,*

injector was set at 1 mm from the nozzle orifice. N_2 dissociation evaluated from the titration point is about 1.5%. In this case TALIF excitation was done at 211 nm. The high atom production was achieved protecting the internal surface of the discharge with a pyrex tube. In this experiment the NO mixing in the jet is regular and the N-loss is linear with NO flow rate. It reveals also that ASE does not effect TALIF measurements. The calibration can be used in other experimental conditions provided that ASE is negligible. In our experiments working typically satisfies this condition with laser intensity lower than 200 μJ.

Remarks

The present measurements evidence that *rf* plasma jets must be handled with care to avoid the regime for which a secondary discharge is ignited in the expansion chamber. The analysis of $N_2(C,v)$ state distribution evidence the condition in which the secondary discharge is ignited. From the diagnostic point of view pulsing of the discharge is favorable to reduce the background radiation. The N density calibration by the *in situ* NO titration procedure is not fully exhaustive since the measurements of temperature and density have not been carried out in accurately scalable experimental conditions. The characterization of the plasma jet is still in progress.

Acknowledgment

The research has been supported by the Italian Space Agency. A. Broc undertook this work as ESA external fellow at CSCP-CNR. A. Parodi is thanked for his valuable technical assistance.

References

[1] R. L. McKenzie, AIAA Journal **31**, 465-477, (1993); D. G. Fletcher and D.J. Bamford, 7th AIAA/ASME Joint Thermophysics and Heat Transfer Conference, (Albuquerque 1998), **AIAA-98-2458.**

[2] A. D. Tserepi E. Wurzberg, T. Miller, Chem. Phys Lett., **265**, 297-302, (1997).

[3] S. F. Adams T. A. Miller, Chem. Phys. Lett., **295**, 305-311, (1998)

[4] K. Niemi, V Schultz von der Gathen H.F. Dobele, Proc. 7th Int. Symp. on High Pressure Low temperature Plasma Chemistry, (Greifswald, 2000).

[5] A.Goehlich, T. Kawetzki H.F. Dobele, J. Chem. Phys., **108**, 9363-... (1998).

[6] G. Dilecce, M. Simek, M. Vigliotti, S. De Benedictis, Appl. Spectrosc., **54**, 824-831 (2000)

[7] A. Broc, G. Dilecce, M. Vigliotti, S. DeBenedictis, Proc. ESCAMPIG-XV, Lillafured 2000, **24F**, p. 308-309.

[8] G. Dilecce, M. Vigliotti, S. De Benedictis, J.Phys. D: Appl. Phys., **33**, L53-56, (2000).

[9] S. De Benedictis, G. Dilecce, M. Simek and M. Vigliotti, Plasma Sorce Sci & Technol, **7**, 557-571 (1998).

The final frontiers of cavity ring down spectroscopy: the mid-infrared.

M. M. Hemerik and G. M. W. Kroesen
Eindhoven University of technology, Faculty of Applied Physics,
P.O. Box 513, 5600 MB Eindhoven, The Netherlands

Introduction

The mid-infrared is a very interesting wavelength range for low pressure plasma diagnostics, since this is the wavelength range of the molecular rotation-vibration spectra. Because of the different masses, bonding strengths, bonding angles, etc., each molecular species has its unique vibrational and rotational transitions. Typical energies of rovibrational transitions are in the order of a tenth of an eV, what makes diagnostics in this wavelength range very non-intrusive. The big disadvantage of those diagnostics is the sensitivity ,which is limited by the available light sources, detectors and other optical devices.

In 1988 O'Keefe and Deacon developed a new method to perform optical absorption measurements: cavity ring down spectroscopy [1]. Their technique was based on the measurement of the rate of absorption, rather than the magnitude of absorption, and they obtained sensitivities which were significantly greater than attained with conventional absorption spectroscopy. This cavity ring down technique has been applied ever since in the complete spectrum, from the uv to the infrared.

During the past four years we worked on the construction of a mid-infrared cavity ring down spectrometer. Our aim is to perform spatially and time resolved radical density measurements on real depositing silane discharges.

Choice of light source

The spectral range we intend to cover with our new diagnostic ranges from ca. 4 to 15 μm, or 600 to 2500 cm^{-1}. At typical discharge pressures of 10^{-2} – 1 mbar, the absorption line width is mostly determined by Doppler broadening, resulting in absorption line widths of 10^{-3} – 10^{-2} cm^{-1}. The light source for the cavity ring down measurements should be tunable in the desired wavelength range and have a line width in the order of, or smaller than the absorption line width. There is only one light source that meets both demands: the helium cooled infrared diode laser. Two problems arise when one wants to use this laser for CRDS experiments. First of all, the output power is very low, typically 100 μW, and at the second place, it is a cw laser.

Chopping of an infrared cw laser

Since the light intensity inside the cavity will only starts its exponential decay when no more photons are fed into the cavity, the cw laser should be extinguished at least one order faster than the expected ring down time. Conventional devices that work in the visible and uv part of the spectrum, like mechanical choppers and optical modulators, do not work in the mid-infrared, so a new method to somehow 'chop' the laser beam had to be developed.

The method developed in our lab is best described as 'mode tuning'. A ring down cavity has an optical mode structure consisting of longitudinal and transverse modes. When the frequency spacing between the different modes is larger than the line width of the laser, there will be laser wavelength that are effectively coupled in the cavity, and wavelengths that

will be fully reflected by the entrance mirror. A small detuning of the laser wavelength, in the order of the line width of the laser, is enough to abruptly switch from a state where light can enter the cavity, to a state where the light is fully blocked from the cavity (Fig. 1). To detune a diode laser over several tens of megahertz, implies a change in current through the diode of ca. 10^{-5} mA, which is only a relative change of 10^{-3}. Such small changes in laser current can be applied at a rate of several hundreds of megahertz, what corresponds to switching times of several nanoseconds.

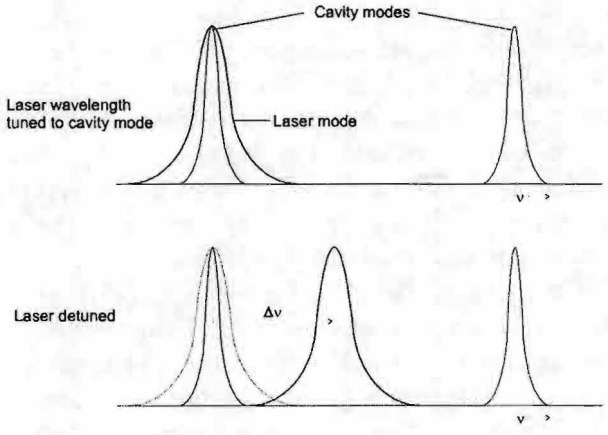

Fig. 1: 'Chopping' the laser by controlled detuning of the wavelength

The cavity construction

The chopping mechanism described above requires a wide mode structure. The widest mode structure is obtained for a confocal cavity, where the distance between the mirror equals the radius of curvature of the mirrors. We therefore constructed a 1 meter long confocal cavity inside a vacuum vessel. The cavity consists of an aluminum tube with an inner diameter of ca. 35 cm and a wall thickness of ca. 3 cm, with a mirror at both ends. One of the mirrors is placed on a piezo, in order to match the cavity length to the laser wavelength.

This cavity is suspended in a vacuum vessel by means of two sets of springs to carry the weight, and rubber flaps to damp all the vibrations (Fig. 2). This results in an optically and mechanically stable cavity.

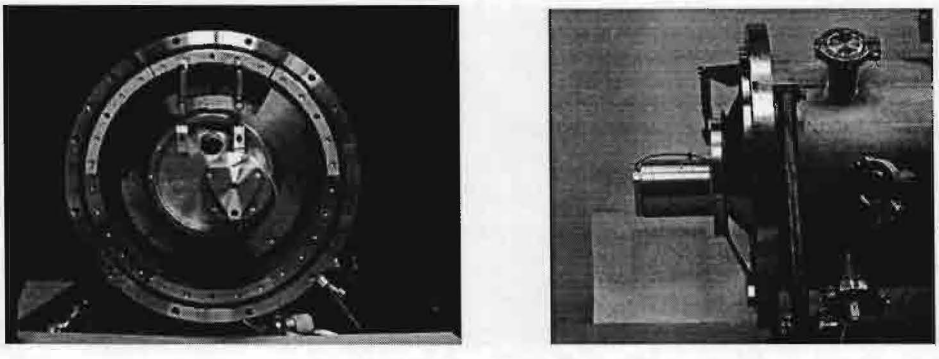

Fig. 2: Front and side view of the optical cavity suspended in the vacuum vessel.

The discharge

The first objective of the setup will be to unravel the complex chemistry in silane discharges. We therefore constructed a modular discharge chamber that can be scanned through the optical beam. The plasma chamber consists of a powered shower head electrode, that is placed in a cylindrical box that forms the grounded electrode. The bottom of this box is formed by a grid, to allow a laminar flow through the plasma region. The distance between the powered electrode and the bottom grid is 33 mm, the inner diameter of the box is 13 cm, and the complete chamber is water cooled. The complete dicharge chamber is placed on a 2-d manipulator, to scan it through the optical beam in both directions perpendicular to the optical beam, for spatially resolved measurements.

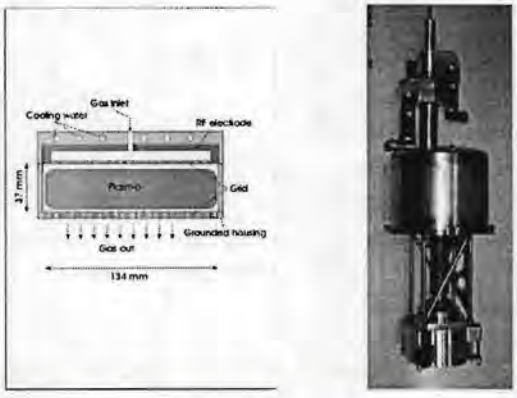

Fig. 3: (left) cross-section of the plasma chamber, (right) plasma chamber on the manipulator

The first results

1. Chopping the laser

Fig. 4 gives an example of the build up of a cavity mode by scanning the piezo, and thereby the cavity length. When there is enough laser power in the cavity, the laser is detuned and the exponential decay is started. The decay time is typically 1 μs, so after several tens of microseconds the laser can be put back to its original wavelength, and the procedure can be started again. In this way, repetition rates of thousands of ring downs per seconds can be reached, what is considerably higher than obtained with pulsed lasers.

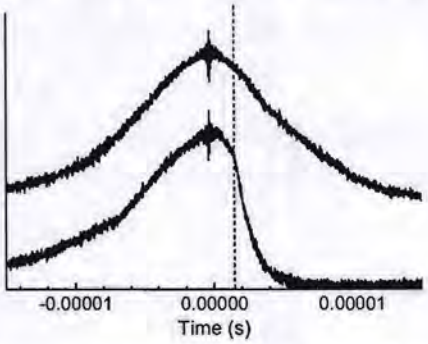

Fig. 4: (Top) Normal build up of a cavity mode by scanning the piezo, (bottom) build up and ring down after detuning the laser (at the dotted line).

2. The first spectroscopic ring down measurements:

To test the new diagnostic the plasma chamber was taken out of the vacuum vessel, and the vessel was filled with 0.01 mbar CO, which has absorption lines in the same wavelength range as silane and silane radicals. The laser wavelength was scanned by scanning the laser current. The Doppler line width of CO at room temperature should be ca. 175 MHz. The measured line width was 202 MHz, which is the line width of the convolution of the Doppler width and a Gaussian laser line width of 50 MHz.

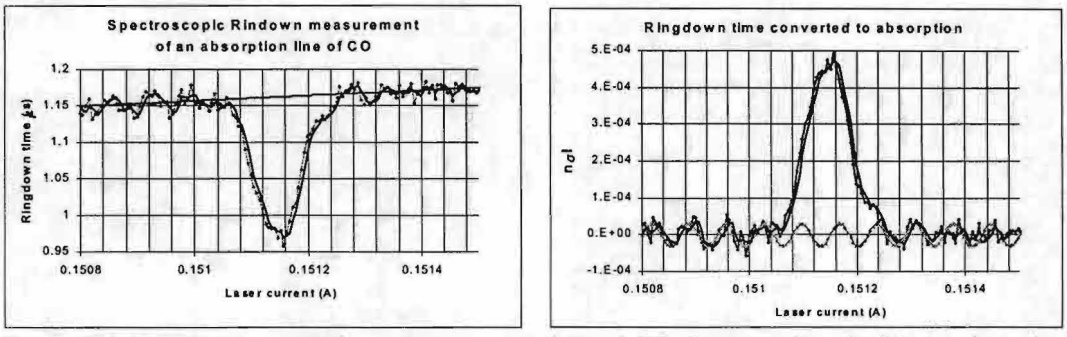

Fig. 5: (left) Spectroscopic ring down measurement of a weak CO absorption line, (right) ring down time converted to absorbance. The periodical background is caused by a malfunctioning piezo.

The preliminary sensitivity of the new diagnostic is in the order of 10^{-5} per pas, or 10^{-6} cm^{-1}, which is already better than conventional infrared absorption spectroscopy. When the final problems with the piezo are solved, this sensitivity will be 10^{-6} or better. This sensitivity can be increased by at least two orders, when mirrors with a higher reflectivity are obtained.

Conclusions / Future work

We succeeded in building a mid-infrared cavity ring down spectrometer. The preliminary sensitivity is already better than of conventional absorption spectroscopy, and will be futher improved by solving the final problems and the use of better mirrors.

In the near future the discharge chamber will be put back in the vacuum vessel and spectroscopic measurements on silane discharges will be performed. The first goal will be to measure spatially and time resolved densities of SiH, SiH_2, SiH_3, Si_2H_5 and Si_2H_6. In the futher future, the research will be extended to the ions and larger clusters, and the growth mechanism of nano-sized particles in silane discharges.

[1] A. O'Keefe and D.A.G. Deacon, *Cavity ring-down optical spectrometer for absorption measurements using pulsed laser sources*, Rev. Sci. Instr. **59**, 2544 (1988)

Advanced diagnostics for exploring the growth mechanism of plasma deposited materials

W.M.M. Kessels,[a,b] J.P.M. Hoefnagels,[a] E.R. Fisher,[b]
E.S. Aydil,[c] and M.C.M. van de Sanden[a]
[a]*Dept. of Applied Physics, Eindhoven University of Technology, Eindhoven, The Netherlands*
[b]*Dept. of Chemistry, Colorado State University, Fort Collins, U.S.A.*
[c]*Dept. of Chem. Engineering, University of California Santa Barbara, Santa Barbara, U.S.A.*

Introduction

Insight into the growth mechanism of plasma deposited materials is essential for full optimization of the deposition process and improvement of the material properties of the deposited films. The complexity of the deposition process requires knowledge on the different aspects of plasma deposition. This means that in addition to measurements of the gas phase densities of the plasma species, also experiments on the species' surface reactivity are required as well as on the "nature" of the surface during film growth. In the following sections, some studies concerning these three different aspects will be shortly reviewed. It will be concentrated on the technologically very relevant deposition processes of a-Si:H and a-SiN_x:H, which are both known to be dominated by radical species rather than by ions.

Radical density measurements

Threshold ionization mass spectrometry (TIMS) and cavity ring down spectroscopy (CRDS) are two powerful diagnostics for studying radical densities in deposition plasmas. TIMS uses electron energies higher than the ionization potential of the radical but lower than the dissociative ionization energy of the parent molecule to distinguish radicals from parent molecule cracking products in the mass spectrometer (Fig. 1) [1]. The advantages of this technique are that it measures radicals very close to the surface/substrate (where deposition takes place) and that it can easily be applied to a large variety of radicals. However, TIMS cannot easily and non-intrusively be applied at several positions in the plasma and the densities are relatively difficult to quantify. This is partially related to the loss of radicals during their extraction into the mass spectrometer. CRDS is a direct absorption technique that

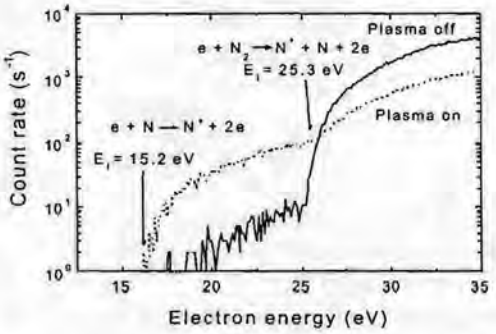

Figure 1: *Electron energy scan at mass/charge ratio 14 showing ionization of N radicals at low energies and mainly dissociative ionization of N_2 at high energies.*

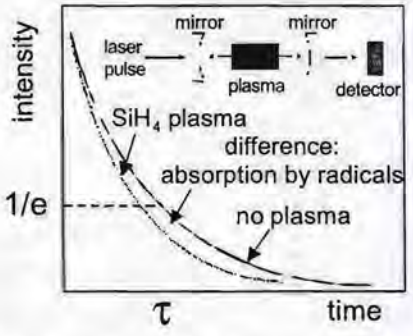

Figure 2: *Basics of CRDS. From the difference in decay time of the laser pulse between "plasma on" and "plasma off" the absorption by radicals and therefore their density can be determined.*

is very sensitive due to the fact that decay times of a laser light pulse in an optical cavity are measured (Fig. 2) [2,3] rather than differences in absolute light intensity. Compared to TIMS and laser-induced fluorescence (LIF), radical densities are very easy to quantify with CRDS, while it's poorer spatial resolution (compared to LIF) can be overcome by Abel inversion. Furthermore, the radicals probed need only to absorb and not necessarily to fluoresce. This enables also the detection of radicals with a very short "radiative lifetime" (due to pre-dissociation) such as CH_3 and SiH_3. Both TIMS and CRDS have been applied in the Expanding Thermal Plasma (ETP) and their results on the radical densities have revealed interesting new insights in the growth mechanism of a-Si:H and a-SiN_x:H (Figs. 3 and 4).

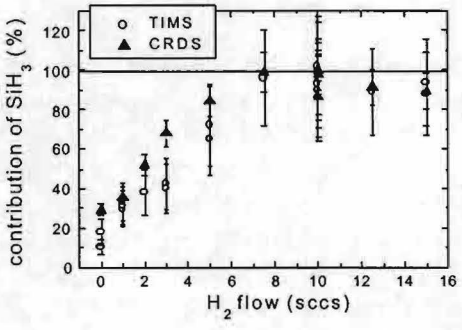

Figure 3: *Contribution of SiH_3 to a-Si:H film growth in an ETP Ar-H_2-SiH_4 plasma [2,3]. Interesting is that the film quality also improves with increasing H_2 flow. At high H_2 flows, the contribution of SiH_2, SiH, Si, and $Si_nH_m^+$ is <5%, ~2%, 0.2%, ~7%, respectively [3].*

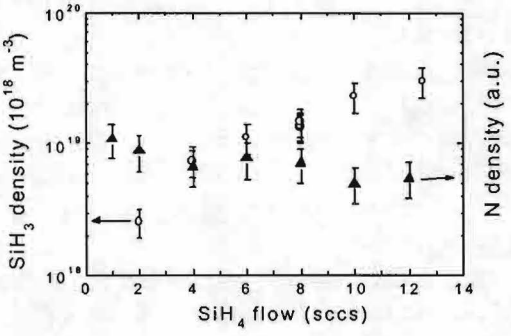

Figure 4: *SiH_3 and (relative) N density in an ETP Ar-H_2-N_2-SiH_4 plasma. Because the Si/N ratio in the films increases with increasing SiH_4 flow, this suggests "nitration" of an a-Si:H-like overlayer by N radicals as growth mechanism.*

Surface reactivity measurements

To determine the relevancy of certain plasma radicals to film growth not only their density needs to be known, but also their surface reaction probability. As a matter of fact, a high gas phase density of a radical can be due to favored production of this radical but can also be due to a very low surface reactivity and therefore a relatively low significance of this radical for film growth. A prominent method to study the surface reactivity of radicals is the "Imaging of Radicals Interacting with Surfaces" (IRIS) technique (Fig. 5) [4]. In the IRIS method a molecular beam is effusively extracted from a plasma and the radical of interest is probed by LIF. The fluorescence, which is proportional to the radical's density, is detected by a 2-D intensified CCD array. In a typical IRIS experiment, first an image is taken of the freely expanding molecular beam (Fig. 6a). Subsequently, a substrate is rotated into the path of the molecular beam and a new image is taken (Fig. 6b). In this image, not only the radicals in the forward molecular beam are detected but also radicals possibly scattered and/or produced on the surface. The difference in the two images shows these radicals (Fig. 6c).

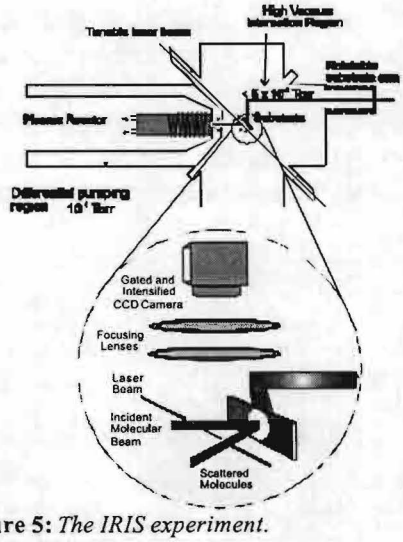

Figure 5: *The IRIS experiment.*

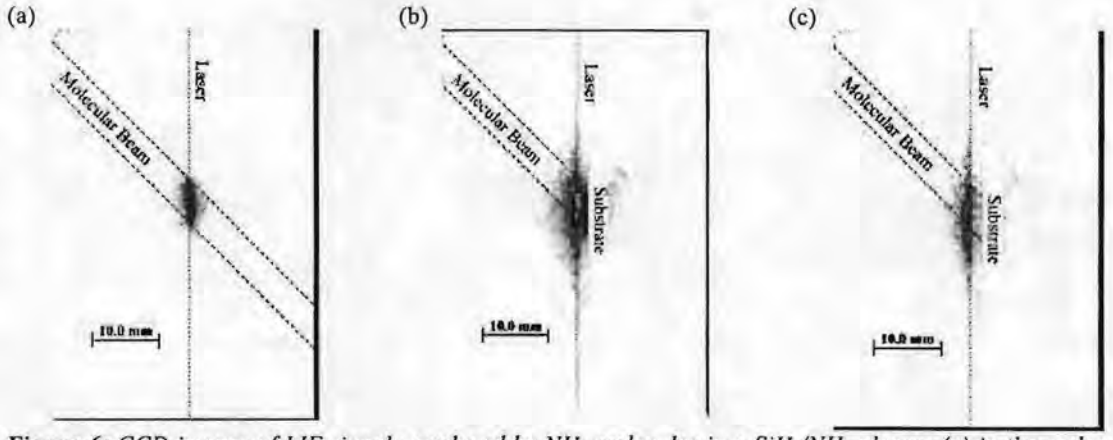

Figure 6: *CCD images of LIF signals produced by NH_2 molecules in a SiH_4/NH_3 plasma (a) in the molecular beam only and (b) with the substrate in the path of the molecular beam. Both images are corrected for spurious signals caused by plasma emission and laser light scattering. Figure (c) is the difference between images (a) and (b) showing the NH_2 radicals scattered from the substrate.*

The reactivity of the radicals is determined from simulations relating the intensity of the scattered radicals to the intensity of the radicals in the incident beam in cross-sectional images along the laser axis (Fig. 7). A scatter coefficient S=1 means that all radicals are scattered at the surface, S<1 means surface loss and S>1 surface production. Although both NH_2 and SiH show surface loss in a NH_3/SiH_4 plasma [5,6], the reactivity of NH_2 is very small to the one of SiH. Depending on their density in the plasma, this might imply that SiH is more important than NH_2 in the deposition of a-SiN_x:H from a NH_3/SiH_4 plasma.

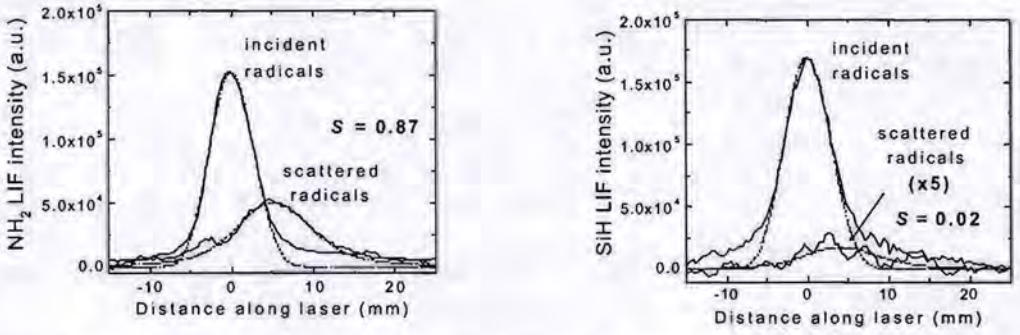

Figure 7: *Cross-sectional images of the radicals in molecular beam and scattered from the surface for (a) NH_2 and (b) SiH in a SiH_4/NH_3 plasma. The surface reaction probability* β=1-S *of NH_2 and SiH is 0.13±0.07 [5] and 0.98±0.05 [6], respectively. The substrate temperature is 300 K.*

In situ film growth measurements

The surface reactivity of radicals depends on the nature of the film's surface. This nature itself depends on the reactions taking place at the surface. Therefore, by probing the chemical species and their bonds in the film and on the surface during film growth, information can be obtained about the atomistic reactions on the surface. Attenuated-total-reflection infrared spectroscopy (ATR-FTIR) (Fig. 8) is a very powerful tool in this respect. Due to multi-passing and/or multiple reflections at the crystal or film surface a very high sensitivity is obtained. Surface selectivity can be obtained by isotope experiments (e.g., D on a-Si:H) or by

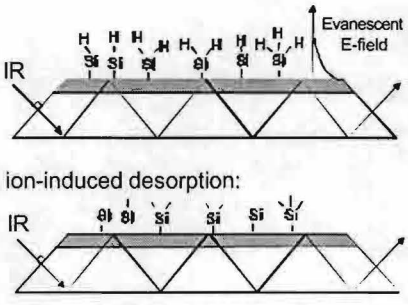

Figure 8: *ATR-FTIR on crystal with deposited a-Si:H film. Surface selectivity is obtained by subtracting the spectrum of the lower film (where surface H-atoms are desorbed by a gentle Ar^+-bombardment) from the spectrum of the upper film.*

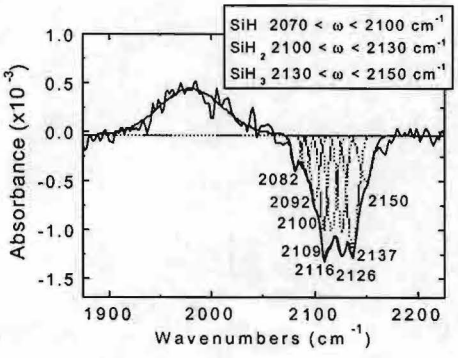

Figure 9: *Spectrum of surface hydrides SiH_x. From literature data on the peak positions it has been established that the surface of this 230 °C film deposited with an inductively coupled Ar-SiH_4 plasma is 26% SiH, 50% SiH_2, and 24% SiH_3 [7,8].*

ion-induced desorption of the surface species (Fig. 8) [7,8]. The latter method has been applied to study the surface hydrides on a-Si:H during growth (Fig. 9). It has been observed that the surface changes from dominantly SiH_3 at low substrate temperatures to SiH_2 and subsequently to SiH at high substrate temperatures. On the basis of this observation, a thermal decomposition set in which $SiH_3 \rightarrow SiH_2 \rightarrow SiH$ has been proposed with crucial importance for H-elimination in SiH_3 dominated a-Si:H film growth [9].

Acknowledgments

F.J.H van Assche, A.A.E. Stevens, M.G.H. Boogaarts, D.C. Marra, and K.L. Williams are gratefully acknowledged for their contribution to this work. Prof. D.C. Schram is acknowledged for the fruitful discussions.

References

[1] W.M.M. Kessels, M.C.M. van de Sanden, and D.C. Schram, J. Vac. Sci. Technol. A **18**, 2153, (2000).

[2] W.M.M. Kessels, A. Leroux, M.G.H. Boogaarts, J.P.M. Hoefnagels, M.C.M. van de Sanden, and D.C. Schram, to appear in J. Vac. Sci. Technol. A **19** (March 2001).

[3] W.M.M. Kessels, J.P.M. Hoefnagels, M.G.H. Boogaarts, D.C. Schram, and M.C.M. van de Sanden, J. Appl. Phys. **89**, 2065 (2001).

[4] P.R. McCurdy, K.H.A. Bogart, N.F. Dalleska, and E.R. Fisher, Rev. Sci. Instrum. **68**, 1684 (1997)

[5] P.R. McCurdy, C.I. Butoi, K.L. Williams, and E.R. Fisher, J. Phys. Chem. B **103**, 6919 (1999).

[6] W.M.M. Kessels, P.R. McCurdy, G.R. Barker, V.A. Ventura, and E.R. Fisher, in preparation.

[7] W.M.M. Kessels, D.C. Marra, M.C.M. van de Sanden, E.S. Aydil, accepted for publication in J. Vac. Sci. Technol. A.

[8] D.C. Marra, E.A. Edelberg, R.L. Naone, and E.S. Aydil, J. Vac. Sci. Technol. A **16**, 3199 (1998).

[9] W.M.M. Kessels, A.H.M. Smets, D.C. Marra, E.S. Aydil, D.C. Schram, and M.C.M. van de Sanden, Thin Solid Films **383**, 154 (2001).

EFFECT OF ATOMIC DEUTERIUM ON a-Si:H THIN FILMS

Sumit Agarwal, Linsie Tagawa, Dimitrios Maroudas, Eray S. Aydil,
M. C. M. van de Sanden Akihiro Takano
Department of Chemical Engineering
University of California, Santa Barbara, CA 93106

Hydrogenated amorphous silicon (a-Si:H) and nanocrystalline silicon (nc-Si:H) are cost effective alternatives to crystalline silicon in photovoltaic and thin film transistors for flat panel displays. Hydrogenated amorphous and nanocrystalline silicon films can be deposited inexpensively at low temperatures and uniformly over large areas using plasma enhanced chemical vapor deposition (PECVD) from SiH4-containing glow discharges. The hydrogen content of the films plays a key role in determining the electrical properties. It is well known that the hydrogen content and the microstructure of the deposited films can be modified by exposure to a hydrogen plasma. However, the interaction of atomic hydrogen with the films is not well understood. More specifically, the mechanism and the energetics of the reactions that occur between the surface and bulk hydrides and atomic hydrogen are not known. Therefore, the goal of this study was to gain insight into the interaction of atomic hydrogen with the deposited films. We have developed an in situ method based on attenuated total internal reflection Fourier transform infrared (ATR-FTIR) spectroscopy to determine the silicon hydride (SiHx, x = 1,2,3) concentration on the surface and in the bulk of the growing film. The films were deposited in an inductively coupled plasma (ICP) reactor from SiH4/Ar feed gas mixture. The films were then exposed to a pulsed deuterium plasma. It is expected that the energetics and mechanism of reactions of deuterium with the film would be very similar to hydrogen. Deuterium exposure helps in observing the removal of hydrogen independent of insertion of deuterium and exchange of hydrogen by deuterium since the SiHx and SiDx stretching modes appear at different wave numbers. Evolution of the SiHx and SiDx stretching modes was observed after each pulse by large number of averaged scans to improve the signal to noise ratio. The data was then used to determine the energetics of surface hydrogen abstraction by atomic deuterium.

Infrared Absorption Spectroscopic Studies of H_2 – Ar - N_2 - Microwave Discharges Containing Methane or Methanol

F. Hempel, L. Mechold, J. Röpcke

Institute of Low Temperature Plasma Physics (INP), Friedrich-Ludwig-Jahn-Straße 19, 17489 Greifswald, Germany

Abstract

In this contribution tunable diode laser absorption spectroscopic (TDLAS) studies of hydrocarbon-containing H_2-Ar-N_2-discharges in a planar microwave reactor (f= 2.45 GHz, P=1.5 kW) under static conditions are presented. Measurements were performed using various ratios of H_2 to N_2 and small admixtures of some percents of methane or methanol at a discharge pressure of 1.5 mbar. TDLAS was used to determine the degree of dissociation of the precursor hydrocarbons methane or methanol as well as the concentrations of the produced molecules like acetylene, ethylene, ethane, hydro cyanic acid, ammonia and the methyl radical.
The degree of dissociation of methane was found to be between 70 to 95 %, showing a considerable increase at small nitrogen contents. Methanol dissociated almost completely (about 97 %) for all H_2-N_2-admixtures.

Introduction

Due to their favorable properties non-equilibrium molecular plasmas are of high potential for plasma processing resulting in growing interests in their volume chemistry. The online monitoring of stable plasma reaction products in chemical reactors, in particular the measurement of their ground state concentrations, is the key to an improved understanding of the plasma chemistry and the kinetics in these molecular discharges. This can be done by appropriate diagnostic methods, e.g. by absorption spectroscopy.
TDLAS in the mid infrared spectral region between 3 and 20 µm is a non-invasive technique for measuring number densities of stable molecules and radicals. Basically this diagnostic method is not restricted to a specific type of plasma. It was used to determine neutral gas temperatures [1] and to investigate dissociation processes [2-5]. Due to their small laser line width (about 10^{-4} cm^{-1}) the lead-salt diode lasers used in the mid infrared region are well suited for high resolution spectroscopy purposes, e.g. of low molecular weight free radicals and molecular ions [6-9].
One of the most successful applications of TDLAS is for studying the decomposition of hydrocarbons in a variety of PECVD processes. Recently, systematic investigations of plasma chemistry and kinetics in plasmas containing hydrocarbons have been published [2,10]. Outside of plasma diagnostics this technique has been used successfully in the field of atmospheric trace gas monitoring and for exhaust gas monitoring of on-road vehicles, e.g. refs. 11,12.
This contribution is focused on TDLAS studies in the mid infrared region which have been performed in a planar microwave reactor. Molecular species concentrations have been monitored in H_2-Ar-N_2-plasmas containing hydrocarbons, either methane or methanol, under static discharge conditions.

Experimental

The experimental set-up of the used TDL arrangement and the microwave reactor is shown in figure 1. Experimental details of this set-up can be found elsewhere. [2,13] The infrared diode laser beam entered the plasma chamber via a KBr window and passes twice through the plasma region. A monochromator in front of the HgCdTe detector was used as a mode filter. The absorption signal of the detector was amplified and transferred to a PC system. Measurements were performed under static conditions in a planar microwave reactor (f= 2.45 GHz, P=1.5 kW) using various ratios of H_2 to N_2 and 7.2 % of methane or methanol with a discharge pressure of 1.5 mbar. In order to reduce the influence of gas transportation processes in the chamber, a specific measurement procedure was used [2]. The discharge was started under flowing conditions with the gas mixture of interest. When a stable plasma had been established the reactor was closed. After one minute the concentration measurements under static conditions were started.
TDLAS has been used to determine the degree of dissociation of the precursor hydrocarbons methane and methanol as well as the concentrations of the produced molecules acetylene, ethylene, ethane, hydro cyanic acid, ammonia and the methyl radical. The identification of the absorption lines and the measurement of their absolute positions was carried out using well documented reference gas spectra and an etalon of known free spectral range for wavenumber interpolation [14,15].

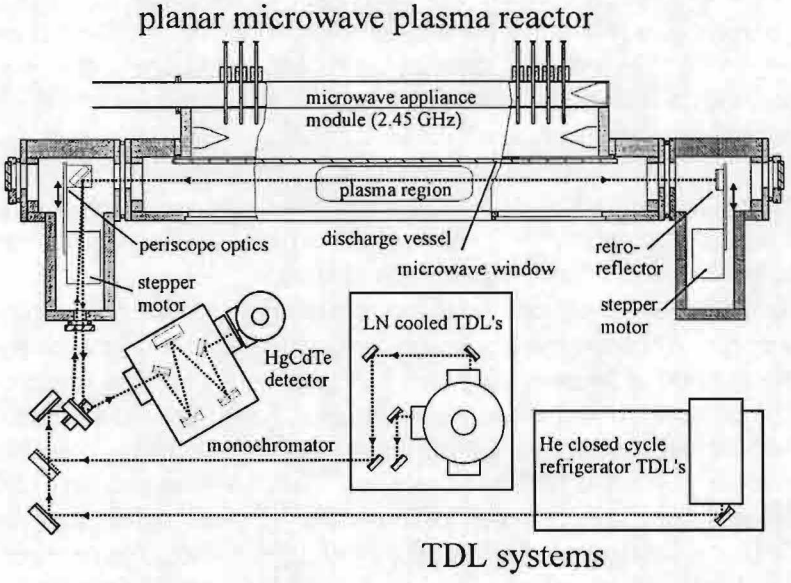

Figure 1: Experimental set-up

Results and Discussion

The degree of dissociation (figure 2) was determined from the measured concentrations of the precursor hydrocarbons before igniting the plasma and in the plasma under static conditions. It was found to be between 70 to 95 % for methane-containing plasmas, showing a considerable increase at small nitrogen contents. The methanol was determined to be dissociated almost completely (about 95 to 97 %) for all ratios of H_2 to N_2.
In H_2-Ar-N_2-plasmas containing methane concentrations of six stable molecular species as well as of the methyl radical were measured for various ratios of H_2 to N_2 (figure 3).

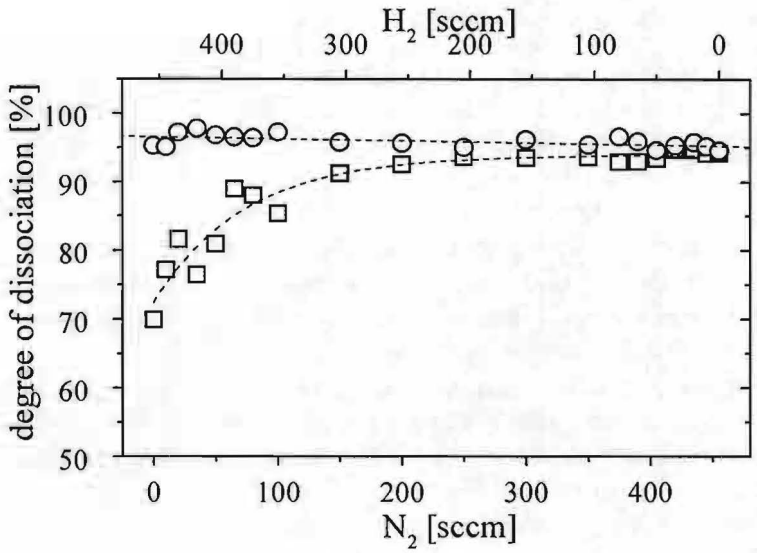

Figure 2: Degree of dissociation of methane and methanol as a function of the H_2 / N_2-ratio with hydrocarbon admixture (O - CH_3OH, □ - CH_4) (P = 1.5 kW, p = 1.5 mbar, sc)

Ammonia and hydro cyanic acid showed to be main products of the plasma. The concentration of hydro cyanic acid in the discharges under static conditions increased for small nitrogen percentages reaching a maximum of about 5 x 10^{14} molecules cm^{-3} for nitrogen contents around 15 %. The concentration of ammonia produced in the plasma showed a similar behavior with a maximum of about 1.5 x 10^{14} molecules cm^{-3} at the same H_2 to N_2 ratio. The concentration of the hydrocarbons C_2H_2 and C_2H_6 decreased for low nitrogen contents to values less than 1 x 10^{13} molecules cm^{-3}. The C_2H_4 density was measured to be one order of magnitude lower. It showed a strong decrease for small nitrogen admixtures. The methyl radical concentration decreases from 1 x 10^{13} molecules cm^{-3} to 1 x 10^{12} molecules cm^{-3} with increasing nitrogen content.

The molecular concentrations in methanol-containing plasmas (figure 4) showed a comparable behavior. Although the degree of dissociation of this precursor hydrocarbon was higher, the concentration of hydro cyanic acid was found to be slightly lower compared to the methane case. Its concentration reached at maximum 2.5 x 10^{14} molecules cm^{-3}. Methane was an additional product in the methanol-containing discharge. It had a concentration between 3 x 10^{13} molecules cm^{-3} and 3 x 10^{14} molecules cm^{-3}. Ammonia as another final product in the discharge had a maximum concentration of about 9 x 10^{13} molecules cm^{-3}. A higher amount of C_2H_2 and C_2H_6 was measured in methanol-containing plasmas. The concentrations of C_2H_4 and the methyl radical showed a strong decrease for small nitrogen admixtures.

Outlook

For further insight into plasma chemistry it is planned to measure concentrations of other radicals like NH_2 and CH_2. The improvement of the sensitivity will be achieved using a multipass setup at the discharge vessel. The experimental results are going to be used for modeling the plasma chemistry in the volume.

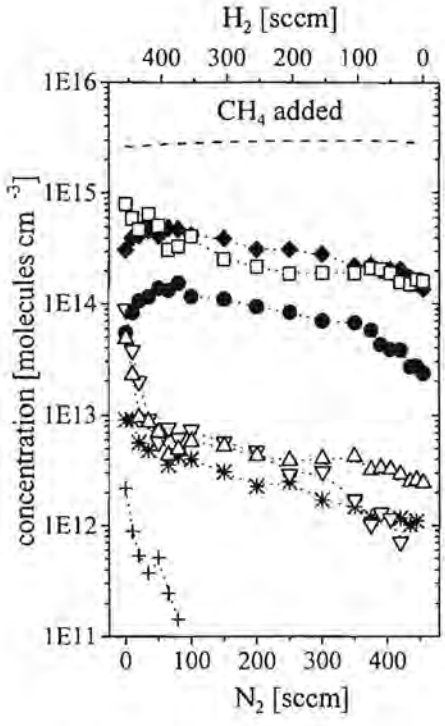

Figure 3: Molecular species concentrations as a function of the H_2 / N_2-ratio with CH_4 admixture (□ - CH_4, ● - NH_3, ◆ - HCN, ✳ - CH_3, Δ - C_2H_2, + - C_2H_4, ∇ - C_2H_6) (P = 1.5 kW, p = 1.5 mbar, sc)

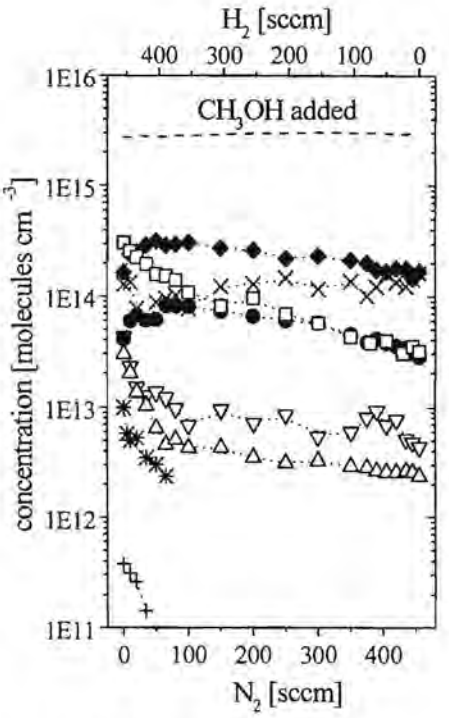

Figure 4: Molecular species concentrations as a function of the H_2 / N_2-ratio with CH_3OH admixture (X – CH_3OH, □ - CH_4, ● - NH_3, ◆ - HCN, ✳ - CH_3, Δ - C_2H_2, + - C_2H_4, ∇ - C_2H_6) (P = 1.5 kW, p = 1.5 mbar, sc)

References

[1] M. Haverlag, E. Stoffels, W. W. Stoffels, G. M. W. Kroesen, F. J. De Hoog, *J. Vac. Sci. Technol.* **A 14**, 380 (1996).

[2] J. Röpcke, L. Mechold, M. Käning, W.Y. Fan, P.B. Davies, *Plasma Chem. Plasma Process.* **19**, 395 (1999).

[3] P. B. Davies, P. M. Martineau, *Adv. Mater.* **4**, 729 (1992).

[4] S. Naito, N. Ito, T. Hattori, T. Goto, *Jpn. J. Appl. Phys.* **34**, 302 (1995).

[5] M. Haverlag, E. Stoffels, W. W. Stoffels, G. M. W. Kroesen, F. J. De Hoog, *J. Vac. Sci. Technol.* **A 12**, 3102 (1994).

[6] K. Kawaguchi, Y. Endo, E. Hirota, *J. Mol. Spectr.* **93**, 381 (1982).

[7] N. T. Hunt, J. Röpcke, P. B. Davies, *J. Mol. Spectr.* **204**, 120 (2000).

[8] Z. Liu, P. B. Davies, *J. Chem. Phys.* **105**, 3443 (1996).

[9] D. M. Smith, P. B. Davies, *J. Chem. Phys.* **100**, 6166 (1994).

[10] W. Y. Fan, P.F. Knewstubb, M. Käning, L. Mechold, J. Röpcke, P. B. Davies, *J. Phys. Chem. A* **103**, 4118 (1999).

[11] D. D. Nelson et al., *SPIE Proceedings* **2834**, 148 (1996).

[12] J. Jimenez et al., *J. Air & Waste Manage. Asso.* **49**, 463 (1999).

[13] A. Ohl, Large Area Planar Microwave Discharges, in Microwave Discharges: Fundamentals and Applications, C. M. Ferreira (Ed.), Plenum, New York, (1993), 205-214.

[14] L. S. Rothman et al, *J. Quant. Spectrosc. Radiat. Transfer* **48**, 469 (1992).

[15] N. Husson et al, *J. Quant. Spectrosc. Radiat. Transfer* **52**, 425 (1994).

Atomic Lithium Beam Spectroscopy for N_e and T_e in Reactive Plasmas

M. Böke and J. Winter

Institut für Experimentalphysik II, Ruhr-Universität Bochum, D-44780 Bochum, Germany

1. Introduction

In a reactive plasma the species composition and the flows of particles to a substrate depend upon the electron energy distribution and its spatial variation and time dependence. The electron density has a large influence on the growth rate of thin films deposited from the discharge gas. To control plasma assisted processes it is important to have a detailed knowledge of these quantities during every phase of a process, preferably with high spatial and time resolution. The emitted radiation of a thermal atomic lithium beam is used to obtain the density of the electrons and their mean kinetic energy. Using an intensified CCD camera in combination with interference filters the light emitted from neutral lithium atoms (excited through collisions with plasma electrons) is detected. The plasma parameters are obtained from appropriate line intensity ratios and will be compared with probe measurements in rare gases. The characterization of the atomic lithium is done by LIF measurements with laser diodes. Discharge geometry is an GEC reference cell with or inductive coupling at 13.56 MHz and at pressures from 0.1 to 50 Pa.

2. Experimental Setup

Using a CCD-camera, optionally in combination with a spectrographical system or with interference filters for the observed lithium lines, the spectral line emission from a beam of neutral lithium atoms after collisional excitation is investigated perpendicularly to the beam direction with spatial and temporal resolution. The atomic beam is produced by a lithium oven which consists in a Knudsen cell - filled with an alloy of copper and lithium (2% lithium) - and an aperture system in order to collimate the beam. By indirect resistive heating of the Knudsen cell up to 950°C one receives a dynamic balance between diffusion from lithium atoms to the surface of the Cu-Li-alloy and evaporation of atoms controlled by vapour pressure in the cell. The advantage of this solid state source in comparison to fluid sources and ion beam sources is a simple construction, its high operating time, optional orientation of mounting and its insensitiveness to unexpected air leakage. The outlet velocity is in the range of 10^3 ms^{-1} and the flux of lithium atoms out of the oven at about 10^{17}-$10^{18}m^{-2}s^{-1}$. The diagnostics is installed on a ICP GEC reference (5 turn pancake coil, L=1.2µH; lower electrode (on ground or defined potential): diameter: 10cm, distance between electrode and quartz plate: 4cm, pressure: 0.1-50Pa, T_e~ eV, N_e~ $10^{17}m^{-3}$-$10^{18}m^{-3}$, f=13.56MHz).

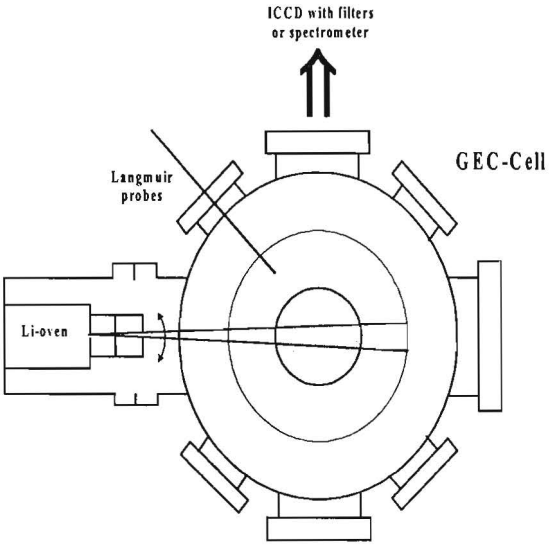

Figure 1: *Experimental Setup*

3. Atomic Lithium Beam supported Emission Spectroscopy

Atomic beam supported Li emission spectroscopy is based on the measurement of line intensities and intensity ratios of electron excited states of the neutral Li- atom. These are in particular the 2S-2P transition at 670.8nm, the 2P-3S transition at 812.6nm, and the 2P-3D transition at 610.4nm, see fig.2. Li-beam spectroscopy has already been used successfully for the diagnostics of the edge region of fusion plasmas to determine plasma density fluctuations [1]. In the case of reactive low pressure plasmas (e.g. ICP or CCP) several factors impede the application. One main obstacle comes from the fact that these low temperature plasmas are usually operated in the 0.1-10Pa range and have a low degree of ionization. Thus a large fraction of neutrals has to be accounted for.

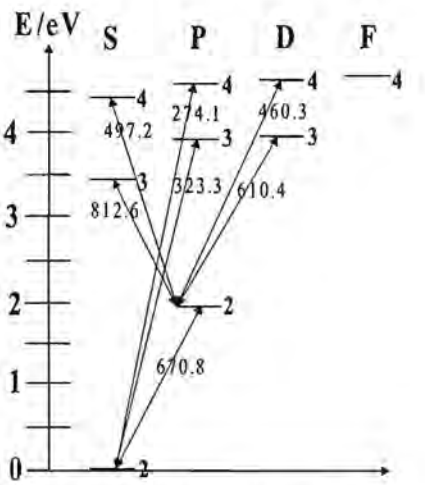

Figure 2: *Term Scheme of Lithium*

At low pressure (0.1Pa) one obtains a well defined narrow lithium beam (see fig. 3) because the mean free path of lithium atoms is in the range of 10 centimeters and it is possible to reach high spatial resolution in the measurement of the plasma parameters. The width of the lithium beam is obtained by laser induced fluorescence (LIF) at the 2S-2P transition (670.8nm) using a tunable diode laser in an external resonator (Littman setup).

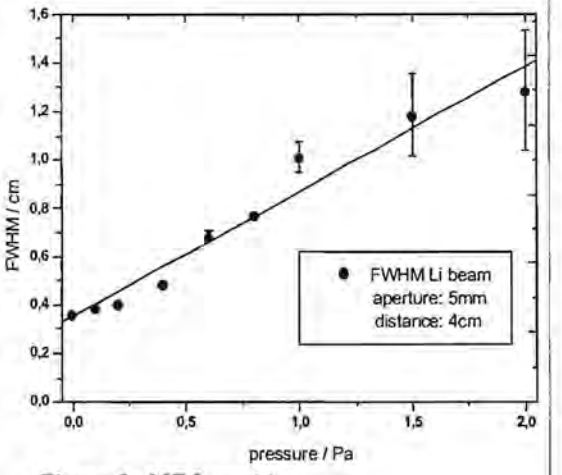

Figure 3: *LIF Intensities: Beam Width*

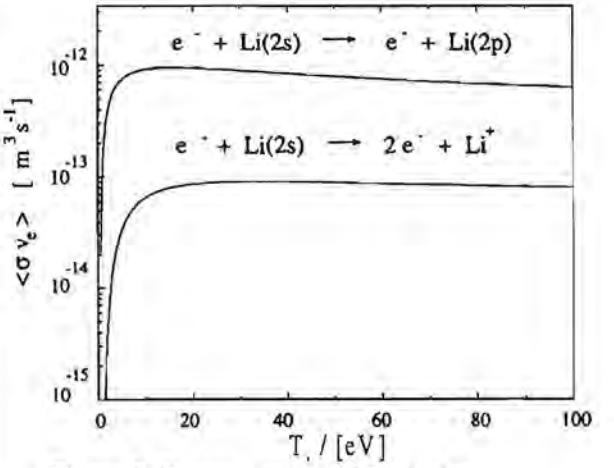

Figure 4: *Crosssections for e⁻-Excitation and Ionization*

At higher pressure (a few 10Pa) the situation changes: The beam becomes broader and degenerates to a lithium cloud due to collisions with the discharge gas. The discolouration of the discharge stays usable but the spatial resolution is limited and the modelling effort becomes higher.

The other problem is due to the low electron temperature in the reactive plasmas. Whereas for fusion edge conditions with T_e values above 10eV energy independent constant cross sections may be used (see fig. 4), the threshold region with significant dependence on energy applies for reactive plasmas with T_e of about 1eV. A collisional radiative model in consideration of all states in Figure 2 is required.

4. Probe Measurements and α–γ–Hysteresis

To prove and to characterize the diagnostics is installed on plasmas in rare gases and compared to probe measurements. The results of these probe measurements in the ICP GEC cell are shown in the following figures. The central electron density (see fig 5) increases with the discharge pressure. Increasing the power (fig. 6) leads the growth of the electron density into a saturation area and the radial density profiles (see fig. 7) become flatter. The zone of high electron density is enlarged.

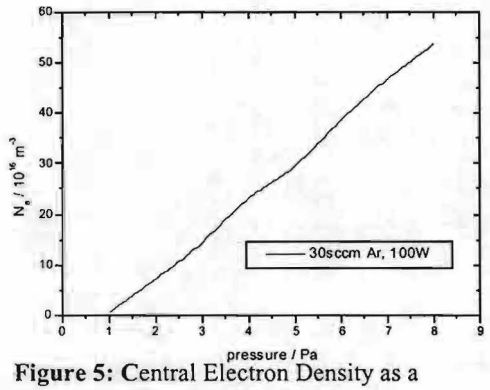

Figure 5: Central Electron Density as a Function of the Power

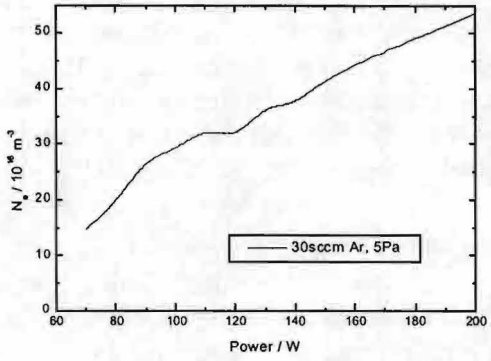

Figure 6: Central Electron Density as a Function of the Pressure

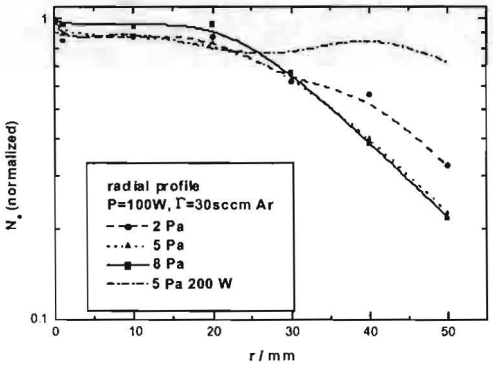

Figure 7: Electron Density Profiles

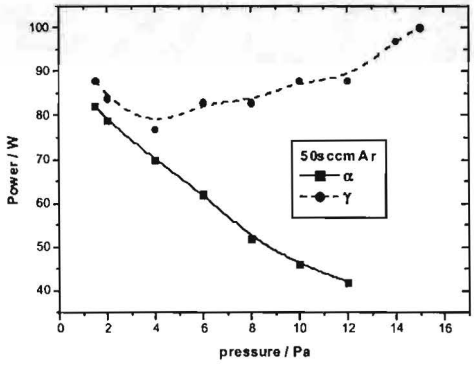

Figure 8: α–γ–Hysteresis

Figure 7 also shows flatter radial profiles at lower pressures. The α–γ–hysteresis of the discharge one can see from figure 8: Increasing the power at a given pressure the discharge switches at the dotted curve from α- into γ-regime (transition from mainly capacitive to mainly inductive coupling). Decreasing the power the transition back into the α-mode takes place when the power reaches the solid curve.

5. Résumé and Outlook

From the measured line intensities and line intensity ratios it is possible to obtain locally the electron energy and density at low pressure. For that purpose a detailed collisional radiative model is in preparation. At higher pressure the spatial resolution of the diagnostics is reduced due to beam broadening and degeneration to a cloud of lithium atoms. In addition in this case the density reduction of the neutral lithium atoms by collisional ionization has to be taken into account.

In order to enlarge the efficiency of the diagnostics and to reach a sufficient beam collimation and penetration depth even at higher pressures the transition to pulsed and fast atomic beams (also with heavier atoms, e.g. potassium) provided by laser ablation [3] is in preparation. Also a comparison to Thomson scattering at the same discharge geometry is in preparation.

This work is supported by Deutsche Forschungsgemeinschaft within SFB 191 (B8).

6. References

[1] A. Dinklage, T. Lokajczyk, H.J. Kunze, B. Schweer and I.E. Olivares; Rev. Sci. Instrum., **69 (1)**, 321-322 (1998)

[2] M. Böke, G. Himmel, B. Schweer and J. Winter "Atomic Lithium Beam Spectroscopy for N_e and T_e in Reactive Plasmas" in: Lausanne Report LRP 629/99 "Workshop on Frontiers in Low Temperature Plasma Diagnostics III", Switzerland (1999)

[3] Y.T. Lie, A. Pospieszczyk and J.A. Tagle; Fusion Technology, **6**, 447-452 (1984)

Two-photon laser induced fluorescence spectroscopy: a powerful diagnostic tool to monitor ground-state atom properties in a plasma environment.

S. Mazouffre, R. Engeln, P. Vankan, and D.C. Schram.
Department of Applied Physics, Eindhoven University of Technology, The Netherlands.

1 Introduction

Radicals like H, N, O, F, play a major role in plasma aided chemistry due to their high reactivity. Moreover, in plasma processing, the buffer or carrier gas is currently composed of Ar, He, Xe atoms. Being able to locally measure the density, the velocity, and the temperature of a particular atomic species is therefore of relevance to get a better understanding of both the dynamics and the kinetics of a given plasma environment. For the species-selective spatially resolved detection of ground state atoms (the most populated state in a low temperature plasma) the very sensitive Laser Induced Fluorescence technique can be used. However due to the large energy spacings involved, monitoring of ground state atoms requires the use of highly energetic photons of which generation is experimentally demanding [1]. Problems connected with single-photon excitation can be avoided with the application of a multi-photon excitation scheme. In this contribution, the Two-photon Absorption Laser Induced Fluorescence (TALIF) spectroscopy [2,3] is presented as a diagnostic tool to monitor ground state atom properties in a plasma medium.

2 TALIF basic principles and 2-photon selection rules

The hydrogen atom energy diagram, see Fig. 1, may serve as an example to explain the basic principles of a 2-photon excitation process. In order to probe ground state H atom, the latter can be excited to the n=2 level using a Lyman-α photon. However, the need of coherent tuneable VUV radiation combined with the detection of the fluorescence yield at the excitation wavelength makes the experiment cumbersome and difficult. One may think about excitation to the n=3 level and subsequent detection of the fluorescence light at the Balmer–α line, but this would necessitate a Lyman-β photon. A possible way of avoiding the problem of generation of extreme UV photons is to use a 2-photon excitation scheme, as depicted in Fig. 1.

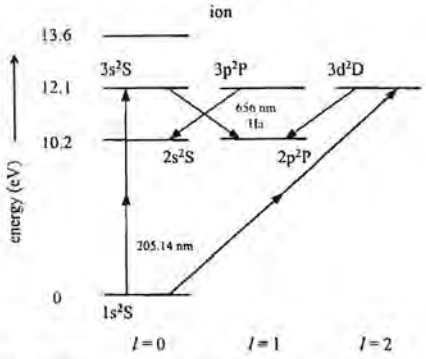

Figure 1: Simplified energy diagram of the hydrogen atom. A possible 2-photon excitation scheme is presented. Two 205 nm photons are used to excite H from the ground-state to the n=3 level. The fluorescence radiation is detected at the Balmer-α line. Because of specific optical selection rules the 3p state is not directly accessible using a 2-photon excitation. However, the 3p state can be populated due to ℓ-mixing, induced by the laser beam electric field for instance. The absorption of a third UV photon (from the n=3 level) leads to the formation of H^+, thus modifying the relation between the fluorescence yield and the laser beam energy. The detection of the created charge particle may be used to measure the H atom density.

A 2-photon excitation scheme has to obey specific electric dipole selection rules: for H it is simply $\Delta\ell = 0, \pm 2$ (ℓ is the angular momentum), but it becomes more complex for multi electron

atoms [4]. Therefore "forbidden" transitions become accessible. Note that ℓ-mixing effects [5,6] can disturb the excitation process (transfer of population between ℓ-states).

3 Experimental arrangement

3.1 UV photon generation

The generation of coherent tuneable UV radiation is based on non-linear optical effects in solids or gases [7]. Photons with λ>195 nm can be produced with birefringent crystals, whereas photons with λ<195 nm can be produced either via third harmonic generation in gases or via stimulated Raman scattering [1]. Here we describe an experimental setup capable of producing a UV laser beam with 200 nm<λ<210 nm (such photons are used to excite H, N, Kr), see Fig. 2.

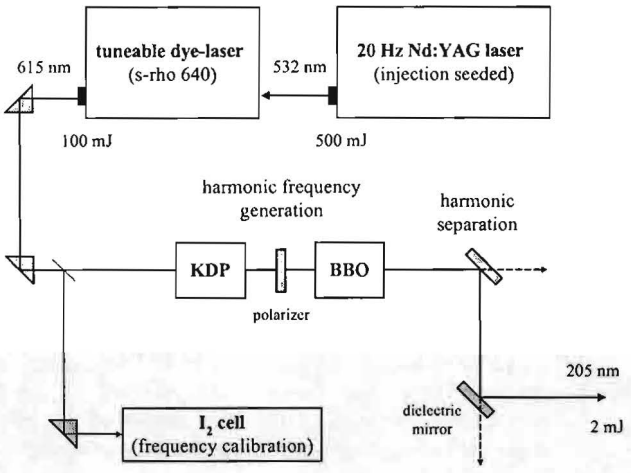

Figure 2: Scheme of a TALIF setup (λ >195 nm). The ouput beam of a tuneable dye-laser is converted into a UV laser beam after (indirect) third harmonic generation in crytals with nonlinear optical properties. The frequency of the laser beam is calibrated using the absorption spectrum of molecular iodine.

A tuneable dye laser is pumped with the second harmonic (532 nm) output beam of an injection seeded pulsed Nd:YAG laser (operating at 20 Hz). The dye laser delivers radiation around 615 nm (sulforhodamine 640) with a pulse energy of 100 mJ. The dye laser output is frequency doubled using a KDP crystal. Upon exiting the KDP crystal the polarization of the generated blue beam is rotated to coincide with the polarization of the red beam. Both collinear laser beams are input to a BBO crystal where sum-frequency process leads to the generation of a UV laser beam around 205 nm with an energy per pulse up to 2 mJ. Both crystal are electronically angle tuned by means of a feed back system to provide a constant output energy when scanning the dye laser. A set of high reflectivity dielectric mirrors centered at 205 nm is used to remove the residual blue and red laser beams. The UV laser beam is horizontally polarized with a measured bandwidth of 0.25 cm^{-1}. Note that the energy fluctuation (pulse to pulse) can be high (up to 50%) and the measured spectrum has to be corrected from these instabilities. The fundamental dye laser frequency is calibrated by simultaneous recording of the absorption spectrum of molecular iodine.

3.2 Fluorescence radiation detection

An example of a possible way to detect the fluorescence radiation is presented. The UV laser beam is often tightly focussed (MgF_2 lens) to obtain a good spatial resolution. The excited state fluorescence yield originating from the focus is imaged perpendicular to the laser probe beam by means of two plano-convex lenses onto an adjustable slitmask, which define the spatial resolution, located in front of a detector (gated PMT for instance). The continuous background light emitted by the plasma can be strongly reduced using a narrow bandwidth interference filter or using a monochromator. The signal from the detector can be fed directly to the input of an

oscilloscope or it can be automatically read using a charge integrator coupled with an ADC. In the later case, the fluorescence signal is not resolved in time.

4 Quantities to be measured and parasitic effects

From a spectral scan over the two-photon transition, see Fig. 3, several local parameters can be determined. The spectral profile is a direct measure of the atom velocity distribution function. A non gaussian shape indicates a departure from thermodynamic equilibrium. The local density is obtained from the integrated intensity. In the case of a maxwellian distribution function, the local temperature is derived from the Doppler width of the profile (taking into account the laser beam spectral profile), and in addition the component of the drift velocity in the direction of the laser beam can be determined from the absolute Doppler shift of the center frequency of the peak. Doppler free two-photon absorption spectroscopy with two counter propagating beams enables the measurement of the local electric field strength in a plasma using the Stark effect [8]. Note that it also has important applications in precision spectroscopy [9].

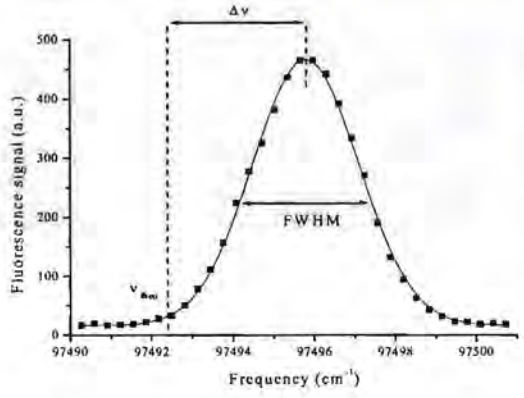

Figure 3: Example of a measured spectral profile of the 1→3 two-photon transition in atomic hydrogen (expanding thermal argon-hydrogen plasma). The fluorescence is detected at the Balmer-α line. The profile is gaussian meaning that H atoms are locally in thermodynamic equilibrium. The area of the peak is a direct measure of the density (after calibration). The temperature is deduced from the Doppler broadening of the line (after deconvolution with the laser spectral profile) and the velocity (in the direction of the laser beam) is determined from the absolute Doppler shift of the line.

The density profiles measured via laser induced fluorescence are relative. To obtain absolute atomic number densities, the LIF set-up has to be calibrated using a well-defined concentration of the species under investigation. In the case of atomic radicals, the needed concentration has to be measured. This is accomplished for instance via a titration reaction in a flow tube reactor using NO_2 for H and NO for N [3]. Another way to calibrate the fluorescence yield is to use a two-photon excitation scheme in a noble gas (Kr for H and N [10], Xe for O [11]).
Information about the life time of the excited state and about collisional deexcitation (quenching) as well as trapping of resonant photons can be obtained from the time resolved fluorescence profile [5,10].

One should pay careful attention to the numerous parasitic effects which can strongly disturbed the measured signal: reabsorption of resonant photons [5] (connected to the optical thickness of the plasma), collisional deexcitation effects [10] (important at high pressure) which lead to an apparent lower density, multi-photon ionisation [2,12] (often used as a diagnostic tool in molecular beam experiments for instance), laser induced dissociation of parent molecules [13], Amplified Spontaneous Emission generation (which can be used as a diagnostic technique [3]), ℓ-mixing processes [5,6], and saturation broadening via AC Stark effect.

5 Examples of applications

In order to illustrate the usefulness of the TALIF technique, two examples are given in Fig. 4.

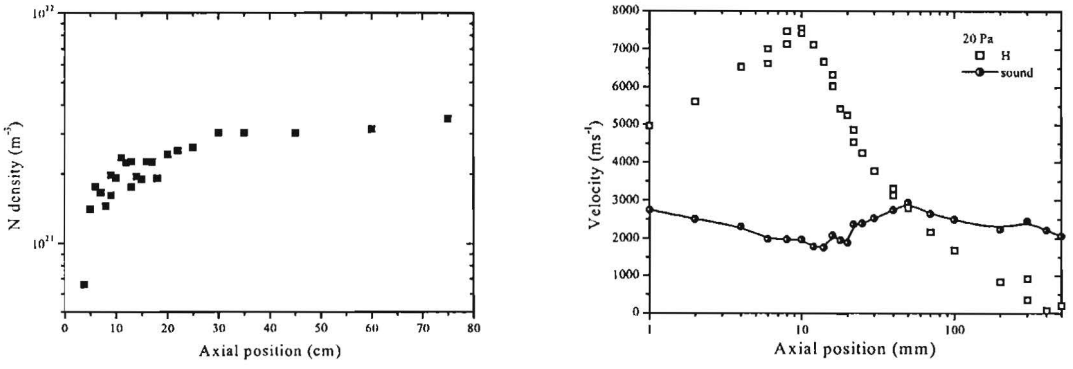

Figure 4: N atom density profile in the afterglow of a nitrogen microwave discharge (left); H atom drift velocity profile along the jet centerline of a hydrogen plasma expansion (right). Also shown is the local speed of sound calculated from the measured H atom parallel temperature.

6 Conclusion

We attempted to provide the reader a rapid overview of the TALIF spectroscopy technique applied to the monitoring of of ground-state atom properties in a low temperature plasma environment. More accurate description of this diagnostic method as well as a more complete review of possible applications can be found in literature [3].

References

[1] H.F. Döbele, *Plasma Sources Sci. Technol.* **4**, 224 (1995) and references herein.

[2] U. Czarnetzki, K. Miyazaki, T. Kajiwara, K. Muraoka, M. Maeda, and H.F. Döbele, *J. Opt. Soc. Am. B* **11**, 2155 (1994).

[3] J. Amorim, G. Bavarian, and J. Jolly, *J. Phys. D: Appl. Phys.* **33**, R51 (2000).

[4] K.D. Bonin and T.J. McIlrath, *J. Opt. Soc. Am. B* **1**, 52 (1984).

[5] H.W.P. van der Heijden, M.G.H. Boogaarts, S. Mazouffre, J.A.M. van der Mullen, and D.C. Schram, *Phys. Rev. E* **61**, 4402 (2000).

[6] B.L. Preppernau, K. Pearce, A. Tserepi, E. Wurzberg, and T.A. Miller, *Chem. Phys.* **196**, 371 (1995).

[7] N. Bloembergen, *Nonlinear optics*, Eds. Benjamin, NewYork (1965).

[8] U. Czarnetzki, D. Luggenhölscher, and H.F. Döbele, *Plasma Sources Sci. Technol.* **8**, 230 (1999).

[9] D.M. Giltner, R.W. McGowan, S. Au Lee, and G.A. Rinker, *Phys. Rev. A* **49**, 2508 (1994).

[10] K. Niemi, V. Schultz von der Gathen, and H.F. Döbele, *Proceedings of Hakone* 7, Greifswald, Germany, Vol. 1, 199 (2000).

[11] A. Goehlich, T. Kawetzki, and H.F. Döbele, *J. Chem. Phys.* **108**, 9362 (1998).

[12] W. Bischel, B. Perry, and D. Crosley, Chem. Phys. Lett. 82, 85 (1981).

[13] K. Miyazaki, T. Kajiwara, K. Uchino, K. Muraoka, T. Okada, and M. Maeda, *J. Vac. Sci. Techno. A* **14**, 125 (1996).

POSTER CONTRIBUTIONS

OH LIF CALIBRATION BY A PULSED LOW PRESSURE RF DISCHARGE

G. Dilecce and S. De Benedictis
Centro di Studio per la Chimica dei Plasmi – CNR
c/o Dip. Chimica Università di Bari, via Orabona 4, 70126, Bari Italy

Introduction

OH is a very important radical in the atmospheric chemistry, since it is the main oxydising specie in the troposphere in the daytime (i.e. under sunlight exposition). The detection of OH is then a crucial but difficult issue in atmospheric research, and to this end techniques based on Laser Induced Fluorescence (LIF) have been largely employed. One of the problems of such techniques is their calibration, i.e. the disposal of a well-characterised source of OH for the calibration of the LIF outcome. In this contribution we propose a N_2-H_2O low-pressure, low-power pulsed RF discharge as a calibrated source of OH. The quantitative determination of OH density comes from the demonstration achieved in [1] that OH(A) and NO(A) states excitation have the same precursor, the nitrogen triplet metastable, in this kind of discharges, through the processes:

$$N_2(A^3\Sigma_u^+, v)+OH(X^2\Sigma)\rightarrow N_2(X^1\Sigma^+)+OH(A^2\Sigma^+, v') \quad (1)$$

$$N_2(A^3\Sigma_u^+, v)+NO(X^2\Sigma)\rightarrow N_2(X^1\Sigma^+)+NO(A^2\Sigma^+, v') \quad (2)$$

Therefore the OH density can be quantitatively correlated to the NO density through the intensity ratio of OH(A) and NO(A) emissions. The OH density can then be measured by the measurement of NO density, that is much easier since NO is a stable specie. We then demonstrate a LIF scheme by which OH and NO can be detected simultaneously by the use of one laser only. Finally we propose a discharge-LIF scheme that can be used as a standard on-line reference for atmospheric OH LIF monitoring.

Principles of the OH density measurement

Both OH(A) and NO(A) have the same excitation precursor, the nitrogen triplet metastable, through processes (1) and (2) respectively. We demonstrated this in [1] in a parallel plates RF discharge and in an external electrodes (EED) discharge (whose scheme is drawn in fig. 1), at pressures going from 0.03 to 1 Torr. For the details of the discharges refer to [1]. The ratio of the emission intensity of the OH 3064 Å system and the NO γ system is therefore proportional to the ratio of the OH and NO ground state density. The proportionality factor is the ratio of the rate coefficients k_1 and k_2 of processes (1) and (2). The OH ground state density measurement finally reduces to the measurement of the OH 3064 Å system (0,0) band and of one of the NO γ-bands, together with a measurement of the NO formed in the discharge. Note that, due to a strong SPS emission in the OH 3064 Å system (0,0) band spectral region, it is necessary to make the emission measurements in the post-discharge of a pulsed discharge. In the post-discharge, in-fact, the SPS emission, mainly due to electron impact excitation, rapidly falls-off, then "cleaning" the OH 3064 Å system (0,0) band. The NO measurement can be achieved by LIF and can be calibrated with great precision in a cell with a known quantity of NO. Since also the

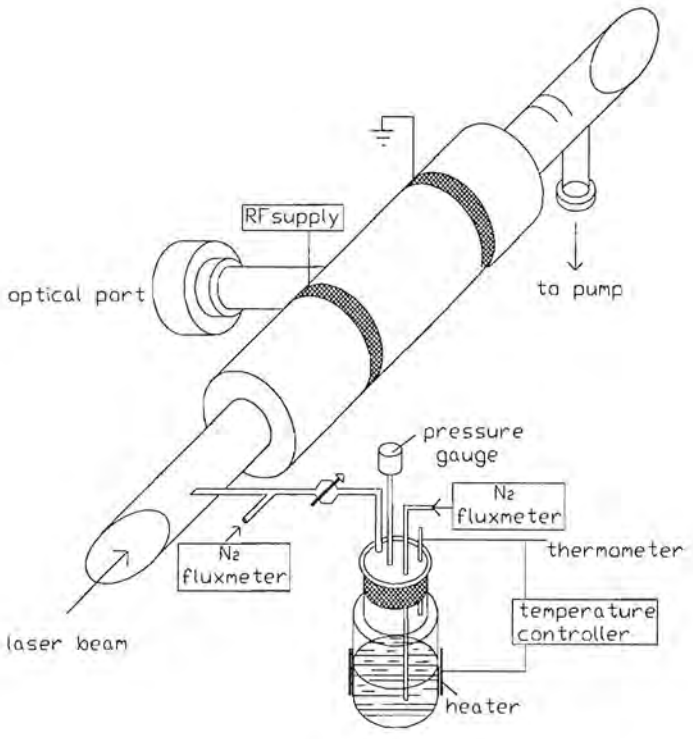

Fig.1 Scheme of the EED discharge with water vapour generator. A controlled flux of water vapour is obtained by flowing a controlled fraction of the main N_2 flux in a chamber partly filled with distilled water at regulated temperature. This mixing chamber is connected to the discharge chamber through a needle valve. The water vapour flux is obtained as a fraction of the fixed nitrogen flux equal to the ratio of the water vapour pressure at the given temperature and the total pressure in the mixing chamber. This latter can be varied by the needle valve at the exit of the mixing chamber.

emission measurements can be made with good precision, the ultimate limit to the accuracy of this procedure is given by the ratio of the rate coefficients. The actual knowledge, [2] - [4], is $k_1/k_2 = 1.44 \pm 0.5$, that is a 35% incertitude. It is clear that a substantial improvement of this accuracy must go through a better knowledge of these rate coefficients. Just to have an idea we have estimated the OH density in our EED discharge. Using a rough spectral calibration in the 220 – 320 nm region and a more than rough LIF measurement of NO density we have evaluated a OH density of the order of 10^{12} cm^{-3}, in a 0.1 Torr 30W cw discharge.
There is actually one method available for the generation and calibration of OH [3], [4], that is based on the reaction:

$$H + NO_2 \rightarrow OH + NO \qquad (3)$$

H atoms are generated in an Ar/H_2 microwave discharge and NO_2 is added downstream the discharge in a flow tube. Also in this case the measurement of OH is reduced to the measurement of NO, provided the ratio of OH and NO density remains constant in the measurement region. The method we propose in this paper has essentially one advantage with respect to this latter, namely that it does not employ hazardous gases like H_2 and NO_2. This can be very useful in the application as a reference source in a LIF apparatus for OH density field measurements, like the FAGE of ref. [5].

Simultaneous OH and NO LIF detection

Since the OH density determination relies on the knowledge of NO density, it would be advantageous to detect the two species simultaneously in the discharge. OH is measured by a LIF scheme involving the (0,0) band of the OH($A^2\Sigma^+$ -- $X^2\Pi$) 3064 Å system, with a laser wavelength in the 3060 - 3090 Å region. This wavelength is obtained as the second harmonic (SH) of a Nd-YAG pumped Dye laser, with R640 dye. The energy per pulse obtained by this device is about 300-450 μJ in the spectral range used, as measured at the exit of the discharge. A LIF spectrum with full band detection and laser wavelength scan is shown in fig.2. The SH beam is used to produce in a second BBO the third harmonic (TH) of the dye that falls in the spectral region of the (2,0) band of the NO γ-system. In this way, at the exit of the third harmonic generator two collinear laser beams are present that, fed into the discharge, can be used to detect simultaneously OH and NO. In particular we have tested the OH excitation of the $R_{11}(3)$ line at 3068.7 Å by the SH, with a corresponding TH at 2045.8 Å that falls well inside the (2,0) γ-band, as shown in fig. 3. With a TH energy per pulse of about 50 μJ, a strong fluorescence signal from the same (2,0) band is observed. We have not yet investigated which rotational lines of the (2,0) band are excited by the TH laser. This issue is relevant to the dependence of the LIF intensity on the NO ground state rotational temperature and to the possibility of increasing the sensitivity by exciting low NO rotational levels. Work is in progress to determine which is the best scheme for the simultaneous OH and NO detection. We finally note here that the excitation of the (2,0) band transitions is advantageous with respect to the classical (0,0) transition at 226 nm. The (2,0) transition probability is about 2.5 times larger than the (0,0) one [6]. Furthermore in the cases of process (2) excitation, like the present one, the NO(A, v=2) state is 300 times less excited than NO(A, v=0) [2], thus giving a much less intense background to the LIF pulse. As a whole then this new scheme provides a much better LIF/background ratio than the classical scheme, with a potentially larger laser absorption.

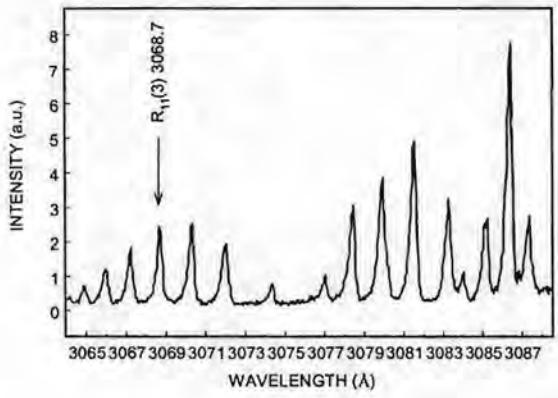

Fig.2 LIF excitation spectrum obtained by scanning the laser wavelength and observing the whole band emission by a monochromator set at zero order

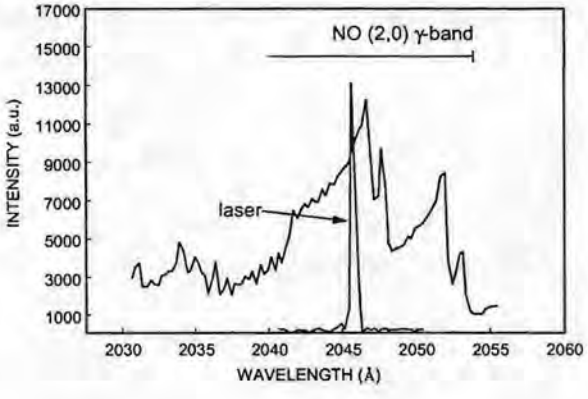

Fig.3 Emission spectrum of the (2,0) band of the NO g-system together with the spectrum of the TH laser beam

Proposal for a discharge as a calibrated OH source

The final step for the determination of OH density in our discharge is the calibration of NO LIF measurement. This can be achieved by sending the TH laser beam into a cell filled with a known quantity of NO at room temperature. The LIF signal from the cell can be compared to the LIF signal from the discharge provided the gas temperature in the discharge is equal to that in the cell. A way to fulfill this condition is to measure the NO LIF at a sufficiently long time in the post-discharge, after a short discharge pulse, such that the gas temperature at the moment of the measurement is equal to the room temperature. Work is in progress to determine the best such condition as a compromise between full thermal equilibrium with the environment, OH production in the discharge and $N_2(A)$ survival in the post-discharge.
The whole apparatus composed by a reactor like that of fig.1 with a pulsed discharge, plus a NO reference cell can then constitute a constant reference for OH LIF measurements. The best procedure requires the simultaneous detection of:

1- the LIF from OH and NO in the post-discharge,
2- the LIF from NO in the cell
3- the post-discharge emission from the (0,0) band of the OH 3064 Å system and from one of the NO γ-system bands.

By such a way an on-line OH density reference source can be built providing a reliable real-time calibration that is intrinsically robust with respect to:

1. variations of the production of OH and NO in the discharge;
2. laser energy drifts, i.e. it is not necessary to monitor the laser energy and to correct for its fluctuations according to *ad hoc* saturation curves;
3. laser wavelength drifts, i.e. complex devices for wavelength stabilisation can be avoided A simpler device can be provided if a stable discharge, producing constant OH and NO quantities, can be set up and standardised by the previous scheme.

Acknowledgements

M. Simek undertook this work in the frame of CNR (Italy)-AVCR (Czech Rep.) Scientific Co-operation. Mr. A. Parodi is thanked for his technical assistance.

References

[1] G. Dilecce, M. Simek and S. De Benedictis (2000) CONTR. PAP. XVTH ESCAMPIG, MISKOLC-LILLAFURED, Hungary, p. 84-85 and full paper to be published in J.Phys.D: Appl. Phys (2001).
[2] L.G. Piper, L.M. Cowles and W.T. Rawlins, (1986) *J. Chem. Phys.* **85** 3369
[3] S.J. Wategaonkar and D.W. Setser, (1990) J. *Phys. Chem.* **94** 7200
[4] G.H. Ho and M.F. Golde, (1991) *J. Chem. Phys.* **95** 8866
[5] M.R. Heal, D.E. Heard, M.J. Pilling and B.J. Whitaker, (1995) *J. Atmos. Sci.* **52** 3428
[6] L.G. Piper and L.M. Cowles, (1986) *J. Chem. Phys.* **85** 2419

CHARACTERIZATION OF PLASMACHEMICAL TREATMENT OF ARCHAEOLOGICAL ARTIFACTS

Frantisek Krcma, Zuzana Raskova
Faculty of Chemistry, Brno University of Technology,
Purkynova 118, 612 00 Brno, Czech Republic, krcma@fch.vutbr.cz

Milos Klima, Jaroslav Kousal
Department of Physical Electronics, Faculty of Science, Masaryk University,
Kotlarska 2, 611 37, Brno, Czech Republic, klima@physics.muni.cz

Introduction

Plasmachemical treatment of archaeological artifacts is a relatively new technique developed during the 1980s [1, 2, 3]. Although this technique has been used for conservation of artifacts whose components are mainly metals, the plasmachemical process as such has been used more or less intuitively [4]. The process is based on using low-pressure hydrogen plasma in which the artifacts are treated for several hours, usually in several steps [4, 5, 6]. The problem is how long period of the plasmatic treatment is optimal and how to characterize its efficiency. The ancient artifacts always contain some corrosion layers on their surface. The studies focused on the composition of the layers show that various oxide and chloride complexes, usually containing crystalline water too, are the dominant compounds of the layer [6, 7]. Naturally, the actual composition of the corrosion strongly depends on the matter surrounding the artifact before the discovery.

Experimental setup

The principle of plasmachemical treatment is based on removal of the oxide and chloride molecules in low-temperature low-pressure hydrogen plasma. The scheme of our experimental device is given in Figure 1.

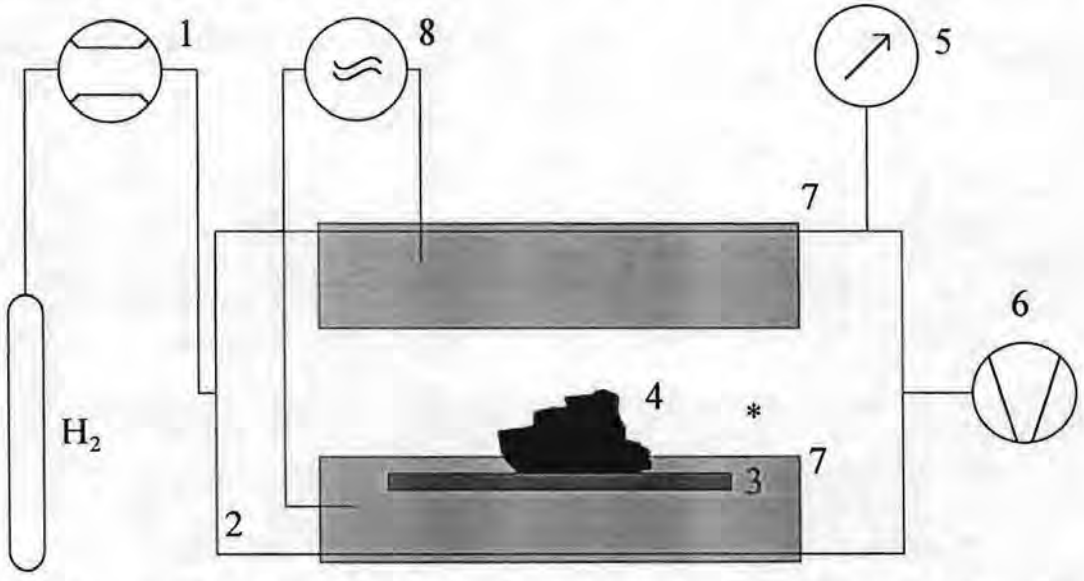

Figure 1: *Experimental setup: 1 – mass flow controller; 2 – Pyrex glass reactor (length 100 cm, inner diameter10 cm); 3 – Pyrex artifact holder; 4 – the treated archaeological artifact; 5 – baratron gauge; 6 – rotary oil pump; 7 – outer cylindrical copper electrodes; 8 – RF power supply; * – point of spectroscopic measurements.*

The experiment usually takes place at total gas pressure of 100 Pa and hydrogen flow rate of 100 Sccm. The capacitively coupled RF power supply gives 500 W of total power. Details concerning the experimental device as well as the operating conditions can be found in [7].

Principle of process monitoring

The optical spectrum emitted from the discharge in the part behind the treated artifact (see Fig. 1) has been measured by a spectrometer Jobin Yvon coupled with a CCD detector. To minimize the disturbing effects we used a relatively long integration time of 10 s. An example of the experimental spectrum is given in Fig. 2.

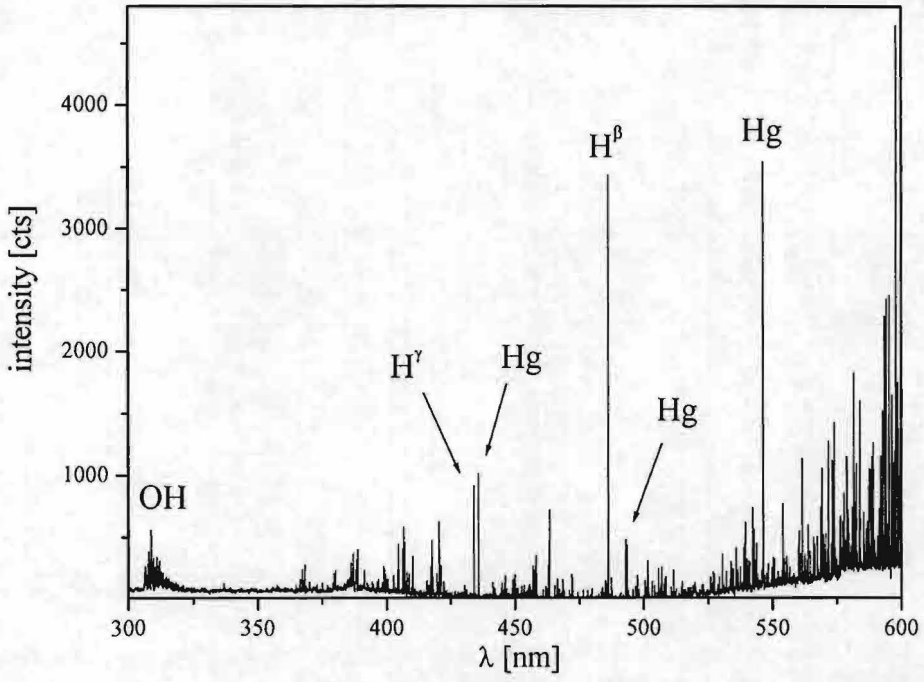

Figure 2: An experimental spectrum obtained during the plasma treatment of an ancient iron hook 10 minutes after the beginning of the treatment. The Hg spectral lines come form the fluorescent lamps in the laboratory.

In the spectrum, various spectral lines of atomic hydrogen as well as molecular spectra of OH radical can be observed. The OH radical is created in an active discharge by reactions of atomic hydrogen with the corrosion layers at the artifact surface. Due to this fact, the OH radical spectrum can be used as a monitor for the oxide reduction in plasma. Our numerous experimental data show the most intense radiation of the $\Delta v = 0$ sequence of OH ($A\ ^2\Sigma^+ \rightarrow X\ ^2\Pi^-$) spectral system. This system is well known – the rotational structure of this system is used in many cases for the determination of neutral gas temperature. The overlap of the OH spectrum by the nitrogen second positive bands is not presented in our case except when some vacuum leakages are presented (these are clearly indicated by the change of plasma color to orange at the end of plasma reactor). Thus the integral spectral intensity over the whole $\Delta v = 0$ sequence range can be used for monitoring of the oxide reduction.

Results

The integral intensity of OH in the spectral range 305-330 nm as a function of the treatment duration is given in Fig. 3 showing plasmachemical treatment of an ancient iron hook. Among the plasmachemical processes, the artifact has been treated by classical conservation methods, both mechanical and chemical. The intensity dependencies in all four stages show initial

strong enhancement of OH intensity (during the first 10 – 15 minutes) resulting from the increase in the artifact temperature [6]. Later on, a slower decrease in the intensity can be observed. During the first stage the main reduction is completed in the first two hours, then the oxide reduction is much slower and it has about constant rate. After the layers reduced in the first stage are reduced, the plasmachemical reduction increases and it is slowly decreasing for many hours. The constant reduction rate is not reached in the presented case, and it could have probably been observed after longer plasma treatment. After at least 9 hours of the plasma treatment, the OH intensity independence was reached in the third stage. Finally, the plasmachemical reduction ends after approximately 3 hours of the fourth stage.

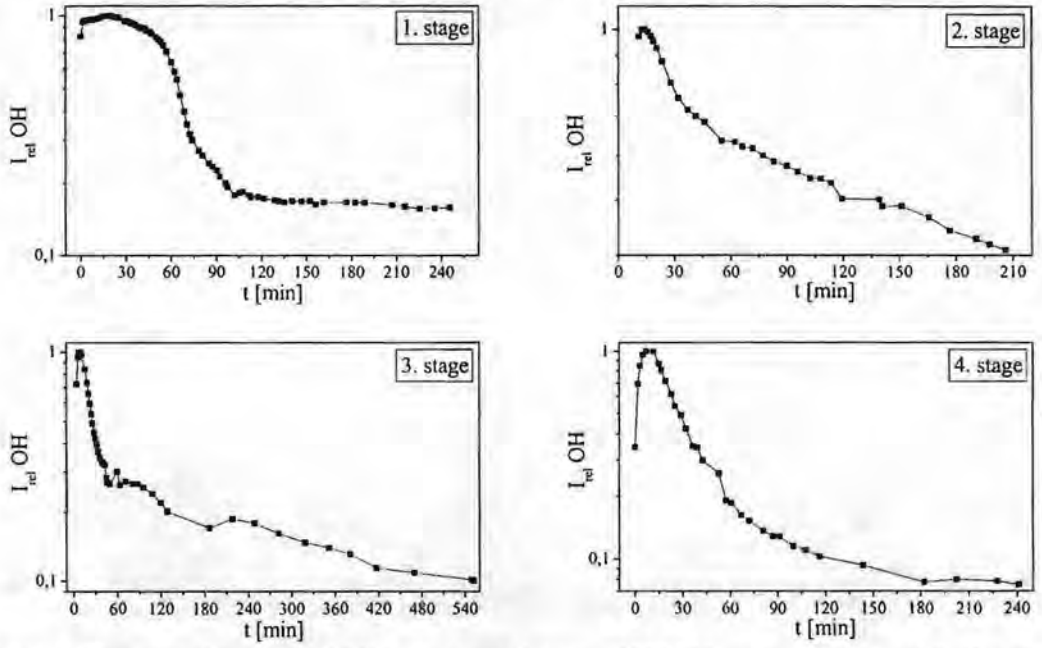

Figure 3: The integral intensity of OH in the spectral range of 305-330 nm as a function of the duration of the iron hook treatment. All graphs are normalized to their maximal values.

Of course, the time dependencies of the plasmachemical treatment necessary for each stage strongly depend on the treated artifact and on the mechanical and chemical operations taking place among the separate stages. It could be concluded from the example given above that there is some optimal treatment duration for each stage of the plasmachemical treatment.
The results of our spectroscopic observations made during the treatment of various archaeological artifacts show that the optimal moment for interruption of the plasmatic stage comes when more or less constant OH intensity is reached. The duration of the OH intensity decrease to the value of 10 % of its maximum during the particular stage can be used to determine whether the further plasmachemical treating stage will be necessary to apply. These experimental results lead us to propose a simple configuration of the device monitoring the plasmachemical treatment.

Conclusions and prospects

Our experimental spectroscopic observations of plasmachemical treatment of archaeological artifacts clearly demonstrate that the measurement of integral OH radical spectral intensity in the range of 305 – 330 nm can be used as a monitor for plasmatic treatment process. The time dependence of the OH intensity can provide important information about the number of

plasmatic stages needed for successful removal of oxides as well as information about the optimal duration of each stage.

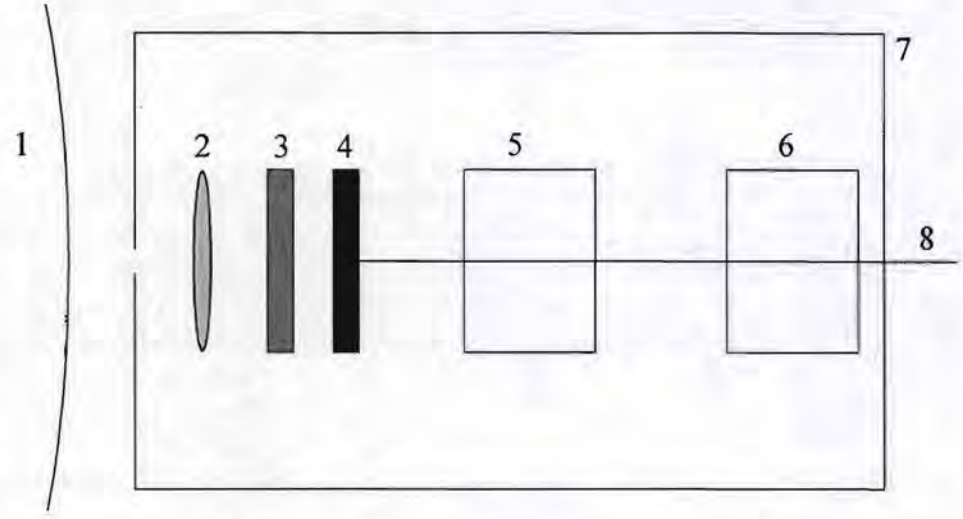

Figure 4: *Schematic drawing of the simple detector for plasma treatment monitoring. 1 – plasma reactor; 2 – lens (transmitting from 300 nm or less); 3 – interference filter (306 nm ± 20 nm); 4 – UV sensitive photodiode; 5 – low noise amplifier; 6 – analogue-digital converter; 7 – grounded box; 8 – digital signal output.*

On this basis the simplified monitoring device can be proposed for wide use in the practice. The scheme of such simple device is given in Fig. 4. This device uses the appropriate interference filter passing the light in the range mentioned above. Due to the fact that the plasma reactor is made from Pyrex glass and the maximum OH intensity is 307 nm, the optimal filter has a maximum transitivity of about 306 nm and band width of about ± 20 nm. The photodiode with UV increased sensitivity or photomultiplier can be used as a detector. The strong RF disturbing radiation for the discharge must be eliminated by sufficient electrical shielding including the impute orifice of the detecting device. The internal AD conversion must be used for the same reason. We have constructed this device for common use in practice. The results obtained in the future could help us identify the processes taking place during the plasmachemical reduction of corrosion layers at the ancient archaeological artifacts.

References

[1] Veprek S., Patscheider J. Elmer J.: Plasma Chem. Plasma Process. **5** (1985) 201
[2] Veprek S., Elmer J., Eckmann Ch., Jurcik-Rajman M.: J. Electrochem. Soc. **134** (1987) 2398
[3] Janca J., Klima M.: Scripta Physics, Proc. of Masaryk University Brno, **22** (1992) 85
[4] Klima M.: Archeologicke Rozhledy, Praha 1998, 255 – in czech
[5] Klima M., Zajickova L., Janca J. *et all*: Zeitschrift fur Schweizerische Archäologie und Kunstgeschichte, **54** (1997) 2398
[6] Klima M., Zajickova L., Janca J.: Zeitschrift fur Schweizerische Archäologie und Kunstgeschichte, **54** (1997) 29
[7] Klima M.: Plasmachemical Regeneration of Degraded Ancient Artifacts, PhD Thesis, Masaryk University Brno, 2000

Deposition of a-C:H Thin Films: Material Characteristics and Plasma Chemistry

J.Benedikt, K.G.Y.Letourneur, D.C.Schram, M.C.M. van de Sanden
Eindhoven University of Technology, Dep. Appl. Phys., P.O.Box 513 Eindhoven The Netherlands

Introduction

It is a known fact that a-C:H can be deposited at high rates by injecting acetylene (or other precursor gases) in an expanding thermal plasma created by means of a cascaded arc. Injected hydrocarbons are dissociated and react differently for various plasma parameters. Using Cavity Ring Down Spectroscopy (CRDS), CH and C_2 radicals were identified and quantified in the gas phase above the substrate for different plasma parameters. Though not spectrally resolved, C_2H is thought to be responsible for the broad band absorption around 270 nm.
In this study, the gas phase absorption by C_2, CH and C_2H radicals are correlated with the material characteristics, that is to say index of refraction and growth rate as measured by in-situ real time ellipsometry. We will propose a model for the growth of a-C:H. It is established that C_2H is a primary dissociation product of the C_2H_2 dissociation leading in some conditions to the creation of secondary products like CH and C_2. Competition between these radicals explains the variations in material quality (in our case characterized by the index of refraction) and deposition rate. The best conditions are reached at high C_2H flux. This coincides well with recent in-situ real time Fourier Transform Infrared absorption measurements of species present on the surface during growth.

Experiments and Discussion

Plasma is created in the cascaded arc at a pressure of around 0.4 bar. The DC current is applied between three cathodes and the arc nozzle. By variation of the arc current it is possible to change and control the amount of Ar ions emanating from the cascaded arc. Typical power is in the range of 1 to 5 kW. The plasma expands into a low-pressure vessel (typically 0.3 mbar) where supersonic and after a shock, subsonic expansion takes place. Into the plasma beam, acetylene is injected[1],[2] (Fig. 1). Because the temperature of electrons is low (around 0.3 eV in the expansion), electron driven processes may be neglected. Thus ion chemistry plays the most important role in the expansion zone. The proposed dissociation reactions are:

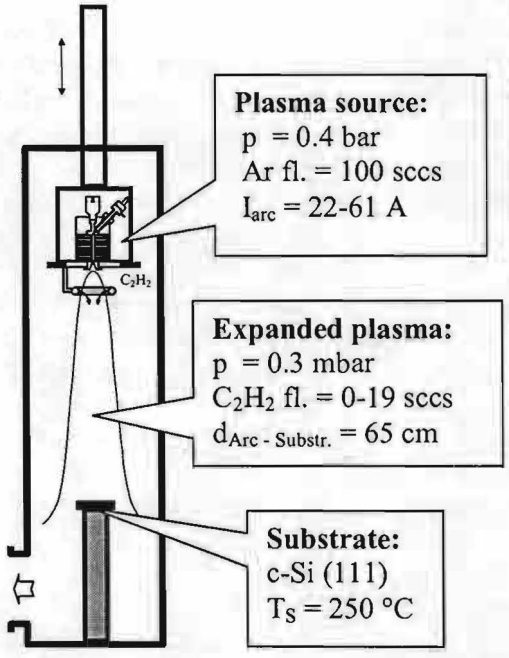

Figure 1: *Experimental setup for the deposition of a-C:H films.*

$$Ar^+ + C_2H_2 \rightarrow Ar + C_2H_2^{+,r,v} \quad k \approx 10^{-16}\ m^3/s \quad \{1\}$$

$$e^- + C_2H_2^{+,r,v} \rightarrow C_2H^{e,r,v} + H^* \quad k \approx 3.10^{-13} m^3/s \quad \{2\}$$

$$\rightarrow CH^* + CH^* \quad \{3\}$$

$$\rightarrow C_2^* + H^*(n) + H \quad \{4\}$$

(so-called *primary reactions*)

$$Ar^+ + C_2H^{e,r,v} \rightarrow Ar + C_2H^{+,r,v} \quad k \approx ? \quad \{5\}$$

$$C_2H^{+,r,v} + e^- \rightarrow CH^* + C \quad k \approx ? \quad \{6\}$$

$$\rightarrow C_2^* + H \quad \{7\}$$

(using second Ar^+ → *secondary reactions*)

Deposition takes place on the substrate at a distance of 60 cm from the cascaded arc. The substrate is crystalline silicon (111) and its temperature can be controlled and is kept at 250 °C. During deposition the vessel is pumped by two mechanical booster pumps (Edwards EH2600, 2600 m^3h^{-1}; Edwards EH500A, 500 $m^3 h^{-1}$) and one rotary piston pump (Edwards, 240 m^3h^{-1}). A turbomolecular pump (Leybold Turbovac 1500, 90 m^3h^{-1}) and a rotary pump (Edwards, 40 m^3h^{-1}) are used to maintain a base pressure (10^{-6} mbar) before deposition.
Two experimental techniques are applied. First the Cavity Ring Down Spectroscopy [3],[4] is used for measuring concentrations of radicals 3 cm above the substrate. A schematical view of the experimental apparatus used for detection of CH radical is depicted in Fig. 2.

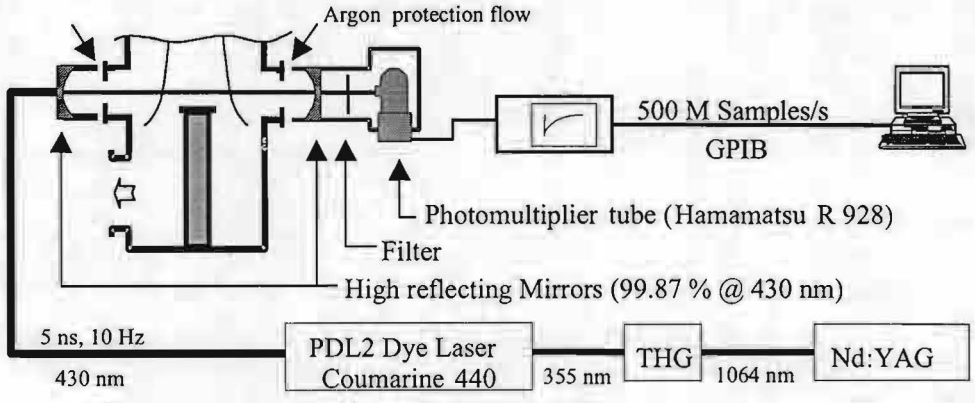

Figure 2: *Schematic view of a CRD experimental apparatus for CH radical detection*

The two high reflectivity plano-concave mirrors are placed 78 cm apart and create an optical cavity. The light used for CRD experiment is produced by a 10 Hz repetition rate Nd:YAG pumped dye laser (Spectra Physics DCR11/PDL2 combination) operating on Coumarin 440. Light pulses with length 5ns, with wavelength around 430 nm and with a bandwidth of about 0.4 cm^{-1} are used. The light that leaks from the cavity is detected by a photomultiplier tube (Hamamatsu R928) connected to an oscilloscope (Tektronix TDS 340A, 8 bit, 350 MHz bandwidth, 500 Ms s^{-1} sampling rate). A narrow band filter in front of the photomultiplier tube blocks the emission of the plasma. A LabView program controls the stepping of the dye laser and reads out the recorded transients via a GPIB interface. At every frequency typically 64 transients are averaged on the on-board 16-bit memory of the oscilloscope. The averaged transient, read out by the PC, is fitted with a standard least-squares fitting routine to an exponentially decaying function. The decay time τ of the transient is stored together with the frequency of the light and can be written as:

$$\tau(\upsilon) = \frac{d}{c\left(1 - R_{eff} + \sigma(\upsilon)\int_0^d n(x)dx\right)}$$

where d is the length of the cavity, c is the speed of light, R_{eff} is the effective reflectivity of the mirrors, $\sigma(\upsilon)$ the frequency-dependent cross-section of the absorbing species and $\int_0^d n(x)dx$ the line-integrated number density. If the species is homogeneously distributed over a path length L in the optical cavity, the integral can be written as $\sigma(\upsilon)nL$.

With CRDS CH and C_2 radicals were successfully identified. The spectrum of C_2H radical is still spectrally not resolved and only broad band absorption, which can be most probably ascribed to this radical, was observed. In Fig. 3 the example of absorption is shown as a function of acetylene flow at the arc current I_{arc} = 48 A.

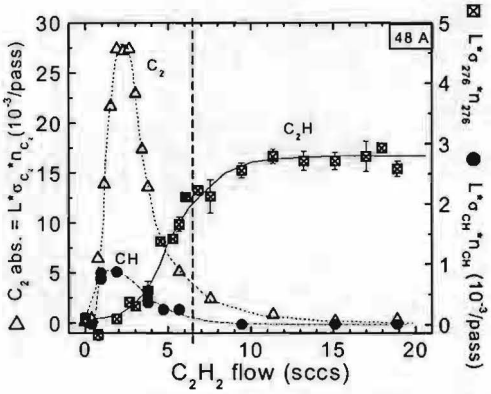

Figure 3: *CRDS measurements of absorption of CH, C_2 radicals and absorption at 276 nm ("C_2H") as a function of acetylene flow. The arc current is 48* A

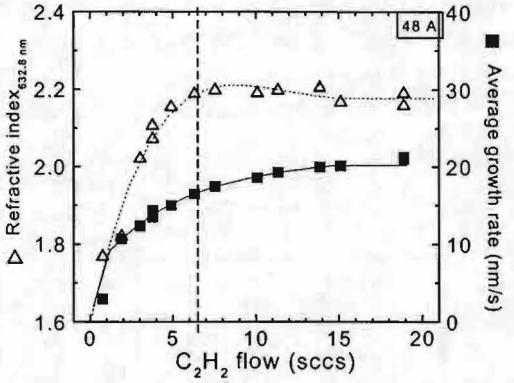

Figure 4: *The growth rate and a refractive index of films as a function of acetylene flow. Arc current is 48 A.*

Second in-situ real time Ellipsometry was used to measure a refractive index (at 632.8 nm) and a growth rate of the films. The principle of ellipsometry is the measurement of the polarization change of light due to the reflection on a surface. This polarization can be expressed in terms of the ellipsometric parameters Ψ and Δ: $R_p/R_s = \tan\Psi.\exp(i\Delta)$, where R_p and R_s are the Fresnel reflection coefficients parallel and perpendicular, respectively, to the plane of incidence including interference effects[5],[6]. The Ψ-Δ plot is recorded during deposition and obtained curve is afterwards fitted with a simulation program. Fitting parameters are refractive index and extinction coefficient of the growing film. The thickness of the film can be deduced from the fitting curve too and because the deposition time is known it gives growth rate of the deposition. The value of refractive index for silicon substrate is taken from the literature and a thin film of native silicon oxide at the top of the substrate is taken into account. It is possible to simulate influence roughness at the top of the film. The measurements were performed using a homemade HeNe ellipsometer in the PCSA configuration. The results of measurements of refractive index and growth rate for the arc current I_{arc} = 48 A are presented in Fig. 4. From previous measurements the dependence of the hardness of the films on the growth rate (Fig.5) and on the infrared refractive index is known[7].

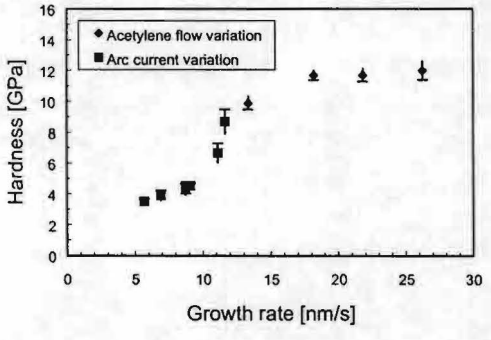

Figure 5: *The hardness of the films as a function of the growth rate. Similar dependence of hardness is also observed for IR refractive index.*

From the measured absorption several conclusions are drawn. The presence of given radical depends strongly on the acetylene flow. This is because the number of Ar ions available in the plasma at a given arc current is constant. Thus with high acetylene flow most of the Ar ions are consumed in primary reactions ({1}-{4}). On the other hand with low acetylene flow there are enough Ar ions for primary and subsequently for secondary reactions ({5} – {7}).

From Fig. 3 it is clear that CH and C_2 radicals are produced mainly at low acetylene flow, thus in secondary reactions {6} and {7}. In the case of high acetylene flows amounts of CH and C_2 radicals in the reactor are below the detection limit (reactions {3} and {4} are negligible) and only the C_2H radical is produced via primary reactions {1} and {2}. The boundary value between these two regimes (only primary reactions **x** secondary reaction) is acetylene flow of about six sccs. This flow approximately matches with the argon ion flow from the cascaded arc[2].

The impact of different radicals in the beam on the quality of the film is seen in Fig. 4. At high acetylene flow films are hard (see growth rate and Fig. 5) and at low flow (smaller than six sccs of acetylene) are soft. From this the conclusion is drawn that the C_2H radical is responsible for hard amorphous DLC films and CH together with C_2 and most probably atomic hydrogen are responsible for soft polymerlike films. The measurements in high and low arc current show the same dependence only the boundary region is shifted to the higher acetylene flow, if the arc current is higher (more argon ions) and vice versa if the arc current is lower (less argon ions). This is in agreement with the proposed reaction scheme {1}–{7}.

References

[1] J.W.A.M. Gielen, M.C.M.v.d.Sanden, P.R.M. Kleuskens, D.C. Schram, Plasma Sources Sci. Technol., **5**, 492 (1996)

[2] A. de Graaf, M.F.A.M. van Hest, M.C.M. van de Sanden, K.G.Y. Letourneur, D.C.Schram, Appl. Phys. Lett. **74**, 2927 (1999)

[3] R.Engeln, K.G.Y.Letourneur, M.G.H.Boogaarts, M.C.M.van de Sanden, D.C.Schram, Chem. Phys. Lett., **310**, 405 (1999)

[4] K.W. Busch, M.A. Busch, Cavity-ringdown spectroscopy : an ultratrace-absorption measurement technique, Washington : American Chemical Society, 1999

[5] H.G. Tompkins,W.A.McGahan, Spectroscopic ellipsometry and reflectometry : a user's guide, New York : Wiley-Interscience, 1999

[6] A.H.M. Smets, M.C.M.v.d.Sanden, D.C. Schram, Thin Solid Films, **343-344**, 281 (1999)

[7] J.W.A.M. Gielen , P.R.M. Kleuskens, M.C.M.v.d.Sanden,Y.L.J.v.Ijzendoorn, D.C. Schram, E.H.A. Dekempeneer, J. Meneve, J. Appl. Phys., **80**, 5986 (1996)

Spectroscopic studies of H_2-Ar microwave plasmas containing diborane

M. Osiac, L. Mechold and J. Röpcke

Institut für Niedertemperatur-Plasmaphysik, 17489 Greifswald, F.-L.-Jahn-Str. 19, Germany.

Introduction

Low pressure molecular microwave plasmas (f = 2.45 GHz) are commonly used for surface processes like thin film depositions. Boron-containing plasma composition provides anti-corrosion layers with a considerable high hardness. Processes in the plasma volume connected with the layer formation are only poorly understood. For improving the understanding of important chemical processes in the plasma it is necessary to study the main plasma parameters, which can be obtained by appropriate diagnostic methods. With respect to ground state concentrations of molecular species several non-invasive diagnostic methods have been developed, particularly, emission and absorption spectroscopy and as well as specific laser techniques. Tunable diode laser absorption spectroscopy (TDLAS) was shown to be a useful technique to measure the absolute concentration of the methyl radical and related hydrocarbon species [1]. In the present spectroscopic study, TDLAS has been applied to monitor the absolute concentration of boron containing molecules in their ground state, and optical emission spectroscopy has been used in order to determine the gas temperature.

Experimental Arrangement

The experimental arrangement of the planar microwave plasma reactor and the spectroscopic diagnostics systems are shown in fig.1. Details of the planar microwave plasma reactor can be found in [2], only a brief account is given here. The microwave plasma source consists of two waveguides, which are placed in a double T-shape. The discrete adjustable coupling elements are used for the gradual coupling of microwave energy from the upper to the lower interface waveguides. A quartz window, which is transparent for microwaves, replaces the lower metal wall of the interface waveguide. The plasma is excited in the vacuum vessel region just below the quartz window.

The InfraRed Multi-component Acquisition system, IRMA, was used to measure absorption lines of diborane, borane and BH radical. A detailed description of the IRMA system can be found in [3]. The IRMA system contains four independent tunable diode lasers. The narrow band infrared emission (line width about $10^{-4}cm^{-1}$) of four lead-salt lasers, which can be temporally multiplexed, is used to monitor the infrared absorption features of the target species. The four diode lasers are mounted in individual cold stations, which are thermally coupled to the cold finger of a closed cycle cryostat. The infrared beam coming from the IRMA system entered the plasma chamber via KBr windows (fig. 1). Its distance from the microwave entry window was aligned over a periscope mirror system in combination with a retro reflector. The measurements reported here were made at a fixed distance of about 40 mm from the microwave entry window with the laser beam making two passes through the plasma. To perform the absorption measurements of the BH radical a multipath White (20 passes) cell has been used. The emission spectra of boron atoms and BH radical have been recorded using an OMA system with a 0.5 m spectrograph (fig.1). The measurements were performed at a microwave frequency of 2.45 GHz and the power was varied between 1.2 and 2.4 kW, corresponding to a power flux in the observation plane between 2 and 5 W cm^{-2}. In addition, the total pressure was changed in the range of 1 to 2.5 mbar. The total flow rate was kept constant at 150 sccm containing 100 sccm of B_2H_6/H_2 and 50 sccm of Ar. The mixture of

hydrogen and diborane contained 4.9 % of B_2H_6 resulting in 3.3 % B_2H_6 in the source gas mixture.

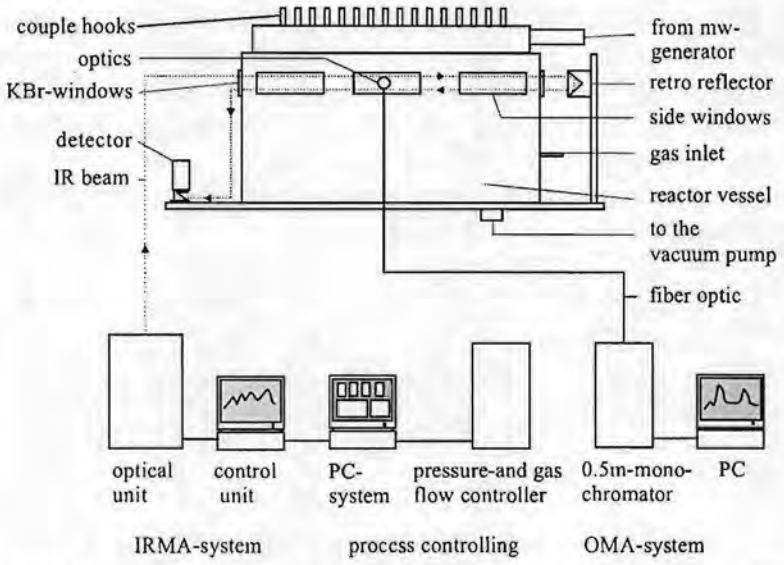

Figure 1: *Experimental set-up of the planar microwave plasma reactor and spectroscopic diagnostic systems. The path of the diode laser beam is indicated by dotted lines.*

Results and Discussion

Typically TDL absorption spectra of the pure gas flow and the microwave plasma (H_2-Ar-B_2H_6, P= 1.2 kW, p= 1.5 mbar) with lines due to diborane and borane can be seen in fig.2.

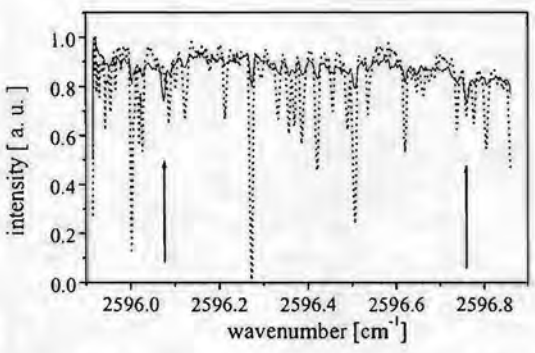

Figure 2: *TDL absorption spectra of the H_2-Ar-B_2H_6 gas flow (dotted line) and the microwave plasma (solid line), respectively. The arrows show the lines of BH_3 at 2596.077 and 2596.764 cm^{-1}.*

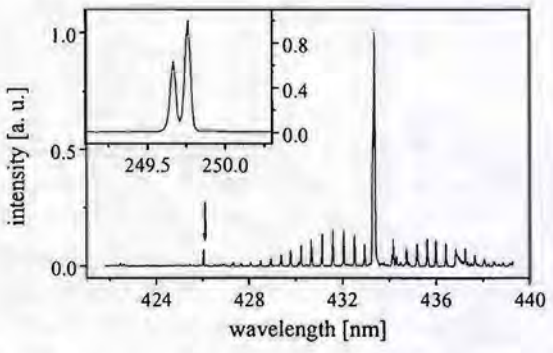

Figure 3: *Emission spectra of the $A^1\Pi$ -$X^1\Sigma$ transition, of BH radical with R, Q, P branches and atomic boron $2^2P^0_{1/2,3/2}$ - $^1S_0$ transitions in a H_2-Ar-B_2H_6 microwave plasma (P = 1.4 kW, p= 1.5 mbar). The arrow shows an Ar line at 425.936 nm used for identification.*

For borane identification four different lines were used and for diborane measurements one line at 1582.4384 cm^{-1} was chosen. To investigate the absorption signal of the BH radical, a line at 2143.3900 cm^{-1} was used, while optical emission spectroscopy provides the BH band $A^1\Pi - X^1\Sigma^+$ at 433.38 nm (Q head). The observed spectra of BH radical containing R, Q, P branches and atomic boron $2^2P^0_{1/2,3/2} - {}^1S_0$ transitions are shown in fig.2. The gas temperature was measured to (700 ± 70) K using emission lines of the Q (2-2) branch of the Fulcher-α band [4], while the rotational temperature of the BH radical was estimated to (600 ± 30) K.
The degree of dissociation of diborane, the relative absorption signals of borane and the BH radical were measured depending on the total pressure and power discharge. Results of the degree of diborane dissociation can be seen in fig. 4.

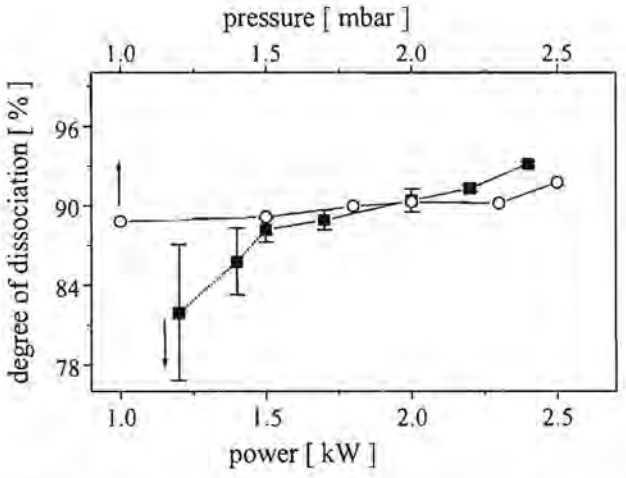

Figure 4: *The degree of dissociation of B_2H_6 under flowing conditions as a function of the discharge power (■) and the total pressure (○) in a H_2-Ar-B_2H_6 microwave plasma (63.3%H_2, 33.3%Ar, 3.3%B_2H_6, P = 1.4 kW, p = 1.5 mbar, Φ_{total} = 150 sccm). The arrows show the corresponding scales.*

High degrees of dissociation of the precursor molecule between 80% and 93% were found under all experimental conditions. Increasing power has lead to an increasing degree of dissociation. To study the nature of the chemical changes in the plasma the degree of dissociation was also measured under static conditions. In that case the degree of diborane dissociation reached values higher than 99.5%. Within the error bars the degree of dissociation is independent of the total pressure. The mean value is 90 %. In accordance with microwave plasmas containing hydrocarbons one of the main dissociation reactions of diborane into BH_3 can be considered to be initiated by electron impact [1]. The rate coefficient of this dissociation reaction is most likely correlated with the EEDF, which might be change with the higher power. On the other hand an increase in the gas temperature with higher power can lead to an effective thermal dissociation of diborane molecules.
The relative behaviour of the absorption signals of borane and the BH radical lines providing information about their relative concentration can be seen in figs. 5 and 6. To make clear the dependencies versus discharge power and total pressure, the intensities of these absorption lines were averaged and normalized to the first point. An almost linear increase of the relative absorption signal of borane was observed with increasing pressure. In contrast to it the relative

behaviour of the absorption signal of the BH radical is almost constant with increasing the total pressure. Because of high amount of hydrogen in the source gas composition (~63%) a high concentration of atomic and molecular hydrogen can be expected to be present and leading to collisions with all other species. Reactions of B_2H_6 and the BH radical with atomic and molecular hydrogen cause probably additional BH_3. The BH_3 relative absorption signal decreased with higher input power while the BH radical shows a considerable increase. In a first approach it can be supposed that BH_3 molecules might dissociate into BH and hydrogen molecules.

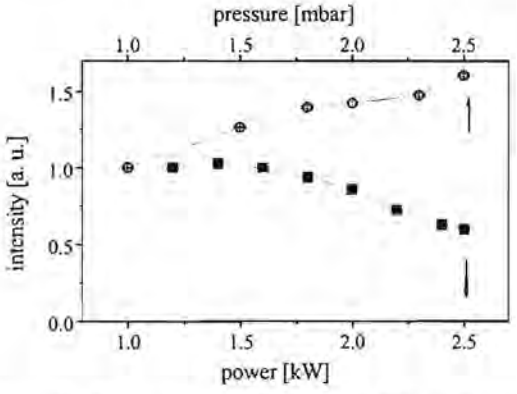

Figure 5: *The relative behaviour of BH_3 radical as a function of the discharge power (■) (p = 1.5 mbar) and the total pressure (○) (P = 1.4 kW) in a H_2-Ar-B_2H_6 microwave plasma.*

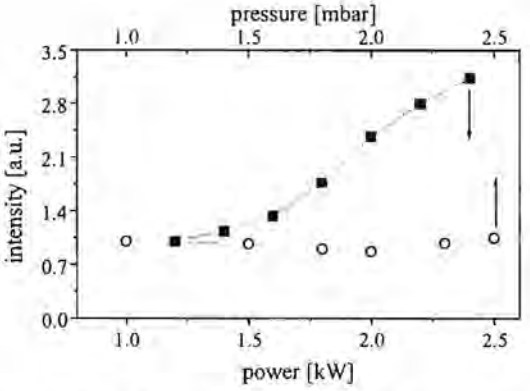

Figure 6: *The relative behaviour of BH radical as a function of the discharge power (■) (p = 1.5 mbar) and the total pressure (○) (P = 1.4 kW) in a H_2-Ar-B_2H_6 microwave plasma.*

Conclusion

The observation of three different molecular species containing boron by TDLAS not only shows the versatility of the technique, but has enabled progress to be made in probing the species present depending on pressure and power and in estimating main pathways of chemical reactions in H_2-Ar-B_2H_6 microwave plasmas. Optical emission spectroscopy provided a useful tool to determine the neutral gas temperature. Diborane was found to be very effectively dissociated in low pressure microwave plasmas.

Acknowledgements

The investigations have been supported by the German BMBF, project-no. 13N7451.
B. P. Lavrov provided helpful discussions and S. Saß valuable technical assistance for which the authors are grateful.

References

[1] J. Röpcke et al., *Plasma Chemistry and Plasma Processing*, **19**, 395 (1999).
[2] A. Ohl, Large Area Planar Microwave Discharges, in *Microwave Discharges: Fundamentals and Applications*, C.M. Ferreira (Ed.), Plenum, New York, 205 (1993).
[3] J. Röpcke, L. Mechold, M. Käning, J. Anders, F.G. Wienhold, D. Nelson and M. Zahniser, *Rev. Sci. Instum.*, **71**, 3706 (2000).
[4] S.A. Astashkevich et al., *J. Quant. Spectrosc. Radiat. Transfer*, **56**, 725 (1996).

Monitoring of plasma processes by using optical emission spectroscopy and plasma modeling

A. C. W. Biebericher, J. Bezemer, W. F. van der Weg, W. J. Goedheer*

Debye Institute, Interface Physics, Utrecht University, P.O. Box 80.000, NL - 3508 TA Utrecht, the Netherlands
**FOM Institute for Plasma physics 'Rijnhuizen' P.O. Box 1207, NL - 3430 BE Nieuwegein, the Netherlands*

Introduction

We report on plasma processes during deposition of hydrogenated amorphous silicon, which is deposited by PECVD, using an amplitude modulated RF signal. Previously, it has been reported that the deposition rate in powder-free (α-regime) plasmas, which are modulated by a square wave, increases up to a maximum at a modulation frequency which is determined by the decay time of the electron density [1]. The increase in deposition rate, up to a factor of three, with respect to the deposition rate in a similar continuously excited (cw) plasma is shown in figure 1. This phenomenon can be ascribed to a large production of radicals by high energy electrons at the onset of the plasma.

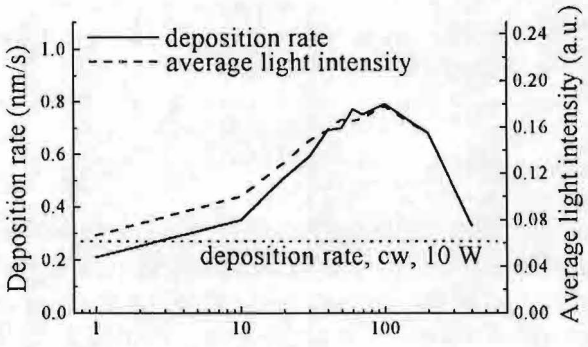

Figure 1. *Deposition rate and average light intensity as a function of the modulation frequency. The deposition rate with a continous wave plasma is indicated by the dotted line.*

The time behavior of the electron density plays an important role in the deposition process. This can be partly unraveled by the use of plasma diagnostics, like optical emission spectroscopy and plasma modeling. In order to optimize the deposition conditions, it is important to understand the plasma processes involved.

Experimental setup

Our deposition experiments have been performed in a capacitively coupled plasma reactor. A SiH_4/H_2 plasma was generated, using an RF signal with a carrier frequency of 50 MHz. The substrate temperature was 250 °C and the SiH_4 flow and the H_2 flow were 30 sccm respectively. In order to pulse the plasma, the RF signal was modulated in amplitude by a square wave. The modulation frequency has been varied in a range of 1 kHz to 400 kHz. The

amplitude modulation (AM) depth has always been 90 %. The duty cycle was fixed at 50 %. The pressure amounted to 0.2 mbar and the *average* power was kept at 10 W.

Plasma diagnostics

Optical Emission Spectroscopy (OES) has been used to characterize the plasma *in situ*. This is a suitable technique to characterize RF plasmas which have a low particle density and a low ionization rate [2]. The electrons dominate the plasma characteristics. The number of gas molecules that is dissociated is determined by the electron energy distribution. Such plasmas are not in an equilibrium state, since the electrons do have much more energy (2-4 eV, corresponding to a temperature of 3×10^4 K) than the neutral particles and ions which have a temperature of 300-600 K. The large amount of energy of the electrons is among others used to dissociate silane-related radicals and ions. Kinetic energy will be transferred from the electron to the atom, in elastic collisions. The main reactions due to inelastic collisions of electrons and neutrals are:

- The dissociation of a molecule: $AB + e^- \rightarrow A + B + e^-$.
- The ionization of an atom or molecule: $A(v) + e^- \rightarrow A^+ + e^- + e^-$.
- The dissociative attachment of a molecule: $AB + e^- \rightarrow A^- + B$.
- The excitation of an atom or molecule, from an initial state v to an excited state w: $A(v) + e^- \rightarrow A(w) + e^-$.

It depends on the plasma properties like pressure, electron density and electron temperature which process prevails. The plasma diagnostic OES is based on the last (excitation) reaction in this list. Since the ionization rate is low, most of the atoms will be neutral and in the ground state. When an excited atom decays from a certain level w to the ground state, a photon will be emitted. This emission of photons leads to characteristic lines in the emission spectrum. The population of a certain level is determined by the electron density and the electron temperature. The emission will depend on the population of a certain level and therefore on the electron density and the electron temperature.

In an SiH_4/H_2 plasma three specific lines are considered, i.e. the line that results from the spontaneous emission of an electronic transition of the free SiH^* radicals (413 nm) and two of the hydrogen Balmer lines, Hα (656 nm) and Hβ (485 nm). The spectral measurements pointed out that the largest contribution to the spectrally integrated emission is due to the SiH^* radicals. Figure 1 shows that the measured time-averaged intensity of the optical emission coincides with the curve of the deposition rate. The behavior of the time-resolved light emission is the same for both SiH^* and the spectrally integrated emission. Therefore, it can be concluded that the SiH^* line intensity reflects the radical production. The formation of SiH^* can be written as:

$$e^- + SiH_4 \rightarrow SiH_4^* + e^-$$
$$SiH_4^* \rightarrow SiH^* + H_2 + H$$

The SiH concentration appears to be determined only by the density of energetic electrons in the plasma bulk [3]. The hypothesis that these radicals originate from a one-electron collision process with silane, and not from a possible excitation of the ground-state SiH radicals, is confirmed by the linear relationship of the SiH^* intensity with the RF power.

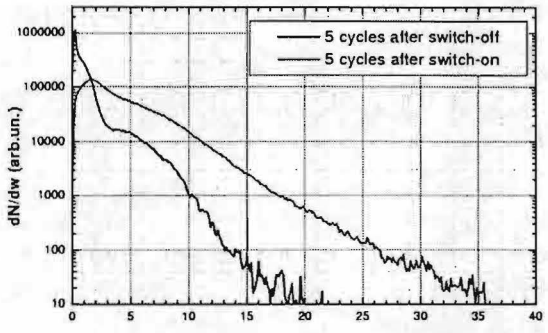

Figure 2: The electron energy distribution of a SiH_4/H_2 plasma at a carrier frequency of 50MHz, a modulation frequency of 25 kHz and a pressure of 0.2 mTorr.

The increase in light emission is an effect of the increase in the electron temperature. The increase in the electron temperature is predicted by the plasma modeling, which can be seen from figure 2. Here, the electron energy distribution of a 50 MHz SiH_4/H_2 plasma is shown. The power was 30 W during the 'on period' and 1 W during the 'off period'. The pressure amounted to 0.2 mTorr, and the modulation frequency was 25 kHz. It is clear that right after turning off the plasma, the electrons are 'cold'. Next they are heated after turning on the plasma.

The increase in electron temperature is confirmed by measurements with an interference filter to select either the Hα and Hβ lines which have been measured with a photo multiplier (Hamamatsu, spectral response: 185 – 900 nm). The ratio of the intensities of the Hα and Hβ lines gives information about the electron energy distribution and the electron temperature in the plasma. When the electron temperature increases, a larger fraction of Hβ photons will be generated, since more energy is needed for this excitation. Therefore, the ratio of Hβ/Hα will be a measure for the electron temperature.

Results

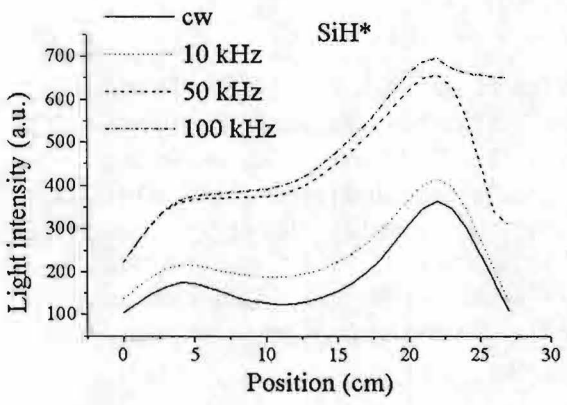

Figure 3: The spatially resolved light emmission of the SiH^* line at different modulation frequencies.

Figure 3 shows the spatial distribution of the light emission of the SiH^* line, at different modulation frequencies. To measure these curves, slits are used and the photo multiplier could be moved over a distance of 27 mm. The curves are asymmetric due to the fact that the powered electrode (x = 2.7 cm) is smaller than the grounded electrode (x = 0 cm). The intensity of SiH^* at 100 kHz is much higher over the whole x-range, as compared to the variation of light intensity of a comparable cw plasma. This result confirms the previous results, described above.

Figure 4 shows the curves of the spatially resolved ratio of Hα and Hβ. This ratio for 10 kHz is slightly higher than the ratio of the cw plasma. The ratio in case of 100 kHz is significanly higher than the ratio of the cw plasma. The increase in the ratio of Hβ/ Hα confirms the results from the calculations that the electron temperature increases at higher modulation frequencies.

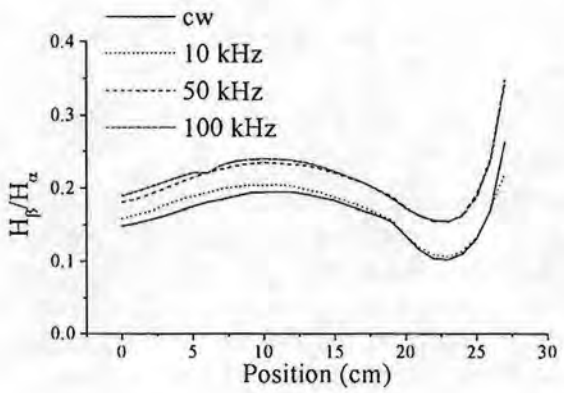

Figure 4: *The spatially resolved ratio of Hβ/Hα.t different modulation frequencies.*

Acknowledgements

The authors gratefully acknowledge experimental and technical support by J. Groenewoud and the support of L. Jacobs with ellipsometry measurements. The authors thank the Netherlands Agency for Energy and the Environment (NOVEM) for financial support.

References

[1] A. C. W Biebericher, J. Bezemer, W. F. van der Weg, and W. J. Goedheer, Appl. Phys. Lett. **76** (15), 2002 (2000).

[2] W. G. J. H. M. van Sark and J. Bezemer, Plasma-onderzoek voor amorf silicium zonnecellen, deel1, Verslag Novem project 146.100-027.1, Vakgroep Atoom- en Grenslaagfysica, Debye Instituut, Universiteit Utrecht, Postbus 80.000, 3508 TA Utrecht (1995).

[3] in *Plasma deposition of amorphous silicon-based materials* (Academic Press, Inc., 525 B street, suite 1900, San Diego, California, 1995), Chapter:Diagnostics of amorphous silicon (a-Si) plasma processes.

Determination of the Electric Field Strength in a Low Pressure Gas Discharge

Z. Altug, J. Neumann, T. Rieper, and V. Helbig

Institut für Experimentelle und Angewandte Physik, Universität Kiel, Leibnizstr. 19, D 24098 Kiel, Germany

Introduction

For the diagnostics of low temperature gas discharges that have a variety of applications in industry new sensitive and reliable methods are needed for the measurement of the local electric field strength. Optical techniques that do not require a complex experimental set-up and expensive and elaborate laser systems are desirable. The aim of the present paper is to show that Doppler-broadened spectra of the first Balmer line of Hydrogen can be used to determine the electric field strength in the cathode sheath of a low pressure glow discharge with high accuracy. Using a home-made Littrow-type diode laser spectrometer and opto-galvanic detection we obtained spectra from which the field strength and the direction of the field could be derived using quantum mechanical calculations of the Stark effect including fine structure

Experimental Setup

We [1, 2] have investigated the possibility to use the Stark-splitting of the H_α line of Hydrogen to obtain the magnitude and the direction of the electric field strength in the cathode fall of a low pressure, low current DC gas discharge. We used opto-galvanic detection to scan the line profile by means of a diode laser system developed in our laboratory. The front face of the diode was anti-reflection coated and was set-up in an external, Littrow-type resonator. In the spectral region of H_α the device could be tuned without mode hops across a spectral band of approximately 120 GHz. This was sufficient to scan the complete Doppler-broadened line profile. The electric field strength was obtained by fitting the experimental profiles to a set of calculated line profiles. Those were obtained from calculations following the procedure outlined by [3]. The theoretical results include the fine structure, the polarization and the field dependence of the intensities of the single fine structure Stark components.

Results

Sets of spectra obtained in π– and σ–light are shown in Fig. 1. Obviously the π–spectra due to their larger Stark-shifts are more sensitive to the electric field than the spectra with the polarizer perpendicular to the field lines in the sheath. Nevertheless the σ–spectra serve as a check for the consistency of the theoretical calculations. Field strengths between 500 and 8000 V/cm could be determined with high accuracy from the fitting routine using the set of theoretical profiles obtained by the calculations. Using a rotating polarizer as chopper for the lock-in amplifier we were able to derive the direction of the electric field in addition to the magnitude. However, up to now the measurements are averaged across the discharge diameter.

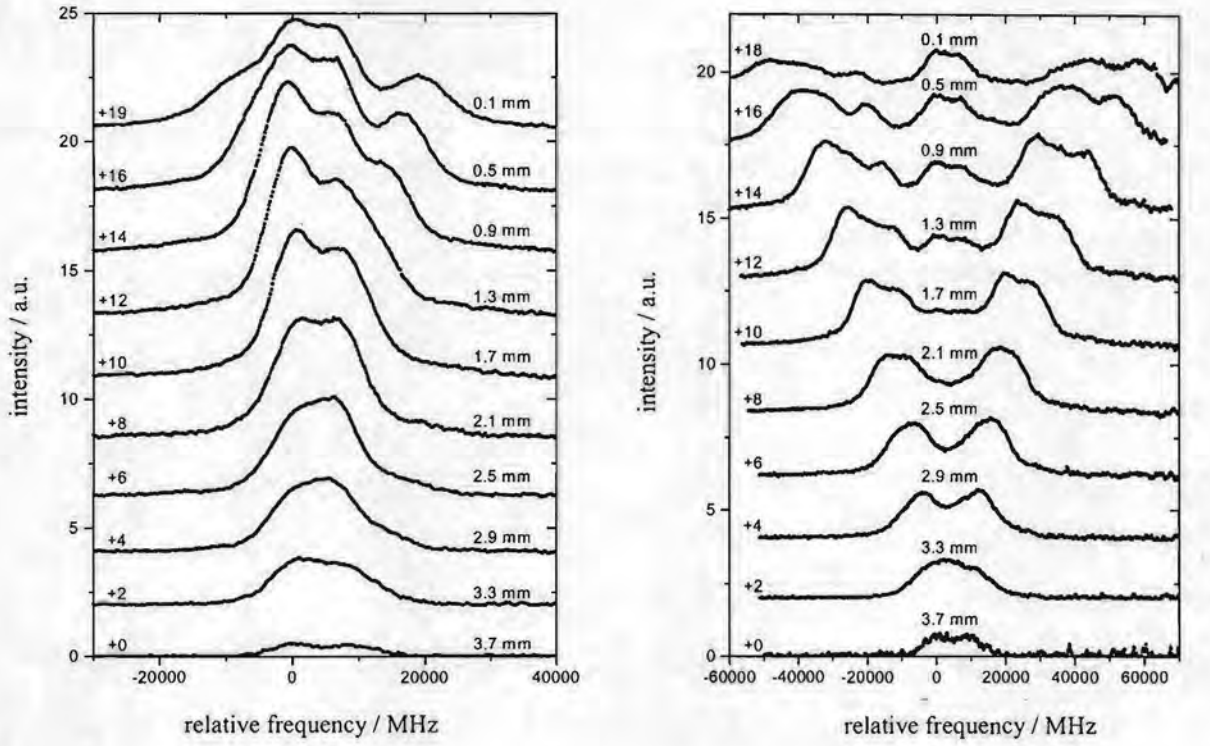

FIGURE 1. *Spectra of the σ– (left) and π– (right) components of the Hydrogen line H_α for various distances from the cathode (given in mm for the respective spectra). On the left the offset is indicated by which each of the single spectra is displaced in order to avoid overlapping of the profiles.*

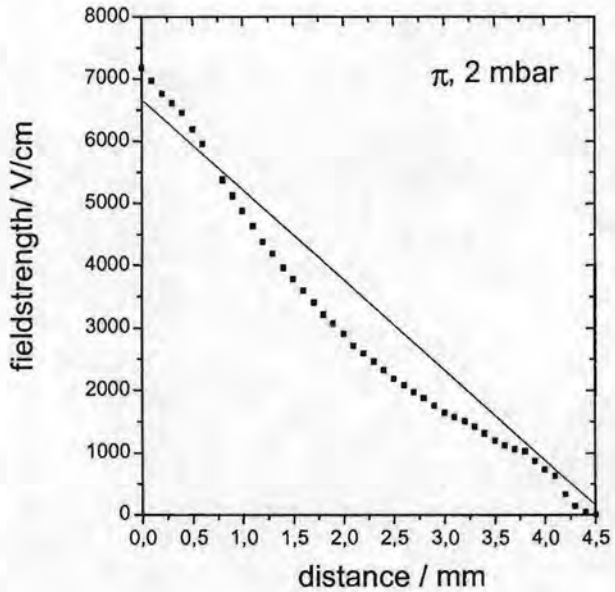

FIGURE 2. *The measured electric fieldstrength in front of the cathode versus distance from the cathode for a discharge pressure of 2 mbar. The values are derived from the spectra of the π–components.*

No attempt has been made up till now to use Abel transformation or the like to obtain spatially resolved field strength profiles of the discharge. Figure 2 shows the measured field strength as function of the distance from the cathode for a pressure of 2 mbar. The uncertainty of the field strength derived from the fitting routine is of the order of a few percent corresponding to an error bar smaller than the spot size in the figure. All measured characteristics deviate systematically from a straight line in the same way that is shown in the figure.

References

[1] Rieper, T., *Ph.D. thesis*, Kiel (2000)
[2] Neumann, J., *Diploma thesis*, Kiel (2000)
[3] Lüders, G., *Ann. d. Physik* **8**, 301 - 321 (1951)

Numerical simulation of a multi-channel light scattering diagnostic system for low temperature plasmas

M. Kaczor, H. Soltwisch
Institut für Experimentalphysik V, Ruhr-Universität Bochum
Germany

Introduction

The aim of our group is the investigation of the complicated interaction between the electron energy distribution function (EEDF) and the different species in reactive plasmas.
Therefore a multi-channel light scattering diagnostic system has been developed in previous works to study the electron component of reactive plasmas using Thomson scattering in a GEC reference cell [1]. Due to the small Thomson cross-section and the special conditions in a reactive plasma a photon counting technique is utilized to detect the temporal behaviour of the scattered light simultaneously in eight spectral channels. A numerical simulation has been developed to investigate the effect of the detection system on the measured signal.

Experimental Setup

The plasma is produced in an inductively coupled GEC reference cell. The discharge parameters are shown in Fig.1. Two laser systems are used for scattering experiments. One is a frequency doubled Nd:YLF laser (527 nm) with an energy of 3 mJ – 10 mJ (multi mode) or 0.5 mJ – 3 mJ (TEM00) per pulse at 1 kHz repetition rate.

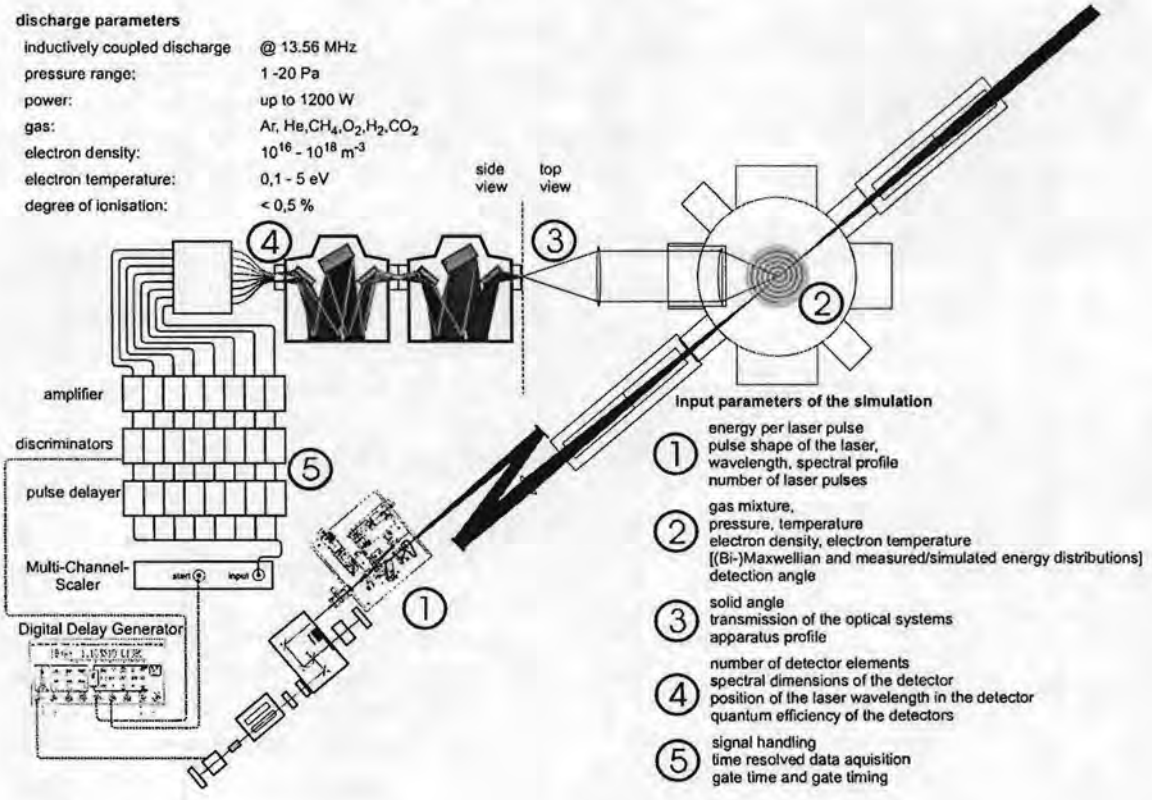

Fig. 1: experimental setup

This laser is also used to pump a tunable Ti:Sapphire laser (intra-cavity frequency-doubled 430 nm – 470 nm) with a maximum of 1 mJ per pulse. The scattered light is collected under a scattering angle of 140° by a lens which is placed in a special flange. This allows us to bring the lens close to the discharge in order to achieve a solid angle of 0.07 sr. The light is collected by eight optical fibres at the exit slit of a double monochromator (2 × ¼ m), which is used to provide a low stray light level. The fibre array covers a spectral range of 5.88 nm with 0.7 nm spectral width for each element. Each of the optical fibres transmits the spectral interval of the scattered light to a photomultilpier, that is used in photon counting mode. The signal is amplified and filtered by discriminators, which improve the signal to noise ratio, as they are gated with the laser pulse and as they supress noise. The signals in the different channels are then delayed relative to each other such that a Multi-Channel-Scaler can be utilised to detect the time behaviour of a signal for each spectral channel. The major draw back of this system is, that the delay units will only process the first signal of a pulse sequence (corresponding to the first photon hitting the photo cathode within the gate). The other pulses of the sequence are dropped. In order to take into account the effects of this counting mode, a numerical simulation was developed, which mimics the light scattering process and the characteristic features of the detection electronics.

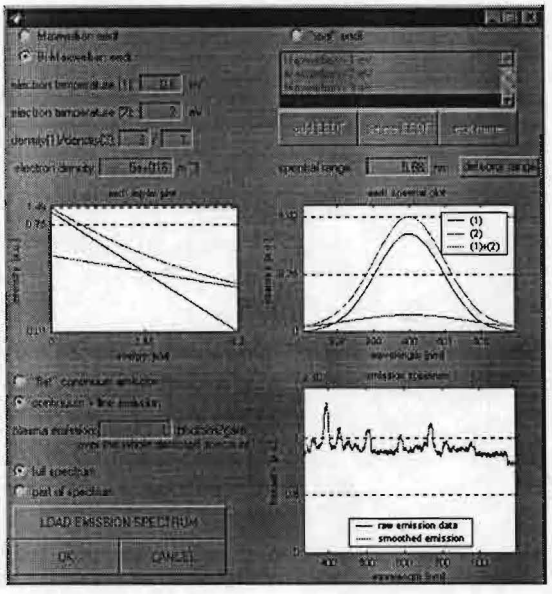

Fig. 2: input dialog for the plasma data

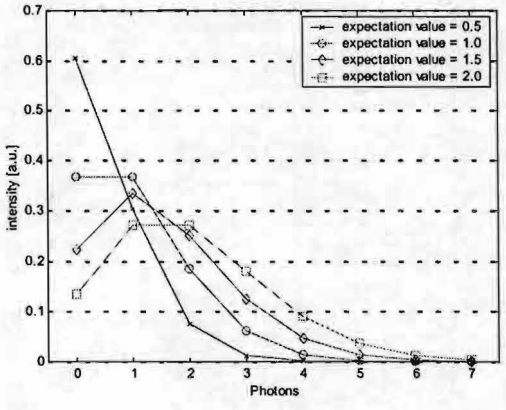

Fig. 3: Poisson statistics for various expectation values

Numerical Simulation

The numerical simulation is used to investigate the effect of the detection system on the measured data. It can also be used to estimate the detection limit of the setup. In addition, it generates simulated data, which can be used to identify errors in the analysis of the measured data. The structure of the simulation is shown in Fig. 7. It provides a graphical user interface that allows to change all relevant parameters of the light scattering process and its detection. The module in which the EEDF and the plasma emission are set is shown in Fig. 2. The simulation is based on the assumption that the statistics of the scattering process follows the Poisson distribution. For small expectation values it shows a significant deviation from the Gaussian normal distribution. Due to the fact that even at very small expectation values (< 1 photon per detector channel) there is a non-negligible number of 2-photon events (Fig. 3), the detected signal is affected by the type of the data aquisition.

This can be seen in Fig. 4, where the measured intensity of the detected light

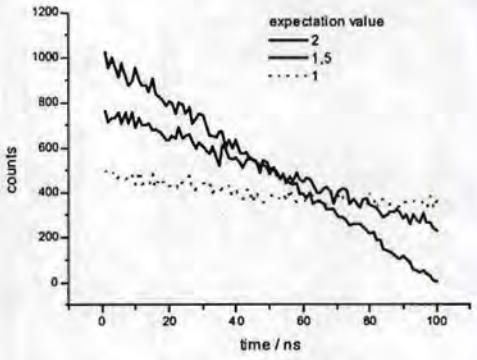

Fig. 4: influence of the counting mode

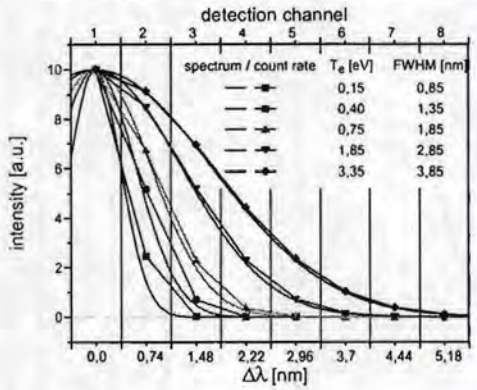

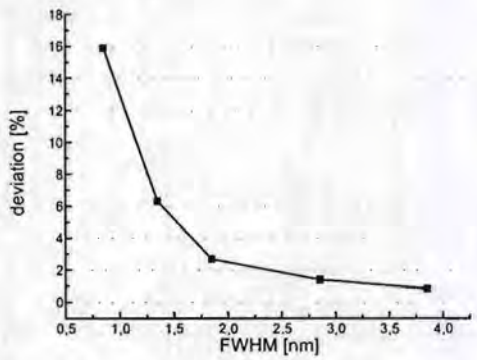

Fig. 5: deviation of the calculated spectrum from the initial spectrum

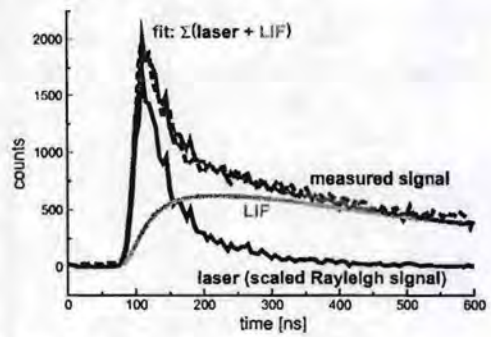

Fig. 6: fluorescence of low intensity

seems to decrease towards the end of the gate.

The influence of the finite spectral width in each detection channel is shown in Fig. 5. Binning the spectrum in rather big spectral intervals yields an over-estimated value for low electron temperatures.

Fluorescence light can affect measurements in molecular plasmas dramatically. [2] An example is shown in Fig. 6. In order to distinguish between Thomson scattering light and fluorescence light of low intensity, the pulse shape of the scattered light has to be analysed.

The implementation of a fluorescence signal into the simulation is currently under development.

Acknowledgement

This work was supported by the SFB191 of the "Deutsche Sonderforschungsbereich".

References

[1] M. Kaczor, H. Soltwisch; Centre de Recherches en Physique des Plasma, EPFL, Lausanne Report LRP 629/99 "Workshop on Fontiers in Low Temperature Plasma Diagnostics III", Switzerland, 15-19 February 1999

[2] H. Soltwisch, M. Kaczor; Centre de Recherches en Physique des Plasma, EPFL, Lausanne Report LRP 629/99 "Workshop on Fontiers in Low Temperature Plasma Diagnostics III", Switzerland, 15-19 February 1999

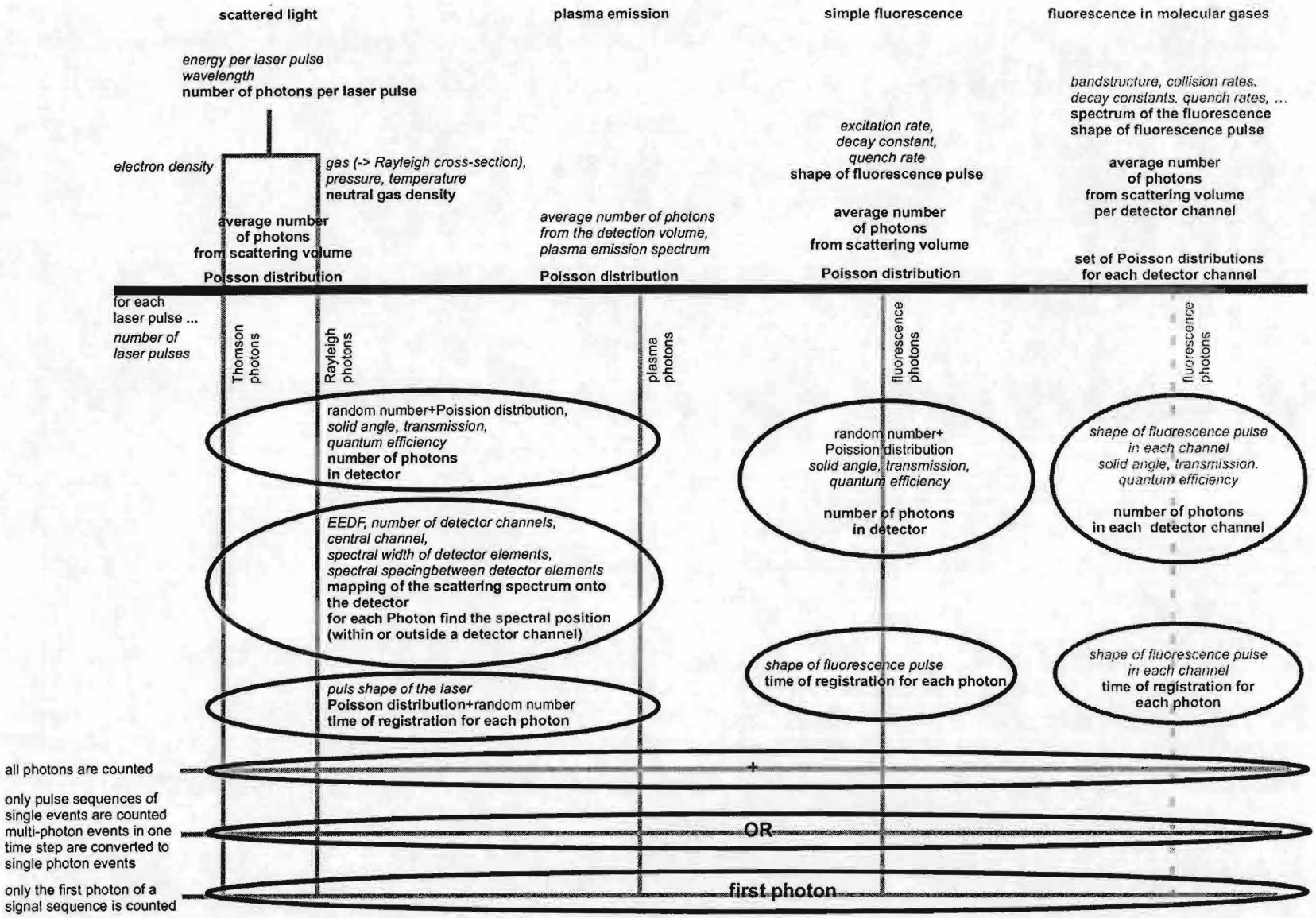

Fig. 7: schematic structure of the simulation

Time-resolved spectroscopy of HF discharges: "low-price" instrumentation approaches

F M Dias
Centro de Física dos Plasma, Instituto Superior Técnico, 1049-001 Lisboa, Portugal

1. Introduction

Detection systems allowing time-resolved measurements are intrinsically expensive. For instance, a streak camera able to record spectra with a resolution of 200 fs costs something like 250 k€! Nevertheless, it is possible to add the time-resolving capability to existing equipment using devices not too expensive or forgotten in a shelf. The following considerations are primarily intended to describe such "low-price" systems and will be mainly presented in Section 2 for single channel detectors since they offer more possibilities. In Section 3 we discuss its application to multichannel detectors and in Table I we present a short summary of system requirements.

2. Single channel detectors

This is typically the case of a photomultiplier tube (PMT) but the following considerations are equally valid for other detectors, *e.g.* semiconductor ones.

2.1. Photon counting

This is maybe the most suited and widely used equipment for the acquisition of time-resolved spectroscopic signals. Indeed, this device is gateable and enables the measurement of low-level light quantities as it is the case for ns-width gates when the count rate can be less than one photon per gate opening. Note that the maximum trigger frequency is typically 1 MHz, meaning a duty-cycle below 1% in HF discharges. Yet, this is not a problem for a photon counter since it accumulates counts.

2.2. Oscilloscope

Although the oscilloscope is probably the best suited equipment for time-domain data recording, it is unusual to see fast time-varying spectroscopic signals on an oscilloscope screen, namely if the detector is a PMT. This is a direct result from detectors being nearly quantum devices: a PMT produces a bunch of electrons each time photoelectric effect takes place (hereafter referred as an event). For instance, the 3 nA dark current of a R928 PMT will be seen on a 50 Ω input impedance oscilloscope as a sequence of pulses greater 20 mV and of a few ns-width, although its average value is 150 nV only. As a result, no digital oscilloscope (DO) has such a high dynamic range which makes it useless for transient recording at low-level light intensities. The situation is quite different when dealing with periodic phenomena as it is possible to average the signal prior to the oscilloscope input without introducing any unnecessary distortion. Indeed, a smooth signal is obtained if high-Q filters are used. The filters must be tuned at all the harmonics of the signal, from DC to the highest frequency of interest. Note that the filtered PMT output signal is usually too small for a direct reading on an oscilloscope and thus a tuned amplifier may be required. A simple implementation is to connect the PMT output to a high impedance input amplifier through a low-loss coaxial cable with an electrical length slightly less then ½-wavelength at the fundamental (for input capacitance compensation). With this arrangement the system is simultaneously tuned at all harmonics but its response becomes frequency dependent due to cable losses. This minor problem can be solved deconvoluting the recorded signal. More drastic solutions, *e.g.* crystal

filters eventually used in conjunction with heterodyne conversion, will be required for low-level light intensities. In this way each harmonic is measured at-a-time, from which the signal can be reconstructed.
When a diode detector is used the situation is not very different from the PMT case. Yet, diodes typically produce one electron per event and the resulting signal must be amplified. High-speed amplifiers have a gain (transconductance × input impedance of next stage) typically of 400 which is much smaller than the typical PMT gain ($\approx 10^7$) or, in other words, an event frequency 2.5×10^4 greater is required for a diode to produce the same output as a PMT. As a result, a diode is commonly used at higher light intensities and then its output looks like a "continuum" which is acceptable to be directly displayed on an oscilloscope.

2.3. Boxcar averager

The boxcar averager (BA) is an instrument somewhere in between a photon counter and an oscilloscope: it accumulates gated measurements, like the former although (hopefully) in an analogic way, and it is the basic front-end of a sampling oscilloscope. Recently, BAs are becoming old-fashioned due to the increasing speed of DOs, which tempts manufacturers to produce BA's digital versions or simply to stop their production. Yet, the "old" BA presents three distinctive features: it can make time-locked measurements (to *stop the time*), it can be used for other time-resolved measurements, *e.g.* probe's, and it is analogic. The latter feature is very important since it provides a theoretically infinite dynamic range (conversely to DOs; see §2.2). Hence, filtering requirements are lower for a BA than for a DO at the same light intensity.

2.4. Bias gated PMT

Controlling the PMT biasing is a simple and inexpensive way to achieve gated measurements. Commercial PMT socket assemblies for such kind of operation (≈ 1 k€) do not require equipment changes other than an additional power supply (≈ 250 V). Unfortunately, the minimum gate width of the above assemblies (≈ 1 μs) is too large for measurements at 13.56 MHz. Yet, we think that nothing prevents that a faster system can readily be built since the inter-dynode control voltage is similar to the one that can be obtained with a single-stage, avalanche transistor generator. The control voltage may be applied to one single dynode but biasing several dynodes with a travelling wave pulse matching the electron transit time is advisable for high switching ratios. Alternatively, the AC scheme described below for Pockels cell gating can also be used here.

2.5. External image intensifier gating

An image intensifier (ImI) consists of a photocathode, a microchannel plate (MCP) amplifier which multiplies the number of electrons emitted by the cathode, and a phosphor screen which produces light upon electron impact. The MCP gain is about 10^4 (single-stage @ 1kV) and gating is achieved by switching the applied HV (≈ 1 kV/stage). Gain is an important feature of these devices since it minimizes the decrease in time-averaged sensitivity due to low duty-cycles under pulsed operation. An ImI gated system is quite expensive (≈ 20 k€) being the ImI itself the major contributor, but the price of the HV pulse generator is also significant although it can be minimized using the sine-wave scheme described below (see §2.7). Note that an ImI should be installed between the spectrometer's exit slit and the detector since ImIs have their own wavelength response.

2.6. Gateable MCP-PMT

This is a new family of PMTs which include a grid electrode for control purposes and where dynodes were replaced by a MCP amplifier. Basically, this is an improved version of a bias gated PMT: they are fast (gate width ≈ 5 ns) and the output signal is cleaner (the MCP shields the anode from the gate which, in addition, only requires a few volts for a full switching ratio). Yet, the sensitivity is lower than the one of a normal PMT (an external high speed amplifier may be required), the switching ratio is wavelength dependent (the gate is located in front of the photocathode), and its price is very high (≈ 25 k€).

2.7. Pockels cell gating

A Pockels cell gate (PCG) is an alternative to an external ImI as a device that can be added at any moment to an existing steady-state spectroscopic system but, conversely to the later, it does not change the wavelength response of the system. As a result, the PCG can be inserted anywhere between the light source and the spectrometer's detector. A PCG is not expensive by itself (≈ 1.5 k€), which usually is not the case for the required HV generator ($\lambda/2$ voltage ≈ 3.4 kV @ 1064 nm for a KD*P crystal). Since the price of HV pulse generators increases with increasing voltage and with decreasing pulse width, solutions to reduce the price are obvious: i) multipassing techniques or multiple cells electrically driven in parallel; ii) not using a pulse generator at all, *i.e.*, driving the cell with sine-waves (the cell is made a part of a resonant circuit; there are commercial PCG systems operating at 2 GHz in this way). The latter solution is clearly the least expensive and presents a duty-cycle of about 50%, in opposition to the much lower value presented by pulse generator (10^{-7} for a 10 ns gate at a 10 Hz trigger rate). This means that the sensitivity of the acquisition system is reduced not much below its DC value. Of course that sine-wave driving has a cost: the measurements need to be deconvoluted since the equivalent gate width is comparable to the period. Note that using a cell resonant circuit tuned at several harmonics allows us to adjust the duty-cycle by changing the amplitudes and phases of the different harmonics. It is the user's responsibility to choose the best tradeoff between price, duty-cycle and need for deconvolution.

2.8. Vector voltmeter

Although lock-in amplifiers are familiar to everyone working on spectroscopy, a vector voltmeter (VV) or a network analyzer, which are basically the same equipment under a different name, are not to be seen at all connected to a spectroscopic data acquisition system. Working in the frequency-domain they make measurements from which the signal can be reconstructed in the time-domain. A modern VV operates up to the lower GHz-band and has a dynamic range of 10^5 which is enough for medium-level light intensity measurements. Anyway, in order to increase the sensitivity, it is advisable to use a tuned preamplifier which additionally provides over-voltage protection to the VV input (maximum input voltage ≈ 2 V typ.).

In addition, the user gets an unexpected gift! The front-end of these instruments is typically a sampler which reconstructs the signal in the kHz region. Therefore, if the sampler output is fed to an oscilloscope or to a data acquisition board, we get a simple way to record the time-varying signal without the need of Fourier analysis (some VVs have the sampler output available at the rear, otherwise the user will have to tamper with the instrument). The resulting sampler–oscilloscope combination has the VV's dynamic range and filtering becomes much easier since most of it can be made between the VV and the DO, *e.g.* with active filters using operational amplifiers. Note that the VV's sampler is asynchronous and

thus a time-reference must be present (the VV's reference channel must be simultaneously recorded or an electrical or a light pulse must be used; a ns-width light pulser can cost 100 € only).

2.9. Laser switched systems

A high-energy, pulsed Laser is a very expensive device (≈ 35 k€) but, if otherwise unused, it can provide alternative ways to gate light signals. Laser radiation can heat a Brewster-angle window, changing its refraction index and thus turning on reflection of vertically polarized light. Alternatively, impinging on a non-linear crystal it provides heterodyne frequency conversion. Yet, these gating systems are far from ideal. The former should be used in conjunction with some other device to close the gate because cooling the window by conduction is a too slow process. The latter features a low conversion efficiency for broad band applications and/or is very wavelength dependent.

3. Multichannel detectors

This is typically the case of charge coupled device (CCD) cameras but the following considerations are equally valid for other kind of multichannel detectors, *e.g.* diode arrays.
Intensified CCD (ICCD) cameras already include an ImI which enables them to make time-resolved measurements. So, ICCDs are a ready to use system, they are more expensive than ImIs or CCDs (≈ 50 k€) and thus we will consider here only the case of an add-on gating device applied to an existing CCD detector. The considerations mentioned at Section 2.5 are valid for the case of multichannel detectors except in what concerns the MCP location: it must be installed at the spectrometer's exit focal plane, a position previously occupied by the CCD. Note that the use of an ImI decreases the CCD resolution.
When a PCG is added to a system with a multichannel detector the situation is not different from what we mentioned above (§2.7). It should be noted that, conversely to the external ImI case, the PCG does not decrease the CCD resolution.
The Laser switched systems described above (§2.9) can be applied without changes to spectrometers equipped with multichannel detectors.

	Single/Multi channel	Max. trigger frequency	Requires freq. division	external delay	Other measur. (*e.g.* probe's)
Photon Counting	S	1 MHz	Yes	No	No
Digital Oscilloscope	# channels	---	No	No	Yes
Boxcar Averager	S	20 kHz	Yes	No	Yes
Bias Gated PMT	S	100 kHz	Yes	Yes	No
Image Intensifier	M	100 Hz	Yes	Yes	No
Gateable MCP-PMT	S	100 MHz	No	Yes	No
Pockels Cell	M	2 GHz	No	Yes	Maybe
Vector Voltmeter	2 channels	2 GHz	No	No	Yes
Laser Switched	M	20 Hz	Yes	Yes	No

Table I: *Short summary of system requirements and of other applications.*

References

Interested readers may find more information in general books on Instrumentation or Optics. Furthermore, we consider reading the manufacturer's Instruction Manuals of the equipment mentioned above as obligatory. We are not making here any further specific referencing to avoid advertising.

DETERMINATION OF QUENCHING COEFFICIENTS BY TIME RESOLVED EMISSION SPECTROSCOPY IN A HYDROGEN RF DISCHARGE

T. Gans, V. Schulz-von der Gathen, and H. F. Döbele

Universität Essen, Institut für Laser- und Plasmaphysik, Universitätsstr. 5, 45117 Essen, Germany

1 Introduction

In gas discharges at elevated pressure radiation-less collisional de-excitation (quenching) has a strong influence on the population of excited states. The knowledge of quenching coefficients is therefore important for discharge simulations taking into account excited states. The knowledge of quenching coefficients is also essential for the correct analysis of the experimental data for plasma diagnostics based on optical emission spectroscopy (OES) [1, 2] and laser induced fluorescence spectroscopy (LIF) with one or two photon (TALIF) excitation [3], since the spontaneous emission intensities indicating the population of the excited states are affected by quenching. Quenching coefficients of noble gases, e.g., are of particular interest, because these are finding widespread application as tracer gases in molecular discharges.

Quenching coefficients are usually determined from measurements of the effective lifetime of excited states. The effective lifetime of excited states can be obtained from the fluorescence decay after a pulsed excitation. The pulsed excitation can be performed by laser radiation. The disadvantages of laser excitation are limitations by optical selection rules and the problem to overcome the energy gap from the ground state to the excited states. For noble gases such as xenon [4], krypton [4] and argon [5] it is possible to cover the energy gap with two photon excitation in the UV or VUV, but for neon and helium the energy gaps are too large for a direct laser excitation. Excitation from metastable levels to higher levels by laser radiation represents a possibility to yield information on self-quenching coefficients in discharges, however. Since the population density of noble gas metastables is very low in the presence of molecules in discharges, the determination of quenching coefficients by laser excitation for neon and helium does not work with molecules (e.g. hydrogen).

Capacitively coupled RF discharges (CCRF discharges) at 13.56 MHz in hydrogen exhibit a field reversal phase of about 10 ns during which an intense electron current provides collisional excitation within the sheath region [6, 7]. After this strongly dominant short pulsed electron impact excitation, it is possible to determine quenching coefficients from the lifetime of the fluorescence at various pressures by time resolved OES even for high energy levels and without any restrictions of optical selection rules. This novel technique allows the measurement of quenching coefficients for atomic and molecular emission lines of hydrogen itself, as well as for emission lines of small admixtures (e.g. noble gases) to the hydrogen discharge, since with a fast gate-able ICCD camera operating at 13.56 MHz it is possible to measure even faint emission lines temporally resolved [8].

2 Experiment

The measurements are performed in an asymmetric (one electrode grounded) CCRF discharge at 13.56 MHz in hydrogen with small admixtures of noble gases. The setup is described in

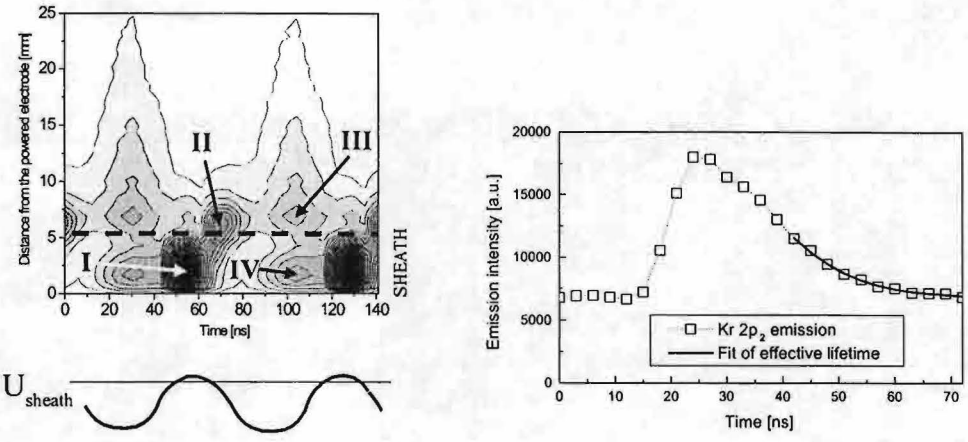

Figure 1: Time and space resolved emission profile of H_α. Sketched is the time development of the sheath voltage [7] (a). Time resolved emission of the Kr $2p_2$ line in front of the powered electrode (b).

detail elsewhere [8]. The flat cooled stainless steel electrodes, 100 mm in diameter, are 25 mm apart. The gas pressure ranges between 20 Pa and 400 Pa at an RF power of 100 W. The discharge axis is imaged onto the entrance slit of a 2m-spectrograph. A fast gateable ICCD-camera samples spectral intervals of about 4.5 nm with a spectral resolution of 0.34 nm/mm and a spatial resolution of about 0.5 mm. Time resolved measurements are possible by locking the gate to a fixed phase position within the RF cycle. The intensities measured over the gate time of 3 ns can be integrated over many RF cycles for this fixed phase setting. A variable delay between the fixed phase and the gate allows one to cover the complete RF cycle.

3 Measurements and results

Understanding the excitation dynamics [6, 7] in a hydrogen CCRF discharge is essential for the measurement of quenching coefficients by time resolved OES. Figure 1 (a) displays the space-time evolution of the H_α line emission. The abscissae comprises two 74 ns RF periods. The transverse axis gives the distance from the powered electrode located at the bottom of the figure. Several emission structures (I-IV) can be distinguished. Structures I and II can be explained on the basis of E-field measurements [7]. Structure I is caused by a field reversal across the space charge sheath - typical for hydrogen RF discharges. Electrons are accelerated towards the powered electrode and induce a strong impact excitation. This excitation in front of the electrode is exploited for the measurement of quenching coefficients, since, when the sheath potential becomes negative again, electrons are pushed out of the sheath towards the plasma bulk. Note that there is no electron impact excitation for the rest of the RF cycle in front of the powered electrode, and the fluorescence decay with the effective lifetime influenced by quenching is observable. Structure II is related to the sheath expansion heating of the electrons moving to the plasma bulk. Structure III results from fast secondary electrons created by ion impact [6]. The secondary electrons are accelerated to energies beyond the maximum of typical excitation cross sections already within a distance shorter than the mean free path for collisions. They can contribute to the excitation only after loosing part of their energy in collisions with the background gas in the plasma bulk where no further acceleration occurs [6]. Structure IV is related to fast hydrogen atoms created at the electrode surface by the impact of hydrogen ions [6]. These fast hydrogen atoms can excite the background gas by heavy particle collisions. Due to the light mass of hydrogen ions they are able to follow the applied electric field with a small delay because of their inertia. Thus, this time dependent ion bombardment of the electrode

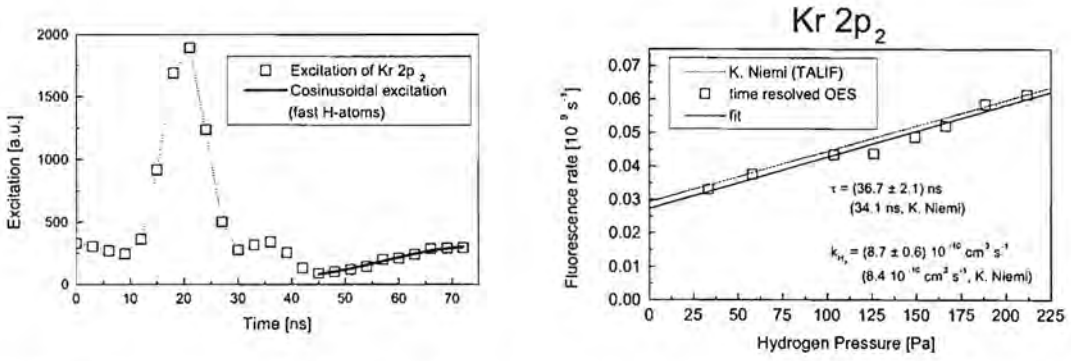

Figure 2: Excitation function of the Kr $2p_2$ line in front of the powered electrode (a). Stern-Volmer-plot for the Kr $2p_2$ line (b).

determines the time dependence of secondary electrons and fast hydrogen atoms related to Structure III and Structure IV, respectively.

In order to determine quenching coefficients for species other than hydrogen, these species have to be admixed in small amounts to the hydrogen discharge. Figure 1 (b) shows the time resolved emission of the Kr $2p_2$ line in front of the powered electrode. After the strong electron impact excitation due to the field reversal, the fluorescence decay with the effective lifetime influenced by quenching with molecular hydrogen can be observed. With the known [4] quenching coefficient and natural lifetime of the Kr $2p_2$ line, the excitation function $E_j(t)$ of the observed level j can be calculated from the emission (proportional to the population density n_j) in the following manner

$$E_j(t) = \frac{dn_j(t)}{dt} + A_j n_j(t) \quad ,$$

because a population by cascading processes is comparable low for this level [9]. The excitation function in figure 2 (a) shows a weak excitation related to heavy particle collisions of fast hydrogen atoms (max. at ≈70 ns), after a strong excitation due to the field reversal (max. at ≈20 ns) and a weak excitation due to the sheath expansion (max. at ≈35 ns). The time dependence of this excitation

$$H_{fast} + X \rightarrow H_{fast} + X^* \quad ,$$

where X represents the observed species, can be described by a sinusoidal function including a delay with respect to the applied voltage.

The time dependence of the population of an excited level including the additional population by heavy particle collisions and cascading processes can, therefore, be described in the interval after electron impact excitation by the following rate equation

$$\frac{dn_j(t)}{dt} = -A_j n_j(t) + A_{ij} n_i(0) \exp(-A_i t) + \frac{U_0}{2}\left[1 + \cos\left(\frac{(t - t_{heavy})2\pi}{T_{RF}}\right)\right] \quad ,$$

where j and i denote the observed level and a higher level responsible for population by cascades, respectively. The effective lifetime can be obtained in this interval by fitting the analytical solution of the rate equation to the measured data.

$$n_j(t) = n_j(0) \exp(-A_j t) + F_{cascade}(t, n_i(0), A_{ij}, A_i, A_j) + F_{heavy}(t, t_{heavy}, U_0, A_j)$$

The parameters $n_i(0)$, A_{ij} and A_i describing the cascade contribution can be determined by taking into account the information of optical measurements of electron impact excitation cross-sections by continuously operating electron guns. Since these measurements are also affected

by cascades, these cascade contributions were investigated in detail (see [9] and references in it).
The measurement of effective decay rates at various hydrogen partial pressures allows to determine the quenching coefficient of the observed level with molecular hydrogen from the slope in a so called Stern-Volmer-plot. The natural lifetime can be determined from the axis intercept at zero pressure. Since the natural lifetime of the observed level is usually known from literature, this result is a good check for measurements of levels with unknown quenching coefficients. Figure 2 (b) is a Stern-Volmer-plot for the Kr $2p_2$ line with known values for the quenching coefficient and natural lifetime. The agreement of the time resolved OES with this TALIF measurement [4] is very good. Quenching coefficients for several emission lines - in particular for helium - were measured for the first time. The natural lifetime is in very good agreement with the literature in all cases. The measurements were performed at a gas temperature slightly above room temperature ($\approx$400 K). The temperature was determined by a time resolved OES measurement of the Fulcher bands of molecular hydrogen [8].

4 Conclusions

The excitation dynamics in a capacitively coupled hydrogen RF discharge was investigated with a fast gateable ICCD camera. This allows a novel time resolved OES technique for the measurement of quenching coefficients based on field reversal excitation for various species (e.g. noble gases) with molecular hydrogen. The technique is independent - in contrast to laser techniques - of the energy gap between the ground state and the observed excited level. It is, therefore, also possible to measure quenching coefficients for helium and neon. Furthermore, the electron impact excitation is independent of optical selection rules. The agreement with known quenching coefficients from TALIF experiments [4, 5] is very good.

5 Acknowledgment

The authors thank C.C. Lin for numerous and fruitful discussions concerning this work, and C. Fischer and J. Leistikow for skillful technical assistance. Support by the Deutsche Forschungsgemeinschaft in the frame of the Sonderforschungsbereich 191 "Grundlagen der Niedertemperaturplasmen" is gratefully acknowledged.

References

[1] V. Schulz-von der Gathen, H.F. Döbele, Plasma Chem. Plasma Process. **16** (1996) 461

[2] H.M. Katsch, A. Tewes, E. Quandt, A. Goehlich, T. Kawetzki, H.F. Döbele, J. Appl. Phys. **88** (2000) 6232

[3] A. Goehlich, T. Kawetzki, H.F. Döbele, J. Chem. Phys. **22** (1998) 9362

[4] K. Niemi, V. Schulz-von der Gathen, H.F. Döbele, Proceedings Hakone VII **1** Greifswald (2000) 199

[5] A. Francis, U. Czarnetzki, H.F. Döbele, N. Sadeghi, Eur. Phys. J. **AP 4** (1998) 239

[6] T. Gans, V. Schulz-von der Gathen, H.F. Döbele, Contr. Plasma Phys., Whype (2000/1)

[7] U. Czarnetzki, D. Luggenhölscher, H.F. Döbele, Plasma Sources Sci. Technol. **8** (1999) 230

[8] T. Gans, V. Schulz-von der Gathen, H.F. Döbele, Plasma Sources Sci. Technol. **10** (2001) 17

[9] J.E. Chilton, M.D. Stewart, Jr., C.C. Lin, Phys. Rev. A **62** (2000) 32714

A new and fast in-situ spectroscopic infrared absorption measurement technique

M.F.A.M. van Hest, A. Klaver, and M.C.M. van de Sanden
Eindhoven University of Technology, Department of Physics,
P.O.Box 513, 5600 MB Eindhoven, The Netherlands

Introduction

Silicon oxide like films are deposited using an expanding thermal plasma (cascaded arc) in combination with HMDSO and oxygen as deposition precursors. These films are deposited at high rate (up to 200 nm/s). In general Fourier transform infrared (FTIR) reflection absorption spectroscopy is a useful tool for *in situ* analysis of the film deposition growth process [1,2]. However this technique is difficult to apply when the film deposition rate is reaching high values (10 to 100 nm/s). At this rate the time to deposit a monolayer of film material is approximately 3 to 30 ms, whereas the typical time to make a single scan by means of FTIR is 0.1 - 1.0 s, which is almost two orders of magnitude longer than the monolayer deposition time. This excludes FTIR spectroscopy as a means to study e.g. initial growth effects. Therefore to study the monolayer or submonolayer growth of films deposited at high deposition rates by means of infrared reflection absorption spectroscopy it is necessary to use another technique instead of FTIR.

To improve the speed of the measuring technique an offer has to be made. FTIR spectroscopy normally measures a broadbanded spectrum (typical for infrared spectroscopy 500 to 7500 cm^{-1}), therefore it is possible to investigate the behaviour of various absorption peaks at the same time. However to gain scanning speed, it is necessary to concentrate on one single absorption peak, i.e. reducing the spectral range.

The Setup

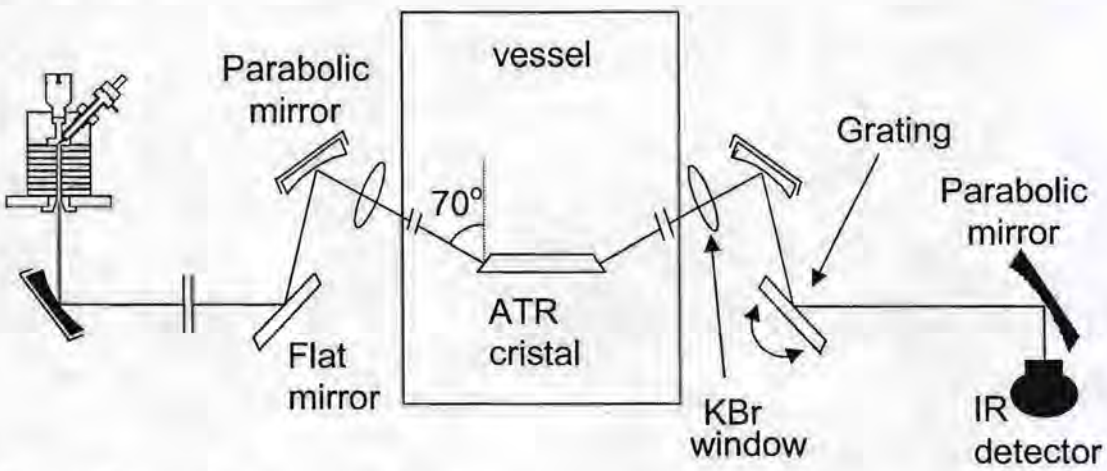

Figure 1: *Overview of the experimental set up.*

In figure 1 an overview of the setup is shown. A cascaded arc light source is used as an infrared light source. This is done because it produces more infrared light in comparison to a glowbar, which is due to the high temperature ($10 - 12 \cdot 10^3$ K) of the gas inside the arc.

The light of the cascaded arc is emitted in a slightly divergent beam (<50 mrad, radiative area: 12 mm^2 [3]); therefore the beam is converted into a parallel beam by means of a 90° off axis parabolic mirror. This parallel beam is guided through a reflection absorption spectroscopy set up. Because the set up is installed on a vacuum vessel, KBr windows have been mounted in the wall of the plasma reactor. After the reflection absorption set up the light is diffracted by a grating, and then focused onto an infrared detector (MCT) by means of another 90° off axis parabolic mirror. Due to the beam properties of the light emitted by the cascaded arc it is fairly easy to align the set up and the losses due to the limited size of the samples and windows used are little.

The heart of the set up is the grating. This grating is mounted on a laser mirror scanner, which is able to scan with a frequency in the range for 50 to 350 Hz. Due to the rotation of the grating and a fixed position of the infrared detector (MCT) a small part of the infrared spectrum will reach the detector. The angle of rotation is limited and therefore the spectral bandwidth with respect to a FTIR spectroscope will be small (200 cm^{-1} at 1000 cm^{-1}). However the time needed for measuring one single scan will be 1.6 to 10 ms, which is of the same order as the time scale needed for the deposition of one monolayer.

To make submonolayer absorbance detectable, single reflection on the surface is ussually not sufficient. Therefore the ATR technique is used [4]. In an ATR crystal the infrared beam has multiple (50 to 60) interactions with the depositing film, leading to a higher measured absorption intensity. To study the deposition process of silicon oxide like films, a ZnSe ATR crystal is used, because of it optical properties, but also because of its resistance to a fluorine containing cleaning plasma. When a silicon ATR crystal would be used, it would be etched in the reactor cleaning process.

Ray trace

At this time of writing the set up is under construction. Ray trace calculations however show that the number of photons collected by the detector will result in a significant signal. In figure 2 the spot size as calculated by a ray trace simulation is shown at different positions along the path of the infrared light beam. The spot size it given at 20 cm from the arc exit, at the initial surface of the ATR crystal and at the surface of the grating.

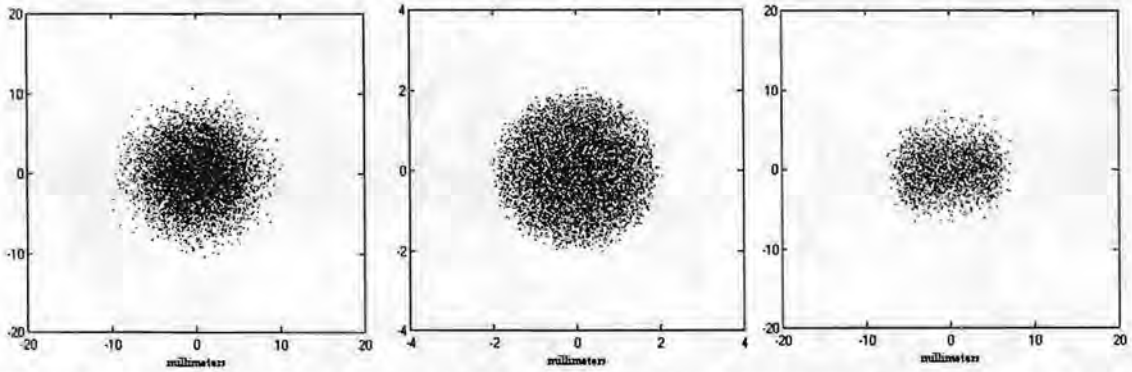

Figure 2: *Spot sizes at different positions in the set up. Spot at 20 cm from the cascaded arc exit (left), spot at the initial surface of the ATR crystal (middle) and the spot at the surface of the grating (right). Obtained by means of ray trace calculations.*

In figure 2 it can be seen that the beam diameter is small (< 20 mm) and that after passing through the ATR crystal the beam is not circular anymore. This is because the surfaces of the ATR crystal are rectangular. At the initial surface of the ATR crystal the diameter of the beam in vertical direction is larger than the ATR crystal dimension (1 mm) and as a result of that only a part of the light is transmitted by the ATR crystal.

When all optical components are taken into account, approximately 40 % of the rays leaving the arc are collected by the detector. This is however without taking into account the reflection losses at the different surfaces. When these are also taken into account then approximately 10 % of the light emitted by the cascaded arc is collected by the detector. This is enough to result in a good signal to noise ratio (expected single scan S/N ≥ 100).

Conclusion

In conclusion it can be said that a theoretical study of the shown set up shows that the set up has high potential and will make it possible to measure submonolayer growth processes at high deposition rates.

References

[1] A. von Keudell, K.G.Y. Letourneur, D.C. Schram and M.C.M. van de Sanden, "*Formation of a-C:H films from hydrocarbon radicals, investigated by means of in situ real time reflection infrared spectroscopy*", Submitted to Journal of Applied Physics

[2] S.M. Han and E.S. Aydil, Journal of Vacuum Science and Technology A, **14**, p2062-70 (1996)

[3] A.T.M. Wilbers, "*A wall stabilized arc as a light source for spectroscopic techniques*", PhD. Thesis, Eindhoven, The Netherlands (1991)

[4] N.J. Harrick, "*Internal reflection spectroscopy*", Chichester, Wiley (1967)

Loss mechanisms of negative oxygen ions in an inductively coupled rf discharge

C. Manthey, H.-M. Katsch and H.-F. Döbele

Institut für Laser- und Plasmaphysik, Universität Essen, 45117 Essen

A high fraction of negative ions (approx. 90 %) is observed in a pulsed oxygen rf discharge (13.56 MHz, 10 Pa). At the end of a discharge pulse of 1 ms duration both the axial and the radial density profiles of the negative ions coincide in the centre of the discharge with the density profile of the positive charge carriers. The dominant loss reactions - in particular of the negative ions - can be found from measurements of the temporal decay of the positive and negative charge carriers in the afterglow. Recombination with positive oxygen ions and collisions with atomic oxygen dominate the decay of the negative ions. These observations are consistent with the determination of the atomic oxygen density and determinations of the ion species (plasma monitor). Probe measurements indicate a production of electrons during this late phase. This can be explained by collisions of negative oxygen ions with atoms, whereby oxygen molecules are formed.

Introduction

Plasmas of electronegative gases can produce a high fraction of negative ions. Energy coupling and loss of charge carriers can be strongly modified by negative ions [1]. As a result the structure of electropositive plasmas can differ from the structure of electropositive plasmas. The significant production mechanism of negative ions (dissociative attachment) is well known for oxygen plasmas, yet the loss mechanisms can differ with the type of the discharge. Results with capacively coupled rf discharges have shown [2] [3] [4], that the following reactions play the dominant role for the destruction of negative ions in these discharges:

$$O^- + O \rightarrow O + e^-$$
$$O^- + O_2(a^1\Delta_g) \rightarrow O_3 + e^-$$

Since the charge carrier density in a inductively coupled discharge is expected to be higher by two orders of magnitude, the following reactions have to be taken into account, too:

$$O^- + e^- \rightarrow O + e^- + e^-$$
$$O^- + O_2^+ \rightarrow O_3$$

It is an open question, which one of these loss mechanisms is dominant in an inductive coupled oxygen plasma and which densities of the negative ions appear. It will be shown that these questions can be answered exceptionally well for a pulsed discharge.

Experimental set up and diagnostics

All measurements are done on a GEC reference cell, which is extensively described in the literature [5] [6]. The experiments are performed with a pulsed inductively coupled 13.56 MHz rf plasma at a gas pressure of 10 Pa and a power of 250 W.

A ½ m monochromator is used for emission spectroscopy. The light of the discharge is focussed with a short focus quartz lens into a quartz fibre which leads to the entrance slit of the monochromator. The focusing unit can be ddispleaced in z- and r-direction, so that a two-dimensional spatial resolution can be achieved. The Langmuir probe measurements are done with a commercial probe system (Smart Probe System). The boxcar mode of the system allows time resolved probe measurements. A second uncompensated probe is used for the measurement of the density of the negative ions. Both probes can be displaced in z- and r-directions. The negative ions are destroyed by photodetachment. The produced electrons are detected by the cylindrical probe and are a measure of the density of the negative ions. A Nd:YAG laser system (Quantel YG 571 G) is available for photodetachment. It provides an output energy of 310 mJ at $\lambda = 532$ nm. At a sufficient photon flux of about 160 mJ / cm² [2] all negative ions in the range of the probe can be destroyed (saturation) [7]. A plasma monitor (Balzers PPM 421) is used to detect the plasma ions and their energy distribution by mass spectroscopy.

Measurements and results

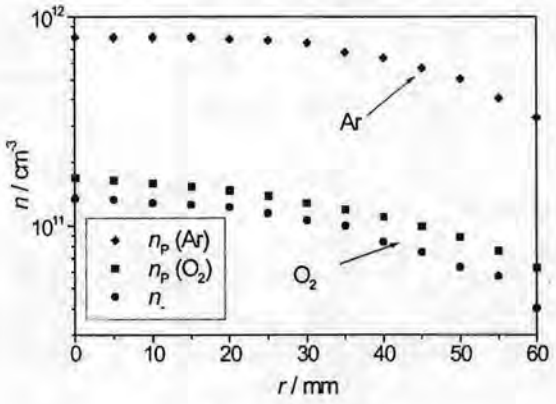

Fig. 1: Radial density profiles

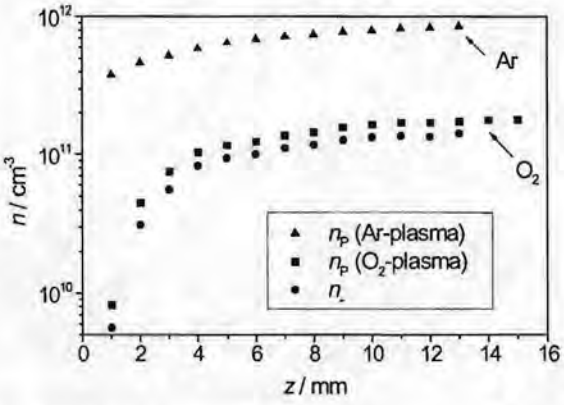

Fig. 2: Axial density profiles (z = 0 mm : lower electrode)

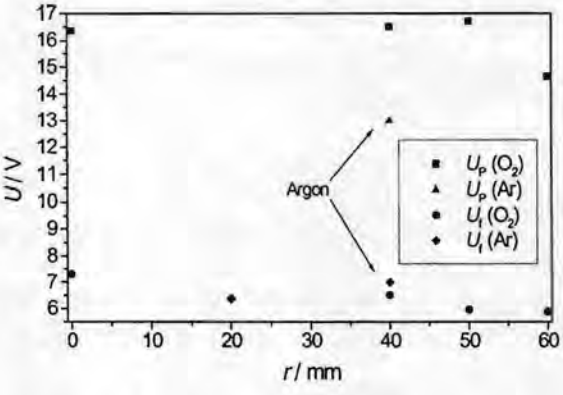

Fig. 1: Radial plasma and floating potentials

In fig. 1 and 2 the measured radial and axial density profiles of oxygen (plasma density n_P and density of the negative ions n_-) and for comparison of argon (plasma density n_P) are shown.

The radial density profiles (fig. 1) show a comparatively flat gradient towards the wall both in argon and in oxygen, whereas the argon discharge shows a significant higher density. The high density of the negative oxygen ions, which nearly coincides with the plasma density, is remarkable. Since the negative ions should drift to the centre of the discharge due to the positive plasma potential U_P (fig. 3), a much higher density of the negative ions is expected in the centre of the discharge. This is obviously not the case. It is, therefore, assumed that the lifetime of the negative ions is too short to reach the centre of the discharge. This is confirmed by calculations of the loss reactions of the negative ions - see below. Computer simulations by Kushner [8] yield a much stronger density gradient of the negative ions towards the centre of the discharge. These predictions could not be confirmed.

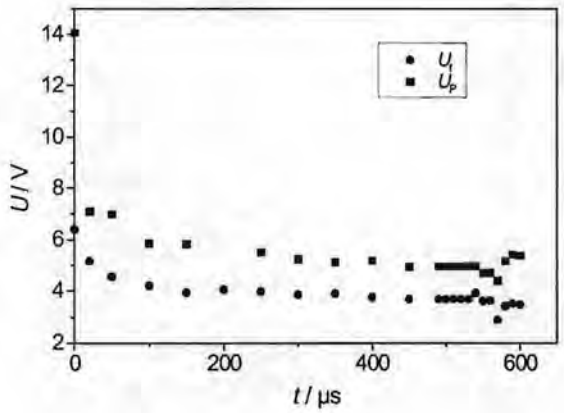

Fig. 2: Plasma and floating potential in the afterglow vs time

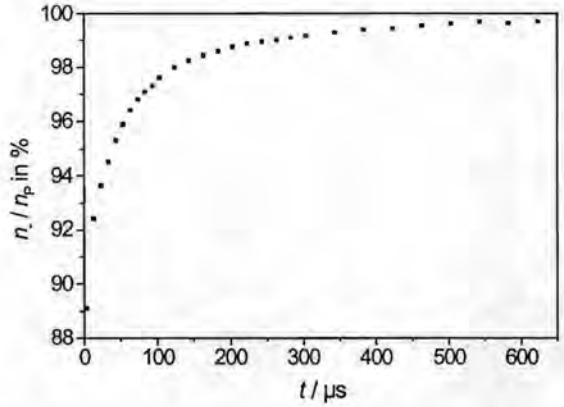

Fig. 3: Ratio of the negative ion density to the plasma density vs time

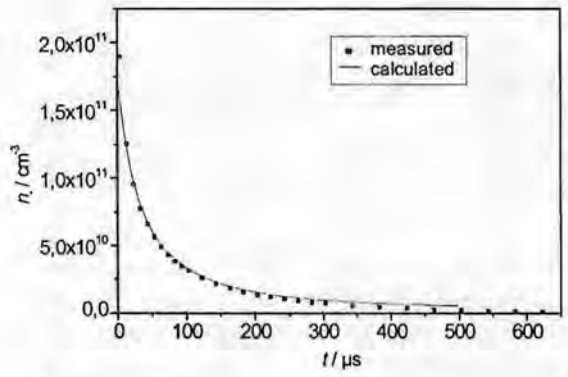

Fig. 4: Measured and calculated densities of the negative ions vs time

The axial profile of the charge carrier densities (fig. 2) shows significant differences between the oxygen and the argon discharges. The density of the argon plasma has a weaker density gradient towards the lower electrode. The differences can be explained by volume recombination of the oxygen plasma charge carriers - see below.

Fig. 4 shows the plasma potential and the floating potential versus time in the post discharge. The plasma potential has a value of +14 V during the discharge and decreases to about +4 V in the post discharge. 500 µs after the switch-off of the plasma an ion-ion-plasma has not been established. The still existing electrons cause a positive plasma potential.

The ratio of the negative ion density to plasma density is shown in fig. 5. 500 µs after the switch-off of the plasma a low amount of electrons still exists in accordance with the positive plasma potential in the post discharge.

Fig. 6 shows the measured and calculated densities of the negative ions versus time in the post discharge. The calculation is based on the assumption that the negative ions are trapped by the positive plasma potential and are being destroyed by the reactions

$$O^- + O_2^+ \rightarrow O_3$$

(rate coefficient $K_{O^- O_2^+} = 1{,}4 \cdot 10^{-7} \frac{cm^3}{s}$) and

$$O^- + O \rightarrow O + O + e^-$$

(rate coefficient $K_{O^- O} = 1.4 \cdot 10^{-10} \frac{cm^3}{s}$).

Consequently, the density of the negative ions, n-(t), is determined by

$$\frac{dn_-}{dt} = -K_{O^- O_2^+} n_- n_+(t) - K_{O^- O} n_- n_0(t)$$

The temporal decay of the density of the atomic oxygen $n_O(t)$ has been determined by emission spectroscopy and the density of atomic oxygen, n_o, at the end of the discharge pulse by actinometry (ratio of $\frac{n_O}{n_O + n_{O_2}} = 2\%$ [9]). The fraction of molecular oxygen ions O_2^+, $\frac{n_{O_2^+}}{n_{O^-} + n_{O_2^+}} = 98\%$, has been measured with the plasma monitor.

The comparison of calculation and experiment shows that the dominant loss process of O^--ions is the recombination with O_2^+-ions during the discharge and in the beginning of the post discharge. The loss reaction with atomic oxygen, which produces additional electrons, is of lower significance. The theoretically expected state of an ion-ion-plasma in early post discharge, 100 µs after the switch-off of the discharge, cannot be observed until 500 µs after the switch-off due to the production of electrons.

This project is supported by the "Deutsche Forschungsgesellschaft" in the frame of SFB 191.

References

[1] I. D. Kaganovich, D. J. Economou, B. N. Ramamurthi, and V. Midha. *Phys. Rev. Lett.*, 84(9) (2000) 1918.

[2] H.-M. Katsch, T. Sturm, E. Quandt and H.F.Döbele. *Plasma Sources Sci. Technol.*, 9 (2000) 323-330.

[3] Ulrich Buddemeier. PhD thesis, Ruhr-Universität Bochum, 1997.

[4] M. Shibata, N. Nobuhiko, and T. J. Makabe. *J. Phys. D:Appl. Phys.*, 30 (1997) 1219.

[5] J. K. Olthoff and K. E. Greenberg. *J. Appl. Phys.*, 100 (1995) 327.

[6] J. K. Olthoff, P. J. Hargis, et al. *Rev. Sci. Instrum.*, 65 (1995) 140.

[7] M. Bacal. *Plasma Sources Sci. Technol.*, 2 (1993) 190.

[8] Peter L. G. Ventzek, Robert G. Hoekstra, and Mark J. Kuschner. *J. Vac. Sci. Technol. B*, 12(1) (1994) 461.

[9] H. M. Katsch, A.Tewes, E.Quandt, A. Goehlich, T. Kawetzki and H. F. Döbele. *J. Appl. Phys.*, 88 (2000) 6232-6238

A triple spectrograph system for low stray light Thomson scattering measurements

Marco van de Sande and Joost van der Mullen
Eindhoven University of Technology
The Netherlands
E-mail: M.J.v.d.Sande@tue.nl / J.J.A.M.v.d.Mullen@phys.tue.nl

Introduction

Thomson scattering is scattering of photons by the electrons in a plasma. From the scattering spectrum, the electron temperature and density (T_e, n_e) of the plasma can be deduced. In the past decade, the development of high power lasers and sensitive detection devices has made Thomson scattering a powerful diagnostic tool for small laboratory plasmas. However, measurements on plasmas close to a plasma applicator or contained in glass (e.g. gas discharge lamps) suffer from an excessive amount of stray light [1]. For plasmas with a low electron density and temperature, this is a serious problem; in fact, stray light often determines the detection limit. This paper discusses the design of a dedicated triple spectrograph detection branch to reduce the disturbing effect of stray light on Thomson scattering spectra.

Stray light redistribution

Because of the high electron velocities in a plasma, Thomson scattered photons are Doppler shifted. The resulting spectrum, reflecting the electron temperature, is a few nanometres wide for common laboratory plasmas. In contrast, stray light is scattered on the surroundings of the plasma and is therefore virtually monochromatic. The scattering spectrum thus consists of a relatively broad Thomson scattering contribution and a narrow stray light contribution in the centre of the spectrum.

If the spectrograph that is used to disperse the scattered radiation were ideal, the shape of the recorded spectrum would be identical to that of the scattering spectrum. However, in practice the narrow stray light peak in the centre of the spectrum is redistributed somewhat by the spectrograph. This redistribution is described by the instrumental profile of the spectrograph (its response to monochromatic light). Because the stray light intensity can be huge compared to the Thomson scattered intensity, the wings of the redistributed stray light peak can obscure a significant part of the Thomson spectrum, thus making the results useless, see Figure 1.

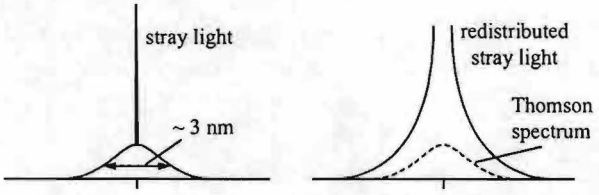

Figure 1: A *true scattering spectrum (left), consisting of a Thomson spectrum and a stray light peak, and the recorded spectrum (right) where the stray light is redistributed by the spectrograph.*

A solution to this problem is to filter the narrow-banded stray light away with a notch filter. The filter must have a very narrow spectral range (~ 1 nm) so as to transmit the major part of the Thomson spectrum. Such narrow a notch filter cannot be obtained commercially, but it can be constructed from a subtractive double spectrograph [2,3].

A subtractive double spectrograph as a notch filter

A subtractive double spectrograph consists of two identical spectrographs, the second cancelling the dispersion of the first. In principle, the spectrum exiting the double spectrograph is thus the same as the spectrum that entered. However, the spectrum that is

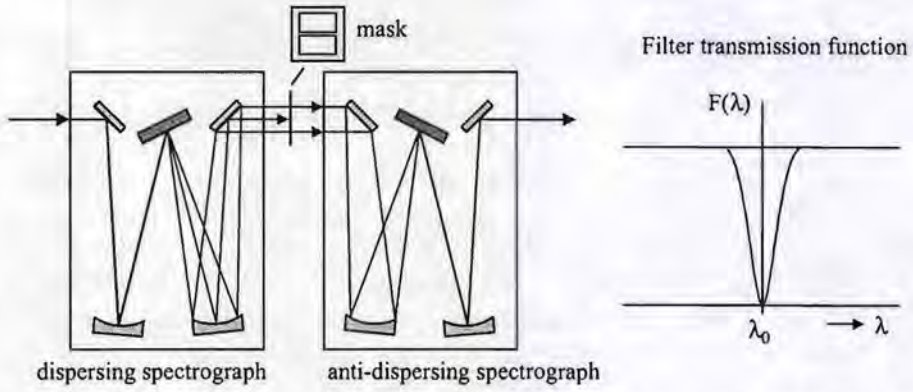

Figure 2: *A double spectrograph as a notch filter. The first spectrograph disperses the light, a mask cuts out part of the spectrum, and the second spectrograph folds the light up into one beam again.*

formed between the two spectrographs can be manipulated by a mask that blocks part of the spectrum. In this way, the subtractive double spectrograph acts as a notch filter, whose width can be chosen by the width of the mask. This principle is sketched in Figure 2.

The shape of the filter profile can be calculated from the instrumental profiles of both spectrographs. For ideal spectrographs, which have a Dirac delta-function instrumental profile, the transmission at wavelength λ_0 is zero and the spectral width of the notch filter can be chosen arbitrarily narrow. However, with an ideal spectrograph the incident spectrum is not redistributed and a notch filter is not necessary. A non-ideal double spectrograph does not block light of wavelength λ_0 entirely, but choosing a wider mask can always lower the transmission at this wavelength. For a better double spectrograph (narrower instrumental profiles), the required mask width for a certain stray light reduction is smaller, resulting in narrower filter profiles. A bandpass $\Delta\lambda_{bp}$ (full width at half maximum of the instrumental profile) on the order of 0.3-0.4 nm can be shown to be small enough for sufficient stray light reduction (factor 10^6) and a sufficiently narrow filter profile (~ 1 nm) [4].

Design of a triple spectrograph system

In order to use a subtractive double spectrograph efficiently with the 'primary' spectrograph used to disperse the scattering spectrum, we decided to design a complete, dedicated detection branch for scattering experiments.

A spectrograph consists of a grating and two imaging elements that collimate the incident light for the grating and focus the diffracted light onto the spectrograph's exit plane [5]. The design parameters of a spectrograph, shown in Figure 3, are the focal length f and size ϕ of the optics, the length a of the collimated beam, the grating constant n, and the angle of deflection by the grating, δ, which is the result of the angle of incidence α and the angle of reflection β. In addition, the imaging elements can be chosen to be either lenses or mirrors.

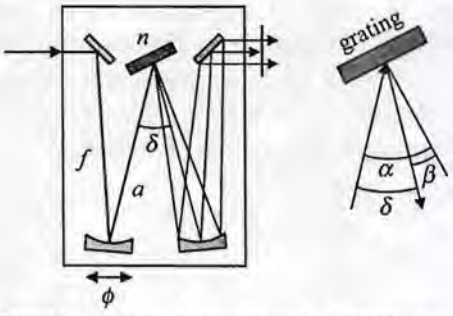

Figure 3: *design parameters of a spectrograph.*

The choice of the design parameters determines single spectrograph properties as the dispersive power d, the bandpass or width of the instrumental profile $\Delta\lambda_{bp}$, and the opening angle of the system $\Delta\Omega$. The dispersion must be such that the iCCD detector that is used can cover the entire Thomson spectrum; a dispersion of one to two mm/nm is satisfactory. As discussed above, the required bandpass is $\Delta\lambda_{bp}\approx 0.3$ nm or better.

The opening angle must be as large as possible to collect as much light as possible, but at least $f/10$ (0.008 sr).

Mirrors are the common imaging element in most spectrographs since they do not exhibit chromatic aberration and can thus be used for a wide range of wavelengths. However, since mirrors have to be used off-axis, they suffer from astigmatism, i.e. the effect that the focal planes of optimal spatial resolution and optimal spectral resolution do not coincide. For our application, spatial resolution is strongly desirable and spectral resolution is indispensable for high stray light reduction. Therefore, we chose to use lenses, which can be used (almost) on-axis and thus suffer less from astigmatism. Lenses do suffer from chromatic aberration, but the spectral range we are interested in is only a few nanometres wide. A more serious problem is spherical aberration. Achromatic doublet lenses, which are also corrected for spherical aberrations and astigmatism, eliminate this problem sufficiently. The design discussed in this work uses achromatic doublet lenses as imaging elements.

The grating constant n was chosen to be 1800 grooves/mm. This results in a large dispersion, yielding a narrow instrumental profile. The deflection angle of the spectrograph was taken δ=30°, being a convenient angle for a compact setup. The corresponding angles of incidence and reflection for light of 532 nm are α=15° and β=45°. In order to achieve a sufficiently small bandpass and sufficiently large dispersion, the focal length of the lenses was taken f=600 mm. Their size is ϕ=95 mm, which is about the maximum size that can be used before aberrations start playing a significant role. The single spectrograph properties that result from these values of the design parameters are listed in Table 1 [6,7]. Because of the absence of severe image aberrations, the bandpass $\Delta\lambda_{bp}$ is mainly determined by the entrance slit width s, which must be broader than the width of the laser beam used in the Thomson scattering experiment. The calculated bandpass is based on an entrance slit width of s=250 μm.

Table 1: *The chosen design parameters and resulting single spectrograph properties.*

Design parameters	Single spectrograph properties
f = 600 mm	d = 1.54 mm/nm
ϕ = 95 mm	$\Delta\lambda_{bp}$ = 0.22 nm
a = 600 mm	$\Delta\Omega$ = 0.0198 sr (f/6.3)
n = 1800 mm^{-1}	
α = 15°	
β = 45°	
s = 250 μm	

Ray-trace simulations were performed to verify the calculated characteristics of the spectrograph system and to determine its spatial and spectral resolution. The spatial resolution ranges from 35 to 100 μm, depending on the position along the entrance slit and the wavelength of the incident light; the optimal condition (on-axis use of all lenses) is light of wavelength λ=532 nm at the centre of the entrance slit. The spectral resolution equals the calculated bandpass (0.22 nm) and is in all cases determined by the entrance slit width.

The final design of the triple spectrograph system is shown in Figure 4. The entrance slit is horizontal (parallel to the laser beam) for simultaneous measurements at different positions in the plasma. In order to keep the optical axis of the system horizontal as well, a 90° image rotator, consisting of three flat mirrors, is used. One additional flat mirror in front of the mask compacts the system. The iCCD camera is placed on a stand that can be moved to the mask position. In this way, it is possible to choose between a triple spectrograph system for efficient stray light suppression and a single spectrograph system for a higher transmission, which results in a lower detection limit if stray light is not the main problem.

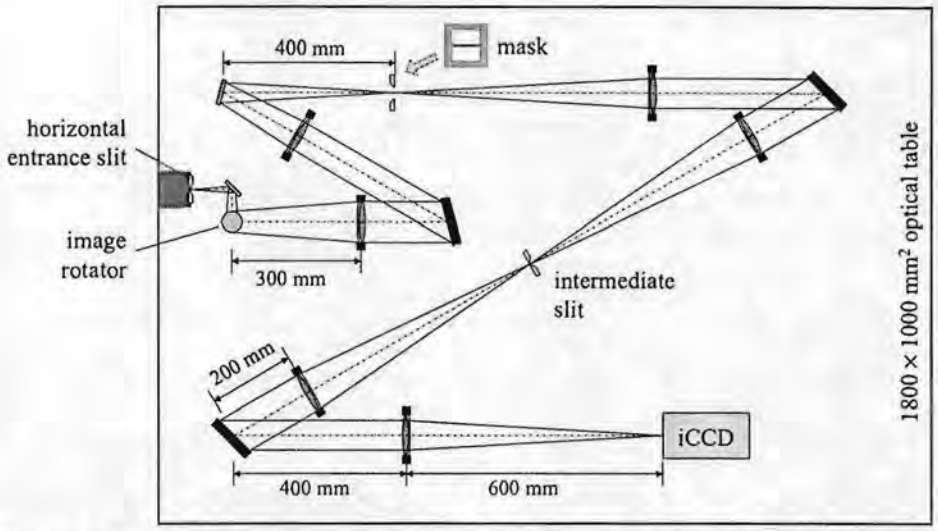

Figure 4: *The final triple spectrograph design. The horizontal entrance slit, parallel to the laser beam, and image rotator enable simultaneous measurements at multiple positions in the plasma. Walls in the system (not shown in the figure) prevent unwanted reflections from propagating through the system.*

Conclusions

Thomson scattering experiments on low electron density plasmas close to a plasma applicator or contained in glass suffer from a huge amount of stray light. Combined with the non-ideality of the spectrograph that disperses the scattering spectrum, this can be a severe restriction to the detection limit. In order to get around this problem, a narrow notch filter can be used to filter the stray light. In this work, a dedicated triple spectrograph system with a notch filter in the form of a subtractive double spectrograph was designed. An image rotator is used to allow for spatial resolution. The triple spectrograph system reduces the effect of stray light by six orders of magnitude compared to a detection system based on a single spectrograph. The opening angle of the system is *f*/6.3 (0.0198 sr) and its transmission is 15%. The spatial and spectral resolutions are estimated from ray-trace simulations at about 100 μm and 0.22 nm respectively.

References

[1] L.P.Bakker, J.M. Freriks, F.J. de Hoog, and G.M.W. Kroesen. *Thomson scattering using an atomic notch filter.* Rev.Sci.Inst. **71**(5), 2007 (2000)

[2] A. Kono and K. Nakatani. *Efficient multichannel Thomson scattering measurement system for diagnostics of low-temperature plasmas.* Rev.Sci.Inst. **71**(7), 2716 (2000)

[3] H. Röhr. *Laser light scattering in presence of very high stray light level.* Internal report IPP 1/157, Max-Planck-Institut für Plasmaphysik (1976)

[4] Y. Barrel. *A double spectrograph system for stray light reduction in a Thomson scattering setup.* Internal report VDF-NT 00-05. Eindhoven University of Technology (2000)

[5] J.F. James and R.S. Sternberg. *The design of optical spectrometers.* Chapman and Hall Ltd. London (1969)

[6] Christopher Palmer and Erwin Loewen. *Diffraction Grating Handbook.* Richardson Grating Laboratory, New York (2000)

[7] J.M. Lerner and A. Thevenon. *The optics of spectroscopy.* `http://www.isainc.com/systems/theory/oos/oos.htm`

Voltage, current and electron density measurements in an air radio-frequency plasma.

M. Sorokine, D. Hayashi, W.W. Stoffels, G.M.W. Kroesen
Department of Physics, Eindhoven University of Technology, P.O. Box, 5600 MB Eindhoven, The Netherlands

A study of a low-pressure (50-800 mTorr) air discharge is presented. Measurements of the electron densities in a 13.56 MHz capacitively coupled plasma are performed by means of a microwave resonance technique. Besides, some power input characteristics were determined by means of Plasma Impedance Monitor device (PIM).

I. INTRODUCTION

Various RF discharges are widely used in different kinds of production technologies. Still, questions of quality improvement often arise. That leads companies to look for a way of improving and optimising production processes. This cannot be done without appropriate diagnostic techniques.

Power input control is really alluring because of its simplicity in implementation. In most experiments the main characteristic for the RF discharge is its consumed power. Nevertheless, in most theoretical works, the rf voltage is taken to be constant, which makes comparisons between experimental and theoretical difficult. Using the technique mentioned above it is possible to get the desired results.

Microwave methods to measure electron density are advantageous due to its time resolution possibilities. Moreover, it is also a non-intrusive in situ measurement technique.

In this work a low-pressure radio-frequency (RF) air discharge is treated. Both methods are used for plasma diagnostics, and the most interesting results are presented.

II. EXPERIMENT

The experiment has been carried out with a 13.56 MHz capacitively coupled air plasma, confined in an aluminium cylinder cavity with two symmetrical slits. A schematic drawing of the plasma chamber is shown on Fig. 1. The dimensions are: diameter – 120mm, height – 37mm, slit width – 10mm, distance between antennas – 90mm, the lower power electrode diameter – 107mm.

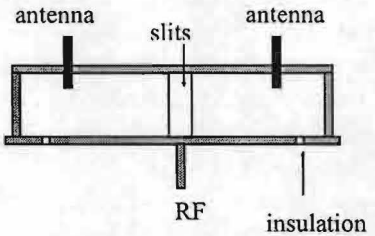

Fig. 1 Cylindrical microwave cavity

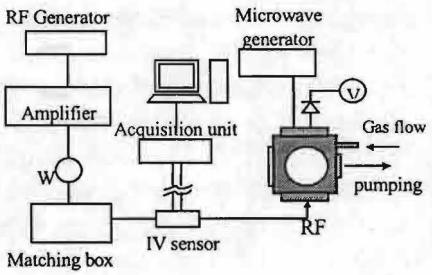

Fig. 2 Experimental setup

Power for the discharge is supplied by an RF generator, followed by an amplifier and matching network to optimise the power dissipation in the plasma. Feed gas is air. The pressure in the chamber is measured by Balzers pressure meter.

III. DIAGNOSTICS

A schematic drawing of the measurements is shown on Fig. 2.

As a rule, the most common and at the same time the easiest way to control RF plasma lies through monitoring of its power consumption. Using a Plasma Impedance Monitor (PIM) device by Scientific Systems we obtain information on the amplitudes of voltage and current for the driving frequency and first four harmonics, as well as on the value of phase shift between them. Along with that, power and impedance are calculated.

The IV sensor was designed to overcome some of the problems associated with conventional methods of sensing the RF current and voltage; it contains a unique current sensing loop and a conventional voltage pickup sensor. The design of PIM IV sensor and the sensor location are shown on Fig. 3 and Fig. 4 [1].

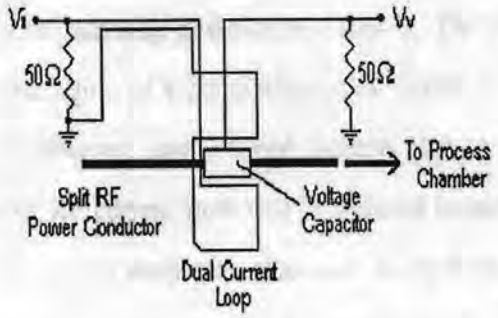

Fig 3 – Schematic of PIM IV Sensor (reproduced from [1])

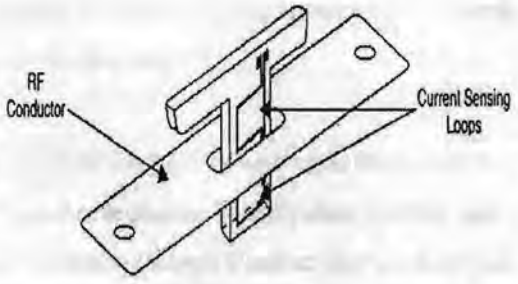

Fig. 4 – RF Power Conductor and Sensor PCB Location (reproduced from [1])

Although PIM provides us with real time measurements, all of the PIM data are being saved on the computer and can be recalled anytime.

In order to measure electron density, a microwave resonance method has been used in which rf electrodes, generating the plasma, simultaneously serve as a microwave-cavity. For this purpose a low power microwave signal is coupled into the plasma cavity by means of an antenna, exiting numerous modes. For our needs we use TM_{110} and TM_{210} modes, with frequencies ~3GHz and ~4Ghz respectively. The transmission of the cavity is picked up by another antenna and its value is being monitored with a digital voltmeter. The resonance frequency of the cavity, which depends on the number of free electrons within, is determined by tuning the microwave generator to maximum transmission. From the shift $\Delta f = f - f_0$ of the resonant frequency f with respect to its value in vacuum (f_0) the microwave field averaged electron density (n_{e0}) is deduced [2]:

$$n_{e0} = \frac{2\Delta f m_e \varepsilon_0 (2\pi f)^2}{f_0 e^2} \qquad (1)$$

with ε_0 the vacuum electric permittivity, and m_e and e, respectively, the electronic mass and charge. This method does not provide any spatial resolution as n_{e0} is merely a space averaged density weight with the square of the field strength (E^2),

$$n_{e0} = \frac{\int_{cavity} n_e(\vec{x}) E(\vec{x})^2 d\vec{x}}{\int_{cavity} E(\vec{x})^2 d\vec{x}} \qquad (2)$$

It is not always obvious which frequency to take for the measurements. Several spectrum peaks were examined during preliminary experiments.

Fig. 5 shows results for 4 of total 7 observed modes. Those that are not presented showed no change in frequency within the error of the measurements.

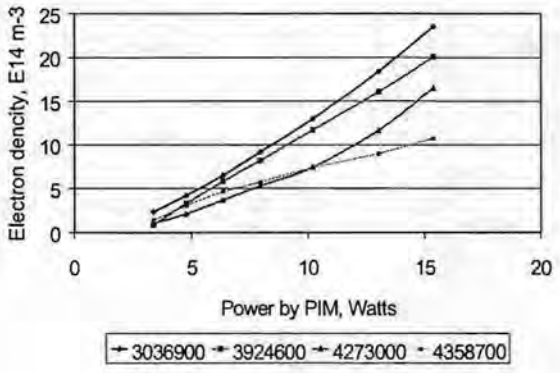

Fig. 5 Preliminary results

Frequencies of the cavity modes were calculated beforehand. As it was expected, the two series (3036900 kHz and 3924600 kHz – the two upper lines), that were believed to correspond to TM_{110} and TM_{210} modes, showed the best agreement between each other. They were also the best distinguishable in the cavity spectrum observed and had the most appropriate frequency for the calculated modes. So, these two modes were chosen for the experiments, presented in this work.

IV. RESULTS AND DISCUSSION

Two measurements series have been carried out: the 1st - Power variation, with keeping the pressure constant (0.10 ± 0.005 Torr), and the 2nd - Pressure variation with constant amplitude of fundamental voltage harmonic (100 Volts).

For every microwave measurement a double PIM measurement has been performed – directly before and right after it. A half of the difference between values showed by PIM at the beginning and at the end was taken as the measurement error. As an error of the pressure measurements a systematic error was taken. During preliminary measurements it was made sure that the presence of the microwave field had no measurable influence on the PIM performance.

As a result, the following graphs can be presented. In Fig. 6 and 7 calculated electrons density values with error bars are presented. Error in each case was estimated based on the accuracy of determination of the mode frequency. The vacuum frequency for TM_{110} mode was taken so, that at the first point in Fig. 6 both modes gave us one and the same value, given by the TM_{210} mode, that is about 10^{13} m^{-3}.

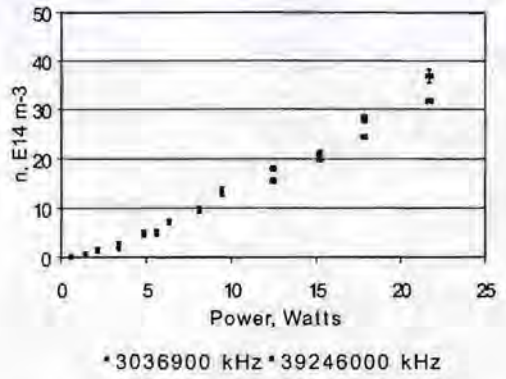

Fig. 6 Electron Density in air discharge. Fixed pressure O.10 Torr.

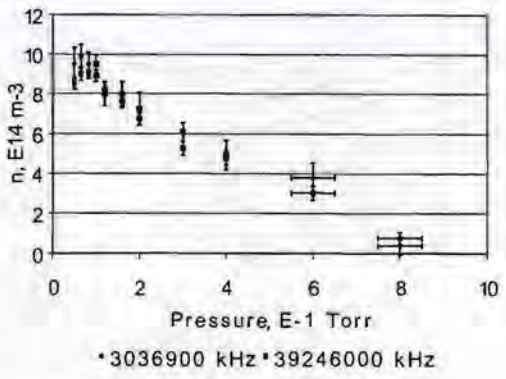

Fig. 7 Electron Density in air discharge. Fixed Voltage (100 Volts)

It was noticed that by changing the discharge pressure from 0.6 to 0.8 Torr the discharged seemed to come to another state.

Also, it was clearly seen from the graphs for the phase difference between harmonics of current and voltage (not presented in the abstract), that in mentioned above pressure range the value for the first and, especially, for the third harmonics experiences dramatic changes. The idea of monitoring certain processes through the study of the phase behaviour is not a new one [1] and can be very promising in commercial production environment.

On the poster the other data will also be available.

V. CONCLUSION

The electron densities in a low-pressure (50 – 800 mTorr) air RF discharge have been measured. The electron density is in the range of $10^{13} - 4 \cdot 10^{15}$ m^{-3}. Various plasma parameter dependences for different conditions of experiment have been presented. It has been noticed that the behaviour of the first harmonics of current, voltage, and power is pretty much the same as the behaviour of the electron density.

VI. ACKNOWLEDGEMENT

This work is supported by the European Commission under contract No. NNE5-1999-0004 H-alpha solar. The research of W.W. Stoffels has been made possible by a fellowship from the Royal Netherlands Academy of Arts and Sciences (KNAW).

---

[1] Kieran Dobbyn, M.Sc. thesis, "Design and Application of a Plasma Monitor for RF Plasma Diagnostics." Dublin City University, 2000.

[2] E. Stoffels, W.W. Stoffels, D. Vender, M. Kando, G.M.W. Kroesen, and F.J. de Hoog. Phys. Rev. **51**, 2425-2435 (1995)

Time and space dependent xenon ($5p^5$ 6s) excited states density in a macroscopic display panel cell*

Th. Callegari[1], R. Ganter[1], J.P Boeuf[1] and N. Sadeghi[2],

[1] *Centre de Physique des Plasmas et de leurs Applications de Toulouse, CPAT, Bat IIIR2, Université Paul Sabatier, 31062 Toulouse Cedex 4, France.*
[2] *Laboratoire de Spectrométrie Physique, Université Joseph Fourier (UMR C5588) BP 87 - 38402 St. Martin d'Hères cedex, France.*

Abstract

Absorption spectroscopy was used to obtain the space and time dependent density of xenon atoms in both metastable $Xe^*(^3P_2)$ and resonant $Xe^*(^3P_1)$ states in a macroscopic PDP cell [Ca-1]. Discharges in Ne-Xe10% mixture for a 5 torr pressure were investigated. According to the amplitude and repetition rate of the applied voltage, the maximum density, occuring always immediately in the end of the discharge pulse, was between 3.10^{16} and 2.10^{17} atoms.m^{-3} for $Xe^*(^3P_2)$ and 1.10^{16} et $1.1\ 10^{17}$ atoms.m^{-3} for $Xe^*(^3P_1)$ atoms. The decay time of the density was about 0.4 ms for metastable and 8 µs for resonant atoms, respectively. We observe a maximum density of the metastable atoms in the end of the cathode sheath, and another maximum close to the anode. Losses of $Xe^*(^3P_2)$ atoms at 5 torr are due to diffusion phenomenom.

I. Introduction

Plasma Display Panels (PDP) are now the best candidate for large area, wall hanging, television screens. But, their luminous efficiency and contrast ratio have to be improved. This needs a better understanding of the discharge medium and of the kinetics of excited species responsible for UV emission, then transformed by luminofores to the three fundamental colors. To simplify diagnostics, a macroscopic PDP cell was built [Ca-1]. In this cell, a scaling factor of 100 was applied to both cell dimensions (d~ 1 cm, instead of ~ 100 µm in the real cell) and pressure (p~ 5 Torr, instead of 500 Torr) in order to conserve the same (p*d). After electrics measurments and CCD imaging [Ca-1], we present in this paper absorption spectroscopy measurments. In the first part, we describe the experimental setup. In the second part, we show time and space evolution of metastables atoms density (instant and place of the maximum, decay time).

II. Experimental setup

Absorption spectroscopy, with a home-made single-mode Littrow type external-cavity tunable diode laser, was used to obtain the space and time dependent density of xenon atoms in both metastable $Xe^*(^3P_2)$ and resonant $Xe^*(^3P_1)$ states by tuning the laser wavelength to 823.1 and 828 nm, respectively. The laser power was a few mW and the fine frequency tuning (~10 GHz) was obtained by angular tuning of the grating with a piezo-electric device. The laser bandwidth (< 1 MHz) is much smaller than the Doppler width of the absorption line. To avoid optical saturation, the intensity of the probe beam crossing the cell was reduced to a few µW/cm^2. The line integrated absorption signal is related to the absorbing atoms density, N, according to:

$$\int \ln \frac{I_0}{I(\nu)} d\nu = S = \frac{e^2}{4\varepsilon_0 mc} \cdot f \cdot \int N(x) \cdot dx \qquad (1)$$

where $I(\nu)$ and I_0 are the transmitted laser intensity with and without absorbing atoms and f is the oscillator strength of the line. For a single absorption line, the pick absorption signal at the line center is given by:

$$\ln\frac{I_0}{I(\nu_0)} = \frac{e^2\lambda_0}{4\varepsilon_0 mc}\cdot\sqrt{\frac{M}{2\pi kT}}\cdot f\cdot\int N(x)\cdot dx \qquad (2)$$

where M≅131 is the Xe mass and T=300 K is the gas temperature. f= 0.29 and 0.12 for 823.1 and 828 nm lines, respectively [Sa-1]. Eq. (2) provides the line of sight integrated atom density along the laser beam trajectory. The absolute density can then be deduced if the density profile is known. Natural xenon has 7 stable isotopes. Due to the isotopic shifts and hyperfine structures for odd isotopes (129 and 131) both 823.1 and 828 nm lines have complex structures. In our experiments, the laser frequency was set at the pick of the absorption lines. After having analyzed line structures, using sub-Doppler spectroscopy [Sa-2], we found that for both lines a correction factor of 0.50 must be applied to Eq. (2). The laser beam crosses the cell parallel to the electrodes at variable distances from vertical electrode, y and the center of this electrode, z. The signal $I(\nu_0)$ is detected with a photomultiplier tube and recorded with a digital osciolcope to obtain the time variation of the absorbing atoms density. To improve the signal to noise ratio, the signal was averaged over 256 discharge pulses.

III. Space-and-time evolution of both metastables and resonants densities

1. Studied discharge area

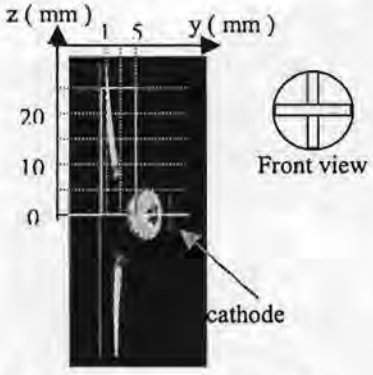

Figure 1 : Side view of the matrix discharge [Ca-1].

The side View of the cell is shown in figure (1) for the matrix structure [Ca-1]. The anode and the cathode, which are 90 mm long and 8 mm wide, are located on the left and right sides, respectively. The distance between the electrodes (gap) is 1 cm. The laser beam crosses the cell at z= 0 to 25 mm and y= 1 to 9 mm. The space-and-time shown on figure (3a) corresponds to the framed area (1≥ y ≥5 mm; 0≥ z ≥25 mm) of figure (1). For each position in this area, the initial plasma thickness, which is necessary in order to calcul the density , was estimated from the front view emission intensity of the discharge.

2. Space-and-time evolution of the metastable state

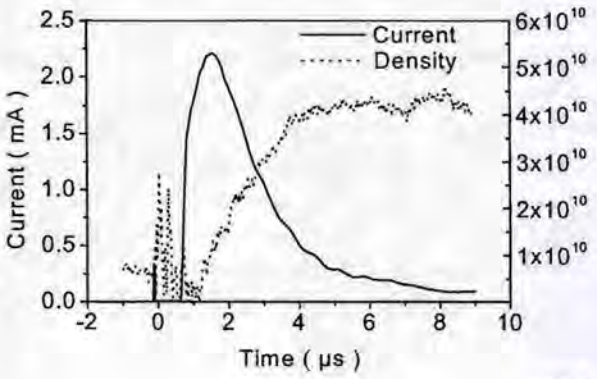

Figure 2 : Current and $Xe^*(^3P_2)$ density (cm^{-3}) for a 5 Torr, Ne-Xe10% mixture, with a sustaining voltage of 260 V and 100 Hz rep. rate. The density corresponds to the maximum point in the cell at 1 mm from the cathode (y = 1 and z = 0).

In figure (2) are plotted the discharge current and the maximum of evolution of the metastables with the time, for a sustaining voltage of 260V and a frequency of 100 Hz. Measurement of the densities were performed at the positon y = 1 mm, z = 0 mm, in the case of a vertical cathode.

We note that the peak of the density is reached when the current is zero. As long as the electric field is sufficient to accelerate the electrons, the density keeps increasing, there is more creations than losses. At the end of the discharge pulse, the voltage accross the gap vanishes, the electrons have no more energy to excite xenon. Metastables atoms diffuse toward the walls as we can see on figures (3a) and (3b). We can note that the duration of the current pulse is in order of 6 μs at 5 torr, wich would correspond to 60 ns at 500 torr in real PDP conditions.

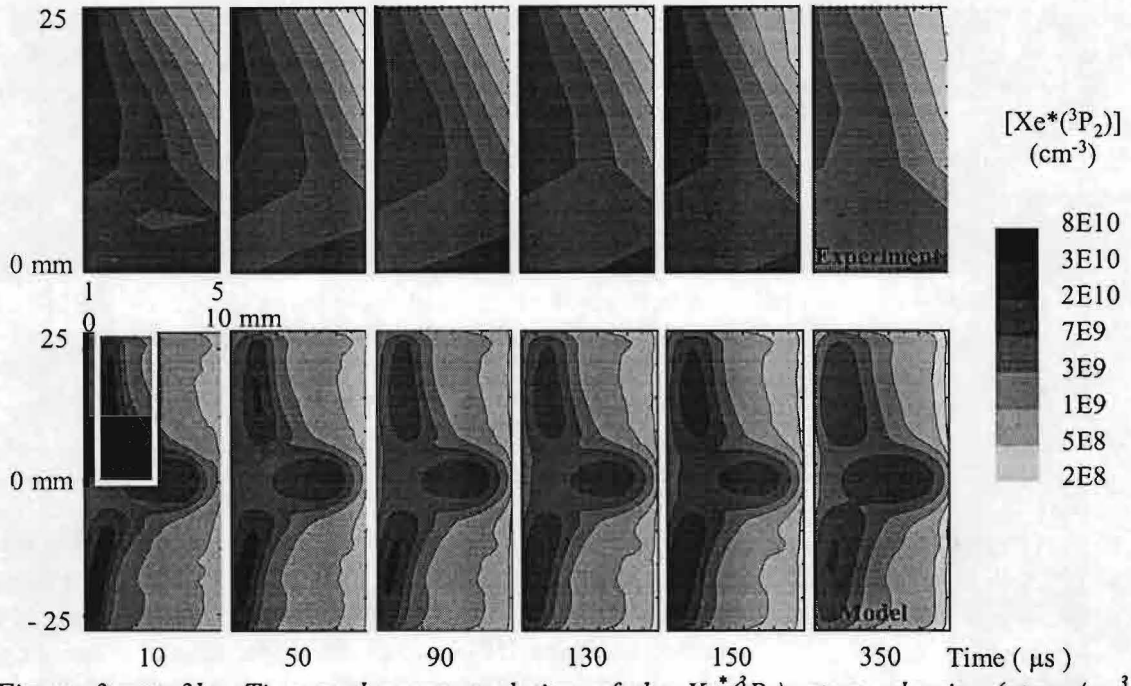

Figure 3a et 3b : Time and space evolution of the $Xe^*(^3P_2)$ atoms density (atoms/cm^3) measured by absorption spectroscopy (3a, top figures), and calculated with a simple 3D diffusion model (3b, botton figures) with a diffusion coefficient of 86.2 cm^2.torr.s^{-1}[Ta-1]. Frequency and voltage of the sustaining pulse were 260 V and 100 Hz. Plasma thickness used in the calcul of the density was deduced from CCD imaging (front view) [Ca-1]. Conditions were Ne-Xe10%, 5 torr pressure, 1 cm gap.

Figure (3a) shows the time variation of the metastable atoms density, between 0 and 350 μs after the beginning of the discharge pulse. Images of figures (3a) correpond to the 4x25 mm^2 frame on figures (1) and (3b). Figure (3b) shows the evolution of the metastables atoms density calculated by a simple 3D diffusion model in a 10x50 mm^2 frame. In both cases, frequency and voltage of the sustaining pulse were 100 Hz and 260 V respectively.

As we can see, there is a maximum in the density in front of the anode, at time10 μs. This maximum value, about 1.3 10^{11} atoms.cm^{-3}, is quite similar to the maximum density observed at the end of the cathode sheath. This maximum in the anode side is due to the electric field parallel to the surface wich is induced by the charging of the dielectric surface [Pu-1]. This field is large enought to heat the electrons to energy above xenon excitation threshold (~ 10 eV), but not above neon excitation threshold (~ 20 eV) [Ga-1]. We can conclude that the anode region is very efficient for VUV production.

In the afterglow, the $Xe^*(^3P_2)$ density decreases by diffusion, the spatial distribution remaining almost the same during this time. The decay time, ranges between 0.4 and 0.6 ms depending on experimental conditions and observation position.

The decay time of the $Xe^*(^3P_1)$ resonant states density (see figure 4b) ranges between 8 and 12 µs.

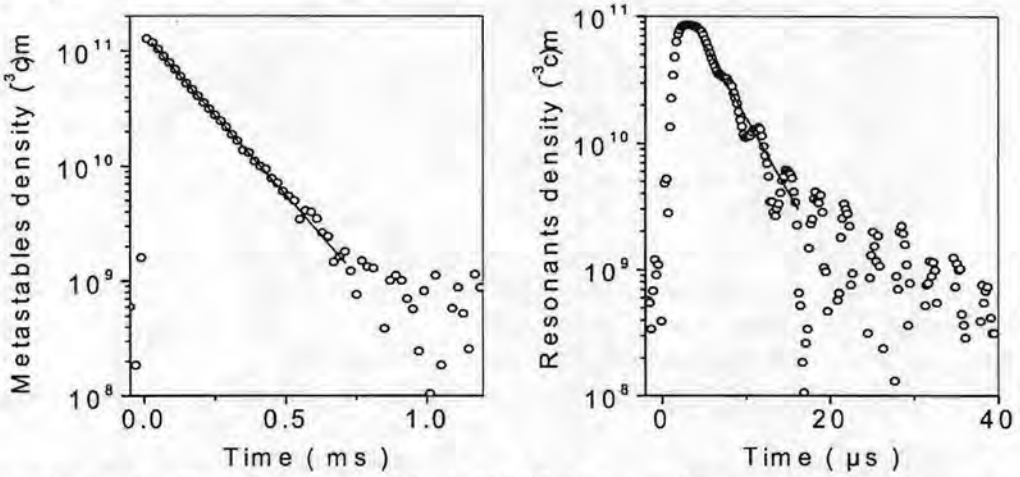

Figure 4a et 4b : Time evolution of both $Xe^*(^3P_2)$ metastable and $Xe^*(^3P_1)$ resonant states densities. Measurements were performed at position y = 1 mm and z = 20 mm. Applied voltage was 260 V and frequency, 100 Hz.

IV. Conclusion

Measurements by absorption spectroscopy on a macroscopic PDP cell (5 torr pressure, 1 cm gap, Ne-Xe10% mixture) permitted us to determine the maximum densities of both $Xe^*(^3P_2)$ and $Xe^*(^3P)$ states, for different frequencies and voltages of the sustaining pulse. The peak density for resonant state is in the range of 1. 10^{16} to 1.1 10^{17} atoms.m^{-3}, and for metastable state in the range of 3.10^{16} and 2. 10^{17} atoms.m^{-3}. This maximum occures at the end of the cathode sheath at 4 µs after the current peack. A second maximum, with quite the same intensity, occures in front of the anode. Decay time of the density is about 0.4 ms for $Xe^*(^3P_2)$, and 8 µs for $Xe^*(^3P_1)$ atoms. Accumulation of metastable occures for frequency around 1 kHz according to the conditions. Measurments on a real PDP cell will be performed soon.

* Work done within the RMNT (Réseau Micro Nano Technologies) program in collaboration with Thomson Plasma.

[Ca-1] Th. Callegari, R. Ganter, and J.P. Boeuf, "Diagnostics and modelling of plasma display panel cell," Journal of Applied Physics **88** (7), 3905-3913 (2000).
[Ga-1] R. Ganter, T. Callegari, B. Caillier, J.P. Boeuf, XVth Europhysics Conference on Atomic and Molecular Physics of Ionized Gases, **24F**, August 2000
[Pu-1] C. Punset, S. Cany, J.P. Boeuf, J. Appl. Phys., **86**, 124 (1999)
[Ta-1] K. Tachibana & al., Jpn. J. Appl. Phys, **33**, 6716-6717 (1994)
[Sa-1] J. Sabbagh and N. Sadeghi, "Experimental transition probabilities of some Xe(I) lines", J. Quant. Spectro. & Radiative Transfers. **17** , 297 (1977).
[Sa-2] N. Sadeghi, *To be published.*

Electric field strength in a Xe-Ne glow discharge

B.Visser, D. Hayashi*, G.M.W. Kroesen
Eindhoven University of Technology, Department of Applied Physics,
P.O. box 513, 5600 MB Eindhoven, The Netherlands
** Philips Research Laboratories, Germany*

Introduction

Many applications of plasma physics are related to light generation. The applications range from TL-tubes until the latest flat displays. The size of discharges is decreasing further and further. At this moment the typical dimensions of a plasma display panel cell are in the order of 100 μm. A model has been developed in the plasma group at Eindhoven to describe these microdischarges [1]. To verify and further improve the model experimental data is needed. Therefore diagnostic tools for this kind of discharge are developed.

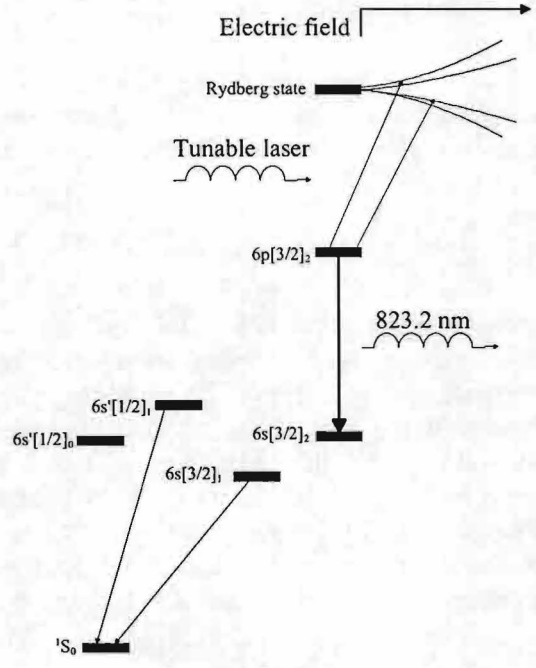

Figure 1: *Schematic overview of the xenon transitions used.*

A laser absorption technique has already been developed by Tachibana et. al. [2]. The diagnostic gives a good insight of the temporal and spatial evolution of metastable xenon in this kind of microdischarge. The diagnostic discussed in this paper tries to use these metastables to measure the electric field. In figure 1 the scheme is depicted. In this scheme the two metastable levels, two resonant levels and the emission dip spectroscopy (e-dip) scheme is illustrated. The e-dip spectroscopy is based on the scheme used e.g. by Döbele et. al. [3] to measure electric field strengths in hydrogen and helium discharges. Xenon is a rare atom and has a closed shell structure in the ground state described in Russell-Saunders notation as $^1S_0$. Exciting one electron out of this structure will leave an inner ion core. This core can have two possible configurations according to Russell-Saunders coupling, $^2P_{3/2}$ or the $^2P_{1/2}$ configuration. Racah notation is used to describe the excited levels. $6s[3/2]_2$ says that the outer electron is excited to the 6s shell. There is no prime so the inner core has $^2P_{3/2}$ configuration. The angular momentum of the outer electron is coupled with the total angular momentum of the core resulting in 3/2 + 0 = 3/2. The total angular momentum is now 3/2 + 1/2 (spin) = 2. The transition from $6p[3/2]_2$ to $6s[3/2]_2$ at 823.2 nm is one of the strongest lines in the xenon spectrum. In this diagnostic we will excite some of the population of the $6p[3/2]_2$ level to a rydberg state. This will result in dips in the 823.2 line. This e-dip spectroscopy is based on the known stark spectrum as function of electric field strength. To study the feasibility a dielectric barrier discharge is used and a very good spatial resolution is not needed. The first part of this paper the experimental set-up will be discussed. Limits of this method and development in the near future are discussed in the second part.

Experimental set-up

In figure 2 a schematic overview of the set-up is given. An eximer pumped dye laser is used to probe the discharge. The detection branch consists of two imaging lenses and a one-meter monochromator. The laser delivers 30 ns pulses to give good temporal resolution. The spatial

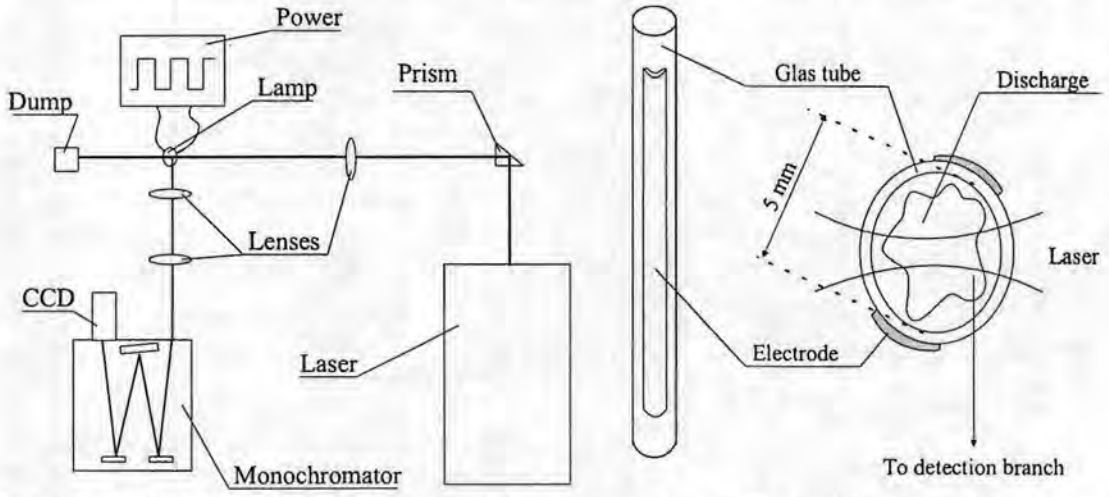

Figure 2: *On the left side there is an overview of the experimental set-up. On the right side the dielectric barier discharge lamp geometry.*

resolution is in the order of mm. The spatial resolution to measure inside a microdischarge has to be about 10 μm. Geometry of display panel cells probably require a confocal set-up in the future. In this feasibility study as stated before spatial resolution is not the main issue and doesn't change the fundamental physics.

The discharge geometry used is illustrated in the left of figure 2. It consists of a tube with two aluminum strips attached as electrodes. The electrode spacing is about 5 mm. The curvature of the electrodes has to be noticed. The discharge will be square wave driven with a frequency of 20 kHz. For a tube with a gas mixture of 10% Xe 90% Ne at a pressure of 10 Torr voltages will range from 300 up to 600 Volts.

Limitations and difficulties

Several processes broaden spectral lines emitted from plasmas. One limiting factor in this method is pressure broadening. In the microdischarges to be studied pressures in the order of 300-500 Torr are used. The splitting of the rydberg levels is about 1 cm^{-1}. Broadening of the lines has to be smaller. Estimating the broadening requires broadening coefficients specific for Xe-Ne gas mixtures.

Imprisonment of UV photons has been studied in microdischarges, because these photons excite the phosphors that ultimately generate the light we see from the display. In this case the broadening coefficients were determined [4]. If we use these broadening coefficients we can estimate the pressure broadening. The normalized emission profile $P(\nu)$ is given by

$$P(\nu) = 1/\{\pi\gamma[1+(\nu-\nu_0)^2/\gamma^2\} \quad (1)$$

The half-width at half maximum is given by γ,

$$\begin{aligned} \gamma &= \gamma_{Xe} + \gamma_{Ne} \\ \gamma_{Xe} &= \xi_{Xe} n_{0Xe} \\ \gamma_{Ne} &= \xi_{Ne} n_{0Ne} \end{aligned} \quad (2)$$

and is proportional with the number densities of colliding partners n_{0Xe} and n_{0Ne}. The coefficients ξ_{Xe} and ξ_{Ne} are determined to be $2.03 \cdot 10^{-15}$ and $8.0 \cdot 10^{-17}$ $m^3 s^{-1}$ respectively.
If we know take a pressure of 350 Torr and estimate the HWHM we find it in the order of GHz. Tachibana [2] obtained a HWHM of about 4 GHz and this seems in confirmation. 10 GHz is about 0.3 cm^{-1}. Therefore it's clear this pressure is pushing the diagnostic to the limit.

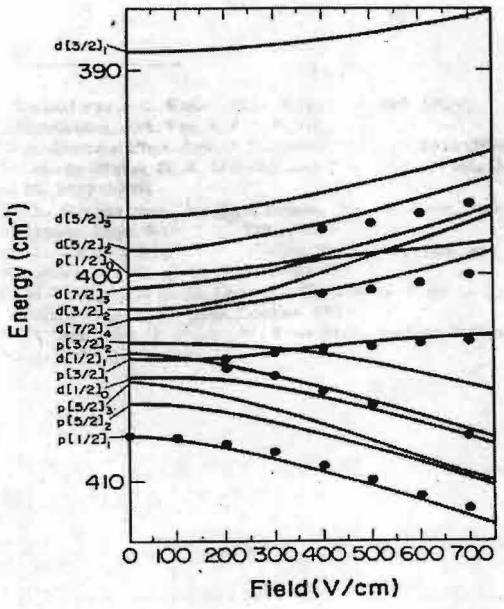

Figure 3: *Observed line positions of overlapping 19d and 20p transitions in xenon after [5].*

Another fundamental limitation will be the stark mixing of the rydberg states. In figure 3 this can be easily observed. Recently some developments have been made in calculating stark mixing probability [6]. Calculating these spectra remains however difficult. And experimentally obtaining spectra by an optogalvanic study is considered.

Future work

First estimations show the possibility of applying this diagnostic to Xe-Ne discharges. At this stage the work is concentrating on two areas. First of all broadening is studied in the dielectric barrier discharge lamp. All the experiments will concentrate on gas mixtures with 10% Xe an 90% Ne. Secondly work is being done in calculating or experimentally obtaining stark spectra. Spatial resolution will be improved in a later stage.

References

[1] G.J.M. Hagelaar, thesis Eindhoven University of Technology, (2000)
[2] K. Tachibana, S. Feng, T. Sakai, J. Appl. Phys., **88**, no. 9, 4967-4974 (2000)
[3] U. Czarnetzki, D. Luggenhölscher, H.F. Döbele, Phys. Rev. Lett., **81**, no. 21, 4592-4595 (1998)
[4] K. Igarashi, S. Mikoshiba, Y. Watanabe, M. Suzuki, S. Murayama, J. Phys. D, **28**, 1377-1383 (1995)
[5] R.D. Knight, L.G. Wang, Phys. Rev. A, **32**, no. 2, 896-870 (1985)
[6] D. Vrinceanu, M.R. Flannery, J. Phys. B, **34**, L1-L8 (2001)

Scaling law for a low-pressure gas breakdown in a DC electric field in oxygen

V.A. Lisovskiy, S.D. Yakovin*, V.D. Yegorenkov
Kharkov National University, pl. Svobody 4, Kharkov, 61077 Ukraine
**Scientific Center of Physics and Technology, Kharkov, 310145 Ukraine*
E-mail: lisovskiy@ftf.univer.kipt.kharkov.ua

Gas breakdown in oxygen in a DC electric field at various interelectrode gaps L is studied experimentally. A scaling law for a low-pressure gas breakdown $U_{dc} = f(pL, L/R)$ is deduced. According to this scaling law, the breakdown voltage U_{dc} is a function not only of the product of the gas pressure p and the gap length L, but also of the ratio of the gap length L to the chamber radius R. It is shown that, for any dimensions of the cylindrical discharge chamber (in the range of L/R under investigation), the ratio of the breakdown electric field to the gas pressure p at the minimum of the breakdown curve remains constant: $(E_{dc}/p)_{min} \approx$ const. A method for calculating the breakdown curve in a cylindrical discharge chamber with arbitrary values of L and R is proposed.

As is known [1–7], the breakdown curves of a glow discharge are described by the Paschen law $U_{dc} = f(pL)$; i.e., the breakdown voltage U_{dc} is a function of the product of the gas pressure p and the interelectrode distance L. The Paschen law implies that the breakdown curves $U_{dc}(p)$ measured for various distances L must coincide if they are drawn as the function $U_{dc}(pL)$. However, the measurements of the breakdown curves of a glow discharge in neon [8] showed that, with equal values of the product pL, the breakdown voltage for a long discharge gap with planar electrodes is significantly higher than that for a short gap. More recent studies [9–18] confirmed this conclusion for some other gases (neon, argon, nitrogen, hydrogen, air, etc.).

We measured the breakdown curves for a glow discharge in the range of DC voltages $U_{dc} \leq 1000$ V and pressures of $p \approx 10^{-2} - 10$ Torr. A discharge tube with an inner diameter of 63 mm was used. The interelectrode distance L was varied in the range 0.5–10 cm; consequently, the studies were conducted in the range L/R = 0.16–3.2. Planar parallel electrodes spanned the entire cross section of the discharge tube. Both the anode and the cathode were made from stainless steel. The breakdown voltage was measured accurate to ±2 V. When determining the breakdown voltage, the growth rate of the discharge voltage did not exceed 1 V/s. In all cases, our procedure for measuring the breakdown curves was as follows. We fixed a certain distance L between the electrodes and then, for various gas pressures p, measured the breakdown voltage U_{dc} . Below, we explain why only this way of measuring the breakdown curves of a glow discharge is correct.

Figure 1 shows the breakdown curves measured by us in oxygen for different distances L between the electrodes. It is seen from the figure that, as L increases, the breakdown curves shift not only toward higher breakdown voltages U_{dc} (as was obtained in [9–14]), but also toward higher values of pL [15 – 18]. Apparently, such a shift of the breakdown curves toward higher values of U_{dc} and pL with increasing interelectrode distance L may be attributed to an increase in losses of charged particles on the cylindrical wall of the discharge tube due to diffusion across the electric field.

Note that, by properly choosing the reference axes, we can make all of the obtained breakdown curves almost coincide. For example, if we take

$$(pL)^* = pL \Big/ \left(1+\left(\frac{L}{R}\right)^2\right)^a, \tag{1}$$

$$U_{dc}{}^* = U_{dc} \Big/ \left(1+\left(\frac{L}{R}\right)^2\right)^a, \tag{2}$$

as the abscissa and ordinate, respectively, where $a \approx 0.03$ for oxygen, then the breakdown curves presented in Fig. 1 coincide accurate to ±5 V (Fig. 2). It is evident that, for $L/R \to 0$, we have the usual Paschen curve $U_{dc} = f(pL)$. It follows from Eqs. (1) and (2) that $U_{dc}{}^*/(pL)^* = U_{dc}/pL = E_{dc}/p$; i.e., the dependences $E_{dc}/p = f((pL)^*)$ for different breakdown curves must also coincide (which is seen in Fig. 2). Here, we also see a reasonable agreement between our results and data from [19]. From our results, it follows that the scaling law for the gas breakdown can be written in the form $U_{dc} = f(pL, L/R))$ or $U_{dc}{}^* = f((pL)^*)$.

Fig. 1.

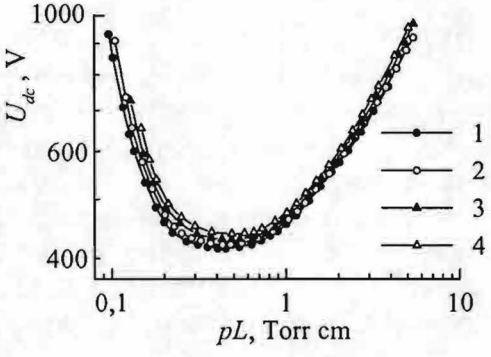

Fig. 2.

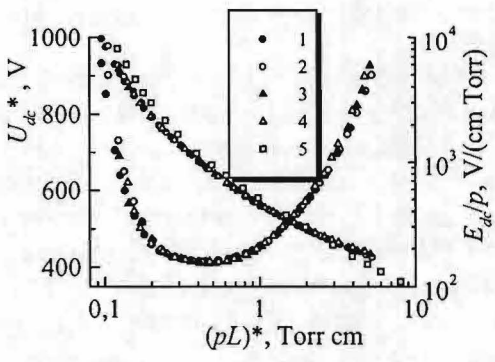

Fig.1. Measured breakdown curves of the glow discharge in oxygen(R = 3.15 cm) for the stainless steel cathode and different interelectrode gaps: 1 - L = 0.5 cm, 2 - 3 cm, 3 - 6 cm, 4 - 8 cm.

Fig.2. Dependencies of $U_{dc}{}^*$ and E_{dc}/p on $(pL)^*$ in oxygen in the discharge tube with R = 3.15 cm and different interelectrode gaps: 1 - L = 0.5 cm, 2 - 3 cm, 3 - 6 cm, 4 - 8 cm, 5 are measured data of paper [19].

Based on Eqs. (1) and (2) and the values of breakdown voltage given in the figures, we can calculate, to a high accuracy, the breakdown curves for any cylindrical discharge chamber for arbitrary values of the distance L and radius R. In the general case, to calculate the breakdown curve in a cylindrical discharge chamber with arbitrary dimensions, one should have the Paschen curve (i.e., the breakdown curve measured in a discharge chamber such that $L/R \to 0$ and with the same cathode material). Then, from Eqs. (1) and (2), one can determine the values of U_{dc} and pL. If the initial breakdown curve has been measured in a discharge chamber with L_0 and R_0, such that the condition $L_0/R_0 \to 0$ does not hold, one should first calculate the dependence $U_{dc}{}^* = f((pL)^*)$ using Eqs. (1) and (2) and then, from the same relations, calculate the breakdown curve for a discharge chamber with the given dimensions L_1 and R_1. This may be written more concisely in the following form:

$$(pL)_1 = pL_0 \left[\frac{1+(L_1/R_1)^2}{1+(L_0/R_0)^2}\right]^a, \tag{3}$$

$$U_{dc1} = U_{dc0}\left[\frac{1+(L_1/R_1)^2}{1+(L_0/R_0)^2}\right]^a, \qquad (4)$$

where the index "1" stands for the breakdown curve to be sought and the index "0" stands for the initially known breakdown curve.

The breakdown curve of a glow discharge is usually measured by two methods: (i) the distance L is fixed, and the breakdown voltage U_{dc} is measured at different values of the gas pressure p; and (ii) the value of p is fixed, and the breakdown voltage U_{dc} is measured at different values of the distance L. However, the results obtained in this study show that the latter method of measuring the breakdown curve (at a fixed value of p and variable L) is incorrect. The breakdown curves obtained in this way are close to the Paschen curve only at small values of L but shift toward higher breakdown voltages with increasing L. Hence, the breakdown curve of a glow discharge must be measured by varying the gas pressure p, the distance L between the electrodes being fixed.

In summary, the breakdown of a glow discharge in oxygen at a variable interelectrode distance L have been studied experimentally. It is shown that, at any interelectrode distance L, the ratio $(E_{dc}/p)_{min}$ at the minimum of the breakdown curve remains constant. In the range of L/R under study, the scaling law for gas breakdown $U_{dc} = f(pL, L/R)$ holds; i.e., the breakdown voltage U_{dc} is a function not only of the product of the gas pressure p and the gap length L, but also of the ratio L/R. A method for calculating the breakdown curve in a cylindrical discharge chamber with arbitrary values of L and R is proposed.

REFERENCES

[1] F. Paschen, Ann. Phys. Chem., Ser. 3 **37**, 69 (1889).
[2] M. J. Druyvesteyn and F. M. Penning, Rev. Mod. Phys. **12**, 87 (1940).
[3] J. M. Meek and J. D. Craggs, *Electrical Breakdown of Gases* (Clarendon, Oxford, 1953).
[4] Yu. P. RaÏzer, *Gas Discharge Physics* (Nauka, Moscow, 1987).
[5] V.A. Lisovskiy and V. D.Yegorenkov, J. Phys. D **27**, 2340 (1994).
[6] A. V. Phelps and Z. Lj. Petrovic, Plasma Sources Sci. Technol. 8, R21 (1999).
[7] M. Sato, Bull. Yamagata Univ. **25**, 119 (1999).
[8] J. S. Townsend and S. P. McCallum, Philos. Mag. 6, 857 (1928).
[9] H. Fricke, Z. Phys. **86**, 464 (1933).
[10] S. P. McCallum and L. Klatzow, Philos. Mag. **17**, 279 (1934).
[11] H. C. Miller, Physica (Amsterdam) **30**, 2059 (1964).
[12] L. Jacques, W. Bruynooghe, R. Boucique, and W. Wieme, J. Phys. D **19**, 1731 (1986).
[13] M. Yumoto, T. Sakai, Y. Ebinuma, *et al.*, in *Proceedings of the 8th International Symposium on High-Voltage Engineering, Yokohama, 1993*, p. 409.
[14] G. Auday, P. Guillot, J. Galy, and H. Brunet, J. Appl. Phys. **83**, 5917 (1998).
[15] V. A. Lisovskiy, S. D. Yakovin, Technical Physics **45,** 727 (2000).
[16] V. A. Lisovskiy and S. D. Yakovin, JETP Letters **72**, 34 (2000).
[17] V.A. Lisovskiy, S.D. Yakovin, V.D. Yegorenkov, J. Phys. D **33**, 2722 (2000)
[18] V. A. Lisovskiy and S. D. Yakovin, Plasma Physics Reports **26**, 1066 (2000).
[19] M. J. Schonhuber, IEEE Trans. Power Appar. Syst. **88**, 100 (1969).

Revisited Kinetics of the Short Lived Afterglow of a nitrogen microwave discharge

C. Foissac and P. Supiot
Lab.GéPIFRéM Université des Sciences et Technologies de Lille, 59655 Villeneuve d'Ascq Cédex, France

S. Mazouffre, R. Engeln, and D.C. Schram.
Department of Applied Physics, Eindhoven University of Technology, P.O. Box 513, 5600 MB Eindhoven (NL)

N. Sadeghi and A. Campargue
LSP, Université Joseph Fourier-Grenoble I and CNRS, B.P. 87, 38402 St. Martin d'Hères, France

1. Introduction

Nitrogen discharges and afterglows at pressures of a few hundreds of Pascal have been very extensively studied in the past two decades. However, most of the experimental works are based on emission spectroscopy and so far no overall description of the plasma together with the kinetics of the neutral species has been reported. Modeling the discharge itself is now routinely achieved through numerical codes [1] but analysis of the afterglow is much more complicated. Indeed, due to the absence of energetic electrons, the kinetics of the afterglow is mainly dominated by neutral energy-carrier species like vibrationally excited ground state molecules, N atoms and metastable molecules. In particular, the case of the well-known Short Lived Afterglow (SLA) of a μ-wave discharge, also called the Pink afterglow, is of primary interest. The most intriguing peculiarity of the SLA, that is expected to be free from the μ-wave field that sustains the discharge, is the appearance of a very bright molecular emission after the dark space that follows the discharge zone.

In an effort to obtain a better understanding of the neutral-neutral reactions responsible for the formation of the SLA, several diagnostic techniques have been implemented in the same flow tube to probe the axial dependence of the density of neutral species $N(^4S)$ and $N_2(A^3\Sigma_u^+)$, but also of the electrons resulting from ionisation processes in the afterglow. The absolute ground state nitrogen atom $N(^4S)$ density is determined by means of an original calibration method based on Two-photon Absorption Laser Induced Fluorescence (TALIF) spectroscopy [2] . The Intra-Cavity Laser Absorption Spectroscopy (ICLAS) [3] was shown as a powerful approach to directly determine the $N_2(A^3\Sigma_u^+)$ absolute density and also the gas temperature, with a very high sensitivity [4]. Additionally, a first determination of the absolute electron density by microwave interferometry was completed. Supported by the set of data obtained under the same experimental conditions, a simple kinetic model is proposed and discussed to account for the observed behaviors of the different species density.

2. Experimental

The Pyrex discharge tube (l=1.70m, ϕ_i=3.8 cm) is basically the same that described in [4]. N atoms and $N_2(A^3\Sigma_u^+)$ metastable molecules are generated in flowing nitrogen ("U" grade, Air Liquide) by a microwave discharge resonant cavity at 433 MHz. The gas pressure, measured by a Pirani gauge, is 440 Pa while the flow rate is 1.5 slm. This results in a flow velocity, before the discharge zone, of 5 m/s. The microwave power supplied to the μ-wave cavity is 300 W and the reflected power is negligible. The flow tube is extended by two arm-tubes at right angle which are closed at both ends with Brewster angle windows (total length of the arm-tubes: l=42 cm, ϕ_i=2 cm). This tube has been either inserted inside the ICLAS system (see Fig. 1) or adapted to detect the fluorescence induced by two-photon (207 nm)

laser radiation in the same region [2]. The TALIF signal was calibrated through the fluorescence yield of krypton. The space resolution is obtained by translating the microwave cavity. Measurements were performed from 4 cm from the centre of the discharge zone (region where the power is transmitted to the plasma) to about 50 cm (late afterglow).

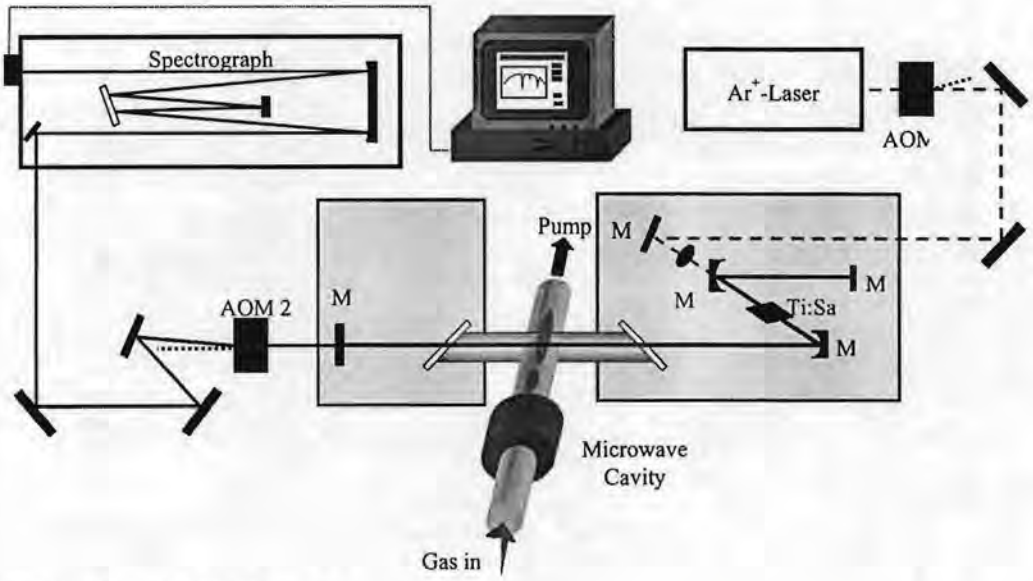

Fig. 1 – Experimental ICLAS set-up

3. Results

- **Gas temperature :** Gas temperature is deduced from the Boltzmann distribution of populations in rotational levels of the $N_2(A^3\Sigma_u^+; v=0)$ metastable state. This rotational temperature, T_r is about 950 K in the end of the discharge zone (z= 4 cm), drops quickly to about 550 K at the minimum of the emission intensity in the SAL (z ~ 12 cm) and then decays slowly to reach room temperature in the late afterglow ($z \geq 50$ cm). Translational temperatures, measured from the Doppler width of the isolated rotational lines, are in quite good agreement with T_r values [5]. The Doppler temperature of N atoms, deduced from TALIF measurements, suffers from a large uncertainty in the early afterglow ($z \leq 10$ cm) and seems to show a radial temperature gradient close to the discharge zone.

- **N atoms density:** As shown in Fig. 2, N density slowly increases from the discharge zone and reaches a plateau of about 3×10^{21} m^3 at long distances, following almost a $1/T_g$ law as a result of the gas flux conservation. This clearly points out that in the afterglow of our system the flux of N atoms is conserved and suggests that both creation and lost mechanisms of N are of little importance [2].

- **$N_2(A^3\Sigma_u^+)$ density :** The space-dependent density of $N_2(A^3\Sigma_u^+; v=0)$ metastable molecules, is shown in Fig. 2. Density of $N_2(A^3\Sigma_u^+)$ molecules is about 5×10^{17} m^3 in the end of the discharge zone (z=4 cm) and then continuously decays by almost two orders of magnitude to reach a minimum at $z \cong 12$ cm before monotonically increasing to a secondary maximum of 5×10^{16} m^{-3} around z=19 cm. It then slowly decays to the longer distances. This density essentially follows the same trend as the emission intensity from $N_2(B^3\Pi_g)$ state, also shown in Fig. 2. [5]. It is clearly seen that for z>12 cm these molecules are locally formed in the SLA and not carried to this region by the gas flow. Production of $N_2(A^3\Sigma_u^+)$ molecules

from the three body N atom volume recombination, as well as by collisional processes involving high vibrational levels of the ground state $N_2(X,v)$ molecules have been analyzed. We propose a strong coupling of the $N_2(A^3\Sigma_u^+)$ state with the $N_2(X,v\geq 8)$ molecules through $N(^2P)$ metastable atoms following reactions [5]:

$$N_2(A^3\Sigma_u^+) + N(^4S) \rightarrow N_2(X^1\Sigma_g^+,v) + N(^2P) \quad (1)$$
$$N(^2P) + N_2(X^1\Sigma_g^+,v\geq 8) \rightarrow N_2(A^3\Sigma_u^+) + N(^4S) \quad (2)$$

Acting together, this pair of reactions recycles $N_2(A^3\Sigma_u^+)$ molecules and results in an effective quenching rate of $N_2(A^3\Sigma_u^+)$ molecules much slower than if only reaction (1) was considered. The initial decay of the density in the early afterglow ($z< 10$ cm) can perfectly be explained by these reactions. The rising edge of the SLA for $z> 12$ cm is attributed mainly to the enhancement of the production rate of the excited nitrogen molecules by three body atom-atom recombination. This results from the increase of the N atom and gas densities, due to the temperature drop, and also the enhancement of the three body recombination coefficient with decaying temperature. A partial contribution from $N_2(X^1\Sigma_g^+,v\geq 25)$ molecules is also possible. The final decay of $N_2(A^3\Sigma_u^+)$ molecules, for $z> 20$ cm, is probably due to the depletion of $N_2(X^1\Sigma_g^+,v\geq 8)$ molecules that reduces the contribution of reaction (2) and consequently increases the effective quenching rate of the $N_2(A^3\Sigma_u^+)$ molecules.

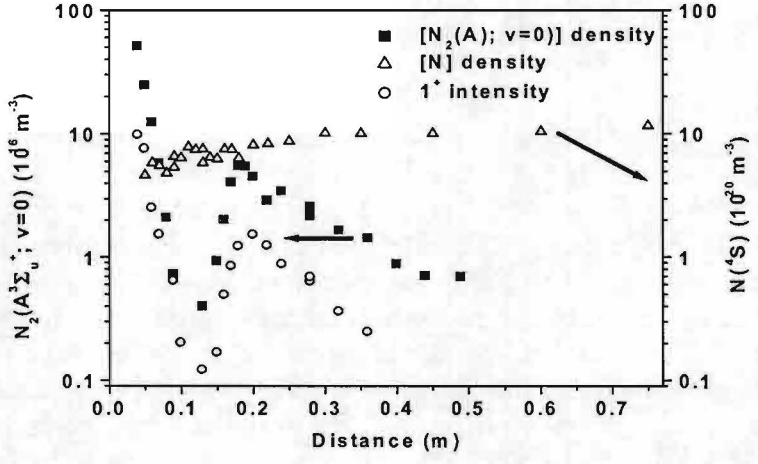

Fig. 2 – Axial variation of $N_2(A^3\Sigma_u^+; 0)$ and N (^{4}S) densities in the SLA of a 440 Pa, nitrogen μ-wave discharge. Note different scales. Is also shown the emission intensity of the 1st positive band.

- **Electron density** : The space dependence of the electron density, measured by microwave interferometry, is almost similar to that of the excited molecules and shows also a pronounced minimum at $z\cong 12$ cm and reaches a maximum of 6×10^{15} m^{-3} around $z=19$ cm. Possible processes for this local ionisation, in the absence of any electric field, could be binary collisions of electronically excited molecules, and/or of vibrationally excited ground state molecules in the $v''\geq 30$ levels.

References:

[1] Guerra V and Loureiro J, (1997) *Plasma Sources Sci. Technol.*, 6, 361

[2] Mazouffre S, Foissac C, Supiot P, Engeln R, Vankan P J W, Schram D C, and Sadeghi N, *Plasma Sources Sci. Technol.*, (2001) submitted

[3] Campargue A, Stoeckel F and Chenevier M (1990) *Spectrochimica Acta Rev.*, 13, 1, 69

[4] Foissac C, Supiot P, Campargue A, Kachanov A, Weirauch G, and Sadeghi N, (2000), J. Phys D:Applied Phys. **31** 1168

[5] Sadeghi N, Foissac C, Supiot P, (2001) J. Phys D:Applied Phys. submitted

Magnetic field effects on cross section of inelastic electron-ion collisions

H.Tavassoli*, F.Sohbatzadeh, H.Latifi, B.Shokri

Physics Department and Laser Research Center of Shahid Beheshti Univ.- Tehran-Iran

I.INTRODUCTION

Many plasma processes behave differently in the presence of the external magnetic field. In the present paper we obtain the magnetic field effects on the cross section of the inelastic electron-ion collisions for $1s \rightarrow 2p$ transition of hydrogenic ions. In section II we derive the scaled cross section of inelastic electron-ion collisions in magneto-active dense plasma as a function of the scaled Larmor frequency. In section III we shall present the results of the calculation.

II. CALCULATION

In plasmas imbeded in an external, constant and homogeneous magnetic field the interaction potential between two charged particle is derived by,

$$V(\mathbf{r}) = \frac{q_1 q_2}{2\pi^2} \int d^3\mathbf{k} \frac{e^{-i\mathbf{k}.\mathbf{r}}}{k_i k_j \epsilon_{ij}(k,\omega)}, \tag{1}$$

where k_i, k_j are the components of momentum transfer, q_1, q_2 are charge of particles, $\epsilon_{ij}(k,\omega)$ are the components of dielectric tensor and $\mathbf{r}$ is the position vector of between two particles. We use longitudinal component of dielectric tensor in the interaction potential. In the magneto-active plasmas the longitudinal component of the dielectric function for magnetic field oriented along the Z-axes is obtained by (see for example Ref. 1)

$$\epsilon^{lo}(k,\omega) = 1 + \frac{1}{k^2\Lambda^2}[1 - \sum_n \frac{\omega}{\omega - n\Omega_e} A_n(Z) I_+(\beta_n)], \tag{2}$$

where Ω_e is the Larmor frequency, Λ is the Debye length, $I_+(x) = xe^{-x^2/2} \int_{i\infty}^{x} d\tau e^{\tau^2/2}$, $A_n(Z) = e^{-Z} J_n(Z)$, $Z = k_\perp^2 v_{T_e}^2/\Omega_e^2$, $\beta_n = (\omega - n\Omega_e)/ \mid k_z \mid v_{T_e}$, and v_{T_e} is the electron thermal velocity and $\omega \cong k_z v_z$. Using the first order perturbation theory the transition amplitude

*E-mail : h-tavassoly@cc.sbu.ac.ir

from an initial state n to an excited state $\acute{n}$ is derived by,

$$T_{n,\acute{n}} = -\frac{i}{\hbar}\int_{-\infty}^{+\infty} dt e^{i\omega_0 t} < \acute{n} \mid V(r) \mid n >, \tag{3}$$

By inputting Eq.(1) in Eq.(4) we derive,

$$T_{n,\acute{n}} = -\frac{iq_1q_2}{2\pi^2\hbar}\int_{-\infty}^{+\infty} dt e^{i\omega_0 t}\int d^3\mathbf{k}\frac{< n \mid e^{-i\mathbf{k}.(\mathbf{r}_p-\mathbf{r}_b)} \mid \acute{n} >}{k^2\epsilon^{lo}(k,\omega)}, \tag{4}$$

where r_p and r_b are the position of projectile electron and the bound electron. We use straight-line trajectory for projectile path, where the position vector r_p of projectile is described as,

$$\mathbf{r}_p(t) = \mathbf{v}_\mathbf{p}t + \mathbf{e}_\mathbf{x}b, \tag{5}$$

where b is impact parameter and $\mathbf{v}_p$ is projectile velocity along the magnetic field and $\mathbf{e}_\mathbf{x}$ is the unit vector perpendicular to $\mathbf{v}_\mathbf{p}$ in the collision plane. Thus the expectation value of Eq.(5) became,

$$< n \mid e^{-i\mathbf{k}.(\mathbf{r}_p-\mathbf{r}_b)} \mid \acute{n} >=< n \mid e^{i\mathbf{k}.\mathbf{r}_b} \mid \acute{n} > e^{-ik_z v_p t}e^{-ik_\perp b\cos(\varphi)}. \tag{6}$$

Considering $1s \longrightarrow 2p$ transition and by inputting Eq.(7) in Eq.(5), we obtain

$$T_{1s,2p} = -\frac{ie^2}{2\pi^2\hbar}\int dk_\perp C(k_\perp)k_\perp\int\frac{dk_z}{k^2\epsilon^{lo}(k,\omega)}A_{1s,2p}(k)D(k_z), \tag{7}$$

where(see for example Ref. 2),

$$A_{1s,2p}(k) =< 1s \mid e^{ik.r_b} \mid 2p >= \frac{i6\sqrt{2}}{a_0^5}\frac{k}{[k^2+(3/2a_0)^2]^3},$$

$$C(k_\perp) = \int_0^{2\pi} d\varphi e^{-ik_\perp b\cos(\varphi)} = 2\pi J_0(k_\perp b), \tag{8}$$

$$D(t,k_z) = \int_{-\infty}^{+\infty} dt e^{i\omega_0 t}e^{-ik_z v_p t} = 2\pi\ \delta(k_z v_p - \omega_0),$$

that for deriving $A_{n,\acute{n}}(k)$ we choose the quantization axis to lie along the momentum transfer $\mathbf{k}$. Using equations (8), we derive

$$T_{1s,2p} = 12\sqrt{2}\frac{e^2}{a_0^5\hbar}\int_0^\infty dk_\perp J_0(k_\perp b)k_\perp\int\frac{dk_z\ \delta(k_z v_p-\omega_0)}{k\epsilon^{lo}(k,\omega)[k^2+(3/2a_0)^2]^3} \tag{9}$$

We assume that the strength of magnetic field to be strong. But for using the semiclassical model the magnetic field should satisfy the following inequality, $\Omega_e \ll E_1/h$, where E_1 is the first orbital energy of hydrogenic atom (see for example Ref. 3). Assuming the large magnetic field and knowing that the integrand in Eq.(10) becomes small for large $k_\perp$ we can use the small Larmor radius,

$$k_\perp^2 a_{ce}^2 \ll 1, \tag{10}$$

where a_{ce} is the gyroradius of electron. We consider the motion of projectile electron along the magnetic field. Therefore the finite Larmor radius effects of projectile electron is negligible. We consider the summation in Eq.(3). The inequality (10) allows all terms except $n = 0$ to be neglected to the sum, because $J_n \approx (k_\perp^2 a_{ce}^2)^n$. Now we can restrict our consideration to only the first term.Then the longitudinal dielectric function becomes

$$\epsilon^{lo}(\Lambda, \bar{\Omega}_e, \bar{v}_{T_e}) \approx 1 + \frac{1}{k^2}[\frac{1}{\Lambda^2}(1 - I_+(\bar{v}_p)) + \frac{1}{\bar{\Omega}_e^2}]. \tag{11}$$

Then the Eq. (10) becomes,

$$T_{1s,2p} = 32\sqrt{2}\frac{F}{Z^2}\int_0^\infty \frac{d\bar{k}_\perp J_0(\bar{k}_\perp \bar{b})(\bar{k}_\perp^{\,2} + F^2)^{1/2}\bar{k}_\perp}{[\bar{k}_\perp^{\,2}(1 + \bar{\Omega}_e^{-2}) + F^2 + \bar{\Lambda}^{-2}(1 - I_+(\bar{v}_p))][\bar{k}_\perp^{\,2} + F^2 + (9/4)^3}, \tag{12}$$

where $\bar{v_p} = v_p/v_{T_e}$, $\bar{\Lambda} = \Lambda/a_0$, $\bar{k}_\perp = k_\perp a_0$, $F = \omega_0 a_0/v_p$, $\bar{b} = b/a_0$ and $\bar{\Omega}_e = \Omega_e/\omega_{p_e}$. The cross section of excitation from an initial state n to an excited state $\acute{n}$ is obtained by,

$$\sigma_c = 2\pi \int_0^\infty P_{n,\acute{n}}(b) b db, \tag{13}$$

where $P_{n,\acute{n}} = \mid T_{n,\acute{n}} \mid^2$, is the transition probability. The scaled cross section of inelastic electron-ion collisions for $1s \longrightarrow 2p$ is derived by

$$[d\bar{\sigma}_{1s,2p}/d\bar{b}]_M \equiv \frac{[d\sigma_{1s,2p}/db]_M}{2\pi a_0} = \bar{b} \mid T_{1s,2p}(\bar{b}) \mid^2 . \tag{14}$$

III. RESULTS

Figure 1 shows the scaled partial cross section of ion-electron inelastic collision as a function of the scaled impact parameter for three cases of the ratio between the plasma frequency and the Larmor frequency: $\bar{\Omega}_e = 2$, 3 and 4. The scaled partial cross section for a plasma without the magnetic field are also illustrated in figure 2. As we see in this figure, it is found that the scaled partial cross section of ion-electron inelastic collision including the magnetic field effect is always smaller than one without the magnetic field. When the Larmor frequency increases, the magnetic field effect decreases. It is found that the results obtained in the absence of magnetic field is the asymptotic limit of our results, ($\bar{\Omega} \to \infty$).

References

[1] N. A. Krall, A. W. Trivelpiece *Principles of Plasma Physics* (Mc GRAW-HILL BOOK COMPANY, 1973).

[2] Y.-D. Jung,Phys.Plasma **4**, 21 January (1997)

[3] J. J. Sakurai, *Modern Quantum Mechanics*, Edited by San Fu Tuan (Addison-Wesley, 1985)

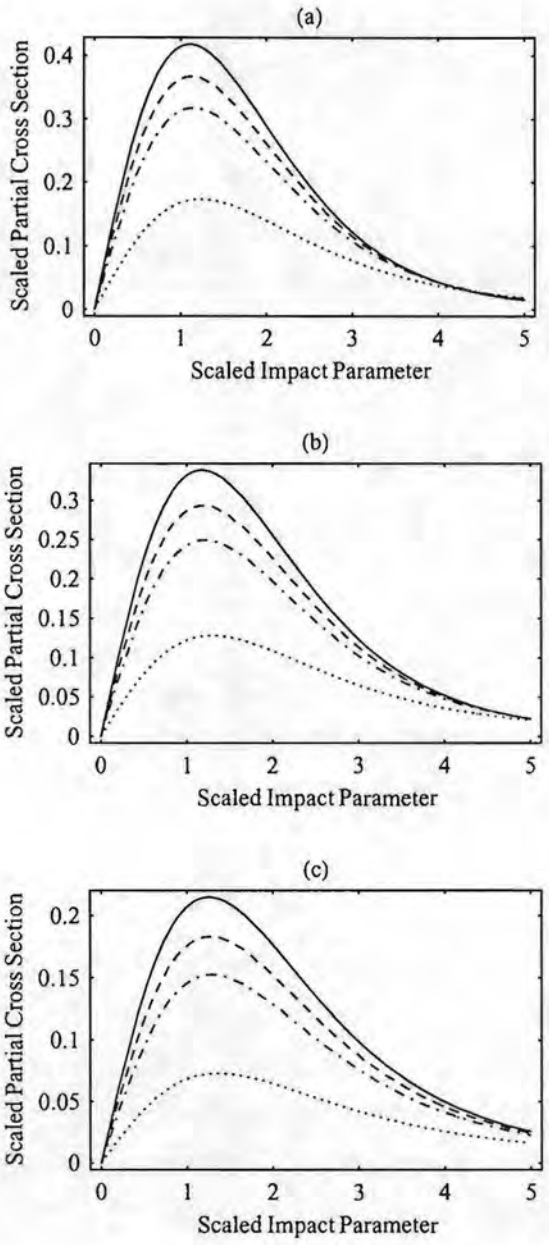

Figure 1: The scaled partial cross section of inelastic electron-ion collisions in a magneto-active dense plasma as a function of the impact parameter. The solid lines represent the partial cross section of inelastic electron-ion collisions without the magnetic field effects. The dashed, dot dashed and doted lines represent the partial cross section of inelastic electron-ion collisions for $\bar{\Omega}_e = 4$, $\bar{\Omega}_e = 3$, and $\bar{\Omega}_e = 2$ respectively. [(a) $F = 0.4$; (b) $F = 0.3$; (c) $F = 0.2$].

Determination of Silicon Densities by Cavity-Ringdown Spectroscopy

A. Brockhaus, St. Geisler, A. Schwabedissen, J. Engemann
Forschungszentrum für Mikrostrukturtechnik – fmt, University of Wuppertal
Germany

Introduction

Today silicon is still the most important material in microelectronics. Plasma and ion beam techniques come into play because the demands for extremely high integration on state-of-the-art chips can only be met by plasmatechnological process steps, e.g. anisotropical dry etch. Process analysis in turn requires a diagnostic method to precisely measure absolute densities of sputtered particles, i.e. atomic silicon.

Another reason to study atomic silicon has to do with unwanted sputtering of quartz. SiO_2 is frequently used as a dielectric wall material in plasma sources. We have set up a sputter experiment where the spatially resolved, absolute atomic silicon density can be determined with the aid of Cavity Ringdown Spectroscopy (CRDS), a very sensitive laser absorption method based on a measurement of the decay time of a high quality optical resonator filled with the absorbing material.

Traditional diagnostics employed for this task are optical emission spectroscopy and laser-induced fluorescence (LIF). In contrast to CRDS they yield relative densities only. On the other hand, LIF gives the best spatial resolution, since CRDS measurements are always integrated over the line-of-sight thus requiring either assumtions or else an independent determination of the density profile.

The majority of contemporary CRDS experiments are performed in the visible and in the infrared region where very high reflectivity mirrors are readily available. Since we are interested in ground state silicon densities, our CRDS measurements are performed at the transitions of the Si resonance line multiplet in the ultraviolet, centered at 252 nm.

Experimental set-up

For the first sequence of experiments we used a typical capacitively coupled radio-frequency sputter diode configuration – a modified GEC cell – to generate gaseous silicon. Target material is either a pure 3" Si wafer or a quartz plate of 8 cm diameter. RF power of 10 W is applied to this target via a matchbox. Sputter gas is argon at 100 Pa. The small area of the target as compared to the grounded chamber wall causes self-bias voltages of about hundred volts. The set-up is displayed in Figure 1.

In a later stage of the experiment we used an ion beam source instead of the self-bias configuration to independently control ion energy and incidence angle.

A pulsed dye laser beam (frequency-tripled Nd:YAG laser GCR170-10 from Spectra Physics, dye laser PrecisionScan from Sirah)

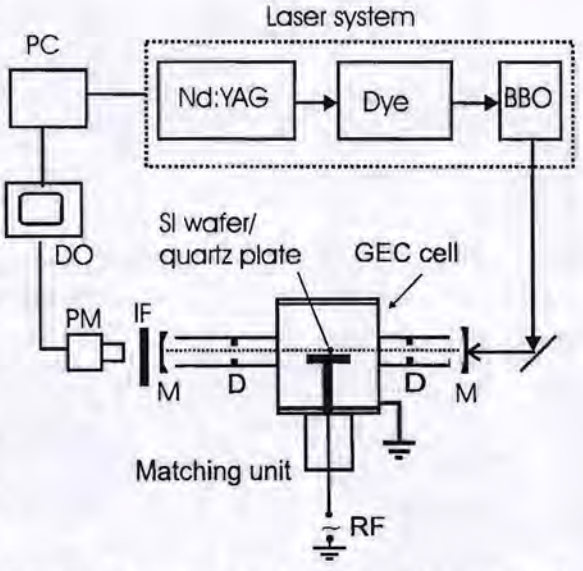

Figure 1: *Experimental set-up. M: mirror, D: diaphragm, IF: bandpass filter, PM: photomultiplier, DO: digital oscilloscope*

is frequency-doubled with a BBO crystal to generate tunable radiation at the Si I $3s^2\,3p^2 - 3s^2\,3p\,4s$ absorption line multiplett around 252 nm. The laser bandwidth has been measured with a Fabry-Perot and is smaller than 0.055 cm^{-1} or 0.35 pm, respectively. Light pulses of typical 10 µJ energy and 6 ns pulse width are coupled into a high-quality optical resonator formed by two dielectric mirrors with 1.5 cm diameter and 6 m radius of curvature (Los Gatos). The resonator length is L = 1.7 m resulting in a round-trip time of $\tau_r = 2L/c$ = 11.3 ns. Radiation leaking out of the resonator forms a pulse sequence of exponentially decreasing intensity with a characteristic ringdown rate f_{CRD}. It is conveniantly measured using a photomultiplier and a fast digital oscilloscope (Tektronix TDS 684B).
If the resonator is filled with an absorbing medium of density n and photo absorption cross section $\sigma(\lambda)$ then f_{CRD} increases, according to the following equation [1]:

$$f_{CRD}(\lambda) = f_{CRD,0} + \frac{c}{L}\sigma(\lambda)\int_0^L n(z)\,dz$$

Thus evaluation of the ringdown rate as a function of laser wavelength yields the absorption profile. The Si multiplett consists of five lower states; however, only three of them are populated at ambient temperature [2]. By measuring transitions originating from these states the overall silicon ground state density – integrated over the line-of-sight – is calculated.

Experimental results and discussion

A typical example is displayed in Figure 2. From a ringdown rate of $f_{CRD,0}$ = 342 kHz far from the absorption structure we obtain a mirror reflectivity of [2]

$$R = \left(1 + \tau_r f_{CRD,0}/2\right)^{-1} = 99.8\%$$

This high reflectivity is readily obtained for clean mirrors. After several days of operation the ringdown time is reduced to about 1 µs but after careful mirror cleaning $1/f_{CRD,0}$ = 3 µs can be achieved again.

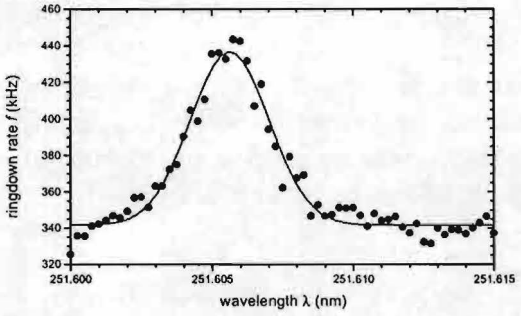

Figure 2: *CRD ringdown rate as a function of wavelength for one transition of the Si multiplett*

In order to relate ringdown rates to particle densities, the photo absorption cross section must be known. For a transition from state i to k the absorption cross section is calculated according to [3]:

$$\sigma_{ik}(\lambda) = \frac{A_{ki}\lambda_{ik}^4 g_k}{8\pi c g_i} P(\lambda)$$

with A_{ki} the Einstein coefficient, g_i, g_k the statistical weights, and $P(\lambda)$ the normalized line profile. The relevant data for the Si multiplett are summarized in the following table [3]:

λ_{ik} (nm)	E_i (cm^{-1})	E_k (cm^{-1})	g_i	g_k	A_{ki} ($10^8\ s^{-1}$)
250.690	77.115	39955.050	3	5	0.417
251.432	0	39760.285	1	3	0.55
251.611	223.157	39955.050	5	5	1.21
251.920	77.115	39760.285	3	3	0.422
252.411	77.115	39683.163	3	1	1.66
252.851	223.157	39760.285	5	3	0.69

For the absorption profile displayed in Fig. 2 we obtain a line-integrated silicon density of $nS = 2.92 \times 10^9$ cm^{-2} for this particular state (S is the effective absorption length, see discussion below). By scanning the laser over the other absorption lines it is possible to obtain sublevel densities. The profile in Fig. 2 exhibits an unusual large width of nearly 2 pm. The sputtered silicon atoms in this case were generated with an ion beam source of 600 eV argon ions at an incidence angle of 30°. However, the detection geometry did not allow a determination of the velocity distribution. Hence, the large width is due to an averaging over a broad range of sputtering angles rather than being evidence of very hot silicon atoms.

For the standard sputter situation refered to in Fig. 1 wavelength scans over the absorption profiles of all six transitions were performed. Since sputtering in this case is caused by argon ions accelerated within the sheath it can be assumed that the sputtering angle is nearly zero. The sputtered silicon atoms, on the other hand, are emitted following the well-known Thompson distribution which implies the following [4]:

(i) The Si atom angular distribution will be a cosinus function with the highest probability for silicon atoms being sputtered just normal to the surface.

(ii) The Si atom main velocity component will be determined by the surface binding energy E_b which is 4.7 eV for pure silicon.

This high ion energy corresponds to a silicon atom velocity of 5.7 km/s or a Doppler shift of 4.8 pm of the absorption line. However, in our geometry only the velocity component parallel to the surface will be detected. Even more important, the background pressure of about 1 mbar argon will effectively thermalize the Thompson velocity distribution. If one therefore assumes Doppler broadening as the main mechanism then from the Doppler width a temperature of 550 ± 150 K is derived for the sputtered silicon atoms. The temperature may alternatively be calculated from a Boltzmann plot if the sublevels are in thermodynamical equilibrium. From this method we get a temperature of 370 ± 70 K which agrees within the error bars to the Doppler temperature.

At 251.43 nm we performed a lateral scan by moving the sputter electrode horizontally. The laser beam was 3 mm above the target. The results are displayed in Fig. 3, namely the normalized extiction coefficient versus the lateral position. The lower plot shows the density profile obtained by applying an Abel inversion to the measured data. The used Abel inversion procedure interpolates the measured distribution with even order polynomials.

It is seen that significant amounts of silicon are detected quite far from the sputter target indicating the diffusion of the sputtered material. From the data we calculate an effective absorption length of $S = 20 \pm 1$ cm which is in turn used to obtain absolute, radially resolved silicon densities.

We also determined silicon densities at different positions above the sputter target as a function of the background pressure. The

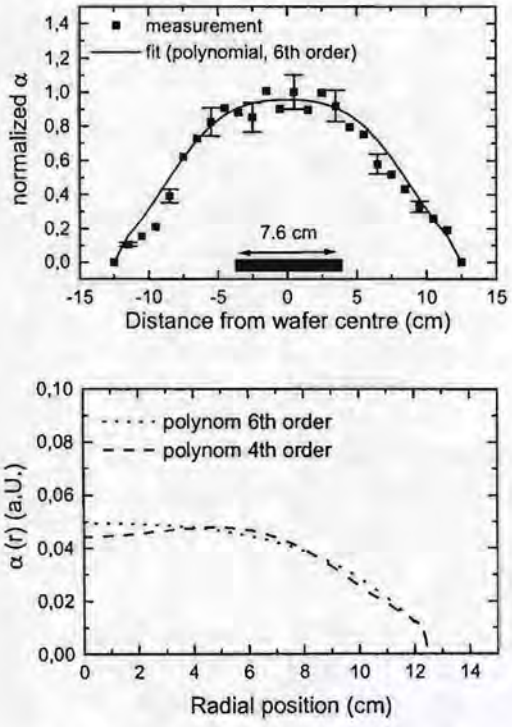

Figure 3: *Lateral scan to obtain radially resolved silicon densities. Lower plot displays the Abel inverted data, i.e., the radial profile.*

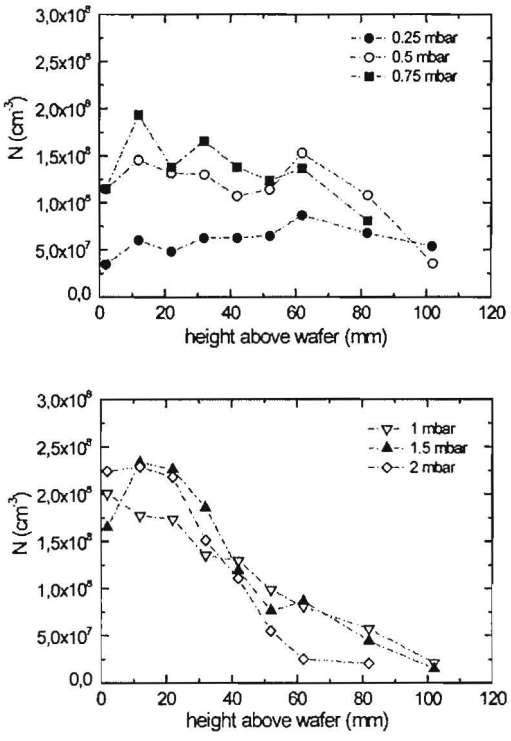

Figure 4: *Silicon density profiles above the sputter target for different argon background gas pressures.*

spatial silicon distributions in this case are displayed in Figure 4. If one assumes a production of silicon atoms with a constant rate at the target surface, then from simple diffusion one would expect a linear density decrease with increasing distance from the wafer. However, at least for higher pressures above 1 mbar this is not observed. We think that the sputtered silicon atoms are ejected with nonzero velocities and subsequently slowed down by collisions with the argon background gas thereby producing a modified density profile.

Although the plasma sputtering set-up resembles a real sputter situation of practical relevance, it suffers from the disadvantages that (i) the properties of the bombarding ions cannot be easily controlled, and (ii) the relatively high background pressure probably influences the spatial distribution of sputtered material. Therefore in a second sequence of experiments we used a separate ion beam source which operates at pressures around 10^{-4} mbar thus eliminating the aforementioned difficulties. We measured density distributions as a function of ion energy and angle of incidence. Angular distributions are displayed in Fig. 5. The results are compared to sputter simulations we performed with the TRIM (TRansport of Ions in Matter, see [5]) program and agree very well.

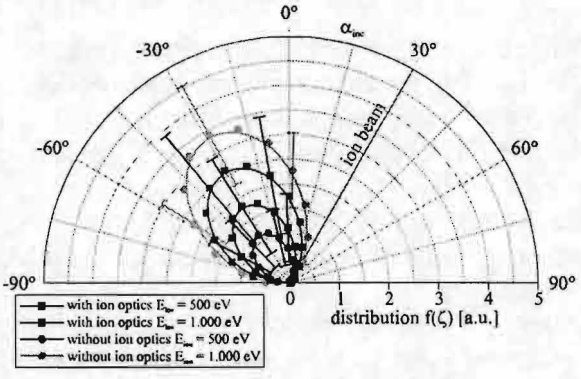

Figure 5: *Angular distributions of sputtered silicon.*

Summary

With the current CRDS set-up atomic silicon densities as low as 10^7 cm^{-3} can be absolutely determined. The sputter densities are typical around 10^7-10^{10} cm^{-3}. Sputter yields obtained with a well-defined ion beam agree well with simulations.

Acknowledgements

This work is supported by the Deutsche Forschungsgemeinschaft.

References

[1] D. Romanini, K.K. Lehmann; *J. Chem. Phys.* **99**, 6287 (1993)
[2] K. Tachibana, H. Tadokoro, H. Harima, Y. Urano; *J. Phys. D* **15**, 177 (1982)
[3] W.L. Wiese, M.W. Smith, B.M. Glennon: *Atomic Transition Probabilities*, NSRDS-NBS-4, Washington (1966)
[4] M.W. Thompson; *Nucl. Instr. and Methods* **B18**, 411 (1987)
[5] http://www.research.ibm.com/ionbeams

Hypothesizing chemical processes in the expansion of thermal plasma generated in Ar/N_2, $Ar/N_2/C_2H_2$, and Ar, Ar/N_2 in contact with cooper or graphite from comparative study of the emitted spectra

G. Dinescu*, A. de Graaf, E. Aldea*, M.C.M. van de Sanden****

*National Institute of Laser, Plasma and Radiation Physics, Magurele-Bucharest, Romania
**Eindhoven University of Technology, Department of Applied Physics, 5600 MB Eindhoven, The Netherlands

Introduction

Although optical emission spectroscopy has limitations when quantitative approaches are envisaged, it is a facile technique for identification of plasma species. Moreover, when emitted spectra in gas mixtures are comparatively studied the occurrence or absence of lines or bands peculiar to the gases in the mixture or specific to their chemical combinations may suggest the mechanism of formation and excitation of species. In this contribution the spectra emitted by thermal expanding plasmas generated in Ar, Ar/N_2, Ar/C_2H_2, $Ar/N_2/C_2H_2$, Ar and Ar/N_2 in contact with a cooper or graphite electrode are compared and discussed.

Experimental

The experimental set-up is based on cascaded arc plasma generated between three cathodes and a nozzle and expanding in a vacuumed vessel. The feedstock gas (Ar:100 sccs, Ar/N_2: 95/5 sccs) is supplied into the arc channel. Additional gases (C_2H_2: 2sccs, N_2: 5sccs) can be injected in expansion, through an injection ring situated downstream the arc nozzle. After a stationary shock, formed at a few centimeters from nozzle, plasma flows with subsonic velocities (1000-500 m/s). The plasma emission was collected by a focusing lens, directed via a quartz optical fiber to the slit of a monochromator and recorded by an adequate acquisition system. The conditions under which the experiments have been performed were: arcing current 48 A, arc pressure 0.5 bar, background pressure 0.25 mbar. Copper or graphite nozzles were used during the experiments.

Results and Discussion

The neglecting of triple collisions and of the excitation of electronic levels by electron collisions simplifies considerably the discussion. These assumptions are based on the peculiar properties of the expansion, i.e. the low value of the pressure (0.25 mbar) and the low electron temperature (0-3-0.5 eV), respectively.

Comparison of spectra from Ar with N_2 injected in expansion and injected in arc

The spectra recorded in expansion are dominated by the argon lines but the molecular nitrogen emissions are present as well, the N_2^+ (FNS) and N_2 (SPS) bands having almost the same magnitude. It is observed that the spectra have a similar appearance, independent of the injection mode. The vibrational and rotational temperatures are also very closed as values for the two injection modes. The meaning is that the same mechanism of spectra excitation is involved. This observation argue that in case of arc injection the nitrogen molecules dissociate in arc, but are formed again in the vessel by association, re-circulated and re-injected in expansion. It follows that the spectra excitation is based on excitation and charge transfer processes: the SPS system is excited by energy transfer from Ar metastables, N_2^+ molecules in the ground X state are formed by charge transfer from Ar^+ ions and are subsequently excited to the B state by V-E transfer from the vibrationally excited $N_2(X,v)$ species.

Comparison of spectra from Ar/N_2, Ar/C_2H_2 and $Ar/N_2/C_2H_2$ plasmas

The expanding Ar plasma with C_2H_2 injected in expansion exhibits the lines of Ar, the bands of CH, and C_2 radicals. The blue violet $CH(A^2\Delta\text{-}X^2\Pi, \Delta v=0)$ and near ultraviolet $CH(B^2\Delta\text{-}X^2\Pi, \Delta v=0)$ bands, $C_2(d^3\Pi g\text{-}a^3\Pi u)$ Swan system and $C_2(C^1\Pi g\text{-}A^1\Pi u, \Delta v=1, 0, -1)$ Deslandres-D'Azambuja bands were observed. If in similar conditions nitrogen is added in the arc channel together with Ar, the new feature added to the previous spectrum obtained

from Ar/C_2H_2 mixture is the presence of violet $CN(B^2\Sigma\text{-}X^2\Sigma)$ bands. The other features of Ar/C_2H_2 spectrum are conserved.

The emission of C_2 and CH bands has a chemical source that is due to exothermic recombination of acetylene ionic fragments ($C_2H_2^+$ and C_2H^+) formed following the charge exchange with the atomic ions (Ar^+, N^+). However, the intriguing aspect is that the nitrogen N_2(SPS) and N_2^+ (FNS) bands, which where present in Ar/N_2 expansions, are not appearing in the spectrum. This indicates that the reaction channels stimulated by the acetylene presence inhibit the excitation channels of the bands of molecular nitrogen. The reaction mechanisms explaining the emission of nitrogen bands in Ar/N_2 plasma, with nitrogen injected in arc, were based on re-association at wall of nitrogen atoms followed by excitation transfer from Ar metastables (for the SPS bands) or charge transfer and excitation transfer from $N_2(X,v)$ molecules (for the FNS) bands. The low level of nitrogen bands emission, at least as observed at our flux values, indicates that the nitrogen ions and atoms are rapidly consumed in other reaction channels, before any possible feeding of the re-association channel. On this basis, enforced by the occurrence of the strong CN bands, one argues that the nitrogen is preferentially trapped to CN molecules. The possible mechanisms are the conversion of CH radicals into CN radicals (suggested by an observed dominance of CN bands over the CH bands along the plasma flow) and/or the consumption of dissociated nitrogen at the vessel walls by surface reaction with the carbon containing deposited film. The last reaction is slightly exothermic and produces volatile CN radicals.

Comparison of spectra from Ar/N_2 plasmas with cooper and graphite nozzles

The experiments have been performed using the settings: arc current 89 A, Ar flow 95 sscs, N_2 flow (arc injected) 5 sccs. When the feeding gas was Ar the plasma emission consisted from Ar lines, without notable differences as comparing with the case of an Ar arc with a cooper nozzle. When the feeding gas is Ar/N_2 the plasma emission intensity strongly diminishes as compared with the use of an Ar/N_2 arc with a cooper nozzle and the CN(B-X) violet spectral system is exhibited. The N_2(FNS) spectral system is still present but has a lower intensity in comparison with Ar/N_2 plasma with a cooper nozzle. The N_2(SPS) is hardly observed. The plasma feeding with carbon species might be explained only by a surface reaction. The etching of the nozzle by atomic nitrogen, followed by desorption of CN or C_2N_2 molecules is the reaction candidate. In the plasma volume CN molecules re-associate to form C_2N_2 as well. CN emission may be explained by ionization of C_2N_2 via charge transfer from the atomic ions followed by recombination and the fragmentation of the molecular ion. The fragments should be excited as the recombination reaction is highly exothermic. Concerning the nitrogen bands one can see that aspects similar to the $Ar/N_2/C_2H_2$ spectra are again encountered. However, the small emissions of the N_2^+(FNS) system still present in the spectra is an indication that not all the nitrogen is consumed in reactions with carbon and molecular nitrogen is formed and re-circulated into the vessel. The energy of the roto-vibrational $N_2(X, v)$ states matches the excitation energy of the CN(B) state. The resonant V-E energy transfer between the $N_2(X,v)$ and CN(X) may be a supplemental a source of excitation of CN radical especially at large distances from nozzle.

Conclusion

By comparing spectra obtained from thermal plasma fed with different gas mixtures injected in various modes (arc, expansion, by nozzle etching) one may conclude about chemistry aspects. It is proved that in case of Ar/N_2 plasmas the charge transfer and excitation transfer are equally important whatsoever the injection mode. Also, spectra may be explaining only considering strong re-association and re-circulation processes. In the case of Ar/N_2 plasmas injected with acetylene the chemistry favors the formation of CN radicals in comparison with formation of CH which leads to depletion of nitrogen molecules. In the case of Ar/N_2 plasmas injected with species from carbon surfaces (nozzle) the carbon is carried out in plasma via atomic nitrogen surface reactions. It is possible that plasma chemistry is driven by C_2N_2 molecules formed by re-association of CN radicals, which are ionized by charge transfer from the atomic ions, followed by recombination and release of fragments in excited state.

APPLICATION OF SYNTHETIC SPECTRA OF DIATOMIC MOLECULES TO PLASMA DIAGNOSTICS IN INDUSTRY

Frantisek Krcma, Hana Hajduchova
Faculty of Chemistry, Brno University of Technology, Purkynova 118, 612 00 Brno, Czech Republic, krcma@fch.vutbr.cz

Pavel Horvath
Faculty of Technology, Brno University of Technology, nam. TGM 275, 762 72 Zlin, Czech Republic

Abstract
The spectra simulated by using the molecular states constants are used for an estimation of neutral gas temperature and vibrational distributions of molecular states. The advantages of this procedure are a relatively simple calculation and a possibility to calculate the spectra of diatomic molecules for them the dipole transition matrixes is unknown. Another advantage of these simulations can also be an identification of the molecular spectra that are not included in spectral tables. The procedure allows the use of spectra with low resolution for the plasma parameters estimation. The disadvantages are especially the inaccuracy of the molecular constants and problems with an estimation of the spectral function of the experimental device.

Spectra calculation
The spectra calculation is based on well known Herzberg's book [1] and Kovacs's later calculations [2]. In the first step, the energy levels (vibrational and rotational) of both electronic states involved in the transition are calculated by the following equations (valid for $^1\Sigma \longrightarrow {}^1\Sigma$ transition only):

$$E_{evJ} = T_e + hc\omega_e\left(v+\tfrac{1}{2}\right) - hc\omega_e x_e\left(v+\tfrac{1}{2}\right)^2 + hc\omega_e x_e^2\left(v+\tfrac{1}{2}\right)^3 + \ldots + F_v(J) \quad ,$$
$$F_v(J) = \left(B_e - \alpha_e\left(v+\tfrac{1}{2}\right) + \gamma\left(v+\tfrac{1}{2}\right)^2 + \ldots\right)hcJ(J+1) - \left(D_e + \beta_e\left(v+\tfrac{1}{2}\right) + \ldots\right)hcJ(J+1)^2 + \ldots \quad , \qquad (1)$$

where all symbols except v and J are constants; their values for many electronic states can be found in Huber's tables [3], in many separate articles for various molecules or through Internet accessible databases. Some of the constants can be calculated from the other constants, for details see [1, 2]. In the case of the multiplet states, the energy levels must be calculated separately for each of the sublevels, for example for the doublet $^2\Sigma \longrightarrow {}^2\Sigma$ transition the $J(J+1)$ must be replaced by $(J+1/2)(J-1/2)$ for lower doublet level or by $(J+1/2)(J+3/2)$ for the higher level. These calculations are done separately for each vibrational band of the electronic transition.
The next step is a calculation of relative populations (vibrational and rotational) at a higher electronic state in the case of emission spectra or a lower state at absorption. The rotational population can be usually approximated by Boltzmann distribution

$$N(J) \sim e^{-\frac{F_J \cdot hc}{kT_R}} \quad ; \qquad (2)$$

the vibrational distribution can be used as Boltzmannian only in some cases and thus the programme allows the manual relative population input.
The intensities of the spectral lines are calculated by the following formula

$$I^{n',v',J'}_{n'',v'',J''} = const \cdot N_{v'} \cdot N_{J'} \cdot \nu^4 \cdot S_{J',J''} \quad , \qquad (3)$$

where $N_{v'}, N_{J'}$ are relative populations at the vibrational level v' and the rotational level J', v is the wave number of the spectral line and $S_{J',J''}$ is the transition strength. The factors $S_{J',J''}$ are functions of the spectral branch and both of the rotational quantum numbers and thus they must be calculated separately. For singlet-singlet transitions there are only 3 branches (P, Q, R – by change of the rotational quantum number), for doublet-doublet transitions there are 12 branches, for triplet-triplet transitions there are 27 branches etc. The other dependence of the $S_{J',J''}$ factors is the dependence on the total orbital momentum of both electronic states and on the change of this number at a dipole transition (allowed change is 0 or 1). The expressions for $S_{J',J''}$ factor calculation can be found in [2] for all types of dipole transitions.

The final step of one vibrational band simulation is the application of the spectral line profile (theoretically or experimentally obtained) on each of the electronic-vibrational-rotational line calculated by Eq. 3 and summarisation over all branches. The final synthetic spectrum in the adjusted spectral interval is thereafter obtained by a summarisation of the entire vibrational band lying in this interval.

Properties of the calculated spectra

The calculated spectra show some interesting features for applications. The high sensitivity of the calculated spectrum with low resolution in order of 0.2 nm is presented in Fig. 1. The accuracy of the rotational temperature obtained by the comparison of the calculated spectrum with the experimental spectrum is more or less the same as the accuracy of the classical estimation of the rotational temperature from the rotational structure.

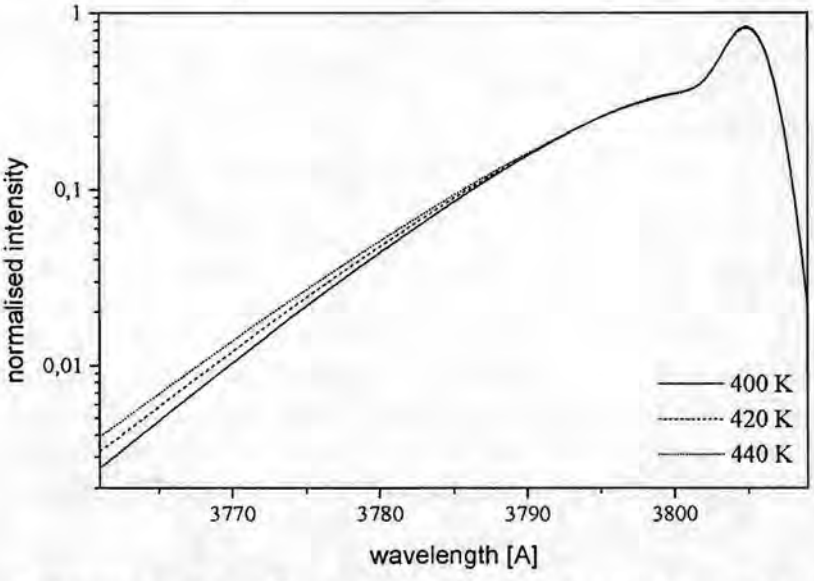

Figure 1: *Calculated spectra of the 2nd positive nitrogen 0-2 band with low resolution for slightly different rotational temperatures.*

The use of numerical simulation thus allows the use of a spectrometer with low resolution instead of an expensive device with high resolution. Using this method, it is also possible to mechanise the rotational temperature estimation from the experimental spectra. An example of estimation of rotational temperature is given in Fig. 2, where the experimental spectrum of the low radiate plasma-chemical deposition of polysilane layer is compared with the numerical spectrum.

The main problems of the calculated spectra emerge from the calculations of the energy levels of both the electronic states where the approximate expressions (Eq. 1) are used and the molecular constants are not known with sufficient accuracy. The shift in rotational line positions is a consequence of the above-mentioned situation as it is demonstrated in Fig. 3. The correspondence between the calculated spectrum and the experimental spectrum is quite satisfactory at lower rotational quantum numbers (at the right side of the figure) but at the higher quantum numbers a slight shift in the line position can be observed; the shift increases with an increase of the rotational quantum number. Of course, this effect could not be observed at the spectra with low resolution. The same effect can be seen in the positions of the vibrational band heads, if the calculated spectrum is compared with the experimental spectrum in a larger spectral interval, especially over more sequences.

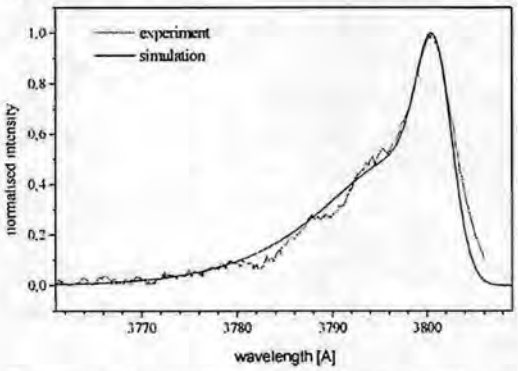

Figure 2: A correlation between an experimental spectrum (deposition of polysilane layer) and a simulation at 340 K (the 2nd positive nitrogen 0-2 band) at the low resolution.

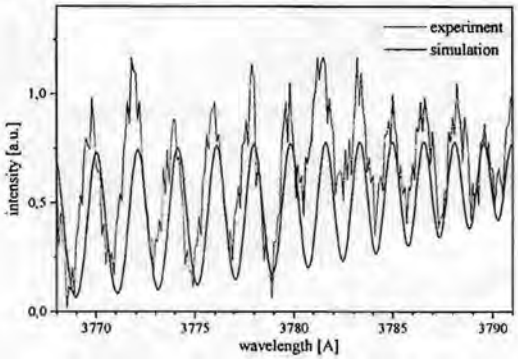

Figure 3: Shifts of the rotational line positions of the experiment and simulation (again the 2nd positive nitrogen 0-2 band) at the high resolution.

Application of the calculated spectra

The calculated spectra of diatomic molecules can be used for three main determinations of the plasma parameters. The first - and probably the most frequently used - field is a determination of the rotational temperature that is usually equal to the neutral gas temperature. The second field is a determination of the vibrational distribution, or the vibrational temperature in the case of the equilibrium or quasi-equilibrium plasma. The third, not commonly used application is an identification of some molecular spectral systems, which are not presented, in spectral tables (for example [4]). Due to the problems with the accuracy of the band head positions this application requires a well-experienced spectroscopist. For all these applications we now prepare a universal programme package whose scheme is presented in Fig. 4.

Initially, the diatomic molecule or molecular ion are introduced (or selected) and thereafter the initial and terminated molecular states are set. The molecular constants are searched in the structured database or - if the corresponding data files are not found - the constants can be inserted manually and automatically saved in database structure. In the database, there are not only constants necessaries for the calculation itself but there are also other parameters, such as the equilibrium internuclear distance and the data source.

The next step is the input of the simulation parameters. Here it is possible to specify the vibrational temperature, if it can be defined in the plasma, or the non-equilibrium vibrational distribution can be inserted manually. The rotational temperature is usually defined and it is inserted as the second simulation parameter. The comparison with an experimental spectrum is usually required and thus it is necessary to get the name of the file containing the experimental spectrum. Due to the fact that many currently used devices have not included the correction of the device spectral sensitivity function, our programme can also provide this

correction. The input of the spectral interval in which the comparison of calculated and experimental spectra will be done allows limiting the number of the calculated points. Finally, the single rotational line profile is specified.

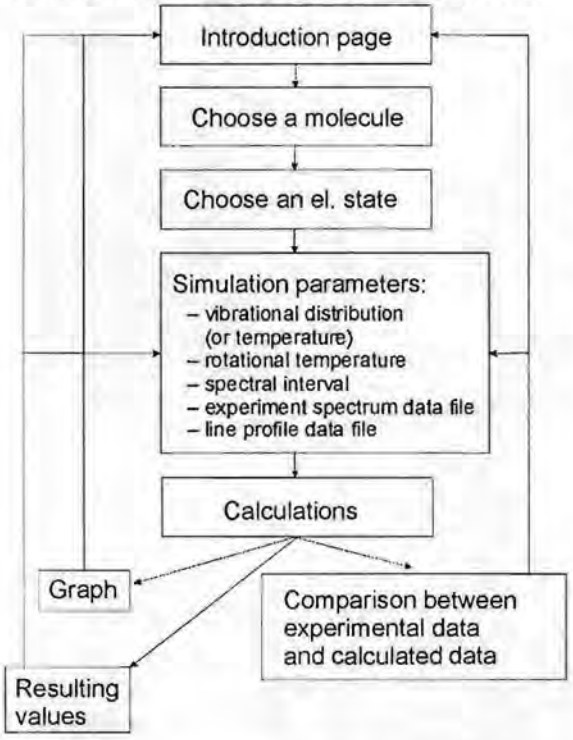

Figure 4: Scheme of the semi-automatised programme package for plasma parameters determination.

The spectra calculation uses the same wavelength positions as there are in the experimental data file. If a comparison with the experiment is not required the number of points must be specified, otherwise 1000 points are used. The main programme chooses the appropriate simulation programme by the type of the transition (singlet, doublet, with or without change of total orbital momentum, etc.). The calculation itself is done by the scheme described in the first paragraph.

The resulting spectrum is saved in a data file and displayed at the monitor with an experimental spectrum. For the best comparison, both spectra are normalised for the same integral value. In the present version the operator makes the comparison visually, in the future we can prepare a simplified version using a comparison of integral values in pre-defined wavelength ranges.

The last step is an optimisation of the simulation parameters to obtain the best correlation between the simulation and the experiment.

Conclusion

The numerical simulation of the diatomic molecular spectra is used for the estimation of the main plasma parameters. We demonstrated the advantages and disadvantages of a calculation based on molecular parameters. The basic scheme of the semi-automatised programme package has been shown.

This work was supported by the Grant Agency of Czech Republic, contracts No. 202/98/P258 and 104/99/0307, by the grant of Czech Ministry of Education No. VS 96084 and by Research Programme of the Czech Ministry of Education No. CEZ:J07/98:1431000019.

References

[1] Herzberg G.: Molecular Spectra and Molecular Structure, Vol. I: Spectra of Diatomic Molecules, D. Van Nostrand Co., New York 1950

[2] Kovacs I.: Rotational Structure in the Spectra of Diatomic Molecules, Akademiai Kiado, Budapest 1969

[3] Huber K. P., Herzberg G.: Constants of Diatomic Molecules, D. Van Nostrand Co., New York 1979

[4] Pearse R. W. B., Gaydon A. G.: The Identification of Molecular Spectra, John Viley, London 1976

Transport of H and H_2 in an expanding hydrogen plasma

P.Vankan, S.Mazouffre, R.Engeln, and D.C.Schram
Department of Applied Physics, Eindhoven University of Technology
P.O. Box 513, 5600 MB Eindhoven, The Netherlands

Introduction

Hydrogen plasma expansions can be found in a wide variety of objects, ranging from large scale, e.g. solar flares, to very small scale, e.g. laser spots [1]. At an intermediate scale many hydrogen plasmas concern the future of energy production like fusion plasmas and expanding plasmas used for thin layer deposition, e.g. hydrogenated amorphous silicon layers (a-Si:H) for the next generation solar cells [2].
In all of these examples the particle transport is a main issue. For instance in a-Si:H deposition hydrogen radicals are essential for the growth and quality of the layers. The location where the radicals are produced is different from the reaction location and different from the deposition location. Therefore it is of importance to understand how the radicals are transported between the different sites. In the experiments reported here the transport of hydrogen atoms and molecules has been investigated by measuring the density, temperature, velocity and velocity distribution in a pure hydrogen expanding plasma jet as a function of the axial position.

Experimental arrangement

A cascaded arc [3] operated at a current of 55 A and a voltage of 150 V is used as a plasma source. The plasma is created from a hydrogen flow of 3.5 slm and expands freely into a vacuum chamber. The stagnation pressure inside the arc is 0.14 bar and the background pressure in the vessel is either 20 Pa or 100 Pa. The arc is mounted on a movable arm enabling spatially resolved measurements.
The hydrogen atoms have been probed using the two-photon absorption Laser induced fluorescence technique (TALIF). Using this technique the hydrogen atom densities, temperatures, velocities and velocity distributions have been determined. The details of the technique are published elsewhere in this proceedings [4].
The hydrogen molecule densities have been measured using Rayleigh scattering. Since the H atom densities are known the H_2 densities can be determined from the Rayleigh signal. The scattering experiment has been performed using the 205 nm laser beam from the TALIF setup. Both techniques can be used simultaneously.

H_2 expansion

In Figure 1 the H_2 density has been plotted as a function of the axial position along the jet axis. In the supersonic part the density decreases until the stationary shock wave is reached. There the density increases because of forward flux conservation. In the background the density increases slightly, since the plasma flows at constant pressure. The H_2 density profile is in agreement with the free jet flow theory. The plasma flow has

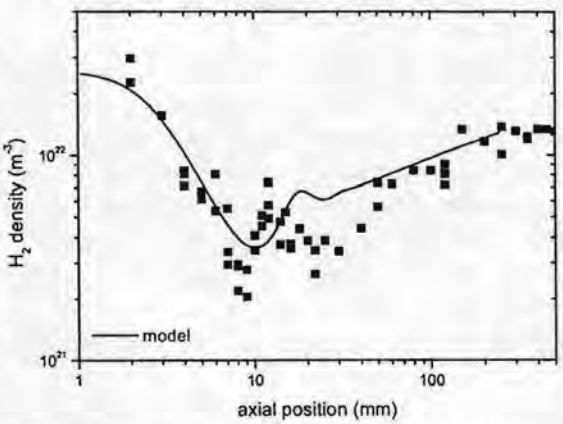

Figure 1: *The axial density profile of molecular hydrogen measured by Rayleigh scattering.*

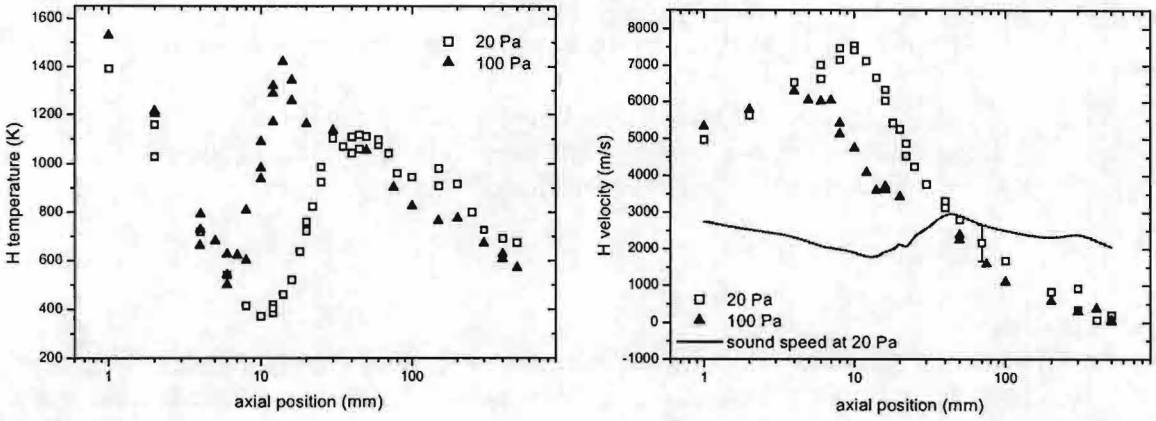

Figure 2: *H atom axial temperature and velocity as a function of the axial position along the jet centerline at 20 Pa and 100 Pa background pressure. The sound velocity at 20 Pa calculated from the temperature is depicted by a solid line.*

been modeled using a hydrodynamic code [5]. The model shows a good qualitative agreement with the measured H_2 densities.

H atom expansion

In Figure 2 the H atom axial temperature and velocity profile have been plotted. The different regions in the expansion have been determined from these profiles. The supersonic region ranges until the temperature increases and the velocity decreases. At the end of the shock wave, where the Mach disk is located, the velocity becomes smaller than the sound speed and the temperature starts to decrease because of heat transfer to the wall.

The H atom density profile has been plotted in Figure 3. In the supersonic part the expected density decay can be seen. Contrary to molecular hydrogen the H atom density profile does not exhibit a density jump at 20 Pa, and at 100 Pa the density jump is far too small. This directly means that the H atom forward flux is not conserved, i.e. the hydrogen atoms are lost from the core of the expansion. This loss is not due to volume recombination since the densities and temperatures in our plasma are far too low for the 3-body recombination process to be efficient. The only other way the radicals can be lost is due to diffusion out of the plasma jet [6]. The hydrogen radicals have a very high probability to recombine on the vessel walls. Combined with the very long residence time in the background this leads to a very large chance that the radicals are lost on the walls. The H atom partial pressure in the background is therefore very low inducing large gradients between the core of the jet and its surroundings. Those gradients are responsible for the diffusion out of the plasma.

This effect is a very general effect. It applies to all radicals having high wall recombination probabilities. This has far-reaching consequences. The radicals are the reactive particles in the plasma, i.e. the particles needed for the chemical processes. Due to the outward diffusion most of the radicals are lost and therefore the chemical potential of the plasma is

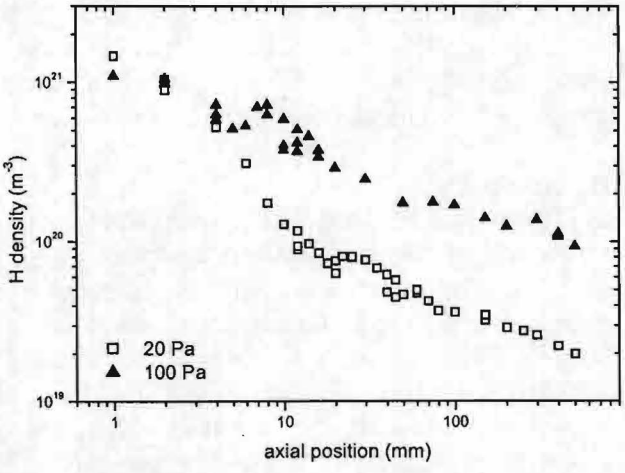

Figure 3: *The H atom density profile at 20 and 100 Pa background pressure.*

reduced drastically. In the design of vessels used for radical expansions one has to take the loss mechanism into account. The wall recombination probability can for example be reduced by using materials at which radicals show a low association degree. If acceptable for the process, higher background pressures can be used to improve the radical confinement.

Velocity Distribution Function

Due to the large axial velocity of the light H-atoms (and thus the large Doppler shift) and the relatively high temperature in the plasma it is possible to determine the velocity distribution function (VDF) from the spectral profile. A Gaussian spectral profile means a Gaussian VDF, determining the flow as Maxwellian, i.e. one mean velocity and one mean temperature. The flow is then in LTE. In Figure 4 H-atom VDF's have been plotted at a background pressure of 20 Pa at different axial positions along the expansion axis. The upper left plot is the VDF in the supersonic region. The VDF is Gaussian pointing to LTE for the H atoms in this region.

When moving along the expansion into the shock region (from z=10 to 50mm) we clearly see a departure from LTE. It can be explained by the essential property of shock waves: the transformation of a supersonic flow into a subsonic flow. During this process the supersonic VDF in front of the shock has to be adapted to the subsonic VDF behind the shock. The H atom VDF has been decomposed into two separate Gaussian VDFs, matching the conditions before and after the shock.

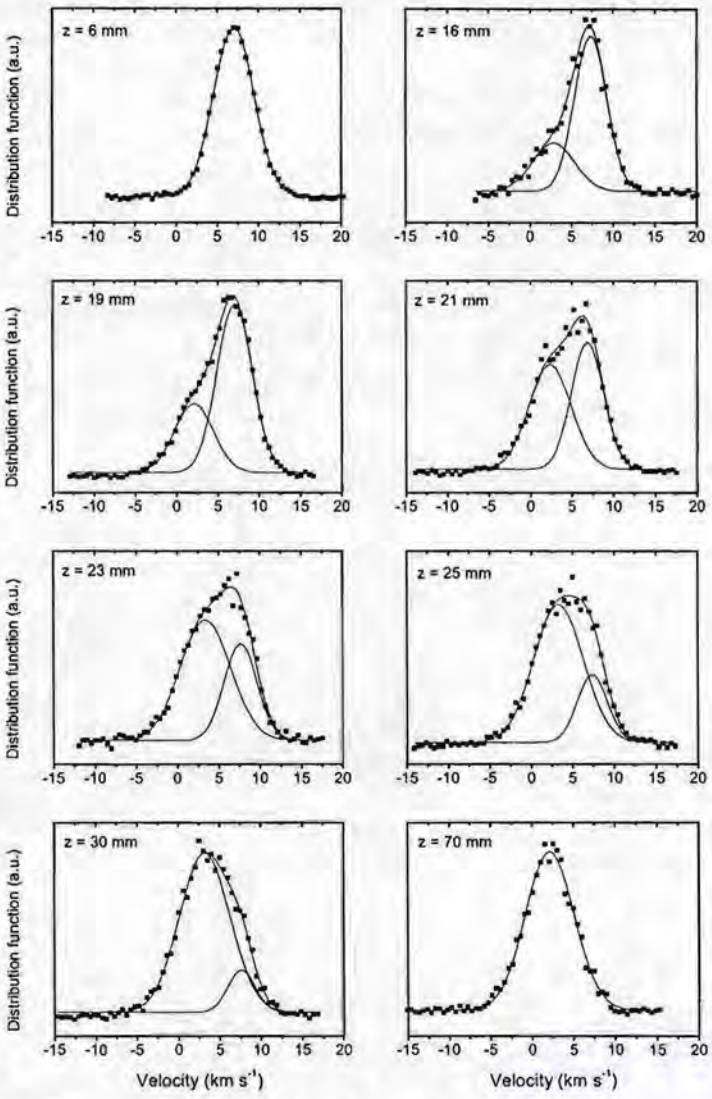

Figure 4: *The H atom velocity distribution function at eight different axial positions (z) in the course of the expansion at 20 Pa background pressure.*

Moving through the shock we can see that the density of the supersonic component is decreased to zero and that the subsonic component appears and the density is increased until the complete flow is subsonic as depicted in the lower right hand side plot. The bi-modal approximation of the VDF in a shock wave has been studied theoretically by Mott-Smitt [5]

Conclusions

The transport of hydrogen atoms and molecules has been investigated using the two-photon absorption Laser induced fluorescence and Raleigh scattering techniques. The results show that radicals can easily escape the plasma jet under the right circumstances. This has to be taken into account when the chemical potential of the plasma is needed. In the shock wave the flow is not in LTE. This is a direct consequence of the transfer of a supersonic flow into a subsonic flow.

References

[1] D.C.Schram, S.Mazouffre, R.Engeln, and M.C.M.van de Sanden in *Atomic and Molecular Beams,* edited by R.Campargue, Springer, New York, 209 (2001)

[2] W.M.M.Kessels, M.C.M.van de Sanden, and D.C.Schram;J.Vac.Sci.Technol. A, **18**, 2153 (2000)

[3] G.M.W.Kroessen, D.C.Schram, and J.C.M.de Haas, Plasma Chem. Plasma Process., **10**, 551 (1990)

[4] see the contribution by S.Mazouffre, P.Vankan, R.Engeln, D.C.Schram in this proceedings.

[5] M.Playez; Von Karman Institute, Brussels

[6] S.Mazouffre, M.G.H.Boogaarts, J.A.M.van der Mullen, D.C.Schram; Phys.Rev.Lett **84**, 2622 (2000)

[7] H.M.Mott-Smith; Phys.Rev., **82**, 885 (1951)

Feasibility study on X-ray spectroscopy on HID lamps

Xiaoyan Zhu, Joost van der Mullen
Eindhoven University of Technology
The Netherlands

Introduction

HID lamps are widely used as light sources because of their efficiency and high intensity. In order to understand the plasma behavior and transport processes in HID lamps, the gas density distribution and temperature profile should be known.
HID lamps have several properties that make it difficult to measure the density in the lamps. First of all, the fused silica or PCA(polycrystalline alumina) envelope is not of good optical quality. It means that PCA is translucent (light can pass), but not transparent (light is diffused). Therefore optical access is complicated, it impedes the optical access, especially in the outer regions of the discharge. So model lamps have been used to do experiments, but these lamps are not exactly the same as the real lamps.
Secondly, the high pressure in the HID lamps also gives difficulties. For various lines, the plasma is optically thick.
Therefore the use of optical techniques is limited. It is almost impossible to detect the spatial distribution of elements in a lamp with PCA tubes with high resolution. Recently X-ray techniques have been used to detect the density distribution in HID lamps [1,2]. This poster will discuss the feasibility study of X-ray technique in diagnostic on HID lamps.

Why to use X-ray techniques

X-ray techniques have the advantages in contrast to the optical methods:
Firstly, the X-ray cross-section depends only weakly on electronic or chemical state of the atom.
Secondly, an X-ray absorption measurement only depends on the absolute density of the detected atoms. The electron density, electron temperature, gas temperature, gas pressure or chemistry do not influence the absorption.
Thirdly, the lack of the background of X-ray emission from the lamp is also an advantage.
Fourthly, X-ray can penetrate the whole region in the lamp, especially in the region close to the electrodes.

Methods

Two X-ray methods may be used to detect the elements distribution in HID lamps:
1. X-ray absorption spectroscopy on mercury (Hg).
When the lamp is burning, the density in the lamp is mainly determined by Hg. In order to detect the Hg density distribution, a Mo(Kα,Kβ) X-ray tube should be used, so the absorption by the PCA or fused silica is small compared to the absorption by Hg.
The X-ray absorption experimental setup is shown in Fig.1.

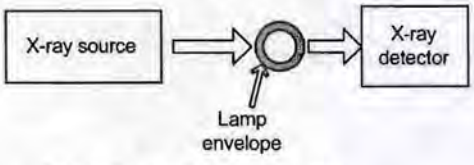

Fig.1. *X-ray absorption setup*

2. X-ray fluorescence spectroscopy.
For additives in HID lamps, such as NaI, CeI_3,TlI, the densities are relatively low compared to the mercury density, so that X-ray absorption is not suitable to detect the additive densities. X-ray fluorescence on the other hand is more sensitive, but it requires a more intensive X-ray beam and more energetic X-ray photons. Therefore a high energy and high flux of X-ray source is needed to do the X-ray fluorescence of the additives.
The X-ray fluorescence experiment setup is shown in Fig.2.

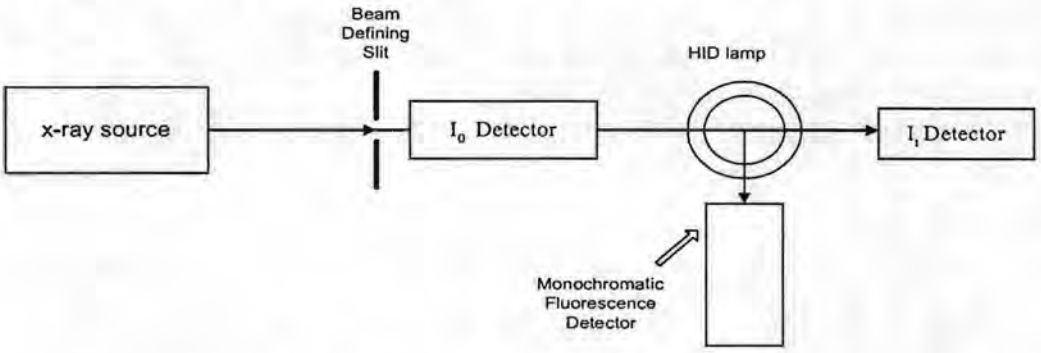

Fig.2. *X-ray fluorescence setup*

A problem might be that PCA is polycrystalline alumina, which may cause serious X-ray scattering on the envelope, especially in the situation that the photon energy is high. This may be the limiting factor for X-ray absorption or fluorescence measurement.

Experiment
For the HID lamp, the spatial density distribution and temporal profile of the density need to be determined.
1. Spatial density distribution. Mapping the lamp to the detector, the spatial resolution should be within 0.1mm.
2. Temporal profile of the density. In order to understand the plasma transport in the lamp, the density distribution in one ac period need to be detected. The resolution should be at least 20μs. Moreover the starting, re-strike and switch-off phenomena must be studied as well.
The transmittance of the X-ray by Al_2O_3 tube and Hg (gas) are shown in Fig.3 and Fig.4.

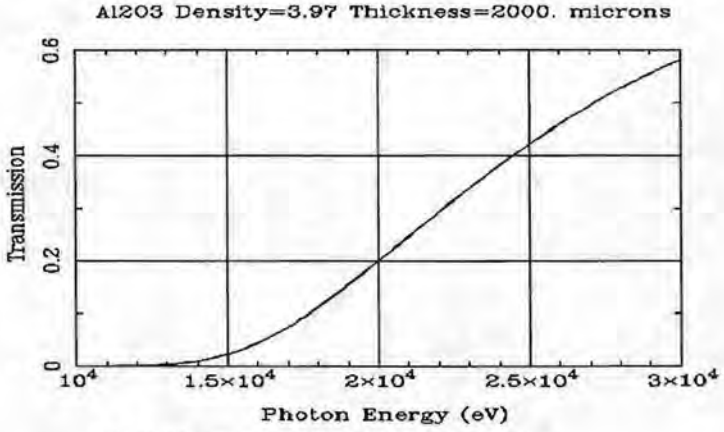

Fig.3. *Transmittance of Al_2O_3(solid state)*

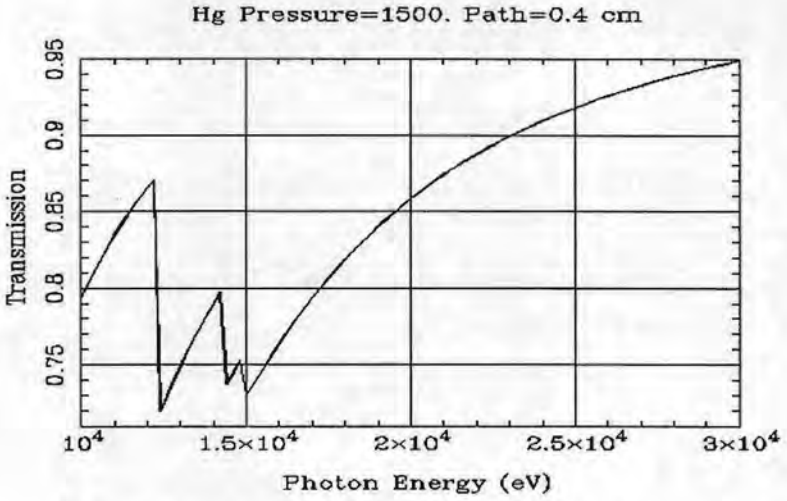

Fig.4. *Transmittance of Hg Gas. (Pressure is 1500 torr)*

Possible difficulties and solutions

1. The resolution of the X-ray detector corresponding to the energy determines the limit of the absorption experiment. For example, for X-ray photon energy is 15kev, the absorption by Al_2O_3 tube is about 95%, the absorption by Hg is about 27%. So only about 1% of the flux of X-ray is received on the detector. That means the flux limit of the X-ray detector is very important. If X-ray energy is higher, then the absorption of the PCA tube is less, but the absorption of the Hg also less, so it will also affect the resolution of the signal.
2. If in HID lamps the dominating gas is not only Hg but also other noble gas like Xe, then the absorption measurement will have difficulties to distinguish between Hg and Xe.
3. For time-resolved measurement, if the X-ray flux is not high enough to get a good absorption image picture, then the exposure time for one picture will be long. If so a higher energy and higher flux X-ray source will be needed.
4. Now a practical solution for detecting the additives instead of X-ray fluorescence might be the combination of the X-ray absorption experiment with the emission spectroscopy of the optically thin line in HID lamps to get the information of the density distribution of additives.

References

[1] J.J. Curry, M. Sakai, and J.E. Lawler. *Measurement of Hg distribution in a high-pressure arc lamp by x-ray absorption.* J. Appl. Phys. **84**, 3066(1998).

[2] Timothy Fohl, Jerry M. Kramer, and Joseph E. Lester. *X-ray measurements of mercury density in arc discharge lamps during warm-up and following extinction.* J. Appl. Phys. **73**, 46(1993)

Dielectric Cherenkov maser with a dielectric rod and plasma column in a Slow-Wave Waveguide

B. Shokri, H. Ghomi, and H. Latifi

Department of Physics and Laser Research Center of Shahid Beheshti University, Evin, 19839, Tehran, Iran.

I. INTRODUCTION

Dielectric Cherenkov maser, traveling wave tube (TWT) and backward-wave oscillator (BWO) usually include an intense electron beam as their active gain medium.[1] However, use of these beams produces some difficulties; not only must the injection of the electron beam be lower than the space charge limit but recent research shows that space charge wave limitations are decreased by injection of background plasma in interaction region of electron with the wave. These studies show that the presence of plasma in the dielectric Cherenkov maser linearizes the growth rate and increases the electromagnetic wave energy. It has experimentally shown that injection of background plasma to BWO increased efficiency to nearly 40 percent.[2] Following this experiment, theoretical studies on plasma filled dielectric Cherenkov maser and BWO have made progress and it can be safely concluded that the variation of plasma density affects the interaction between the wave and electron beam.[3] In this paper, we shall present a self-consistent relativistic field theory of a dielectric rod Cherenkov maser with a annular plasma and we shall compare its results for two different radii of the thin annular relativistic electron beam (TAREB) and with pervious work.

II. EQUILIBRIUM CONFIGURATION AND DISPERSION EQUATION

The equilibrium model which we employ is shown in Fig.1. The plasma column with outer radius R_p and inner radius a and electron beam are around of a dielectric rod with a relative permittivity ϵ_r and with radius a, enclosed by a loss-free conducting wall with radius b. For purpose of analytic simplification, it is assumed that the plasma column has a sharp-boundary with plasma density $n_p(r) = n_{po}\theta(r-a)H(R_p-r)$, where n_{po} denotes the equilibrium density of the plasma column, R_p denotes the plasma column radius, H is the Heaviside function [4] and θ is step function.. The TAREB with radius R_b, thickness ΔR_b, density $n_b(r) = n_{bo}\Delta R_b\delta(r-R_b)$ and equilibrium velocity $\mathbf{v} = v_0\mathbf{e}_z$,[2] propagates uniformly only along the symmetrical axis (i.e.,z) of the dielectric rod. For analytic simplification it is assumed that the TAREB does not diverge.

We can obtain the perturbed electric field equation from Maxwell's equations[3–5]

$$\nabla^2\delta\mathbf{E} - \nabla(\nabla.\delta\mathbf{E}) + \epsilon_d(\omega^2/c^2)\delta\mathbf{E} = i\omega\mu_0\delta\mathbf{J}, \qquad (1)$$

where $\epsilon_d = \epsilon_r$ and $\delta \mathbf{J} = 0$ for $0 \leq r \leq a$, and for $a \leq r \leq b$, $\epsilon_d = 1$. In this idealized model, only the interaction of the longitudinal field with electron beam exists.

By solving Eq. (1) and applying the boundary conditions, one can obtain the dispersion equations

$$F(\omega - \beta v_0)^2 = \frac{\omega_b^2 p \Delta R_b}{1 - \omega_p^2/\omega^2}\left(\frac{B(pR_b, pR_p)A(k_c b, k_c R_p)}{\gamma_0^2 A(pR_b, pR_b)} D_1 + \frac{B(k_c R_p, k_c b)A(pR_b, pR_p)}{\gamma_0^2 A(pR_b, pR_b)} E_1\right), a < R_b < R_p \tag{2}$$

$$F(\omega - \beta v_0)^2 = \frac{\omega_b^2 k_c \Delta R_b B(k_c b, k_c R_b)}{\gamma_0^2 A(k_c R_b, k_c R_b)}(B(k_c R_p, k_c R_b)D_2 - A(k_c R_b, k_c R_p)E_2), R_p \leq R_b < b, \tag{3}$$

where

$$F = A(k_c b, k_c R_p)\left(\frac{p}{k_c}(1 - \frac{\omega_p^2}{\omega^2})J_0(qa)A(pR_p, pa) - \frac{p^2 \epsilon_r}{k_c q} J_0'(qa)B(pR_p, pa)\right) +$$
$$B(k_c R_p, k_c b)\left(\frac{p\epsilon_r}{q}(1 - \frac{\omega_p^2}{\omega^2})J_0'(qa)A(pa, pR_p) - (1 - \frac{\omega_p^2}{\omega^2})^2 J_0(qa)C(pa, pR_p)\right), \tag{4}$$

$$D_1 = \frac{p^2 \epsilon_r}{q k_c} J_0'(qa)B(pR_p, pa) - \frac{p}{k_c}(1 - \frac{\omega_p^2}{\omega^2})J_0(qa)A(pR_b, pa), \tag{5}$$

$$E_1 = \frac{p\epsilon_r}{q}(1 - \frac{\omega_p^2}{\omega^2})J_0'(qa)B(pR_p, pa) - (1 - \frac{\omega_p^2}{\omega^2})^2 J_0(qa)A(pR_b, pa), \tag{6}$$

$$D_2 = (1 - \frac{\omega_p^2}{\omega^2})^2 J_0(qa)C(pR_p, pa) + \frac{p\epsilon_r}{q}(1 - \frac{\omega_p^2}{\omega^2})J_0'(qa)A(pa, pR_p), \tag{7}$$

$$E_2 = \frac{p^2 \epsilon_r}{k_c q} J_0'(qa)B(pR_p, pa) - \frac{p\epsilon_r}{k_c} J_0(qa)A(pR_p, pa), \tag{8}$$

$$k_c^2 = \frac{\omega^2}{c^2} - \beta^2, \quad q^2 = \epsilon_r \frac{\omega^2}{c^2} - \beta^2, \tag{9}$$

$$A(x, y) = J_0(x)Y_0'(y) - J_0'(y)Y_0(x), \tag{10}$$

$$B(x, y) = J_0(x)Y_0(y) - J_0(y)Y_0(x), \tag{11}$$

$$C(x, y) = J_0'(x)Y_0'(y) - J_0'(y)Y_0'(x), \tag{12}$$

and J_0 and Y_0 are Bessel and Neumann functions of the zero order, respectively, and superscript prime denotes the derivative.

IV. DISCUSSION

The calculation results, which are obtained by solving the dispersion equations for TM_{01} are shown in Figs. 2 and 3. In these calculations the parameters of the frequency such as ω_p, ω_b, G_1, G_2, G_3, and G_4, are normalized by b/c, and the parameters of the radii such as R_b, R_p, a and β are normalized by b. In these calculations we have defined $\epsilon_r = 2.1$, $\omega_0 b/c = 14$, $\beta b = 16.3$, $a/b = 0.5$, $R_p/b = 0.7$, $\Delta R_b/b = 0.05$, $\omega_p b/c = 2.5$, $I_b = 1kA$ and $V_0 = 0.6(MV)$.

The plots of the growth rate as a function of the beam current and the normalized electron plasma frequency are shown in Figs. 2 and 3. It is shown that, the normalized

growth rate increases with increasing the beam current. This increment of growth rate for the TAREB surrounding the plasma column ($R_b/b = 0.85$) is smaller than that for the TAREB inside the plasma column ($R_b/b = 0.6$). The increase of growth rates obtained in the Ref. 3, is similar to our work but that is much smaller than that of our work, as shown in Fig. 2. In Fig. 3, the growth rate increases with increasing plasma frequency for the TAREB inside the plasma column and decreases for the TAREB surrounding the plasma column. In the work 3 the growth rate decreases slightly and is larger for the TAREB surrounding the plasma column than that for the TAREB inside the plasma column. However, the growth rates of our work for different radii of the TAREB is much lager than that of those work.

VI. SUMMARY AND CONCLUSIONS

In this paper we consider the interaction of electromagnetic wave with TAREB and plasma in the absence of an external magnetic field inside the dielectric rod Cherenkov maser slow-wave waveguide. This medium includes a dielectric rod with a plasma column and a TAREB. The effects of the beam current and the background plasma density on the growth rate of the wave are numerically calculated and discussed. Comparing the growth rates of the TM mode for two different radii of the TAREB, surrounding and inside the plasma, it can be concluded that the former is greater than the latter. Also results are numerically compared with pervious works and is shown that the effect of accelerating voltage, beam current and plasma density on the growth rate, is formally similar but grater than that obtained in the pervious works. So we can conclude that, by a placing dielectric rod in the center of waveguide, the growth rate of the wave increases.

References

[1] V. L. Ganatstein and I. Alexeff *High Power Microwave Sources* (Artech, Boston, MA, 1987)

[2] Y. Carmel, K. Minami, W. Lou, R. A. Kehs, W. W. Destler, V. L. Ganatstein, D. K. Abe, and J. Rodgers, IEEE Trans. Plasma Sci. **PS-18** 497 (1990)

[3] Wu Jian-Qiang, Phys. Plasma **4**, 3064 (1997).

[4] H. P. Freund, M. A. Kodis and N. R. Vanderplaats, IEEE Trans. Plasma Sci. **PS-20**, 543 (1992).

[5] B. Shokri, H. Ghomi, and H. Latifi, Phys. Plasma **7**, 2671 (2000).

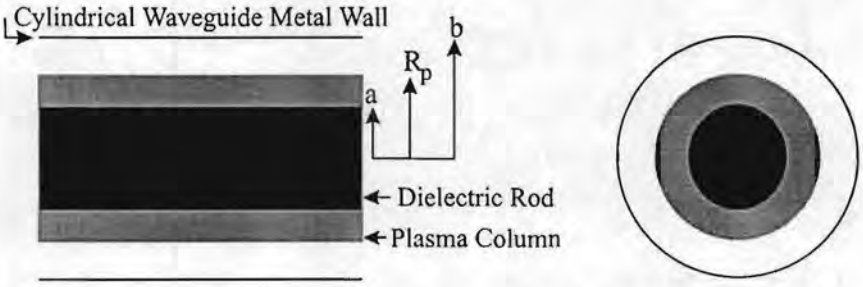

Figure 1: Dielectric rod slow-wave system with a plasma column.

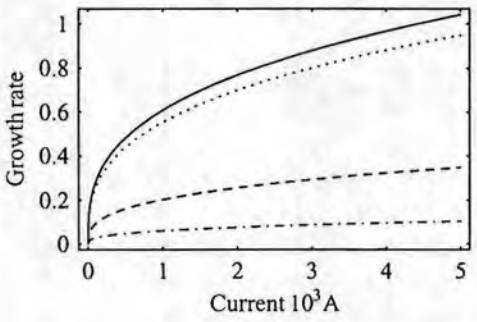

Figure 2: Plot of the growth rate of the wave as a function of the beam current for different radii of the TAREB.

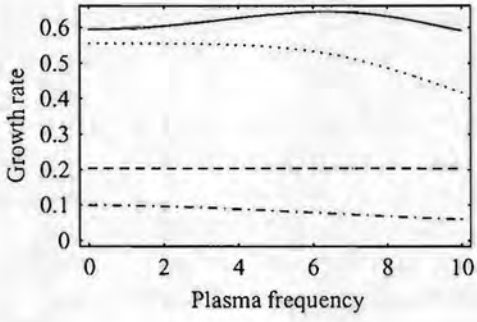

Figure 3: Plot of the growth rate of the wave as a function of the electron plasma frequency for different radii of the TAREB. The solid lines represent the TAREB inside the plasma column ($R_b/b = 0.6$) and the doted lines represent the TAREB surrounding the plasma column ($R_b/b = 0.85$). The dashed lines represent the TAREB surrounding the plasma column ($R_b/b = 0.65$) and the dotted dashed lines represent the TAREB inside the plasma column ($R_b/b = 0.45$), in the last work,[3] ($\epsilon_r = 2.1$, $\omega_0 b/c = 14$, $\beta b = 16.3$, $a/b = 0.5$, $R_p/b = 0.7$, $\Delta R_b/b = 0.05$, $I_b = 1kA$ and $V_0 = 0.6(MV)$).

Characterisation of an ICP source: Electron density profiles in He, Ar and H_2/He

P. Scheubert[1], P. Awakowicz[1], U. Fantz[2]

[1] *Lehrstuhl für Technische Elektrophysik, Arcisstr. 21, Technische Universität München, D-80290 München*
[2] *Lehrstuhl für Experimentelle Plasmaphysik, Universität Augsburg, Universitätsstrasse 1, D-86135 Augsburg*

1 Introduction

During the last years planar inductively coupled plasma sources (ICP) became more and more popular for industrial applications as well as for principle research projects due to two obvious key advantages. First of all, ICPs can easily serve as high density plasma sources. Electron densities up to $10^{18}\,m^{-3}$ can even be achieved in low process pressure ($\approx$ 1 Pa). The second advantage is the mutual independence of discharge power and bias voltage. Parasitic coupling can be suppressed easily by using a Faraday shield. If additional bias voltage is required (like for dry etch applications) it can be adjusted by introducing an additional capacitive electrode in the discharge and applying a certain amount of RF-power. Due to the increasing application of planar ICPs the demand of theoretical and experimental investigations is large. Of particular interest is the correlation of external parameters like process pressure and discharge power with internal parameters like average electron density, ion fluxes or electron temperature. Additionally, the influence of discharge geometry on relevant process properties like homogeneity of ion flux to a substrate is relevant. Obviously, simulations can provide valuable answers to those questions but have to be verified by measurements.

In a previous publication [1] simulations based on a electrodynamic-hydrodynamic plasma model have been verified by experimental results from Langmuir probe and emission spectroscopy for the case of helium plasmas. In this paper, the influence of different working gases on the important discharge parameters like electron density will be shown. Theoretical and experimental results for argon and helium discharges as well as admixtures of 10% hydrogen to helium are presented. The performed investigations revealed essential correlations between RF-generator power, process pressure and electron density as well as temperature.

2 Experimental and Diagnostics

A cylindrical symmetric ICP chamber was equipped with five flanges for diagnostic purposes (Langmuir probe and optical emission spectroscopy). The discharge chamber was 150 mm in diameter (d) and 100 mm in height (h) as shown in Fig. 1.

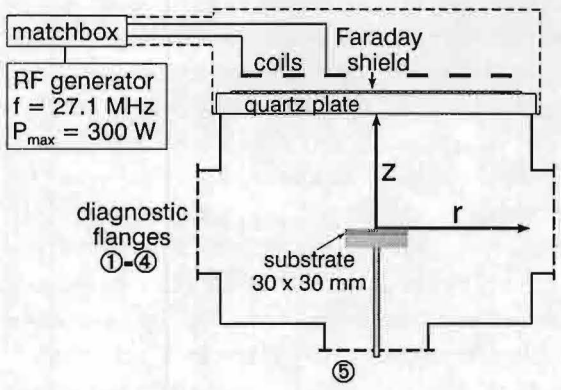

Figure 1: Schematic experimental setup.

The chamber wall was water cooled. Inductive coupling was achieved by using three coils above a quartz plate (thickness 10 mm) in a distance of 7 mm. A grounded Faraday shield was placed between the coils and the quartz plate in order to avoid capacitive components which might cause self bias. An RF-generator operating at a frequency of 27.1 MHz could deliver a maximum power of 300 W. A network consisting of two adjustable capacitors was used as a matching network.

A minimal background pressure of some 10^{-5} mbar was achieved using a turbo pump system. Typical operating conditions were a gas inlet of 20 sccm and a RF-generator power of 250 W in the pressure range of 5 - 50 Pa. A substrate (30 × 30 mm) can be placed in the center of the chamber, defining the origin of an r, z cylindrical coordinate system as can be seen in Fig. 1.

Electron density profiles were obtained by the Langmuir probe system *APS3*-system discussed in detail in [1]. An important feature of this system is the effective RF-compensation. Spatially dependent measurements in radial or axial direction are enabled by means of a high-speed stepping motor and membrane bellows which serve as ultra high vacuum feed-through. Radial parameter-profiles with a step distance of 1 cm and total length of 40 cm can be obtained in not more than one second. In order to minimize the disturbance of the plasma at the position where the measurement takes place, the probe tip is guided in a small quartz or ceramics capillary tube (Ø 1 mm, 15 mm length) mounted at one end of an aluminum oxide tube (Ø 8 mm, 250 mm length) which enables radial or axial resolved measurements over this length. While remaining in zero-position the probe tip is automatically drawn back into the capillary tube to prevent it from coating or etching in reactive plasmas.

The transport processes in the reactor chamber were described by hydrodynamic balance equations derived from Boltzmann's equation [2], [3]. For the ions, conservation of mass and momentum were considered. Electrons were treated by using a mass as well as an energy balance equation. For details see [4], [1]. The plasma model was coupled with an electrodynamic model to be able to calculate the energy transfer from the RF-field to the plasma.

3 Results

A comparison of theoretical and experimental data is shown in Fig. 2. For pressure values in the range $5 - 50$ Pa measured and calculated axial (z-direction) electron density profiles are in excellent agreement (Fig. 2a). With increasing pressure the discharge becomes more localized in the proximity of the coils i.e. in the region with high z-values.

The peak value of the electron density shows an increase with neutral gas pressure for constant RF generator power (P_{RF} = 250 W). For the simulation two important input paramters were needed: The gas temperature and the RF power transferred to the

plasma. While the temperature could be determined by optical emission spectroscopy the RF power heating the plasm could not be measured. Therefore the input power for simulation was chosen to match the peak electron density of measurement and simulation. This yields the efficiency of the whole RF system. The input power was obtained to be 50, 70, 95 and 112 W at 5, 10, 20 and 50 Pa, respectively. The system efficiency increases from 20% to 45%. In order to illustrate the change in shape, Fig. 2c shows the calculated normalized density profiles for the various pressures. Clearly visible is a shift towards the quartz window with increasing pressure. This correlates with Fig. 2b where calculated as well as measured mean electron energy profiles are shown for the same series of measurements. The increase in temperature with increasing z-value, i.e. in proximity of the coils, indicates that the heating of the discharge takes only place in a thin region directly below the quartz window. This is also in accordance with the electrodynamic model which predicts an exponential decrease of the heating with increasing distance from the antenna. In radial direction the electron density profiles are represented by a Bessel function (zero order) whereas the mean electron energy remains constant over the radius. In summary, the agreement of measured and calculated data is excellent.

In Fig. 3 the electron density, measured by the Langmuir probe, in the discharge center of a 20 Pa helium discharge is plotted versus the RF generator power. The electron density depends almost linearly on the input power which is in accordance with theoretical considerations. The corresponding mean energy seems to depend only very slightly on the generator power.

The localization of the discharge in the heating zone which was observed for a helium pressure higher than 20 Pa can also be observed for other gases. In Fig. 4 normalized axial electron density profiles for argon discharges operating at 1, 2 and 5 Pa are shown, measured by the Langmuir probe. The corresponding peak values are $n_e = 21$, 14 and 8.3 $\times 10^{16} m^{-3}$ at a RF generator power of $P_{RF} = 50$, 74 and 250 W, respectively. Comparing peak electron densities of argon and helium plasmas of the same RF generator power and similar pressure (1 Pa and 5 Pa), argon yields higher densities ($n_e = 21 \times 10^{16} m^{-3}$) as helium ($n_e = 3.8 \times 10^{16} m^{-3}$) which is also expected from theoretical calculations. In analogy to helium discharges for higher pressure the discharge tends to become more constricted and the maximum moves towards the quartz window. Remarkable is that this already happens for pressure values of a few Pascal while for the case of helium (c. f. Fig. 2) the locality starts to develop for pressure values above 20 Pa. The reason is the different mass of helium and argon ions as well as the different resonant charge exchange cross sections. The ambipolar diffusion process is for argon much slower than for the light and mobile helium ions.

The influence of different working gases on electron density illustrated in Fig. 5. Axial electron density profiles are compared for $P_{RF} = 250$ W for an argon discharge at 1 Pa, a helium discharge at 20 Pa and helium discharge with an admixture of 10% of hydrogen at 20 Pa. Remarkable is the absolute value of the electron density which is almost equal for an argon discharge (1 Pa) and for helium (20 Pa). The admixture of 10% H_2 to helium results in a drastic decrease of the electron density. Simulations for helium plasmas at 20 Pa agree well with the measurements. In case of hydrogen admixtures a deviation in the remote plasma zone is indicated. The different electron densities can be explained again by the transport properties of the different gases. In the case of argon the large ion mass as well as the resonant charge exchange cross sections are the reason that the diffusion process is relatively slow which results in an accumulation of electrons in the discharge center and a comparably high electron density.

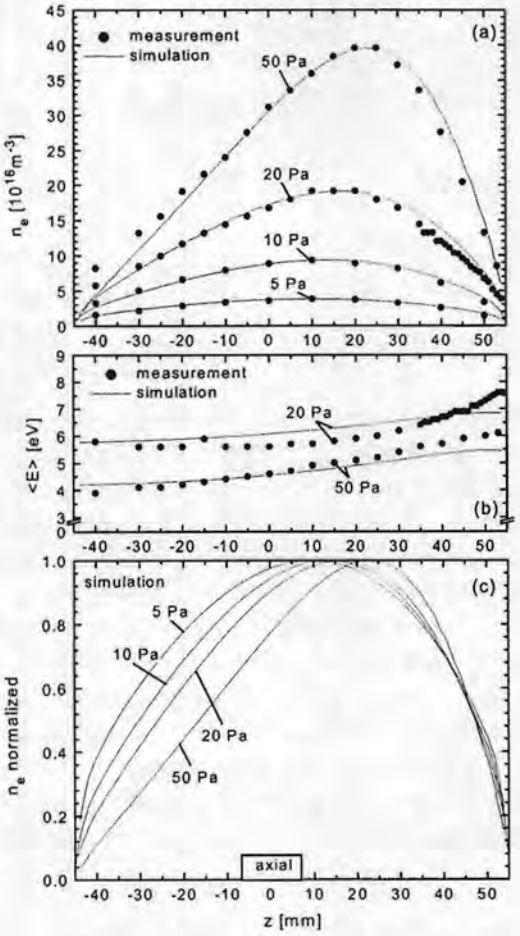

Figure 2: Axially resolved probe measurements and simulations of electron density (a),(c) and mean energy (b) for helium discharges.

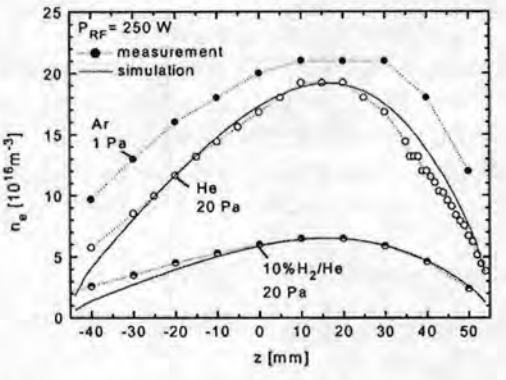

Figure 5: Axial electron density profiles depending on the working gas.

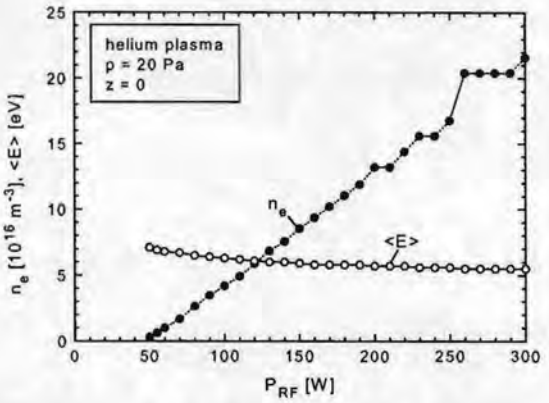

Figure 3: Measured electron density and mean energy in the discharge center versus of the RF generator power.

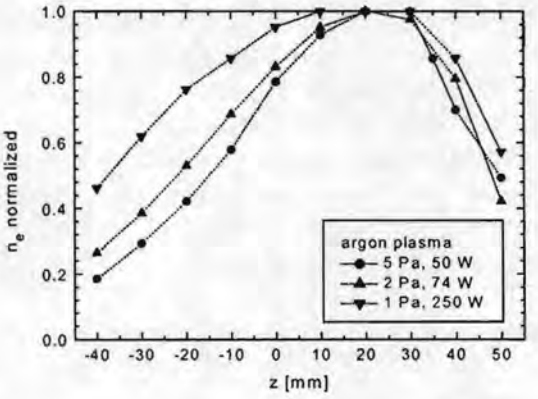

Figure 4: Measured axial electron density profiles for argon discharges (normalized).

References

[1] P. Scheubert, U. Fantz, P. Awakowicz, and H. Paulin. Experimental and theoretical characterization of an ICP source. *submitted to J. Appl Phys.*, 2000.

[2] V.E. Golant, A.B. Zhilinsky, I.E. Sakharov, and S.C. Brown. *Fundamentals of plasma physics.* John Wiley and Sons, New York, 1980.

[3] I.P. Shkarofsky, T.W. Johnston, and M.P. Bachynski. *The particle kinetics of plasmas.* Addison-Wesley, New York, 1996.

[4] P. Scheubert, P. Awakowicz, R. Schwefel, and G. Wachutka. Diagnostics and modelling of an ICP discharge. In *Frontiers in Low Temperature Plasma Diagnostics III*, page 171, Saillon, Switzerland, 1999.

Expanding Thermal Plasma for Case Hardening of Surfaces

R.P. Dahiya, A.K. Bandopadhyay, R.K. Garg and S.S. Chauhan
Centre for Energy Studies
Indian Institute of Technology, New Delhi – 110 016
e-mail : rpdahiya@ces.iitd.ernet.in

Introduction

The technology of case hardening has numerous industrial applications for the treatment of several components and parts of automobile engines and other machineries. Surfaces of these components and parts, subjected to stresses during their usual operations, are nitrided to minimise their wear and tear. The conventional process of surface hardening utilises ammonia gas or salt bath at high temperatures. Advanced process of plasma nitriding is now-a-days replacing the conventional ammonia gas or salt bath type thermal nitriding methods. In the process of plasma nitriding the substrate is given a negative bias and immersed in hydrogen seeded nitrogen plasma generated in a vacuum vessel. There is no need to use the polluting substance ammonia. Positively charged ions and reactive radicals created in the ionised medium interact with the negatively biased substrate and contribute to the formation of hardened surface layers penetrating beneath the substrate surface. The plasma nitriding process is not only more efficient than the conventional thermal process, it operates at lower temperatures[1] resulting into less distortion of the components. Moreover, it has minimal environmental hazards.

Plasma nitriding by glow discharge method is well established[2] for case hardening of materials. In this method the work piece is used as cathode to generate low density, non-equilibrium plasma. In this paper we have investigated case hardening of ferrous material in high plasma density, thermal plasma system. All the species present in the plasma, i.e. neutrals, ions, electrons and radicals are in thermal equilibrium.

Thermal Plasma System

The experimental system consists of [3] a cascaded arc plasma source, vacuum vessel, roots blower cum rotary pumping system, gas injection manifolds, substrate bias power supply, thermocouples and electrostatic probe for plasma diagnostics. Argon gas is injected in the cathode region of the cascaded arc to initiate the plasma and nitrogen and hydrogen gas are added in the arc channel through an orifice in a plate. Experimental parameters used to perform the surface nitriding are given in Table 1. The flow of respective gases is controlled

Table 1. Experimental parameters

Chamber diameter	30 cm
Chamber length	125 cm
Pumping speed	1000 m^3/hr
Central bore inside cascade plates	2 to 4 mm
Gas composition	Ar + H_2 + N_2
Arc current	30-60 A

by means of mass flow controllers. The working pressure is kept in the range of 50-100 Pa. A programmable logic control (PLC) unit is configured with the system to control its sequential operations. The thermal plasma emanating from the nozzle embedded in the cascaded arc anode expands radially while propagating axially away from the arc source in the vacuum vessel. An electrostatic Langmuir probe has been handy in making the spatial mapping of the electron density and electron temperature in radial direction and a cromel-alumal thermocouple attached to the sample immersed in the plasma provides its temperature.

Results and Discussion

The thermal plasma nitriding experiments are performed on untreated steel samples cut from crankshaft meant for internal combustion engines. It is EN8 (1040 AISI) steel, which contains typically 0.35-0.45 % C, 0.1-0.35 % Si, 0.6-0.9 % Mn, 0.06 % S and 0.06 % P. There is no need of auxiliary heating of the sample inside the plasma. It attains steady state temperature ~ 800 K after nearly 30 minutes of operation. The time and temperature, however, depend on the power supplied to the arc source and the composition of the gas mixture.

A negative bias of –150 V is applied to the sample while the nitriding process is on. The hydrogen percentage in the gas mixture significantly influences the ionic current flowing to the sample, as is shown in Figure 1. It is primarily due to the decrease in the plasma density as

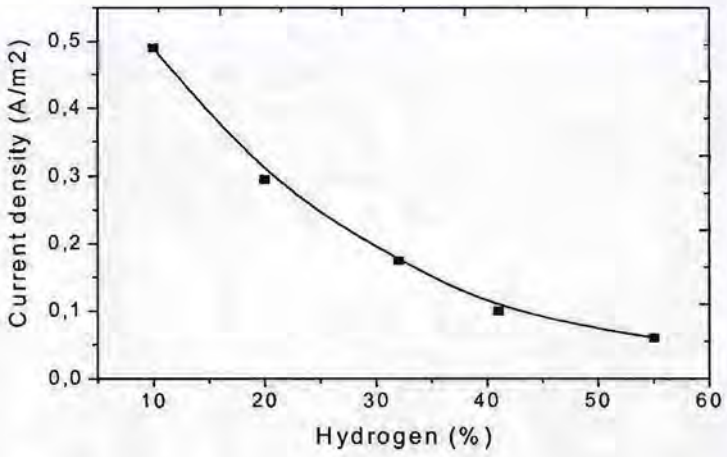

Figure 1. *Current collected by the sample as a function of hydrogen percentage in the gas mixture of Ar + N_2 + H_2 injected in the arc plasma source*

the hydrogen percentage is enhanced. The drop in plasma density is substantiated by the probe measurements. Temperature of the sample also goes down considerably with the increase in hydrogen percentage.

Continuous experiments are run on the time scales from 1 to 7 hours to nitride the samples for different times under identical plasma conditions. After each run the surface hardness of the samples is measured using Vicker's microhardness tester at 100 g load. Figure 2 shows a steady increase in the surface hardness with the plasma treatment time. The parameters used in various runs are: Ar = 0.01 slpm, N_2 = 1.0 slpm, H_2 = 0.2 slpm and substrate bias = -150 V.

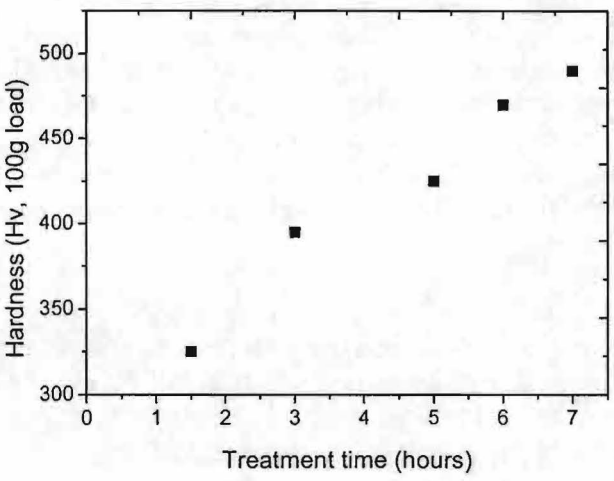

Figure 2. *Increase of surface hardness of the steel sample with the plasma treatment time*

Under these conditions the sample draws 3.8 A/m^2 current density and attains a steady state temperature of 780 K after 30 minutes of the treatment time.

Acknowledgements

The experimental system has been set up at the Indian Institute of Technology, New Delhi with partial financial assistance of European Commission and in co-operation with Technical University Eindhoven (TUE). Several fruitful discussions and continuous support provided by Prof. D.C. Schram from TUE are thankfully acknowledged. Mr. M.J.F.v.d. Sande and Mr. A.B.M. Husken from TUE have given valuable technical inputs. Dr. Sanjay Singh and Mr. Naresh Kumar, IIT Delhi contributed to the experimental measurements.

References

[1] B. Finnern, 'Gas and Salt Bath Nitriding', Carl Hanser Verlag, Munich (1965)
[2] C.K. Jones and S.W. Martin, Met. Prog. **85,** 94 (1964)
[3] R.P. Dahiya, M.J. de Graaf,, R.J. Severens, H.Swelsen, M.C.M. van de Sanden and D.C. Schram. Phys. Plasmas **1,** 2086 (1994).

Investigation of reactive plasmas in an inductively coupled GEC reference cell by absorption spectroscopy

I. Möller and H. Soltwisch
Institute for Experimental Physics V, Ruhr-University Bochum
Germany

Introduction

Hydrocarbon plasmas with admixtures of oxygen are widely used in technical applications although the understanding of the complex kinetics is far from being complete. Densities and temperatures of molecular species can be derived directly by absorption spectroscopy. The required sub-Doppler resolution is ensured by the usage of tunable diode lasers. Measurements in an inductively coupled GEC reference cell with methane and oxygen as feed gases are presented. The dependence of molecular densities on external parameters as the applied power, the flow rate and the gas composition is shown and compared with results from a capacitively coupled plasma where the behavior of the source gases and an intermediate species (the methyl radical) can be understood on the basis of simple rate equations.

Experiment

The experimental set up is shown schematically in figure 1. The discharge reactor is based on the Gaseous Electronic Conference reference cell defined in 1988 with only a few modifications. We can use the cell with capacitively (CCP, parallel-plate configuration) or inductively (ICP, 5-turn coil) coupling. Typical external parameters are pressures of 10-100 Pa, power up to 500 W, flow rates of 2-10 sccm and varying mixtures of CH_4 and O_2. The absorp-

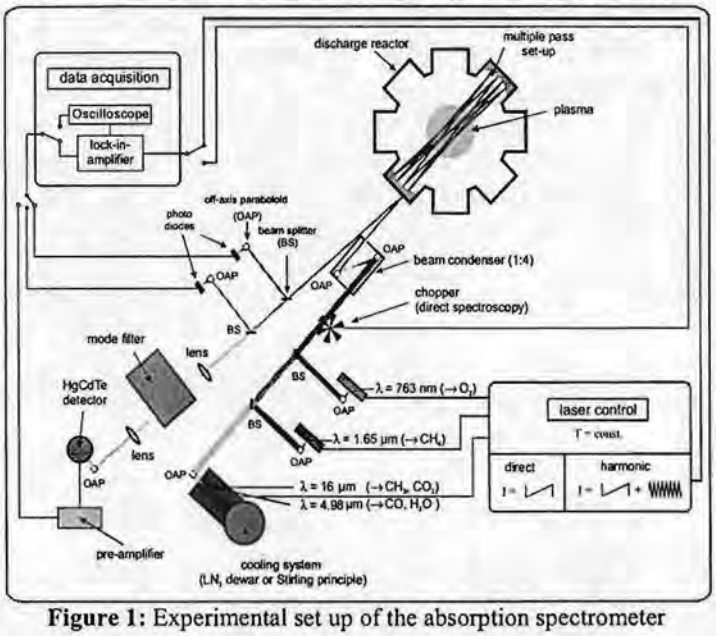

Figure 1: Experimental set up of the absorption spectrometer

tion spectrometer includes three different diode laser set-ups for different wavelength regions. In the visible and near infrared we use single-mode diode lasers operating at room temperature, whereas for longer wavelengths multimode diode laser and a mode filter (grating monochromator) are employed which require a liquid nitrogen dewar or a cryogenic cooling system. To increase the sensitivity, a multipass arrangement (Herriott type [1]) is installed,

which provides 40 passes through the reactor chamber. This leads to an effective path length of 18.4 m for stable products like CO, which fill the whole chamber, and 4 m for reactive species like CH_3, which are localized inside the plasma. A further decrease of the detection limit can be achieved by using a frequency modulation technique [2] where the current of the diode laser is modulated sinusoidally and the signal is detected via a phase sensitive lock-in amplifier.

In case of saturation-free absorption, the transmitted intensity I is given by the Beer-Lambert law:

$$I(\tilde{\nu}) = I_0(\tilde{\nu}) \exp\left\{ -S(T_{rovib}) g(\tilde{\nu}, T_{trans}) \int_0^L n dl \right\} \qquad (1)$$

(with the line strength S, the profile function g, the particle density n and the absorption length L). Using this equation, the determination of several molecular quantities is possible. Due to the multipass arrangement only line-integrated values representing the sum of 40 passes are obtained. In the pressure range of our experiments the line profiles are dominated by Doppler broadening and, therefore, the direct determination of the translational temperature from the halfwidth of the profiles is possible. The rovib-temperature can be obtained from a Boltzman plot if all used quantities are known, or from the normalized quantity *n x S(T)/S(296 K)* as explained in [3].

In figure 2 (a) some measurements from a capacitively coupled GEC-like reactor are shown. The source gases CH_4 and O_2, one intermediate species CH_3 and two stable products CO and CO_2 are measured in dependence on the external parameters flow rate, gas mixture and power (fixed pressure of 100 Pa). Simple rate equations are found which describe the production and depletion of CH_4, O_2 and CH_3 self-consistently [3]. Rather high CO and CO_2 densities for pure oxygen discharges indicate that the deposition on electrodes and walls are not negligible. A description by simple rate equations could not be found due to the multitude of possible reaction channels.

Investigations in the inductively coupled reactor have just been started. Therefore only the development of CH_4 can be presented so far. The most obvious difference between CCP and ICP is the much higher dissociation rate of CH_4 which is expected due to the increased electron density. Furthermore, the transition from E- to H-mode induces an instantaneous decrease of the methane concentration due to the rapid increase of the electron density, whereas the transition from H- to E-mode is dominated by diffusion and therefore the CH_4 density increases rather slowly. More data and detailed interpretation will be presented on the poster.

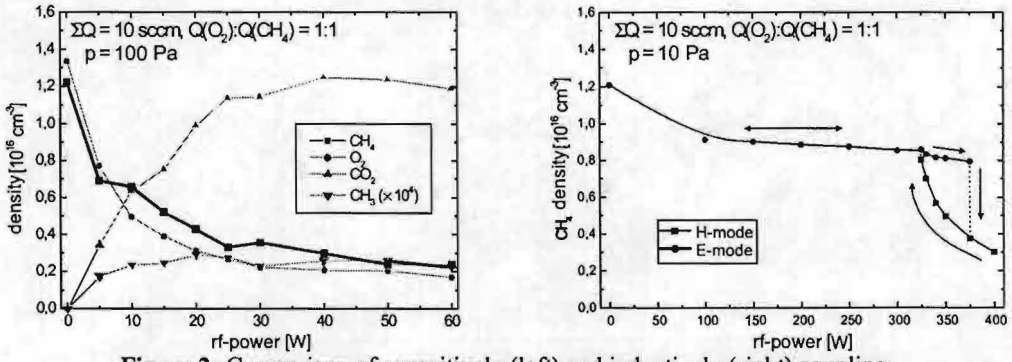

Figure 2: Comparison of capacitively (left) and inductively (right) coupling

References

[1] D. Herriott, H. Kogelnik, and R. Kompfer. Appl. Opt., **3**, 523-526 (1964)

[2] C. R. Webster, R. T. Menzies and E. D. Hinkley, Chemical Analysis, 94, chapter 3, 163-532, Wiley and Sons (1987)

[3] C. Busch, I. Möller, and H. Soltwisch, submitted to Plasma Sources Sci. Technol.

Spectroscopic Determination of the Dissociation Degree in Pulsed Plasmas Containing Hydrogen

N. Lang[(1)], B.P. Lavrov[(2)], J. Röpcke[(1)]
[(1)]*Institut f. Niedertemperatur-Plasmaphysik, 17489 Greifswald, F.-L.-Jahn-Str. 19, Germany*
[(2)]*Faculty of Physics, St.-Petersburg State University, 198904 St. Petersburg, Russia*

Introduction

The dissociation degree of hydrogen in plasmas is very important for basic research and numerous applications. In particular for plasma technology simple and reliable methods of its determination are highly necessary. In this contribution a new method is proposed to determine the time evolution of the dissociation degree in a pulse-modulated microwave discharge containing hydrogen by time-resolved optical emission spectroscopy (OES). This method is a modification and correction of a well-known method developed by Devyatov et al. [1] widely used in plasma spectroscopy [2,3]. The improvements are concerned to the consideration of the rotational structure of the molecular levels under the study (previously neglected) as well as the usage of new values of cross sections, radiative life times and transition probabilities. It is shown that in this case the determination of the dissociation degree can be reduced to the measurement of just two line intensities (one atomic and one molecular) and the gas temperature. The new method was applied to investigate the time behaviour of the dissociation degree in a pulse-modulated microwave discharge at low pressure.

Experiment

The discharge under the study was a large planar microwave plasma source [4]. A schematic illustration of the experimental set-up is shown in Fig. 1. The microwave plasma (f_{MW}=2.45GHz) was modulated by rectangular pulses with a frequency of 500 Hz at 50% duty cycle (gas flow: 50 sccm, H_2+Ar (0.3%), pressure: 50 Pa). In the pulse maximum a power of 3.6 kW was coupled into the plasma, 600 W in the minimum. The spectrometrical system provided a spectral resolution of 0.006 nm and a time resolution of 10 μs and was calibrated for spectral sensitivity with the help of tungsten ribbon lamps.

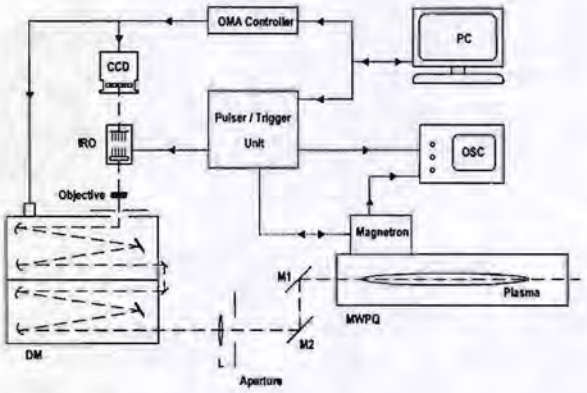

Figure 1: *Scheme of the experimental set-up.*

Method

Devyatov's method bases on a measurement of the ratio between the total intensity of diagonal Fulcher-α bands and of the Balmer line H_α. The basic approach is the validity of corona conditions, i.e. electron impact excitation from the ground state and spontaneous emission balances the population of the excited states. In the case of the atomic line additionally the dissociative excitation is taken into account. The drawback of this method is the disregard of the rotational structure of the excited levels both in the analysis of the

measured spectra and in the formulation of corresponding balance equations. On one side it is a well known problem of overlapping of individual rotational lines particular if the spectral resolution is not very high. On the other side the choice of correct cross sections and therefore of rate coefficients describing the emissions of all diagonal transitions is still questionable.
The following method starts from the consideration of rotational population distributions in the vibronic ground state ($X^1\Sigma_g^+$,v=0). Assuming Boltzmann distributions of the rotational population densities in $X^1\Sigma_g^+$,v=0 (with $T_{rot}=T$), the population of the Nth level may be written as:

$$N_{X0N} = \frac{g_{a,s}\cdot(2N+1)\cdot[H_2]}{P(T)}\cdot exp\left(-\frac{E_{X0N}}{kT}\right) = f(T,N)\cdot[H_2] \qquad (1)$$

where N – rotational quantum number excluding spin of electrons, $g_{a,s}(2N+1)$ – the total degeneracy of the level accounting for nuclear spin, E_{X0N} – the energy of level N in $X^1\Sigma_g^+$,v=0 $P(T)$ – the partition function is. The temperature dependence of the expression $f(T,N)$ is shown in Fig. 2 demonstrating the importance of taking into account T if it is changed in the plasma under the study. It was shown in [5] (see also [6]) that under certain conditions the rotational ground state populations are copied in the excited rotational levels neglecting a change in angular momentum. Thus the intensity of one rotational line, e.g. Q1(2-2) Fulcher-α, may be expressed as:

$$I_{Q1} = const\cdot f(T,1)\cdot[H_2]\cdot n_e\cdot\left\langle\sigma_{Q1}^{dir}v\right\rangle_{em} \qquad (2)$$

with the emission rate coefficient $<\sigma_{Q1}{}^{dir}v>_{em}$ for direct excitation of this line. The corresponding expression for the Balmer line H_α taken into account dissociative excitation reads:

$$I_{H\alpha} = const\cdot\left(n_e\cdot[H]\cdot\left\langle\sigma_{H\alpha}^{dir}v\right\rangle_{em} + n_e\cdot[H_2]\cdot\left\langle\sigma_{H\alpha}^{diss}v\right\rangle_{em}\right) \qquad (3)$$

From equation (2) and (3) one obtains for the ratio of atomic to molecular hydrogen concentration:

$$\frac{[H]}{[H_2]} = f(T,1)\cdot\frac{\left\langle\sigma_{Q1}^{dir}v\right\rangle_{em}}{\left\langle\sigma_{H\alpha}^{dir}v\right\rangle_{em}}\cdot\frac{I_{H\alpha}}{I_{Q1}} - \frac{\left\langle\sigma_{H\alpha}^{diss}v\right\rangle_{em}}{\left\langle\sigma_{H\alpha}^{dir}v\right\rangle_{em}} \qquad (4)$$

which may be used for the detemination of the dissociation degree κ_D: $\kappa_D = \frac{[H]}{2[H_2]+[H]}$

The emission cross section of the Fulcher-α (2–2) Q1 line was calculated from the corresponding excitation cross section [7] with appropriate values for the transition probability and radiative life time from [8]. The relevant cross sections in the case of the atomic emissions were taken from [9,10]. The sensitivity of the method is demonstrated in Fig. 3. Here the line ratio of H_α/Q1 was calculated as a function of $[H]/[H_2]$ for various electron and gas temperatures. The rate coefficients were determined for Maxwellian electron energy distribution functions. It can be seen that the line intensity ratio is sensitive to the dissociation degree from 5% ($[H]/[H_2] > 0.1$) up to at least 80%. Moreover the influence of the gas temperature on the line intensity ratio is obvious and proves the importance of its consideration.
However, if direct electron impact and dissociative excitation as well as spontaneous emission processes are the dominant de-/population processes the ratio $[H]/[H_2]$ is determined using equation (4) with measured intensities of one molecular and atomic line as well as the gas

temperature. Otherwise appropriate corrections can be introduced if processes like collisional quenching or stepwise excitation have to be taken into account [3].

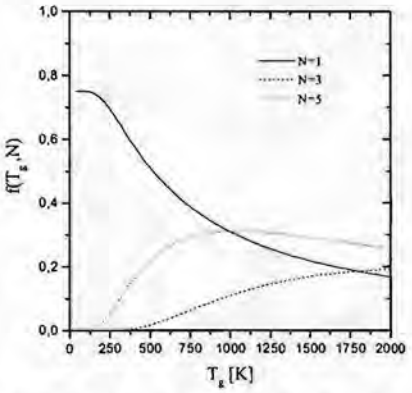

Figure 2: *Relative population of the first 3 rotational ground state levels of ortho-H_2 in dependence on the temperature.*

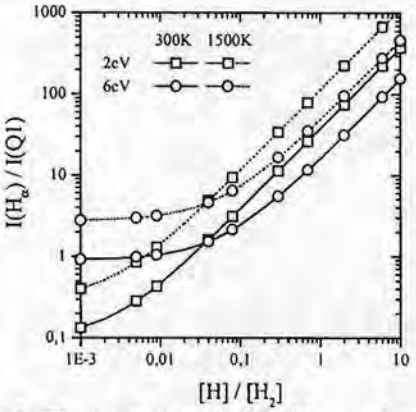

Figure 3: *The intensity ratio $H_\alpha/Q1$ as a function of $[H]/[H_2]$ for different electron and gas temperatures.*

Results and Discussion

The temporal variation of the gas temperature was obtained from rotational population density distributions of H_2 ($d^3\Pi_u^-$) molecules and from Doppler broadening of molecular and H_α lines, taken into account the fine structure. The result is presented in Fig. 4 showing an increase of T_g by almost a factor of 2 during the pulse.

The temporal variations of the electron characteristics were determined by Langmuir probes. In a first approximation the EEDF was treated to be Maxwellian, the corresponding electron temperatures are shown in Figure 5 [11].

Therefore usage of equation (4) leads to the time evolution of the dissociation degree derived from measured intensity ratios of Balmer H_α (□), H_β (○) lines to H_2 Fulcher-α Q1 line (v'=v''=2) as shown in Fig. 6. The error bars reflect only random errors of the intensity measurements. Inside the uncertainties both line intensity ratios reflect the same value of the degree of dissociation and its variation in time. One may see that under our conditions κ_D is growing from about 40% to 70% during the active phase of the pulse. With the knowledge of the gas temperature the absolute atomic and molecular concentrations of hydrogen could be determined assuming constant pressure. The corresponding variations in time are presented in Fig. 7 together with results from TALIF measurements for [H] performed under the same plasma conditions [12]. Nevertheless the comparison is limited because of the local character of TALIF the relative behaviour of the atomic concentration is in good accordance with that derived from OES.

It can be seen that for all available data from the OES measurements the amount of atomic hydrogen exceeds the molecular one. Both concentrations decrease during the active phase of the pulse which is a consequence of gas heating whereas the pressure remains constant. Remarkable is the high concentration of atomic hydrogen even to the beginning microwave pulse. The main reason is considered to be caused by the non-vanishing microwave field between the pulses. In fact time-resolved investigations of the dissociation continuum with a photo-multiplier showed the evidence of H atom production processes in that pulse regime [13].

The proposed method serves as an improved diagnostic tool to determine the degree of dissociation of hydrogen, especially in non-stationary plasmas just by measuring two relative line intensities and the gas temperature.

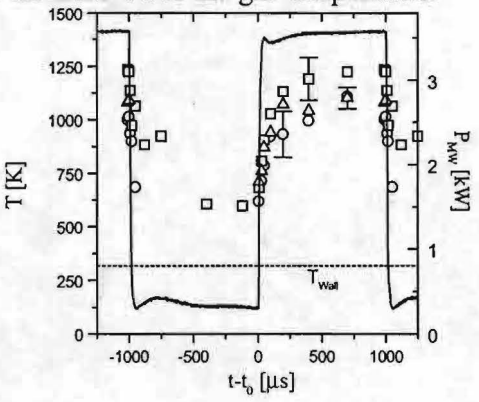

Figure 4: *Variation in time of the gas temperature derived from Doppler broadening of H_α (□) and H_2 (○) lines and from rotational intensity distributions in the Q branch of the $d^3\Pi_u^- \rightarrow a^3\Sigma_g^+$, v'=v''=2 band (Δ).*

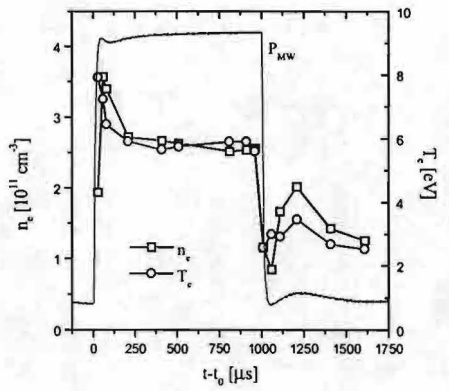

Figure 5: *Time evolution of the electron temperature and the electron density measured with Langmuir probes [11].*

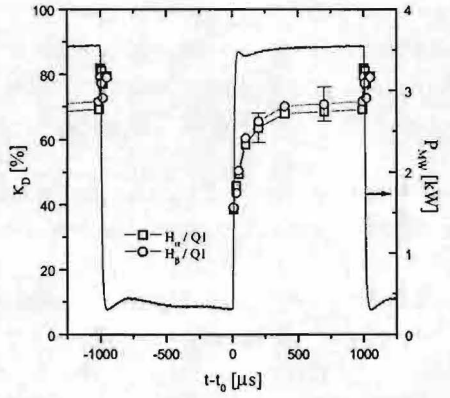

Figure 6: *Time evolution of the dissociation degree derived from intensity ratios of Balmer H_α (□), H_β (○) lines to H_2 Fulcher-α Q1 line (v'=v''=2).*

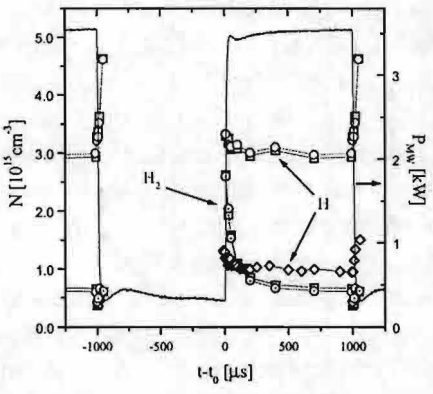

Figure 7: *Variation in time of the absolute atomic and molecular concentrations of hydrogen derived from (□) H_α /Q1 and from (○) H_β/Q1 line ratios during the pulse in comparison with TALIF measurements [12].*

References

[1] A. M. Devyatov et al., *Opt. Spectrosc.* **71** (1991), 525.

[2] V. Schulz-von der Gathen et al., *Plasma Chem. Plasma Process.* **16** (1996), 461.

[3] E. Tatarova et al., IV Workshop on Microwave Discharges (Zvenigorod,Russia), book of abstracts (2000), 42.

[4] A. Ohl in Microwave Discharges, C.M. Ferreira & M. Moisan, Plenum Press, 1993.

[5] B. P. Lavrov, *Opt. Spectrosc.* **48** (1980), 680.

[6] S.A. Astashkevich et al., *J. Quant. Spectrosc. Radiat. Transfer* **56** (5), 1996, 725.

[7] B. P. Lavrov et al., *J. Phys. B.: At. Mol. Phys.* **14** (1981), 4701.

[8] B. P. Lavrov et al., *Phys. Rev. E* **59** (1999), 3526.

[9] L. Vriens et al., *Phys. Rev. A* **22** (1980), 940.

[10] G. R. Möhlmann et al., *Chem. Phys.* **25** (1977), 103.

[11] N. Lang et al., Verhandl. DPG (VI) **35**, p.1021, (2000).

[12] X. R. Duan et al., 9th LAPD (Lake Tahoe, California) 1999, 217.

[13] N. Lang et al., to be published.

Time-resolved cavity ring down measurements for the determination of the surface and gas phase reactivity of plasma radicals

J.P.M. Hoefnagels, A.A.E. Stevens, W.M.M. Kessels, and M.C.M. van de Sanden
Dept. of Applied Physics, Eindhoven University of Technology, Eindhoven, The Netherlands

Introduction

At the Eindhoven University the so-called expanding thermal plasma (ETP) is studied, which is capable of depositing device quality a-Si:H up to growth rates of 10 nm/s. Up to now, the plasma processes and the contribution of the different plasma species to film growth in the ETP have extensively been investigated [1,2,3]. Key element in these studies is the determination of the absolute gas phase number densities of various SiH_4 radicals by use of the highly sensitive cavity ring down absorption spectroscopy technique (CRDS) [4,5]. The next step in gathering fundamental information on the deposition process is the study of the plasma dynamics, especially with respect to the surface and gas phase reactions of the radicals. For this reason, a completely new experiment has been set up to perform time-resolved CRDS (τ-CRDS) measurements. These measurements are performed by applying a pulsed rf bias to the substrate holder in addition to the regularly operating ETP. This creates an additional, modulated density of plasma species in front of the substrate holder without causing major disturbances to the ETP itself. The additional density of a specific radical is subsequently sampled using CRDS at various times in the afterglow of the additional rf bias plasma. Crucial herein is the real-time handling of the CRDS signal by a new-developed and fully computer controlled 'state of the art' 100 MHz, 12 bit physics data acquisition system [6].

In the following sections, the experimental setup of the τ-CRDS measurements, some initial results and future objectives will be presented. These first studies have been performed on the SiH radical, which has already extensively been studied by means of CRDS under stationary plasma conditions (Fig. 1) [3]. In addition to the surface and gas phase loss of SiH, the τ-CRDS measurements on this radical can possibly also yield information on the observed background absorption underlying the SiH absorption peaks (Fig. 1).

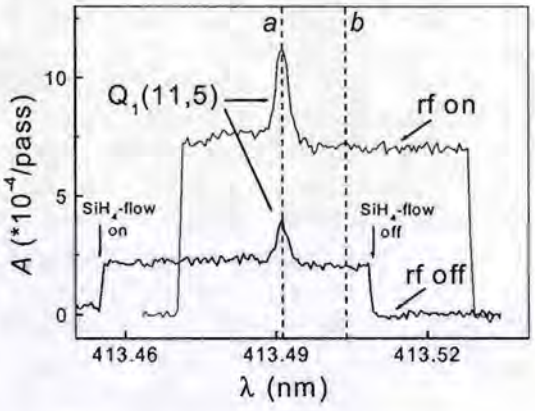

FIG. 1: Wavelength scans of the $Q_1(11,5)$ peak of the SiH $A^2\Delta \leftarrow X^2\Pi$ transition around 413 nm. During each scan, the SiH_4 flow is turned on and off at the beginning and end of the scan. The experiments with only the ETP ('rf off') have been used to determine the SiH density in the ETP plasma. These measurements showed also a featureless broadband absorption, which has not been identified up to now [3]. The experiments with an additional rf bias plasma ('rf on') are used in the time-resolved CRDS measurements. From the figure, it is clear that the application of the rf bias creates an additional SiH density as well as an increase in the broadband background absorption. In the figure, also the 'on resonance' wavelength *a* and 'off resonance' wavelength *b* are shown as will be used throughout this paper.

Experimental Setup

The experimental setup for the τ-CRDS measurements is schematically depicted in Fig. 2. The conventional CRDS technique [4,5] is used to probe the SiH $A^2\Delta \leftarrow X^2\Pi$ transition at ~413 nm. Therefore, laser radiation is produced by a tunable dye laser operated Exalite 411 dye (~10mJ/pulse energy, 3 pm linewidth), which is pumped by a frequency-tripled Nd:YAG laser (100mJ/pulse energy at 355 nm, 10 Hz repetition rate). The light pulse is coupled into an optical cavity consisting of two highly reflective mirrors (R=~99.6 at 413 nm) situated around the plasma. The intensity of the light leaking out from the cavity at the second mirror shows an exponential decay in time depending on the absorption of the light in the plasma and is detected by a photomultiplier (PMT). For all measurements discussed here, the optical cavity has been aligned ~5 mm in front of the substrate holder.

The PMT signal is sampled by a 'state of the art' 100 MHz 12 bit physics data acquisition system (PhyDAS) [6], which allows for real-time signal handling up to a repetition rate of ~2 kHz using a digital signal processor (DSP). A transimpedance amplifier with a bandwidth of ~47 MHz has been developed to match the output range of the PMT to the input range of the PhyDAS.

An rf signal (13.56 MHz) is generated by a function generator that is amplified by a high frequency, 100 W amplifier. The rf signal is fed through a matching network (L-type) to the top of the substrate holder. The function generator can be triggered to produce a pulsed rf signal with a low repetition rate. The pulsed rf signal is synchronized with the Nd:YAG laser pulse by means of a delay generator. Finally, a fully computer-controlled experimental procedure has been written in LabVIEW for the τ-CRDS experiments.

The principle of the τ-CRDS measurements, which is generally applicable for all plasma species, will now be explained for the specific case of the SiH radical using the 'timing scheme' in Fig. 3. An rf signal is applied to the substrate holder in addition to the normally operating ETP to generate extra plasma and thus additional SiH density in front of the substrate holder (Fig. 1). After the negative slope of every rf pulse, i.e., during the rf afterglow, this additional density will exponentially decay to the density that is present during normal ETP operation. To 'map' the com-

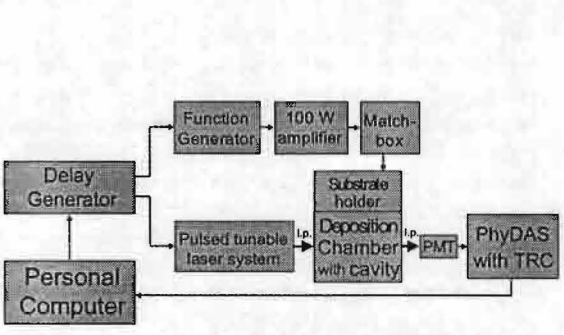

FIG. 2: Experimental scheme for the τ-CRDS measurements. The dashed arrows indicate control lines, whereas the solid arrows indicate signal lines. The laser pulses (l.p.) are indicated with the two bold arrows.

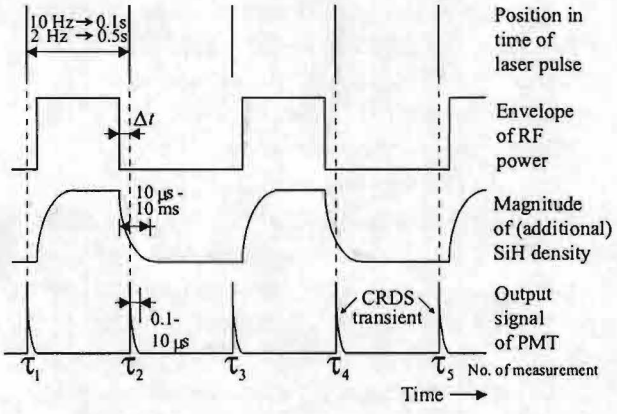

FIG. 3: Schematic time diagram of the absorption measurements at different times in the additional rf bias plasma afterglow. The laser pulse is scanned in time Δt relative to the negative slope of the rf pulse. In the figure, also the exponential decay time of the additional SiH density and of the output signal of the PMT is indicated.

plete exponential decay time, the absorption of the SiH radicals is sampled at various times during the rf afterglow (Fig. 2). This is done by varying the time Δt between the negative slope of the rf pulse with respect to the laser pulse. Between every measurement of the density in the rf afterglow, a reference density measurement is taken just before the onset of every rf power pulse. Note the different time scales involved (Fig. 3): the probing of the density by CRDS will take less then 10 μs, whereas the exponential decay of the additional SiH density has been estimated at 100-1000 μs. The typical residence time of stable gas species in the chamber is ~400 ms.

Initial measurements

Initial τ-CRDS measurements, performed on the SiH radical, are shown in Fig. 4. Fig. 4(a) shows the τ-CRDS measurement performed at the 'on resonance' wavelength *a*. The absorption values in this figure are due to absorption by SiH together with the featureless absorption that underlies

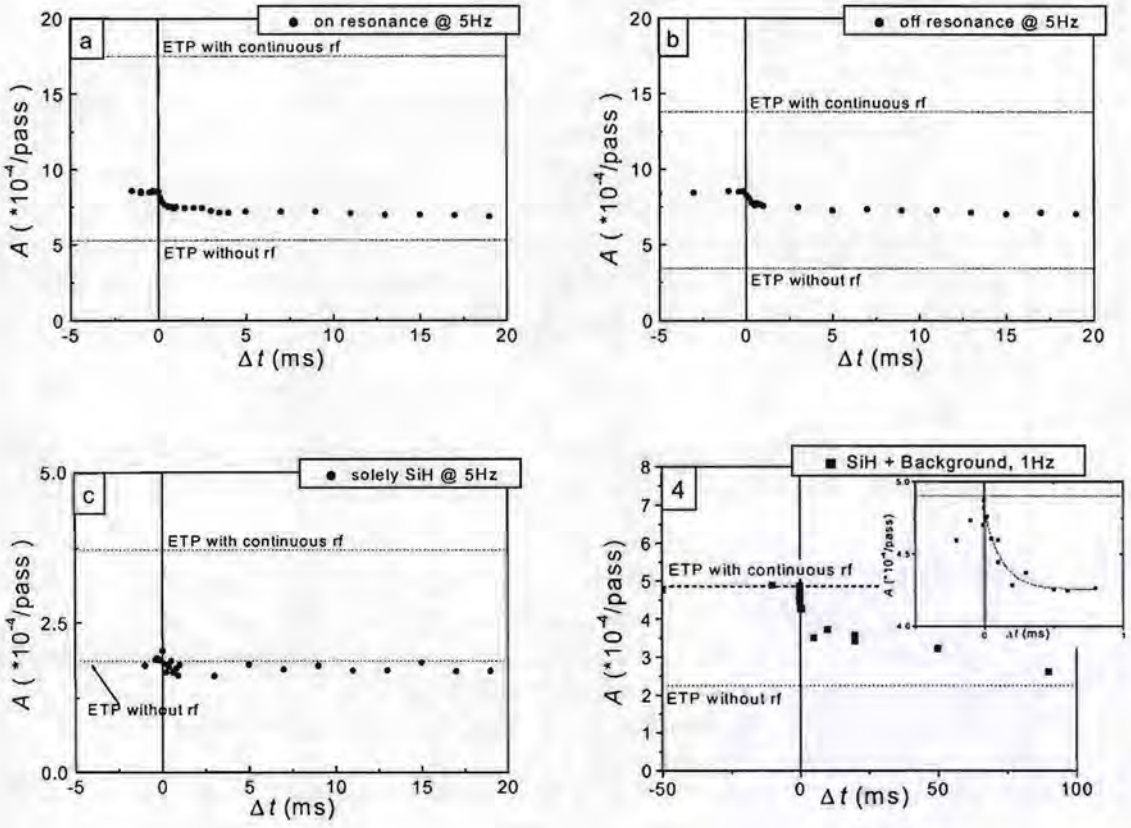

FIGS. 4: Initial τ-CRDS measurements on the SiH radical: absorption A vs. the time Δt in the afterglow of the additional rf bias plasma. In all figures, dashed lines are used to indicate absorption values measured at two stationary plasma conditions: only ETP and ETP combined with an additional continuous rf bias applied to the substrate holder (Fig. 1). Figs. (a)-(c) are obtained using an rf pulsing frequency of 5 Hz and a duty cycle of 40%. Fig. (a) shows absorption values measured at 'on resonance' wavelength *a* (Fig. 1), whereas (b) is measured at 'off resonance' wavelength *b*. Fig. (c) shows the difference between (a) and (b), yielding the absorption solely due to SiH. Fig. (d) is obtained with an rf pulsing frequency of 1 Hz and a lower SiH_4-flow than in Figs. (a)-(c). The figure shows absorption values measured at 'on resonance' wavelength *a*. The inset shows a magnification around $\Delta t = 0$.

the SiH line spectrum. Both these absorptions respond independently to the rf pulsing. Therefore, another τ-CRDS measurement has been performed at the 'off resonance' wavelength *b* [Fig. 4(b)], which has subsequently been subtracted from Fig 4a. This has yielded the time response solely due to absorption by SiH [Fig. 4(c)].

Fig. 4 shows the feasibility of the experimental setup: in Fig. 4(a) and 4(b) clearly an exponential decay of the absorption during the rf bias afterglow ($\Delta t > 0$) can be seen. However, the exact interpretation of the data is still unclear. For instance, in Fig. 4(c) no additional SiH has been observed for $\Delta t < 0$ whereas even a 'negative' additional SiH density is present for $\Delta t > 0$.

On the other hand, already one conclusion can be made from the measurement performed with 1 Hz pulsed rf [Fig. 4(d)]. After 400ms rf application at $\Delta t = 0$ (duty cycle = 40%) the absorption is equal to the absorption during continuous rf application, whereas this is clearly not the case for measurements at 5 Hz pulsed rf [Figs. 4(a)-(c)]. Therefore, it can be concluded that the background absorption must be due to a stable gas species and that the plasma stabilizes after 400 ms, which coincides with a residence time in the system.

Future objectives

In the near future the dynamic behavior of the SiH radical in the ETP will be further explored by performing τ-CRDS measurements for various rf power and rf duty cycle conditions and ETP plasma settings. After that, an attempt will be made to determine the surface loss probability (β) and the gas phase reactivity of the SiH radical. For these experiments, the plasma in front of the substrate holder will be modeled and τ-CRDS measurements at several positions in front of the substrate holder will be performed. The long-term goal is to determine surface loss probabilities for all interesting SiH_x radicals present in the ETP.

Acknowledgments

Prof. D.C. Schram and the Technical Laboratory Automation group of the Department of Applied Physics are gratefully acknowledged for their contribution to this work.

[1] W.M.M. Kessels, A. Leroux, M.G.H. Boogaarts, J.P.M. Hoefnagels, M.C.M. van de Sanden, and D.C. Schram, J. Vac. Sci. Technol. A **19**, 467 (2001).

[2] W.M.M. Kessels, M.G.H. Boogaarts, J.P.M. Hoefnagels, M.C.M. van de Sanden, and D.C. Schram, to appear in J. Vac. Sci. Technol. A **19** (May 2001).

[3] W.M. M. Kessels, J. P. M. Hoefnagels, M. G. H. Boogaarts, D. C. Schram, and M. C. M. van de Sanden, J. Appl. Phys. **89**, 2065 (2001).

[4] K.W. Busch and M.A. Busch (Eds.), *Cavity-Ringdown Spectroscopy: An Ultratrace-Absorption Measurement Technique*, American Chemical Society, Washington, DC (1999).

[5] M.G.H. Boogaarts, P.J. Böcker, W.M.M. Kessels, D.C. Schram, and M.C.M van de Sanden, Chem. Phys. Lett. **326**, 400 (2000).

[6] R. Smeets and F.C. van Nijmwegen, internal report, BLN 99-15 UM, Eindhoven University of Technology (July 2000).

TALIF CALIBRATION WITH NOBLE GASES FOR QUANTITATIVE ATOMIC DENSITY MEASUREMENTS

K. Niemi, V. Schulz-von der Gathen, and H. F. Döbele

Universität Essen, Institut für Laser- und Plasmaphysik, Universitätsstr. 5, 45117 Essen, Germany

1 Introduction

Fluorescence spectroscopy is a well established diagnostic to measure atomic ground-state densities in plasmas with high spatial and temporal resolution [1]. The atomic species - usually in its ground state - is excited by resonant absorption of tunable narrow bandwidth laser radiation to a higher electronic state. The subsequent fluorescence radiation yields information on the ground-state density. In order to obtain absolute values, not only a suitable calibration technique is necessary, but effects of collisional quenching of the generated population have to be included.

Only in the low pressure case will the excited state be depleted solely by spontaneous emission and independently of plasma parameters. Collisional processes become competitive with increasing pressure and lead to an additional radiationless decay which depends on the density of all effective collision partners. A detailed knowledge of the quenching coefficients is required in this situation in order to obtain quantitative results.

The one-photon excitation wavelengths for light atoms are located in the VUV spectral range and are difficult to generate. Furthermore, VUV radiation is strongly absorbed in air, many other gases and at elevated pressure even in the investigated medium itself.

Two-photon Absorption Laser Induced Fluorescence spectroscopy (TALIF) circumvents these problems. Focused laser radiation is usually used due to the low efficiency of a two-photon process. Good spatial resolution - determined by the focal dimensions - is an appreciated consequence. For calibration a reference source can be applied, e.g. so-called "flow tube reactors" which generate well-defined atomic densities with the aid of titration methods [3]. This procedure requires that the reference source can be attached to the experimental chamber in accordance with the vacuum requirements.

2 Experiment

The objective of this work is to provide an alternative calibration method for TALIF diagnostics to determine atomic hydrogen, nitrogen and oxygen ground-state densities even in plasmas where collisional effects are present. The method is based on a comparative measurement with a noble gas with a two-photon resonance spectrally close to the investigated atomic transition [2]. Suitable transitions in krypton and xenon exist for the two-photon excitations of atomic hydrogen at $\lambda=2\times205.1$ nm, nitrogen at $\lambda=2\times206.6$ nm and oxygen at $\lambda=2\times225.5$ nm. We investigated these resonances using the TALIF schemes listed in table 1 and measured the atomic data required for this calibration: the radiative lifetimes and the quenching coefficients of the excited states interacting with several important species and the relevant ratios of two-photon excitation cross-sections.

Atom	Two-photon excitation	λ_{Laser}(nm)	Final state	$\lambda_{Fluorescence}$(nm)
Kr	$4p^6\,{}^1S_0 \rightarrow 4p^5\,5p'[3/2]_2$	204.2	$4p^5\,5s'[1/2]_1$	826.3
H	$1s\,{}^2S_{1/2} \rightarrow 3d\,{}^2D_J$	205.1	$2p\,{}^2P_J$	656.3
N	$2p^3\,{}^4S^0_{3/2} \rightarrow 2p^2\,3p\,{}^4S^0_{3/2}$	206.6	$2p^2\,3s\,{}^4P_J$	742-746
Xe	$5p^6\,{}^1S_0 \rightarrow 5p^5\,7p[3/2]_2$	225.5	$5p^5\,6s[3/2]_2$	462.4
O	$2p^4\,{}^3P_2 \rightarrow 2p^3\,3p\,{}^3P_2$	225.6	$2p^3\,3s\,{}^3S$	844.6

Table 1: TALIF schemes of the investigated atoms

The experiment was perfomed at a vacuum system equipped with a flow tube reactor. Figure 1a) shows the experimental set-up. The pump radiation around λ=205 nm is generated with a Nd:YAG-laser (second harmonic at λ=532 nm) pumped dye-laser system (max. energy 0.5 mJ, pulse duration 8 ns, repetition rate 10 Hz) and at λ=225 nm with an excimer-laser pumped dye-laser with frequency doubling (max. energy 2 mJ, pulse duration 10 ns, repetition rate of 2 Hz). The focused laser beam (f=30 cm) is adjusted through orifices in the flow tube. The energy dependencies of the excitation processes are investigated with a variable attenuator consisting of two coated substrates, rotatable in opposite sense, to avoid a beam displacement. Figure 1b) shows the experimental arrangement of the flow tube reactor. The atomic species are produced in a microwave discharge (2.45 GHz, 100 W, 900 Pa, ϕ_{He}=700 sccm, ϕ_{H_2,N_2,O_2}=5 sccm). The absolute atomic density in the observation region is determined by titration [3] on the basis of the fast reactions: $H+NO_2 \rightarrow OH+NO$, $N+NO \rightarrow N_2+O$, $O+NO_2 \rightarrow NO+O_2$. Atomic hydrogen and nitrogen densities in the order of 10^{13} cm^{-3} and atomic oxygen densities in the order of 10^{14} cm^{-3} are generated under typical conditions. The composition of the applied NO/He and NO_2/He mixtures are verified by FTIR-spectrometry.

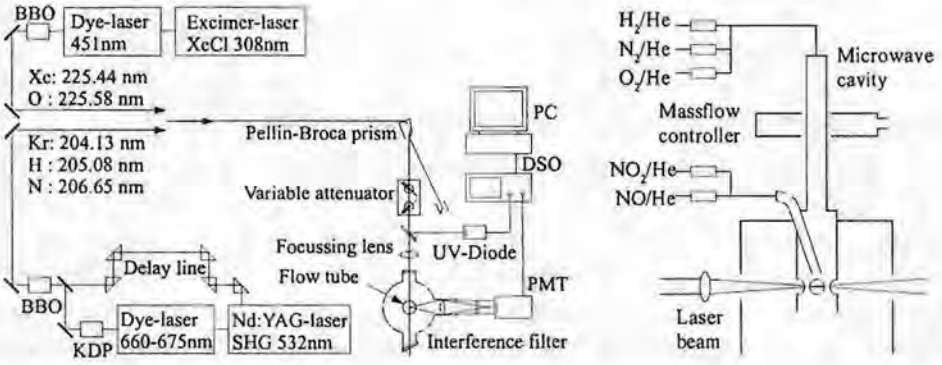

Figure 1: a) Experimental set-up, b) Experimental arrangement of the flow tube reactor.

3 Measurement: Radiative lifetimes and quenching coefficients

The radiative lifetimes of the excited states and the quenching coefficients in H_2, N_2, O_2, He, Ar, Xe, Kr and CH_4 were determined from time resolved measurements. As an example, figure 2a) shows the TALIF signal obtained with a fixed H-atom density in presence of different H_2 admixtures. Stern-Volmer plots for the decay rate of the signal versus the partial pressure of different collision partners are shown in figure 2b). The pressure was increased until the signal duration converges to the time resolution. The dependence was linear throughout.The radiative lifetimes were deduced form the zero-pressure intercepts of the plots and the quenching coefficients from the slopes. The gas temperature of T=300 K was verified by measuring the thermal population distribution in the fine-structure-split ground state of atomic oxygen. The results (with an esti-

mated uncertainty of 15%) are summarized in table 2. Satisfactory agreement is found with data published elsewhere [4, 5, 6, 7, 8].

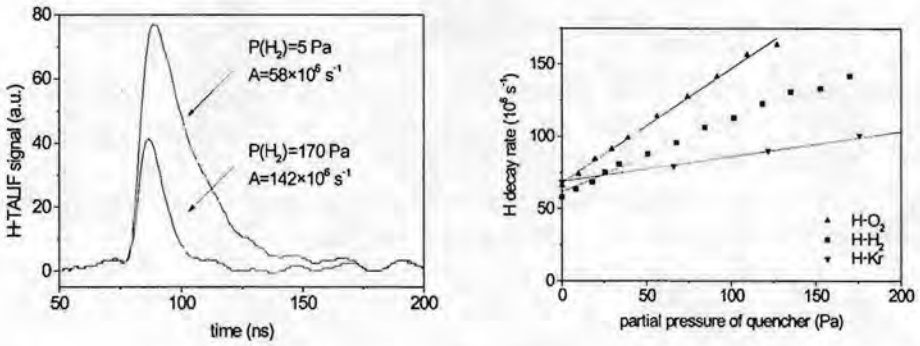

Figure 2: a) Time resolved H-TALIF signals at different H_2 pressures. b) Decay rate of the H-TALIF signals versus partial pressure of O_2, H_2 and Kr.

Reagent		H_2	N_2	O_2	He	Ar	Kr	Xe	CH_4
Excited state	τ(ns)	$k_q(10^{-10}\mathrm{cm^3s^{-1}})$							
Kr($5p'[3/2]_2$)	34.1	8.44	3.35	6.34	0.78	1.29	1.46	3.78	6.27
H($3d\,^2D_J$)	17.6	20.4	20.1	32.6	0.18	3.93	7.15	19.8	25.0
N($3s\,^4P_{3/2}$)	29.6	1.11	0.41	6.63	0.11	0.37	3.16	7.75	5.81
Xe($7p[3/2]_2$)	105.6	28.5	14.0	20.6	2.33	3.71	5.91	5.05	-
O($3p\,^3P_J$)	35.1	10.9	5.9	9.3	0.07	0.25	-	-	-

Table 2: Radiative lifetimes τ and room temperature quenching coefficients k_q of the investigated states.

4 Measurement: Ratios of two-photon excitation cross-sections

The procedure used to determine ratios of excitation cross-sections of neighbouring two-photon resonances is the same as for the calibration except that it is performed with a known atomic density. The time and spectrally integrated TALIF signal is measured with a fixed density of an atomic species as a function of the laser energy. This series of measurements is repeated with a known density of the appropriate noble gas under otherwise identical experimental conditions. The fluorescence signals exhibit at small energy the quadratic intensity dependence of an unsaturated two-photon excitation process. This low energy range was used to fit the straight lines shown in figure 3. Their comparison yields:

$$\frac{I_\mathrm{F}(X)}{I_\mathrm{F}(R)} = \chi\frac{n_\mathrm{X}}{n_\mathrm{R}} = \gamma\frac{a(X)}{a(R)}\frac{\sigma(X)}{\sigma(R)}\frac{n_\mathrm{X}}{n_\mathrm{R}}. \tag{1}$$

X denotes the investigated atomic species, R the noble gas, I_F the integrated TALIF signal normalized to the square of the laser energy and χ the calibration factor which depends only on experimental and atomic constants. γ is the ratio of the detection sensitivities for the fluorescence wavelengths (transmission of observation optics and quantum efficiency of the PMT), a the branching ratio of an observed transition corrected by the effective quenching rate and σ the two-photon excitation cross-section. The effective branching ratios were calculated using results from section 3 and $A_{ik}/A_i = 0.958$ the branching ratio of the krypton 826.3 nm line in absence of quenching from [8] and $A_{ik} = 2.18\times10^6\ \mathrm{s}^{-1}$ the transition probability of the xenon 462.4 nm line

from [9]. The following ratios of two-photon cross-sections were deduced from experimentally determined calibration factors:

$$\frac{\sigma(Kr)}{\sigma(H)} = 0.62 \qquad \frac{\sigma(Kr)}{\sigma(N)} = 0.67 \qquad \frac{\sigma(Xe)}{\sigma(O)} = 0.36. \tag{2}$$

The estimated uncertainty of these values is 50% due to the numerous input parameters and the reproducability of the laser profile. Note that the laser radiation is linearly polarized and the fluorescence radiation is observed parallel to the direction of polarization. If the fluorescence characteristics of two compared species are different, the stated cross-section ratio includes a correction factor which is only valid in the present geometry.

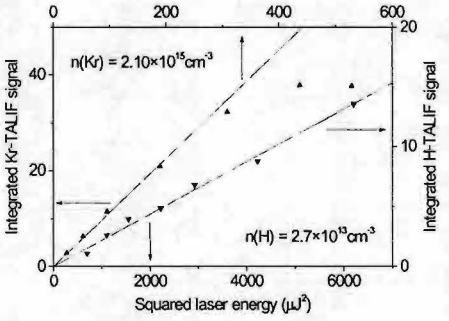

Figure 3: Dependence of the Kr- and H-TALIF signal on the laser energy.

5 Conclusion

The required atomic data - radiative lifetimes, quenching coefficients and two-photon cross-sections ratios- are now available to calibrate atomic hydrogen, nitrogen and oxygen densities by reference measurements with krypton and xenon in low temperature plasmas even at elevated pressures.

6 Acknowledgment

This work is funded by the DFG in frame of the SFB 191 and the Graduiertenkolleg "Hochtemperatur Plasmaphysik"

7 References

[1] J. Amorim, G. Baravian, J. Jolly, J. Phys. D **33** (2000) R51

[2] A. Goehlich, T. Kawetzki, H. F. Döbele, J. Chem. Phys. **108** (1998) 9362

[3] D. W. Setser. Reactive Intermediates in the Gas Phase (Academic Press, New York, 1979)

[4] J. Bittner, K. Kohse-Höinghaus, U. Meier, Th. Just, Chem. Phys. Lett. **143** (1988) 571

[5] B. L. Preppernau, K. Pearce, A. Tserepi, E. Wurzberg, T. A. Miller, Chem. Phys. **196** (1995) 371

[6] V. Alekseev, D. W. Setser, J. Phys. Chem. **100** (1996) 5766

[7] S. F. Adams, T. A. Miller, Chem. Phys. Lett. **295** (1998) 305

[8] R. S. F. Chang, H. Horiguchi, D. W. Setser, J. Chem. Phys. **73** (1980) 778

[9] J. Sabbagh, N. Sadhegi, J. Quant. Spectrosc. Radiat. Transf. **17** (1977) 297

Langmuir probe measurements in an ICP

C.Maurice, F. H. R. Feijen and G.W.M. Kroesen
Dept. of Applied Physics, Eindhoven University of Technology,
P.O. Box 513, 5600 MB Eindhoven, The Netherlands.

Introduction

In the last years, interest for high densities etching sources has rose dramatically in the semiconductor industry. Process machines need to be adapted to the manufacturer leitmotiv " as small as possible" and achieve at the same time a high aspect ratio of the etched layers. Low pressure Inductively Coupled Plasma (ICP) sources proved to be a better candidate for that purpose than capacitively coupled plasma (CCP) sources. Their advantage is that they are intrinsically capable of producing high density plasmas and of independently controlling the energy of the particles (with an additional bias) when they reach the substrate electrode.

In this study we had a look with a Langmuir probe on the validity of this affirmation in our vessel. We performed a quite exhaustive study concerning the influence of the plasma conditions such as gas pressure, source power, radial position and bias on the plasma parameters. However we will only present in that abstract the influence of the bias on the bulk plasma parameters (the rest of the results will be presented in the conference).

Experimental set-up and theory

Our vessel (Fig.1) is closed on the bottom by a 12-mm thick quartz plate and sealed on the top by an Energy Resolved Mass Spectrometer PPM 422 from Balzers. The mass spectrometer head is integrated in the same plane that the substrate electrode. Ion Energy Distribution Functions (IEDF's) are recorded at the surface and give information on the bombarding ions behavior.

The rf source power at 13.56 MHz (varied from 100 Watts to 400 Watts) is applied to a 3-turn, 5 cm radius antenna located under the quartz plate. The antenna and the plasma are forming a transformer where the plasma plays the role of the secondary coil. The rf current circulating in the antenna produces an induced electric field which heats up the electrons. As there's no contact between the antenna and the plasma (the power is transferred through the quartz plate[1]), these plasmas are also sometimes called "electrodeless" plasmas.

An other particularity of these sources is the existence of two modes of operation: A capacitive mode (E-mode) and an inductive mode (H-mode)[2,3]. For a low power which correspond to a low current in the coil, the discharge is sustained mostly by the electrostatic field present due to the potential difference across the coil, the inductive electrical field being insufficient to maintain the plasma. These state is called the E-mode (or capacitive mode) and is visually characterized by a very dim bulk light (the densities are very low). Above a certain threshold current, the induced electrical field becomes more important than the electrostatic field and the plasma jumps then to the H-mode (or inductive mode) characterized by a very bright plasma and very high densities. To get read of the electrostatic field, a faraday shield might be added to the set-up. However it is quite difficult to get a purely inductive discharge.

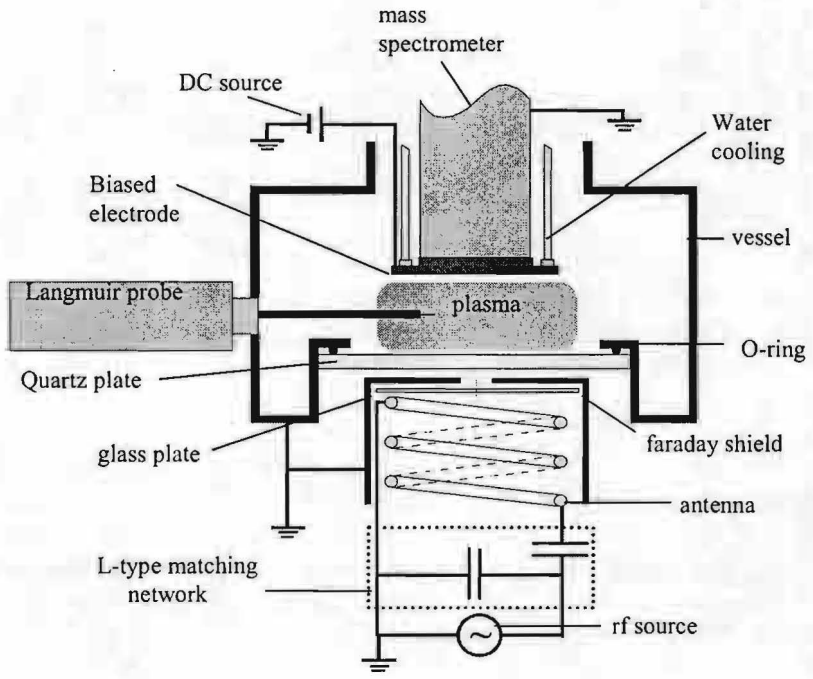

Figure 1: *Experimental Set-up*

In our set-up we can place, between the antenna and the quartz plate, a removable faraday shield and look at its influence on the plasma (the measurements presented here were all performed without faraday shield). A DC bias (varied between 0 V and -50 V) can be applied on the top electrode to accelerate the ions reaching its surface. Typical operation pressures are between 5 and 50 mTorr.

The plasma parameters are measured using a fully automated rf compensated Langmuir probe from Scientific Systems. The probe is positioned at a distance of 3cm away from the top electrode and can be moved radially inside the vessel. We can thus cover with its moving range a full radius of our vessel. It allows us to measure the plasma potential (Vp), the floating potential (Vf), the electronic temperature (Te), the ionic and electronic densities (resp. Ni and Ne), and the ion flux at the surface of the probe (Ii) at any radial position . EEDF's (Electron Energy Distribution Functions) were also recorded. Laframboise theory is used to fit the curves.

Results

We varied the DC bias on the top electrode from 0 V to –50 V and we looked at its influence on the plasma parameters. If the control of the impinging ions energies is really independent from

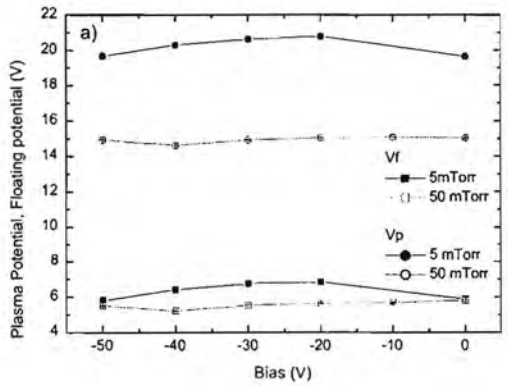

a)

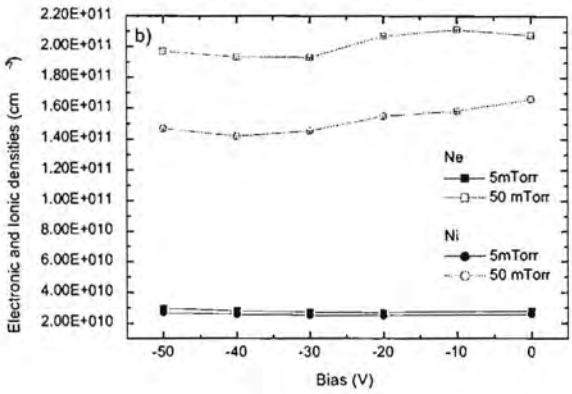

b)

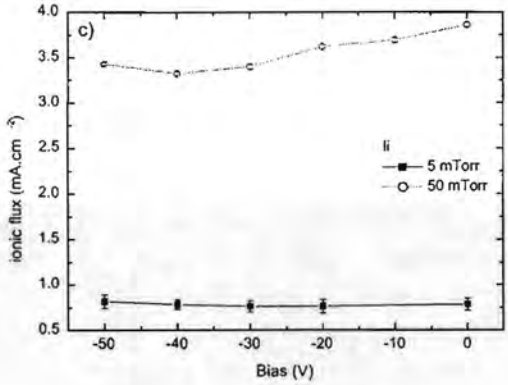

c)

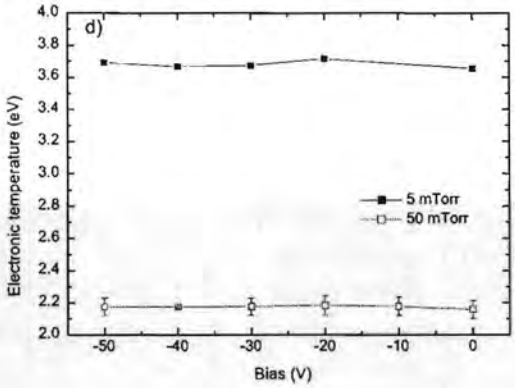

d)

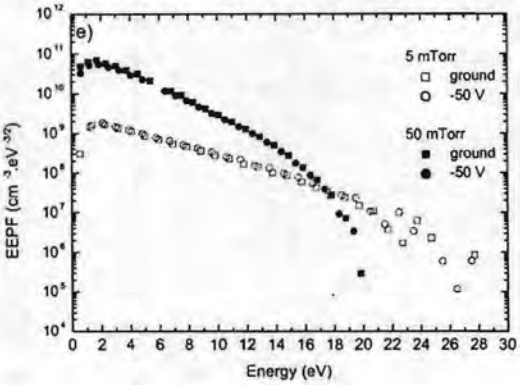

e)

Figure 2: Bias dependence of

a) Plasma potential (Vp) and Floating potential (Vf)
b) Electronic and Ionic densities (Ne and Ni)
c) Ionic flux (Ii)
d) Electronic temperature (Te)
e) Electron Energy Probability Function (EEPF)

the rest of the plasma conditions, the ions should be accelerated only in front of the substrate and we should not see any changes in the bulk. The results are shown on Figure 2 (graphs a) to e)) for 5 and 50 mTorr at a fixed power of 400 W in the inductive mode.

When the pressure increases from 5 to 50 mTorr , the neutral density increases and the ionization degree rises. The electrons on their side lose their high energy population in more inelastic collisions. As a consequence, Ne, Ni and Ii increase and Te and Vp decreases.

In opposition to the pressure whose influence is quite dramatic, the bias does not have any significant influence on the plasma parameters which leads us to the conclusion that the energy control of the ions at the substrate surface doesn't not interfere with the plasma bulk.

Conclusions and future

In this abstract we presented a study of the influence of a DC bias applied to the substrate electrode on the plasma parameters in an ICP source. The measurements obtained with a Langmuir Probe showed that the bulk plasma is not modified by this bias.
We have thus an apparent good decoupling of the accelerating electric field subsequent to the bias from the production of the plasma by the rf inductive power.
More measurements are though needed to know what happens at the surface. These measurements will be performed with the Mass Spectrometer and should be available at the time of the conference together with the rest of the measurements performed with the Langmuir probe. (Moreover the Doppler Shifted Laser induced Fluorescence (DSLIF) technique can be applied to determine the axial Ion Velocity Distribution Functions (IVDFs) of Ar^+ metastables along the path from the center of the plasma to the substrate surface.) These three techniques combined should give a good overview of the ions behavior in our ICP.

References:

[1] *Magnetic induction and plasma impedance in a planar inductive discharge*
J. T. Gudmundsson, M.A. Lieberman, Plasma Sources Sci. Technol. 7 (1998) 83-95
[2] *Hysteresis in the E- to H-mode transition in a planar coil, inductively coupled rf argon discharge*
M. El-Fayoumi, I.R. Jones, M. M. Turner, J. Phys. D: Appl. Phys. **31** (1998) 3082-3094
[3] *RF plasmas and RF Biasing of Remote Plasmas*
D. Vender, Lecture notes of Socrates Intensive Course CLTPP-4, July 7-9, 1999. Eindhoven, the Netherlands

Investigations on Electric Field Distributions in a Microwave Discharge in Hydrogen

D. Luggenhölscher, U.Czarnetzki, and H.F. Döbele
Institut für Laser- und Plasmaphysik, Universität Essen, Germany

Introduction

Microwave discharges play an important role in plasma sources for industrial applications like surface modification and thin film deposition. The electric field distribution in the plasma determines the electron density and energy distribution and the homogeneity of the discharge. The typical amplitude of the electric field is of the order of 100 V/cm. Up to now, this low field strength was not within the reach of laser spectroscopic techniques for electric field measurements. Recently, we have developed a novel technique in atomic hydrogen that allows the measurement of low electric fields down to 5 V/cm. The electric field is determined from the Stark splitting of high Rydberg states. (typically n = 14 - 20). Here, this technique is applied to a pulsed microwave discharge at 2.45 GHz in hydrogen with a 10 % argon admixture. The spatial and temporal field distribution is investigated in a commercial plasma source (SLAN). For the first time, we can measure both the microwave field and the microfield, originating from the plasma charges by a laser spectroscopic technique with high spatial and temporal resolution.

Spectroscopic Method

Neutral hydrogen atoms in the plasma can serve as probes for the local electric field strength. Due to the Stark effect, the energy levels of these atoms are shifted by the electric field. The shift and splitting of the according spectral lines scales with the principal quantum number n like n(n-1). Here, atomic hydrogen is excited in a first step by a Doppler-free two-photon excitation at $\lambda = 205$ nm to n = 3, and fluorescence light at Balmer-α, $\lambda = 656$ nm, is observed. In a second step the atoms are further excited by a tunable infrared beam around $\lambda = 850$ nm to the Rydberg state (typically n = 14 - 30). When this radiation is in resonance with a transition to a Stark shifted level, population is transferred from n = 3 to the Rydberg state, and the fluorescence at Balmer-α decreases accordingly: The spectrum is represented as a series of dips in the UV-laser. The field strength is inferred from a comparison of the measurement with calculated spectra. With this fluorescence-dip technique static fields as low as 5 V/cm can be measured[1].

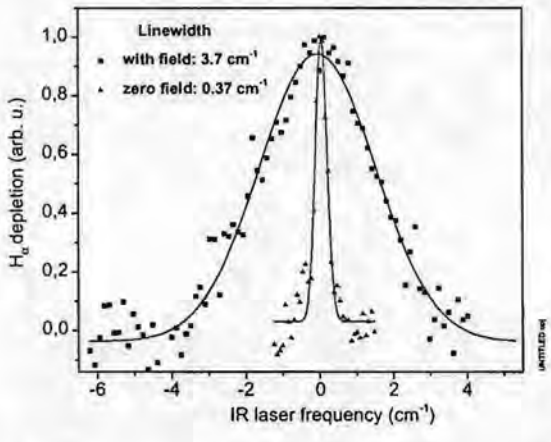

Fig.1: Line broadening in the microwave field in comparison to the field-free line shape.

The high frequency field of the microwave causes a Stark broadening which is different from the static analogon[2]. Each static Stark component is further split in a series of satellites which are separated by the microwave frequency ω. The maximum intensity of these so called 'Blochnizew satellites' is located close to the spectral position of the static Stark shift and a tail of satellites extends towards smaller

[1] U. Czarnetzki, D. Luggenhölscher, and H.F. Döbele , Phys. Rev. Lett. **81**, 4592 (1998)
[2] E. Oks, *Plasma Spectroscopy* (Springer Verlag Heidelberg Berlin 1995)

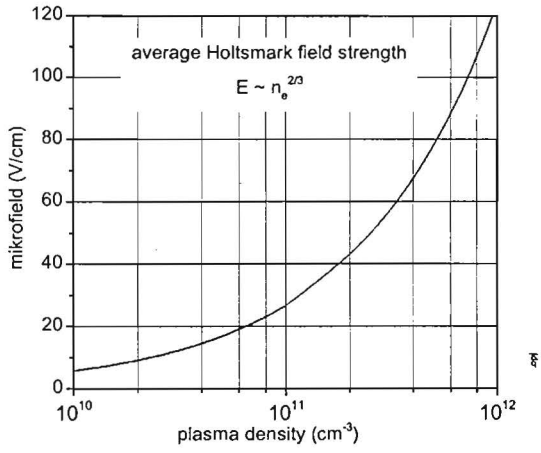

Fig.2: Average microfield from the Holtzmark distribution as a function of ion density.

shifts. The separation of the satellites $\omega = 15.4$ GHz is too small to be resolved in our measurements, and an unstructured line broadening is observed. An example is shown in fig. 1. As a result of this satellite structure, the line broadening is a little smaller than for a static field with the same amplitude. We have not included the Blochnizew satellites in our analysis yet, but apply the static broadening theory instead. The correct field strength of the microwave is probably higher by a few 10 %.

The electric fields related to the local charge distribution can also cause a line broadening[3]. The cold ions show a static distribution of local field strength. For most cases in low temperature plasmas this is well approximated by the so called Holtsmark distribution. The average field of this distribution E_H scales like $E_H = C\ N^{2/3}\ n(n-1)$, where N is the plasma density and n the principal quantum number (fig. 2). Further, fast electrons can give rise to a high frequency, dynamic field (collisional broadening). This contribution depends strongly on the temperature and the density of the electrons and is neglected here. A rough estimate shows that the error is probably less than a factor of two.

Experimental Set-Up

The plasma source is a commercial reactor, the so called „Slot Antenna Microwave Plasma Source (SLAN)"[4]. The microwave power at 2.45 GHz is distributed around a waveguide ring resonator (fig. 3). At the inner side of this ring the microwave is coupled to the plasma by 10 slit antennas. These antennas are separated by half a wavelength. The plasma is confined in a quartz cylinder of 16 cm diameter. Experimental parameters are: pulsing frequency: 200 Hz (30 % on, 70 % off), pressure: 30 Pa (90 % Hydrogen, 10 % Argon), microwave power: 540 W forward, 260 W reflected (cycle average), 1800 W forward, 870 W reflected (microwave on). The laser system consists of two Nd:YAG pumped dye lasers. One laser is frequency tripled and radiates at $\lambda = 205$ nm for the excitation of atomic hydrogen. The frequency of the second laser is shifted into the near infrared region around $\lambda = 850$ nm by a hydrogen filled Raman-cell. The fluorescence light is imaged onto a gated CCD-camera which allows simultaneous spatially resolved detection along the laser beam.

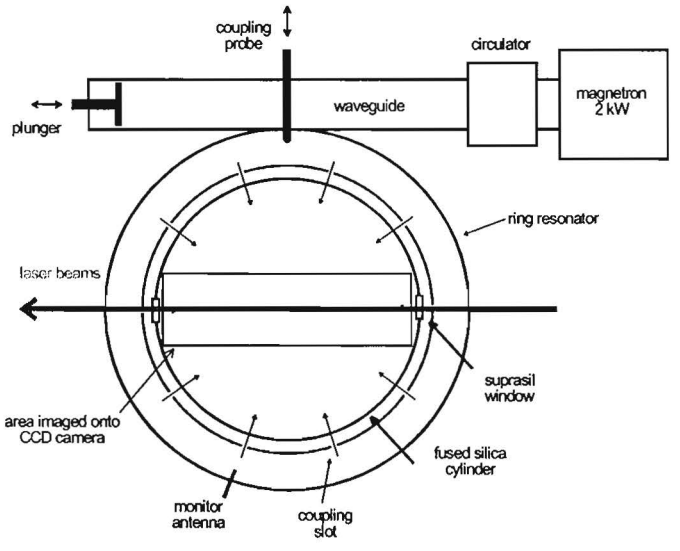

Fig. 3: Experimental setup: Top-view showing the ring resonator and the beam paths.

[3] H. R. Griem, Spectral Line Broadening by Plasmas (Academic Press, New York, London 1974)
[4] F. Werner, D. Korzec, J. Engenmann, Plasma Sources Sci. Technol. **3**, 473 (1994)

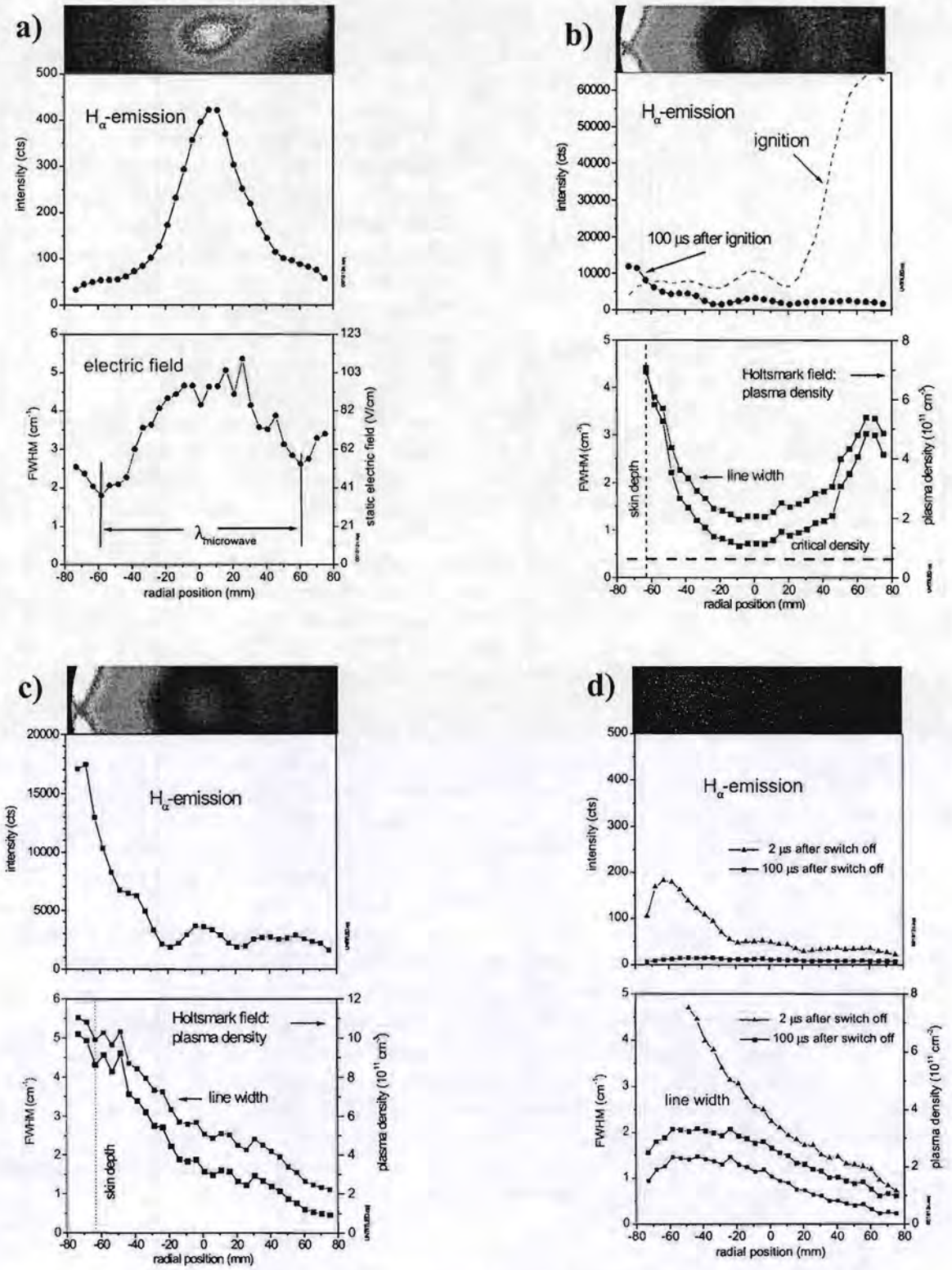

Fig. 5: Plasma indced emission at Balmer-α and electric field distributions at various phases during the microwave puls. The four figures are related to the numbers shown in fig. 4 as: a) 1, b) 2, c) 3, d) 4

Results

During the temporal evolution of the pulsed discharge, five phases can be destinguished: 1) prior to ignition, 2') ignition, 2) immedeately after ignition, 3) quasi stationary 4) afterglow. Electric field measurement are not possible in the not well reproducable ignition phase 2'). The four phases electric field measurements can be performed are indicated in fig. 4. The plasma induced emission profiles at Balmer-α and the electric field and plasma density distributions are shown in fig. 5.

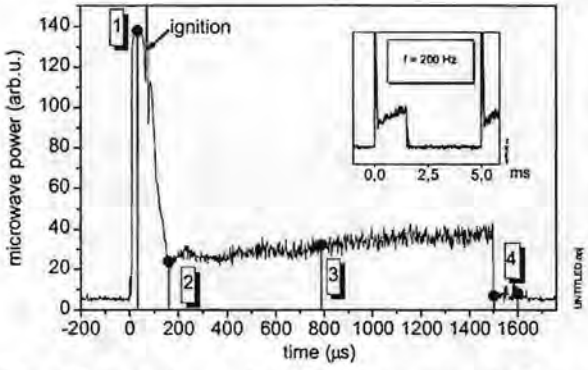

Fig. 4: Temporal evolution of the microwave puls. The numbers indicate points where electric fields were performed (see fig. 5).

Prior to ignition the microwave power is high inside the vessel but plasma induced emission is still very weak. Here we can measure the microwave field (fig 5 a).

The discharge ignites outside of the field of view of the CCD-camera at the surface of the quartz cylinder at a point close to the coupling probe (top of the scheme shown in the experimental setup). Then, the region of strong plasma emission moves clockwise around the wall of the cylinder until it stabilizes as an asymmetric discharge which is located mainly at the left hand side. The exact time of the ignition and the amplitude of the plasma emission is not exactly reproduceable in the pulsed mode for each repetition. Therefore, the plasma background emission at Ha shows strong fluctuations which are of the same order or even stronger than the dips in our laser spectroscopic measurements. This prevents electric field measurements in the ignition phase.

First measurements are possible about 100 ms after ignition (fig. 5b). The plasma stabilizes at the left side of the cylindrical tube. Charges produced during the ignition phase still remain on the opposite side. The plasma density is high on the left side and the microwave is strongly absorbed within a small layer of about 2 cm. Here the microfield is measured. The plasma density is deduced on the basis of the average Holtsmark field. The discharge finally stabilizes in a quasi stationary mode (fig. 5c). Plasma generation is only at the left side. Inside the vessel, charges are transported to the right side by diffusion. The microwave is absorbed within ~ 17 mm.

Within about 2 µs after switching off the plasma emission vanishes (fig. 5d). The plasma density decays much slower over several 100 µs by recombination and diffusion. The switch off of the microwave power is indicated by an immediate decrease of the monitor antenna signal, and the plasma emission goes down to zero within about 2 µs. However, the line broadening measured in the plasma decays much slower on a time scale of the order of 10 µs - 100 µs. This broadening is caused clearly by the microfield of the charged particles in the plasma. The spatial structure of the plasma density immediately before and after switch off is identical. The decay of the plasma density is much faster than the characteristic time for the fundamental diffusion mode which is of the order of ms. This fast decay can be caused by higher diffusion modes and recombination, preferably with molecular ions H^{3+}.

Acknowledgment

This project is supported by the „Ministerium für Schule, Wissenschaft und Forschung des Landes Nordrhein-Westfalen".

Challenges of Thomson scattering in molecular gas plasmas.

C.E.Thompson, P.G.Steen, G.Craig, T.Morrow & W.G.Graham
Dept. of Pure and Applied Physics, The Queen's University of Belfast, Northern Ireland.

Thomson scattering is an established technique for the determination of parameters (electron temperature and density) in relatively high-density (~$10^{20}m^{-3}$) plasmas. Recently Thomson scattering has been extended to investigate electron densities and energy distributions in lower density plasmas. Its non-intrusive nature and relatively straightforward interpretation make it an attractive alternative to techniques such as Langmuir probes. However, the small cross section for light scatter from free electrons means that signals are very low (typically ~20 photoelectrons/pulse for electron density $10^{17}m^{-3}$), and can be swamped by stray light and other types of scatter.

Here a Thomson scattering system was set up using the second harmonic of a 10 Hz Nd:YAG laser (0.5 J at 532 nm). The system was configured to minimise stray light scatter and collect as much light as possible from a small detection volume within the plasma. Instead of a photomultiplier as a detector, an intensified charge-coupled device (ICCD) and its associated software were used, allowing data to be collected over 5000 laser pulses in a relatively short period to increase signal-to-noise ratio. Fig.1 shows a schematic overview of the experimental set-up.

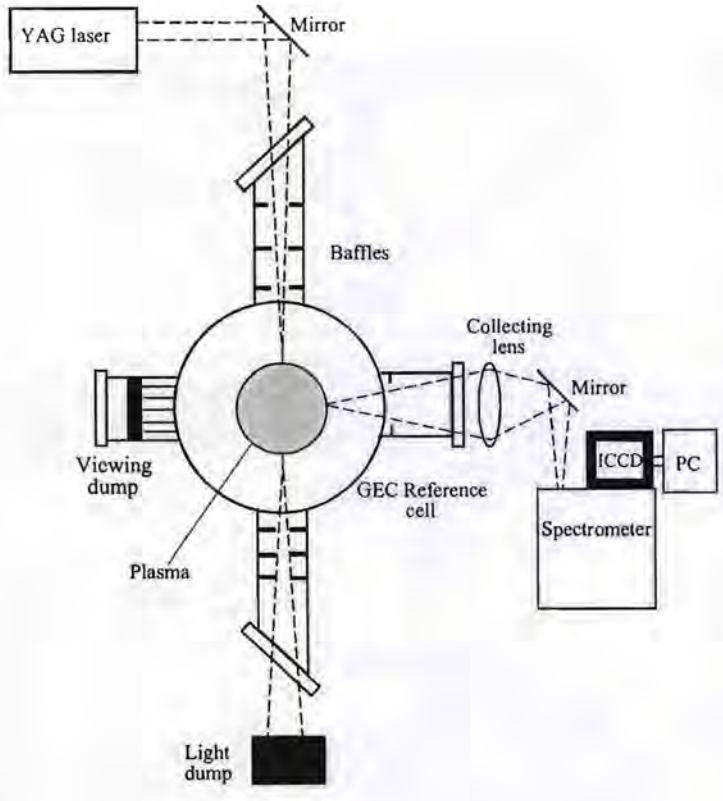

Figure 1: *Experimental schematic*

The plasma chamber was an inductively coupled version of the GEC reference cell, operable in either inductive or capacitive modes. The discharge was driven by a 13.56MHz rf field from a five-turn flat copper coil placed above a dielectric (quartz) window. Experiments were carried out in argon plasmas in a pressure range of 3-125mTorr (0.4-16.7Pa) and a power range of 10-100W. Absolute electron densities were obtained by calibration with equivalent pressures of neutral argon gas; the gas Rayleigh signal was normalised to the peak of the plasma signal to account for neutral gas density drop due to plasma heating. Electron densities and temperatures and constructed EEPF's deduced from these experiments compared well with Langmuir probe data taken in equivalent plasma conditions.

Initial experiments in nitrogen plasmas in the same system indicated the greater challenge presented by molecular gas. Electron densities tend to be much lower than for similar power and pressure conditions in an atomic gas plasma; Thomson scattered signals are consequently much lower (typically by an order of magnitude or more) and harder to extract from noise and extraneous signals. In addition to this, spontaneous plasma emission is more complex, and may vary over time. Ionisation effects, absorption and metastable states may affect emission, and the possibility of laser interaction with the plasma may therefore need to be considered. Vibrational and rotational effects are obviously an issue in a molecular gas, and a potential problem is Raman scattering. A calculated ground state Raman spectrum for nitrogen was found to fit closely the signal obtained from neutral nitrogen gas, as shown in Figure 2. In the plasma state, however, the presence of excited states may significantly change the shape of the Raman spectrum, making it difficult to distinguish the Thomson signal.

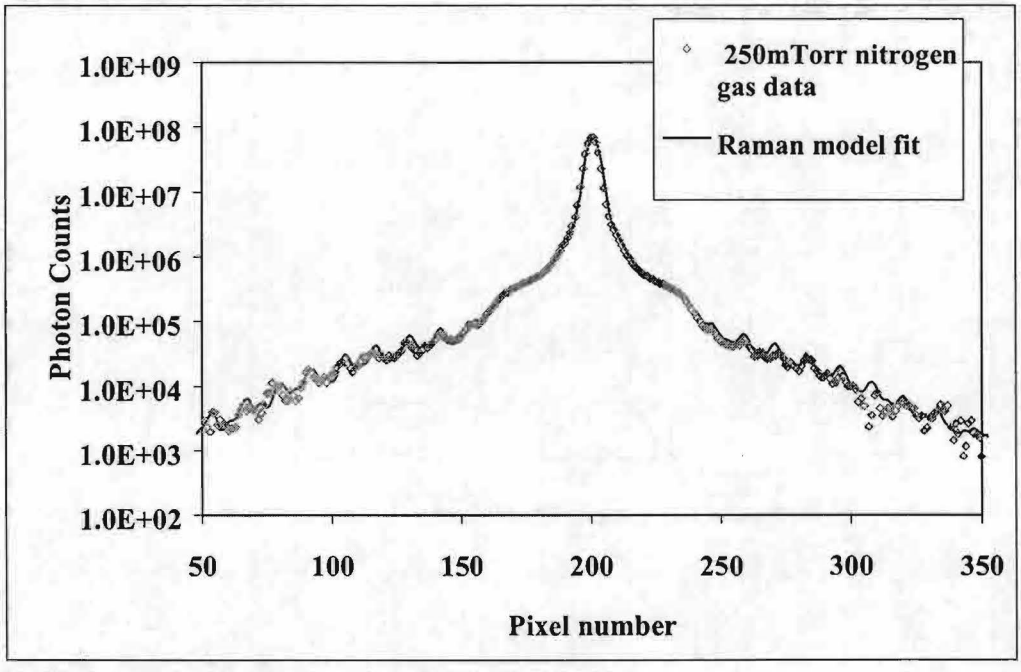

Figure 2: *Nitrogen gas data showing presence of Raman scattering.*

The poster will present an overview of the successful use of Thomson scattering in argon plasmas. The wider range of problems presented by extension of the technique to molecular systems will be illustrated with reference to experiments in nitrogen, and possible ways of dealing with some of these discussed.

Saturation phenomena in cw Cavity RingDown Spectroscopy, total density depletion by collisional transfers

P. Macko, D. Romanini and N. Sadeghi

Laboratoire de Spectrométrie Physique, Université Joseph Fourier-Grenoble I and CNRS (UMR C5588)
B.P.87, 38402 Saint-Martin-d'Hères Cedex, Franc

1. Introduction

Cavity Ring-Down Spectroscopy (CRDS) is a powerful technique, well adapted for the observation of very weak absorption signals. It uses the enhancement of the effective optical pathlength when laser light coupled into an optical cavity is reflected back and forth by the high reflecting mirrors of the cavity. The technique is based on the measurement of the decay of the intensity of the light leaking from one of the mirrors when a laser light pulse is injected into the cavity from the other mirror [1]. For linear absorption, this decay is exponential with decay time, $\tau(\nu)$, given by:

$$\frac{1}{\tau(\nu)} = \frac{1}{\tau_0} + \frac{d}{L} c\alpha(\nu) \qquad (1)$$

where τ_0 is the decay time in the absence of any absorption, d and $\alpha(\nu)$ are the length and absorption coefficient of the absorbing medium and L is the length of the cavity.

But, when the laser power injected inside the cavity is high, or when strong electronic transitions are considered, non-linear absorption can occur due to the well known saturation phenomena [2]. This saturation may results from either depletion of the lower sate or overpopulation of the upper state and it gives rise to a laser power dependent effective absorption coefficient $\alpha(\nu)$. As the power density inside the cavity is decaying during the ring-down (**RD**) time, consequently the decay of the intensity is no longer an exponential function. The purpose of this work is to show the importance of this phenomenon even when very weak diode laser sources are used. The absorbing medium was a weak neon + argon discharge, producing neon metastable atoms, and the laser frequency was tuned on the 653.288 nm ($3s'[\frac{1}{2}]_0 \rightarrow 3p[1\frac{1}{2}]_1$) neon line, absorbing from $3s'[\frac{1}{2}]_0$ (or $^3P_0$) neon metastable atoms.

2. Experimental

The experimental set-up for cw-CRDS was extensively described in Ref. [1,3], except that the dye laser was replaced with an external cavity single mode tunable diode laser working around 655 nm. One of the supermirrors (R=99.995%; f=90 cm; distance L≅88 cm) was mounted in a piezoelectric device in order to adjust the length of the cavity to match the laser frequency to one of its TEM_{00} modes. The acoustooptics modulator (AOM) interrupts the laser beam once the RD signal is detected by PMT. The 50 μm pinhole **P** and lenses **L** match the laser beam to the TEM_{00} cavity mode. The beam waist of ω=0.32 mm was located in the center of the plasma tube. The laser power, a few mW, was reduced to about 0.1 mW before entering the cavity. Laser frequency was scanned over about 8 GHz, by steps of 0.01 GHz. A 17 cm long Fabry-Perot gives the precise frequency shift calibration. A weak dc discharge (i≅0.1 to 3 mA) in a slowly flowing Ne-Ar mixture (p= 13 to 500 Pa, 7 to 30 % of argon) produced a very low concentration of neon metastable atoms in the central part of a ϕ= 3.0 cm; l= 80 cm cell. The length of the discharge zone, d, was a few cm. Absorption from a dc glow discharge in a neon cell provides the non-saturated line profile. At each frequency,

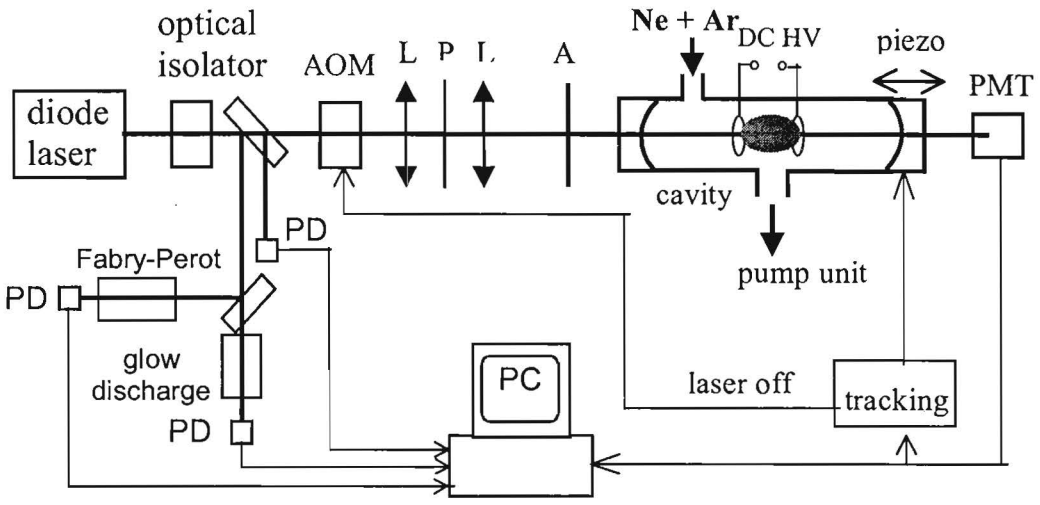

Fig. 1 – Experimental set-up. (**AOM**) acoustooptic modulator; (**L**) lens; (**P**) 50 μm pinhole; (**PD**) photodiode; (**A**) attenuator; (**PMT**) photomultiplier.

the RD decay curve, laser intensity, absorption signal from the cell and FP signal were acquired and stored in a PC.

3. Experimental Results

Fig. 2 shows an example of the CRDS signal decay curves at different laser frequencies. When the discharge is off, the decay, due only to the mirrors loss (τ_0) is an exponential. With the discharge on and laser set on the absorption line, we observe a faster but non exponential decay. In Fig. 2 are shown decay curves for the laser frequency set at –0.1, –0.6 and –1.2 GHz, respectively, relative to the line center frequency ν_0. With increasing RD time, the laser intensity inside the cavity decreases, leading to a weaker saturation and consequently to a larger apparent absorption coefficient. To build the absorption profiles at a given laser power, the slopes of the different decay curves, obtained at different laser frequencies, are deduced for the same amplitude of the RD signal (represented by horizontal lines in Fig. 2). This signal is in fact proportional to the light power inside the cavity. At each frequency the corresponding value of $\alpha(\nu)$ is then calculated. Fig. 3 shows the absorption line profiles built from the slops of the RD curves at different signal level. The total pressure was 66 Pa with 14% of argon in neon. The highest curve (S=0) is deduced from the weakest RD signals of the latest part of the RD period, when the laser power inside the cavity is very small. This curve can perfectly be fitted with the Doppler profile of the 653.288 nm line at 300 K. The asymmetric profile results from ^{22}Ne isotope, present at 9.2% in the natural neon, whose line is shifted by 1.530 GHz relative to the ^{20}Ne line. The lowest curve (S=10) is built from the slops deduced from RD signals at 1000 mV. The estimated laser power inside the cavity is about 0.3 mW for this curve. The other curves are from RD signal levels 2, 4, 8, 16, and 32 time smaller than for this former curve, respectively. As expected, the higher the light power inside the cavity is, the smaller the absorption coefficients are. This is due to the optical saturation effect that reduces $\alpha(\nu)$ [2]:

$$\alpha(\nu, I) = \alpha(\nu, 0) / \sqrt{1+S} \qquad (2)$$

where S, the saturation parameter is proportional to the light intensity [2].

Our results show that CRDS is also a powerful tool for sub-Doppler spectroscopy. However, if the saturation phenomena is not considered, the absorbing species density can be

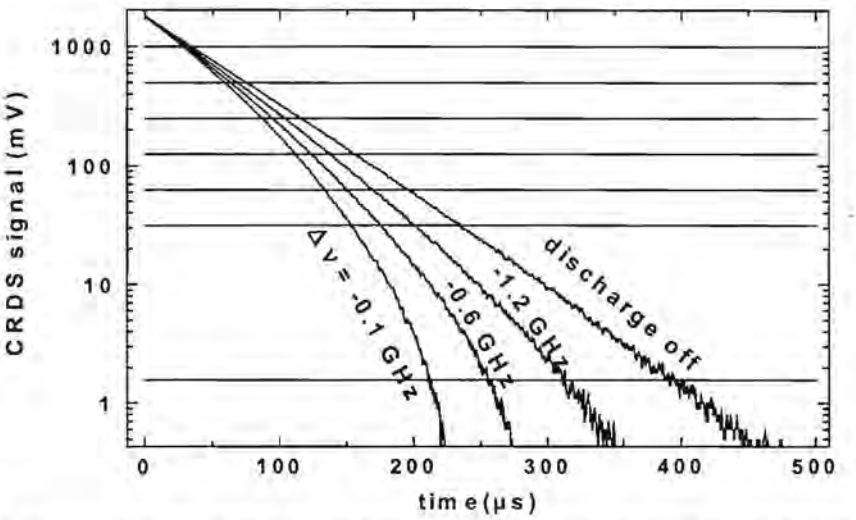

Fig. 2: Decay curves of CRDS signal at different laser frequency. $\Delta\nu$ is relative to the rest frequency ν_0.

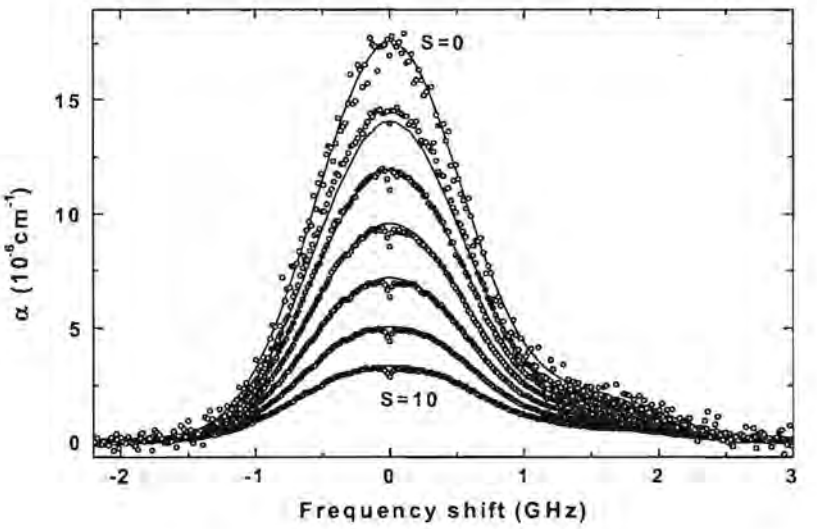

Fig. 3: Absorption line profiles built from the slopes of the RD decay curves, shown in Fig. 2, at different signal levels of Fig. 2. The upper curve corresponds to the non saturated condition, at 1.6 mV. The lowest curve is for the highest RD signal (1000 mV) and the following curves are for the RD signal levels of 500, 250, 125, 62 and 31 mV, respectively. Solid lines are from our model.

largely underestimated. The density of Ne($^3P_0$) atoms, deduced from the non saturated curve (largest $\alpha(\nu)$) is about 1x 10^6 cm^{-3}. Also, a Gaussian fit of the S=10 profile gives a temperature of about 500 K, instead of room temperature. Note the presence of Lamb dips at the center of the experimental line profiles of Fig. 3. When the laser is set at the line center ν_0, Ne ($^3P_0$) metastable atoms crossing perpendicular to the cavity axis absorb photons traveling in both directions. Therefore, the depletion of this group of atoms by optical pumping is two times more efficient than when the laser frequency is shifted and photons traveling in opposite directions interact with two different groups of atoms [2].

4. Modeling

To fit the experimental absorption profiles we model the laser-atom interaction by considering two groups of Ne ($^3P_0$) atoms for each isotope. The first group is composed by atoms interacting with the laser radiation. The velocity w along the cavity axis of these atoms is in the interval $w \pm \delta w/2$, where $w=(c/\nu_0)(\nu-\nu_0)$ satisfy the Doppler shift condition and $\delta w=(c/\nu_0)\delta\nu$, with $\delta\nu$ being the homogeneous linewidth [2]. For this group, populations of the lower and upper states of the transition are described in terms of radiative and collisional processes. The second group includes all other Ne($^3P_0$) atoms having their velocity outside the $w \pm \delta w/2$ interval. Velocity-change and metastability-exchange collisions couple theses two groups, as well as populations of the two isotopes. So, the Ne($^3P_0$) density depletion of the first group by optical pumping induces also a depletion in the total density of Ne($^3P_0$) atoms. Transport of atoms by diffusion between the 0.64 mm diameter laser irradiated volume and outside this volume must also be considered to account for the renewal of metastable atoms in the interaction volume. Solid lines in Fig. 3 are model simulations, without including Lamb dips, for different laser intensities. They perfectly reproduce our experimental curves.

References:

[1] D. Romanini, A.A. Kachanov, N. Sadeghi and F. Stoeckel, *Chem. Phys. Lett.* **264** (1997) 316

[2] W. Demtröder, *Laser Spectroscopy*, 2nd Ed. (Springer, Berlin, 1996).

[3] A. Campargue, D. Romanini and N. Sadeghi, *J. Phys. D : Appl. Phys.* **31** (1998) 1168

Instabilities in Inductively Coupled Plasmas

C.S. Corr, P.G. Steen and W.G. Graham,
Dept. Of Physics, The Queens University of Belfast, BT7 1NN, Northern Ireland.

Low-pressure inductively coupled discharges operating with electronegative gases are increasingly used for industrial materials processes such as etching and deposition. Previously, instabilities have been studied in dc glows[1-3] and capacitive discharges[4] and more recently in low-pressure inductive discharges[5,6]. The first reported study of instabilities in an inductive discharge was by Michel Tuszewski[5] with the cylindrical configuration using O_2 and Ar/Sf_6 plasmas. This source was operated with a 12-turn copper coil and the driving frequency was 0.46 MHz with a power range of 200 – 500 W and pressures of 0.25-10 mTorr. The instabilities were observed using a cylindrical Langmuir probe with frequencies in the range of 1-40 kHz. The instabilities are observed to be self-excited modulations of the ion plasma density perhaps similar to those which have been observed in glow discharges and capacitive discharges. More recently, instabilities were observed in O_2 and SF_6 by Lieberman *et al*[5] using the planar coil configuration. The applied power to the coil at 13.56 MHz was 100-1000 W. In this case instabilities were observed with frequencies in the range 1 Hz – 900 kHz as detected by the optical emission to a photomultiplier tube and the current to an unbiased Langmuir probe. It has been suggested that a possible cause of this instability is due to the switching between capacitive and inductive modes where the relaxation oscillations had sometimes 100 % modulation i.e. the electrons were almost completely expelled during the oscillation.

In this work a low-pressure radio frequency oxygen discharge is investigated. Oxygen plasmas have been used in industrial material processing such as ashing and the production of oxide films. The simplicity of oxygen in comparison to other electronegative gases (e.g. CF_4 and SF_6) and the availability of a wide database of reaction rates make oxygen discharges a good subject for experimental investigation.

A reproducible instability has been observed in a low-pressure, 13.56 MHz inductively coupled GEC[7] rf cell operating in oxygen. The antenna is a 5-turn water-cooled copper coil that couples power to the plasma through a quartz window. The grounded lower electrode diameter is 165.1 mm with an electrode-quartz window spacing of approximately 40.5 mm. The coil is powered through a close coupled, rf matching network by a 350 W rf power supply. Oxygen is fed into the chamber through a 0-10 sccm MKS flow meter. The discharge is operated in the pressure range of 1-100 mTorr. As can be seen from Fig. 1, there is a power and pressure regime that can support either a capacitive or an inductive mode discharge, where the mode

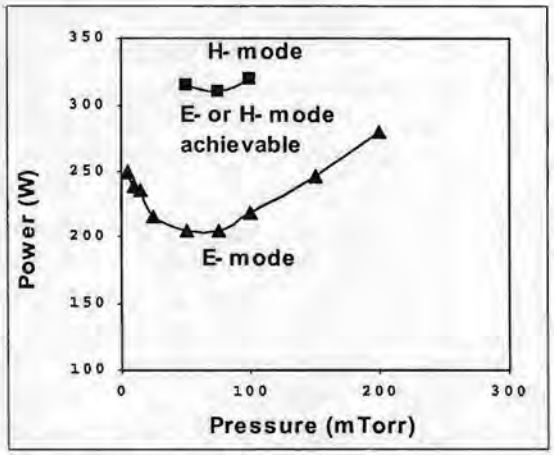

Fig. 1. Hysteresis of an oxygen inductively coupled plasma

present depends on the history of the system[8]. Such behaviour is called hysteresis[9]. It is within this power and pressure regime that the instabilities are observed to occur.

An uncompensated Langmuir probe and a photodiode with fibre optic were used to observe the time variation of the instability. Spatial and temporal variation of the optical emission through one oscillation period of the instability was observed with an ICCD. Currently, probe-assisted laser photodetachment measurements are being made. This setup consists of a frequency doubled Nd:YAG laser with a Langmuir probe detecting the detached electrons. A compensated Langmuir probe is used to make electron density measurements.

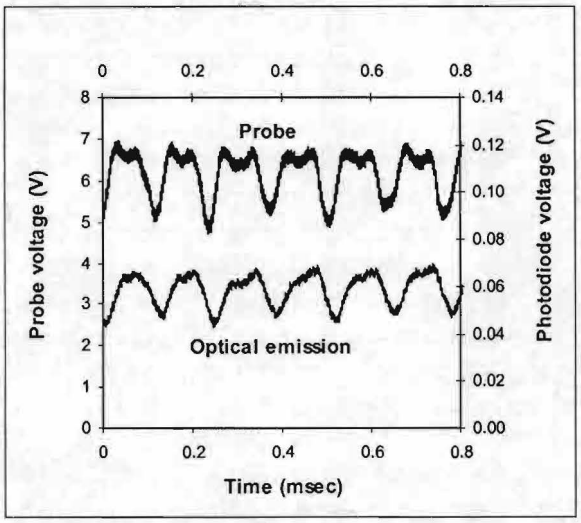

Fig. 2. Time variation of optical emission and probe current at 11 mTorr and 250 W

The instability is observed in the form of periodic modulations in the output of a photodiode and an unbiased Langmuir probe (Fig. 2). The instability occurs at operating powers between 240 and 340 W (at all times reflected power is kept to a minimum i.e. < 13 W) and at gas pressures from 5 to 23 mTorr. The frequency of oscillations increases with increasing gas pressure from 3 to 21 kHz but do not vary significantly with power. The amplitude of the oscillations varies with both gas pressure and power. These results are consistent with Lieberman et al[6] and Tuszewski[5]. No instabilities have been observed with argon gas.

The instability has also been observed as the spatial movement of the plasma emission as detected by an ICCD. The ICCD was gate triggered at the minimum of the Langmuir probe signal and the variation of the optical emission was observed through one oscillation period (Fig. 3). The frequency of this instability is ~ 10 kHz. It has previously been suggested that the instability is due to the expulsion of negative ions from the plasma core. This is perhaps an explanation for what we have observed.

The instabilities in inductive discharges are thought to be due to negative ions as there has been no reported studies of instabilities in inductively coupled electropositive plasmas such as argon. Probe-assisted photodetachment[10] is a valuable technique for determination of negative ion

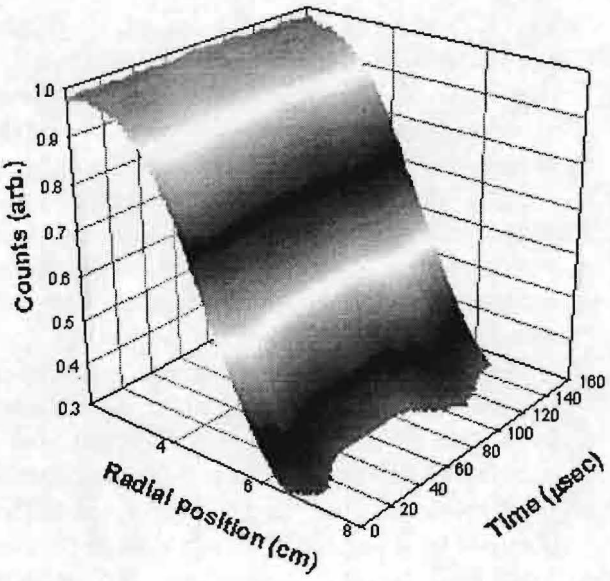

Fig. 3. Spatial variation of emission at 844 nm through one oscillation period

densities. In a plasma, photodetachment produces an increase in the electron density without an immediate increase in the positive ion density. Thus, by simply collecting the extra electrons on a positively biased Langmuir probe after the negative ions have been destroyed by the laser pulse, the negative ion fraction can be obtained.

The technique of probe-assisted photodetachment has been employed at Queens University to determine negative ion density measurements with both an uncompensated and a compensated Langmuir probe at low pressures (<100 mTorr). A typical photodetachment signal is shown in Fig.4. Preliminary experiments have shown the negative ion fraction to be between 4 and 80% in the capacitive mode and between 1 and 25% in the inductive mode. It is found that the negative ion density decreases with increasing rf power in both capacitive and inductive modes. As a function of pressure, the negative ion fraction is at an optimum pressure of ~15 mTorr in both capacitive and inductive. The results are similar to those of Stoffels *et al*[11]. Currently, time resolved photodetachment and eedf measurements are being performed in the instability region.

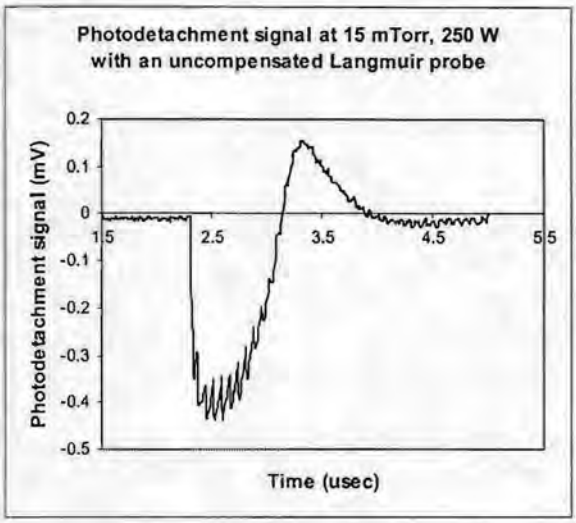

Fig.4 A typical photodetachment pulse in a oxygen discharge

Acknowledgements:

The authors gratefully acknowledge the assistance of Sergi Gomez and Charlie Mahony and the stimulating conversations with Pascal Chabert.

References

[1] R.A. Hass, *Phys. Rev. A* **8**, 1017 (1973)
[2] W.L. Nighan and W.J. Wiegand, *Phys. Rev. A* **10**, 922 (1974)
[3] A.D. Barkalov and G.G. Gladush, *Sov. Phys. Tech. Phys.* **24**, 1203 (1979)
[4] E. Metsi, E. Gogolides, A. Boudouvis, *Phys. Rev. E*, **54**, 782 (1996)
[5] M. Tuszewski, *J. Appl. Phys.* **79**, 8967 (1996)
[6] M.A. Lieberman, A.J. Lichtenberg, and A.M. Marakhtanov, *Appl. Phys. Lett.* **75**, 3617 (1999)
[7] P.A. Miller, G.A. Hebner, K.E. Greenberg, P.D. Pochan, and B.P. Aragon, J. Res. Natl. Inst. Stand. Technol. **100**, 427 (1995)
[8] I.M. El-Fayoumi, I.R. Jones, and M.M. Turner, *J. Phys. D* **31**, 3082 (1998)
[9] M.M. Turner and M.A. Lieberman, *Plasma Sources Sci. Technol.* **8**, 313 (1999)
[10] M. Bacal, G.W. Hamilton, A.M. Bruneteau, and J. Doucet, *Rev. Sci. Instrum.* **50**, 719, (1979)
[11] E. Stoffels, W.W. Stoffels, D. Vender, M. Kando, G.M.W. Kroesen, and F.J. de Hoog, *Phys. Rev. E* **51**, 2425 (1995)

Measurements of Substrate Charging After Plasma Processing

A. Howling, L. Sansonnens, Ch. Hollenstein, A. Belinger*, E.Turlot*, J. Perrin*, J. Schmitt*
Centre de Recherches en Physique des Plasmas, EPFL, CH-1015 Lausanne, Switzerland
**Unaxis France SA, Displays Division, 5 Rue Leon Blum, F-91120 Palaiseau France*

Introduction

An electrostatic charge can be left on an insulating substrate after RF plasma processing, despite the fact that the plasma and surfaces are globally neutral. If the glass has non-zero conductivity, charge appears also on the back face where there is no contact with the plasma. In this case, the glass sticks electrostatically to the electrode, and partial discharging occurs when it is lifted. Analysis of *in situ* charge measurements reveals the mechanism responsible for the charging, which is analogous to electrostatic chucking of the glass to the electrode when exposed to plasma.

Electrostatic Discharge Damage due to Substrate Charging

Electrostatic charging of an insulating substrate when exposed to a plasma is a concern for electronic device fabrication where several plasma processing steps (deposition, etching and ashing) are involved. In particular for thin film transistors (TFT's) on glass substrates in active-matrix liquid crystal displays (AM-LCD's), the residual charge left on the substrate at the end of the process can induce large electric fields along the glass surface when manipulating it afterwards. Via the interconnecting circuitry within the matrix this field can induce high local voltage across thin dielectrics resulting in breakdown and irreversible damage.

To measure the value of this residual charge after a plasma processing step we propose an *in situ*, non intrusive technique easily implemented in any production reactor using a system of movable pins for substrate handling [1]. We also discuss the dependence of this charge on the plasma process parameters.

Experimental Arrangement

Experiments were performed in a KAI "plasma-box" reactor [2] devoted to PECVD of amorphous silicon, silicon nitride and silicon oxide films on 370×470 mm^2 glass substrates for mass production of AM-LCD's. The RF (13.56MHz) discharge is capacitively coupled via a *L*-type matching circuit involving a series capacitor. The inter-electrode distance d is 24 mm. The glass substrate is placed on the grounded electrode and can be moved up and down for loading and unloading by four ceramic pins. Taking advantage of these movable pins we propose an original method for measuring the residual charge Q on the glass substrate just after the plasma. As shown in figure 1 an electrometer is inserted between the grounded and the RF electrode. After the plasma extinction the electrometer circuit is closed by a switch. Then the glass plate is moved at a constant uprising velocity u ($\approx$0.5 $cm.s^{-1}$) so that the distance between the glass plate and the grounded electrode varies linearly with time : $d_l = ut$. Simultaneously the current J between the electrodes is recorded.

After the extinction of the discharge and during the plate movement the equivalent electrical circuit of the system is shown also in figure 1 where the effects of inductance are neglected on the time scale of the current variation.

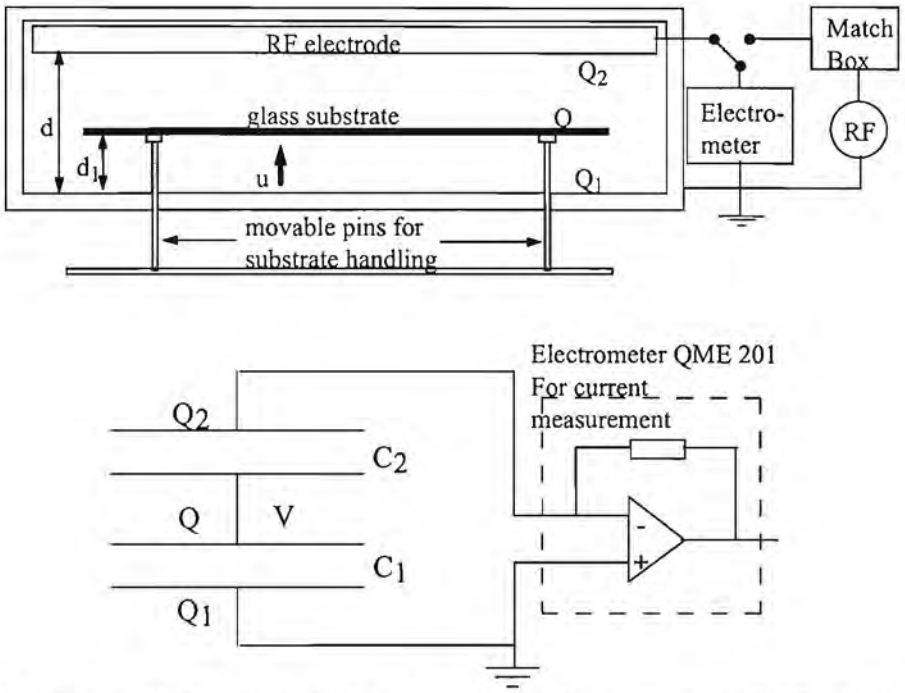

Figure 1: *Experimental set-up (top); equivalent circuit during the measurement after the plasma (bottom)*

C_1 and C_2 are the capacities formed by the substrate with the grounded electrode and by the substrate with the RF electrode respectively. The RF electrode potential is forced to 0V by the connection to the electrometer. The neutrality of the reactor gives:

$$-Q=Q_1+Q_2 .$$

Q_1 and Q_2 are the stored charge in the capacities given by:

$$Q_1=-C_1V, \text{ with } C_1=\varepsilon_0 A/d_1 \text{ and } Q_2=-C_2V, \text{ with } C_2=\varepsilon_0 A/(d-d_1)$$

where V is the potential at the charged substrate surface, A is the substrate area, d the inter-electrode distance, and d_1 the distance between the substrate and the grounded electrode. Substituting for Q_1 and Q_2 gives

$$V=Q/(C_1+C_2)=Qd_1(d-d_1)/\varepsilon_0 Ad \quad \text{and}$$

$$Q_2=-C_2Q/(C_1+C_2)=Qd_1/d .$$

The time derivative yields

$$\frac{dQ}{dt}=\frac{-Q}{d}\frac{d(d_1)}{dt}=\frac{uQ}{d}=J$$

where u is the lifting speed of the substrate and J is the current measured through the electrometer. If the substrate is lifted at constant speed, the total residual charge on the substrate is simply:

$$Q=\frac{Jd}{u}$$

Figure 2 shows typical results of the measurement of residual charge on a float glass substrate following an argon plasma at 0.1 mbar, 13.56 MHz, 60 W RF power at room temperature. The substrate was moved up and down at a constant speed of 0.5 cms^{-1}. The slow time response at the beginning and end of the measured current is due to an *RC* noise reduction filter in the electrometer output circuit. The total residual charge on the substrate is calculated from the current plateau. For the case shown, Q = -13.4 nC.

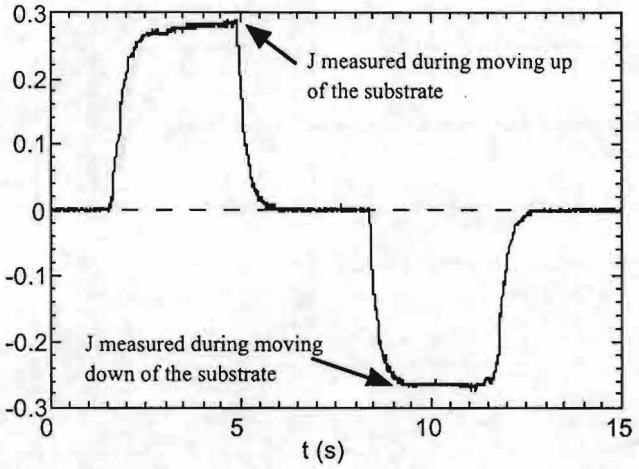

Figure 2: *Typical measurement of current J (x10^{-8} A) during moving up and down of the substrate*

This charge measurement technique is *in situ* and non-intrusive: it can be applied directly to the reactor just after a plasma process, without breaking vacuum. A charge as low as 1 nC is detectable, corresponding to a maximum substrate potential of 5V which is well below the damage threshold for electrical breakdown of devices on the substrate. The measurement gives the total residual charge on the substrate which represents the algebraic sum of the charge distributed over the substrate area. However, for a uniform plasma, we can expect the residual charge to be almost uniform across the substrate area. In production lines, this technique can detect a charge problem at the beginning of substrate unloading, before any irreversible damage occurs.

The glass substrate potential V is maximum for $d_1 = d/2$. For the largest measured value of Q (1.2 10^{-7} C for low pressure H_2 discharges) V can exceed 500 V. This shows the risk encountered when unloading the plate. Various solutions to compensate this residual charge by a post-treatment in the reactor are currently examined.

Mechanism of Substrate Charging

If both electrodes were perfect insulators, the average steady-state charge Q_{plasma} when the discharge is on should exactly compensate the positive space charge sheath, and after discharge extinction Q should come back to zero. But here the RF electrode is conducting and connected to the match box series capacitance which is charging up and builds a DC self bias voltage (negative). During the discharge the charge is distributed between the glass plate, the RF electrode and the match box, and during the post discharge a redistribution occurs together with the sheath decay and ambipolar diffusion of ions and electrons. Thus the sign and magnitude of Q are difficult to predict.

If the glass has non-zero conductivity, charge can also appear on the back face where there is no contact with the plasma. A simple model to describe the charging mechanism assumes a small vacuum gap h (several μm) between the glass and electrode where electrical contact is poor due to surface roughness. An equivalent circuit of the plasma-glass-electrode system is shown in figure 3. The effective capacitance and resistance of the gap depend on the roughness, density, Young's modulus and resistivity ρ of the glass. The plasma maintains a DC potential V_{dc} of a few volts across the glass thickness due to a combination of RF sheath voltage rectification and plasma self-bias. The charge remaining on the glass back face after plasma extinction depends on the glass dielectric relaxation time $\tau = \rho\varepsilon$, V_{dc}, the plasma

duration and kinetics of the discharge afterglow; the maximum possible charge density being $\varepsilon_o V_{dc}/h$. The Arrhenius nature of glass resistivity means that the magnitude and decay time of the observed residual charge vary enormously with process temperature. Taking for example a Corning 1737F display-quality glass substrate, the dielectric relaxation time varies from 4 seconds at 280 degrees Centigrade to 1700 years at room temperature, a factor of 10^{10}!

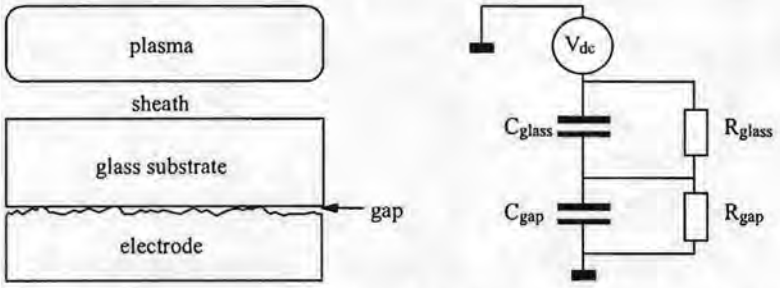

Figure 3: *Schematic of the plasma-glass-electrode system and its equivalent circuit*

In the case of backface charging, the glass can stick electrostatically to the grounded electrode: this is observed in practice and can even lead to glass breakage when attempting to lift the glass. The electrostatic sticking force per unit area is given by:

$$F=\varepsilon_0\varepsilon_r V_{dc}^2/2h^2$$

where V_{dc} is the DC potential maintained across the distance h during the discharge. If the discharge duration (plasma processing time) is long compared to the substrate dielectric relaxation time, then the voltage V_{dc} will eventually appear across the vacuum gap. Supposing $V_{dc} \sim 20$V and a vacuum gap of 5 μm, we obtain a sticking force of 7 gram cm^{-2} which is larger than the glass specific weight of 0.3 gram cm^{-2} for 0.7 mm glass thickness. On the other hand, if the charge is assumed to remain only on the top surface, the force is only approximately 0.001 gram cm^{-2}, which is far too small to account for the observed electrostatic sticking.

A consequence of the backface charging is that the potential difference between the glass and the ground electrode will increase one thousand fold if the glass is lifted several mm. In fact, the first time that the glass is lifted after processing in a hot reactor, a sharp initial peak in the current measured by the electrometer is indicative of micro-discharging between the glass and electrode, i.e. partial discharging occurs when the charged glass is first lifted. Moreover, this initial current peak does not occur if the back face has a conductive layer, or if the substrate is placed on thin glass spacers to prevent close contact with the ground electrode ($h >> 1$ μm).

This description of substrate charging is analogous to electrostatic chucking of the glass to the electrode when exposed to plasma. Various methods to eliminate the residual charge by post-treatment in the reactor are currently under investigation.

References

[1] L. Sansonnens, A. Howling, Ch. Hollenstein, J. Perrin, J. Schmitt, E. Turlot, Proc. 3rd Int. Conf. Reactive Plasmas ICRP-3, Nara, Japan p309 (1997).

[2] J. P. M. Schmitt, T. Emeraud, E. Turlot, N. Szidlo, H. Lebrun, and J. F. Teissier, Proc. Display Manufacturing Technology Conf., Santa Ana, 1995 p69.

Excitation coefficients for ionic levels of Xe

N.Sadeghi[a], Z.Lj. Petrović[b], G.N. Malović[b] and A.I. Strinić[b]

a) Laboratoire de Spectrométrie Physique, Grenoble, France

b) Institute of Physics, P.O.B 57, 11001 Belgrade, Yugoslavia

Introduction

Electron energy dependent cross sections for excitation of ionic levels of xenon are required for modeling of low pressures xenon discharges, plasma thrusters in particular. In the present work, we present the electron excitation coefficients of several ionic levels of xenon from the ground state of neutral xenon.

Experimental setup

Measurements were performed in two different drift tubes with similar geometry. One setup [1-3] allowed absolute calibration of the emission with poor spectral resolution, so only for a few isolated lines. In this case, the electric field to xenon atom number density ratios (*E/N*) was 3 10^{-19} Vm^2 to 1 10^{-17} Vm^2. Emission from plasma was analyzed with a monochromator backed by a PMT.

The other setup allowed higher resolution measurements with *E/N* between 1.2 10^{-18} Vm^2 and 4 10^{-17} Vm^2. In this case the PMT was replaced by an Intensified Optical multichannel analyzer with very high sensitivity allowing multiplex detection of different lines with high spectral resolution.

The gap between the two parallel electrodes was 1.7 cm in the former and 2.1 in the latter tube, while the diameter was 8 cm for both, allowing uniform field. The cathode was made of stainless steel and the anode of vacuum-grade sintered graphite in the first case and stainless steel in the second case. The quartz tube around the electrodes enables operation below the Paschen minimum by preventing the long path breakdown. Operating dc current was 2 μA in all measurements in order to reduce the space charge effects on the electric field [4,5].

Results

The emission from the 6s ^4P - 6p $^4D^0$ and 5d ^4D – 6p $^4P^0$ ionic transitions of xenon was used to obtain the absolute excitation coefficients (see Fig 1. and Fig. 2). The excitation coefficient data for ionic and neutral levels of argon and xenon were also used to establish the absolute calibration in the second drift tube. The ionization coefficients were also determined from the spatial emission profile. In the analysis we have taken advantage of the fact that our measurements have been performed mostly at very low pressures where quenching by parent gas is negligible. Excitation coefficients were obtained for additional XeII lines on the basis of the second drift tube. These measurements required greater sensitivity and resolution to isolate different lines. The data were obtained between moderate *E/N* values, when the electrons energy is in equilibrium with the local E field, and very high *E/N* values, where electrons may not be in equilibrium with the local field. The transition probabilities were taken from tables by Aymar and Columbe [6].

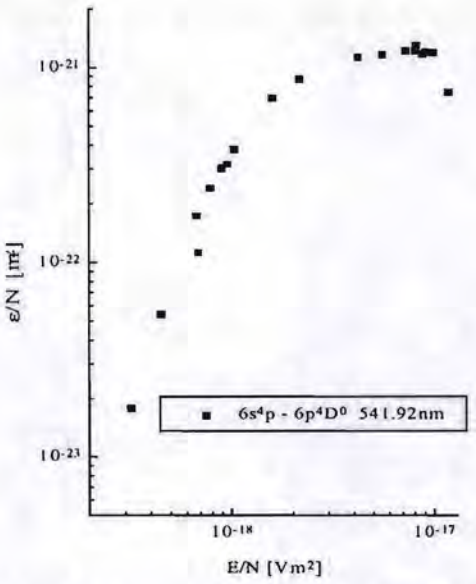

Fig.1. Emission coeficients for 6s ^4P-6p$^4D^0$ 541.92 ionic xenon line.

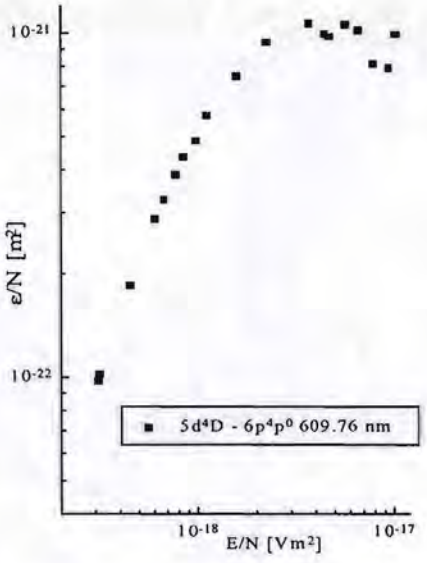

Fig.2. Emission coeficients for 5d ^4D- 6p $^4P^0$ 609.76 ionic xenon line.

In addition to the absolute value of excitation coefficients significant data may be obtained from the spatial profiles of emission. These profiles may be normalized to the excitation coefficients and be used to obtain the cross section data with the aid of some numerical techniques [7,8]. In particular such data may be used to identify heavy particle

excitation that is recognized by its growth towards the cathode. In Fig.3 and Fig. 4 we show spatial emission profiles of two ionic lines obtained in xenon.

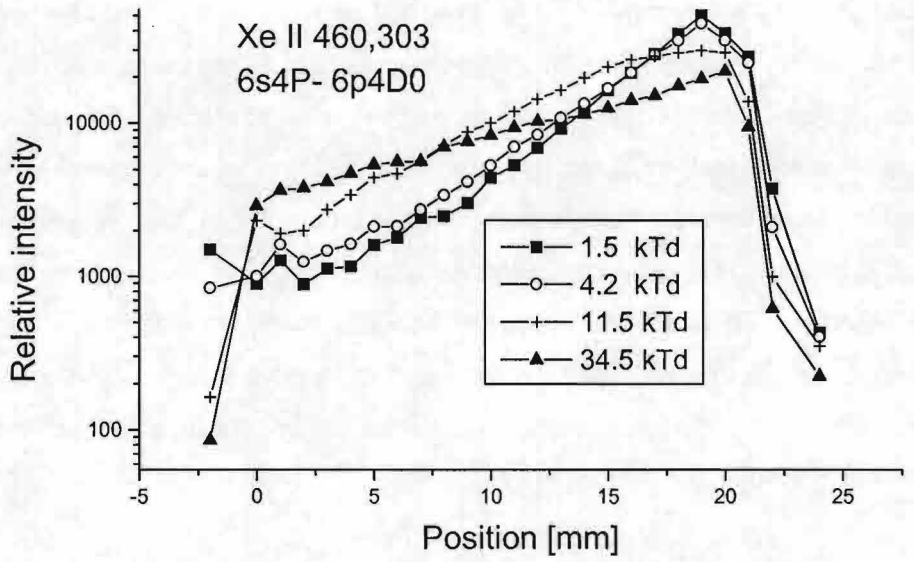

Fig. 3. Spatial profile of emission of Xe II (460.303) line for four different values of E/N (1 kTd ≡ 1 10^{-18} Vm^2).

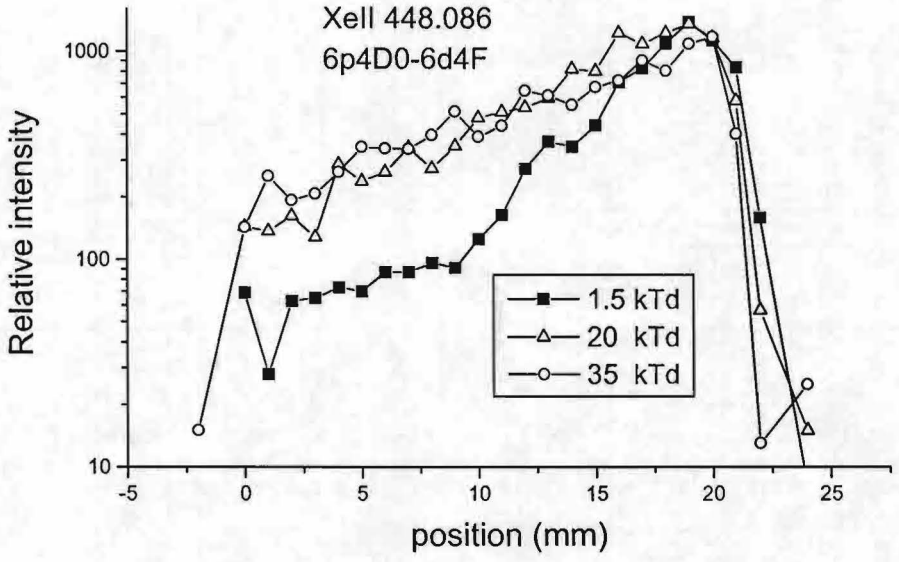

Fig. 4. Spatial profile of emission of Xe II (448.086) line for three different values of E/N.

The highest values of *E/N* were extended as compared to the previous measurements up to 5 10^{-17} Vm^2 and it was found that the heavy particles (ions and fast neutrals) make some contribution to excitation above 2 10^{-17} Vm^2 but that their effect is very small.

Conclusion

The data that were obtained will be used to establish the cross sections for excitation of ionic levels of xenon which are required in modeling of xenon discharges at low pressures, plasma thrusters in particular. The data may be used directly for diagnostics purposes under assumption of local field equilibrium.

References:

1. Z. M. Jelenak, Z. B. Velikić, J. V. Božin, Z. Lj. Petrović, B. M. Jelenković, *Phys.Rev. E* 47 (1993) 3566.
2. V. Stojanović, J. V. Bozin, Z. Lj. Petrović and B. M. Jelenković, *Phys. Rev.A* 42 (1990) 4983.
3. G. N. Malović, J. V. Božin, B. M. Jelenković, Z. Lj. Petrović, *Nucl. Instrum. and Methods B* 129 (1997) 317.
4. Z.Lj.Petrović and A.V.Phelps, Phys. Rev. E 47 (1993) 2806.
5. I.Stefanović and Z.Lj.Petrović, Jpn.J.Appl. Phys. 36 (1997) 4728.
6. M. Aymar, M. Coulombe, *Atomic Data and Nuclear Data Tables* 21 (1978) 537.
7. B. M. Jelenković, A. V. Phelps, *Phys. Rev. A* 36 (1987) 5310.
8. Z. Lj. Petrović and A.V. Phelps, *Phys. Rev. E* 56 (1997) 5920.

Coating of particles by plasma enhanced chemical vapour deposition

G.V. Paeva, W.W. Stoffels, E. Stoffels, R. P. Dahiya*, G.M.W. Kroesen

Department of Applied Physics, Eindhoven University of Technology, P.O. Box 513, 5600 MB Eindhoven, The Netherlands
** Centre for Energy Studies, Indian Institute of Technology, New Delhi*
E-mail: g.paeva@tue.nl

Introduction

The interest in dusty plasma research, which is a relatively new field in plasma physics, has increased with the development of microelectronics. The dust particles appear as pollutant in this industrial processing. Recently, however, they are seen from a different point of view – they can be useful in various technologies: chemical catalysis, solar cell fabrication, ceramics etc.[1,2,3] In this investigation we have concentrated on coating of dust particles. This process allows us to obtain composite particles with combined properties of the base powder material with those of the deposited layer. The process of particle coating has applications in different fields: the toner production, the chemical catalysis, fluorescence etc.

Experimental set-up

We have performed experiments using low density non-equilibrium plasma generated by capacitively coupled 13.56 MHz radio frequency (RF) plasma source. The experimental set-up is shown in figure 1. The input power is variable in the range 3-15 W. In a low pressure RF plasma (in our case p = 0.05–0.5 mbar) the particles are charged negatively and it is easy to trap them separated from each other. This facilitates uniform coating on their surfaces. Barium magnesium aluminate (BAM) particles are introduced into the plasma using a manipulator arm having a sieve at the end. They are fluorescent in the range 400-500 nm with a maximum at $\lambda = 477$nm. For better confinement of the particles we have placed a metal ring in the centre of the powered electrode. An Ar ion laser is used for alignment of the optics with the particle cloud suspended in the plasma.

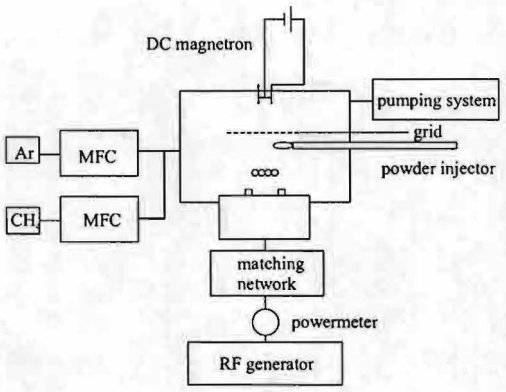

Figure 1: *Schematic diagram of the experimental set-up. The DC magnetron is used for metal coating and the methane plasma – for coating with hydrogenated carbon.*

The vessel is mounted on a table equipped with an electric motor. This allows us to move the complete plasma chamber in vertical direction with respect to the detector and to scan the particle cloud.

The RF plasma is produced in different gases – Ar, CH_4 or their mixture. We have used two methods of particle coating. One of them is through magnetron sputtering of copper in Ar plasma and the other is by plasma enhanced chemical vapour deposition in methane plasma. The magnetron is mounted at the top of the vessel. To avoid or at least to decrease the electrostatic perturbation caused by the magnetron source on the RF plasma a metal grid is positioned parallel to the powered electrode. In the methane-argon plasma the speed of the hydrogenated carbon coating can be controlled by different mixture ratios of $Ar:CH_4$.

For diagnostics we have used Ar ion laser light scattering and the fluorescence light induced by the plasma (in Ar plasma) or by a mercury lamp (in methane plasma). Both of them are measured as a function of time. In the detection system (fig.2) the image of the cloud is focussed at the end of an optical fibre connected to an optical multi-channel analyser (OMA).

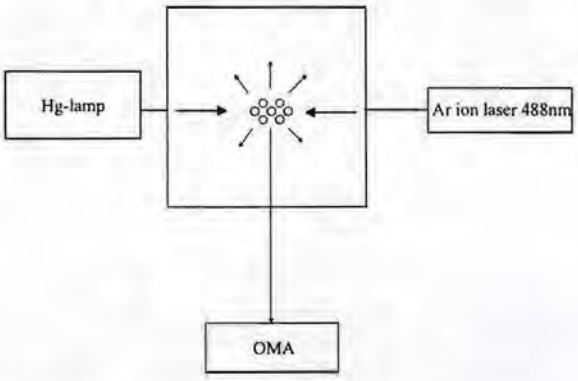

Figure 2: *Schematic diagram of the detection system*

Results and discussion

In the RF plasma the dust particles are trapped in the sheath of the powered electrode. A scan of the dust cloud is made and the dependence of the cloud position on the gas pressure is shown in figure 3. The magnetron sputter source also influences the characteristics of the dust cloud.

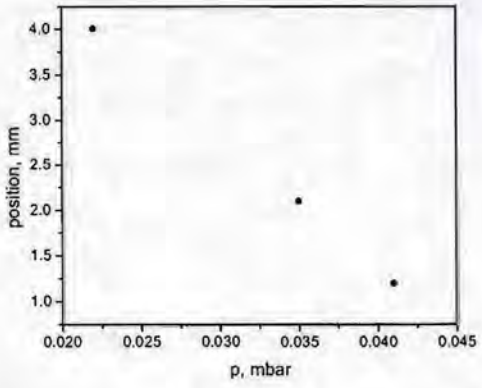

Figure 3: *Position of maximum particle density in the cloud as a function of gas pressure*

As we use fluorescent particles we can measure not only the scattered signal but also the change in the fluorescence in the course of coating. The fluorescence spectrum of the BAM particles is given in figure 4. The UV light emitted by the Ar plasma is sufficient to excite the particles. In CH_4 plasma, however, an additional UV source is needed.

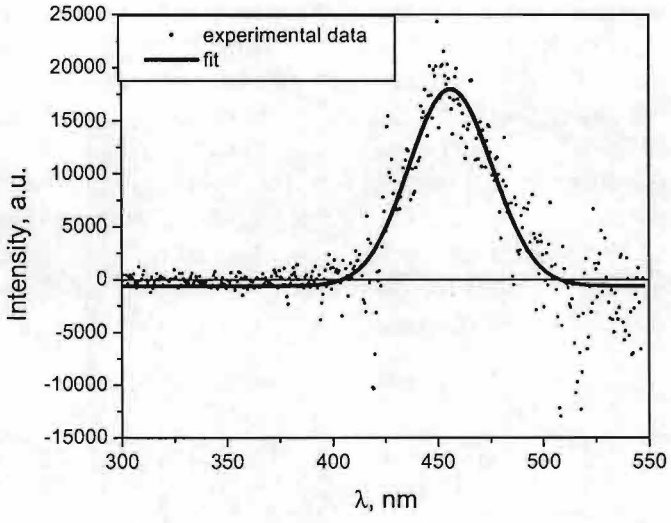

Figure 4 *Fluorescence spectrum of the BAM particles, measured by the OMA system.*

We have measured the spectrum of the plasma before introducing the dust particles. This is needed as in the range of the fluorescent light both Ar and CH_4 have spectral lines. The background plasma spectrum is subtracted from the one measured in the presence of the BAM particles. By measuring the fluorescence as a function of time we can monitor the coating process until optical thick layer is obtained.

Acknowledgements

Part of the work is supported by the Dutch Technology Foundation (STW). R.P. Dahiya acknowledges the Eindhoven University of Technology for granting the Philips stipend. E. and W.W. Stoffels wish to acknowledge the support of the Royal Dutch Academy of Science (KNAW).

References

[1] *Dusty Plasmas: Physics, Chemistry and Technological Impacts in Plasma Processing*, ed. by A. Bouchoule, J. Wiley & Sons, 1999

[2] E. Stoffels, W.W. Stoffels, G. Ceccone, R. Hasnaoui, H. Keune, G. Wahl and F. Rossi, J. Appl. Phys., **86**, p. 3442, 1999

[3] Roca i Cabarrocas, P. Gay and A. Hadjadj, J.Vac.Sci.Technol. A, **14**, p. 655, 1996

Defect Density Measurements of a-Si:H by means of the Cavity Ring Down Absorption Technique

A.H.M. Smets[a], J.H. van Helden and M.C.M. van de Sanden[b]
Department of Applied Physics, Eindhoven University of Technology
P.O. Box 513, 5600 MB Eindhoven, The Netherlands
[a] A.H.M.Smets@phys.tue.nl, [b] M.C.M.v.d.Sanden@tue.nl

Introduction

The defect density in hydrogenated amorphous silicon (a-Si:H) films, or so called dangling bonds (db) density, is an important parameter which determines the performance of the a-Si:H thin film solar cells. Furthermore, it's believed that during a-Si:H deposition the surface is almost fully hydrogen passivated, and a small surface coverage (10^{-3} to 10^{-6}) of dangling bonds operates as growth sites, at which the over the surface diffusing weakly absorbed radicals are able to stick [1-4]. To improve the insight in a-Si:H growth mechanism, a technique is needed to monitor the dangling bond evolution during growth. Recently it has been demonstrated that the *in situ* electron-spin-resonance (ESR) technique is capable of measuring dangling bond densities of 10^{13} cm^{-2} in the surface region during growth [5]. Here we will show that the Cavity Ring Down (CRD) absorption technique is suitable to detect the dangling bonds in the bulk and at the surface.

Experimental setup and results

The defect states are positioned in the middle of the band gap and are responsible for the rather small sub gap absorption ($\alpha = 0.1$ up to 100 cm^{-1}) in the 0.8 – 1.3 eV range [6]. The sub gap absorption can be measured indirectly using opto-electronic techniques such as constant photoconductivity measurements (CPM) [7] and dual beam photoconductivity (DBP) [8] and opto-thermal techniques as photothermal deflection spectroscopy (PDS) [9,10]. The latter technique is reported to be the most sensitive for surface defects [9]. One main disadvantage of these techniques is the fact that they are *indirect* absorption measurements. Furthermore these techniques can not be applied *in situ*, i.e. during growth.

The CRD technique [11] is a sensitive absorption technique (sensitivity around ~ 10^{-6}), which enables us to measure this sub gap absorption *directly*. The technique is based upon the measurement of the rate of absorption of a light pulse confined in an optical cavity. The optical cavity is formed by two plano-concave mirrors, separated by a distance L, the so-called cavity length. A small part of the laser pulse is coupled into the cavity, the rest being reflected. Due to losses at the mirrors and additional absorption within the cavity the laser light intensity decays exponentionally with a characteristic CRD time τ [12]:

$$\tau = \frac{L/c}{(1-R)+A} \qquad (1)$$

where R is the mirror's reflectivity, A the additional absorption per pass in the cavity and c the velocity of light. Measuring the light intensity leaking out the cavity at the back mirror the absorption A can be deduced. Absorptions per pass down to 10^{-6} can be obtained depending on the mirror's reflectivity and the accuracy of the determination of τ.

To demonstrate the technique we first applied it *ex situ*. The cavity used for *ex situ* sub gap measurements was a *mirror –sample(Corning ± a-Si:H) - mirror* configuration and the 1.17 eV output of a Nd:Yag (DCR 11) laser was used as light source (Fig. 1). From

simulations we concluded that the multiple light ray trajectories, due to the introduction of the samples surfaces in the cavity, does not affect the validity of Eq. (1), as long as the sample's transmission $T >> (1 - R)$ ($\approx 3 \times 10^{-4}$).

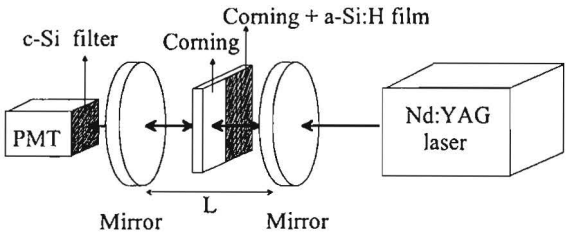

Fig. 1 Schematic representation of the ex situ CRD setup.

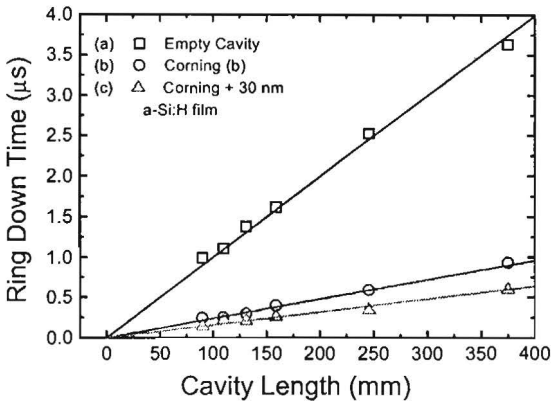

Fig. 2. *The measured ring down time for an empty cavity (a, squares), corning substrate (b, circles) and cornig substrate with on top a 30 nm a-Si:H film (c, triangle) versus L.*

The ring down time of an empty cavity (a), corning sample (b) and corning with a-Si:H film (c) in the cavity have been measured as function of the cavity length. In Fig. 2 the results on a 30 nm a-Si:H film are shown. The dependence is linear, meaning that the scatter losses at the surfaces can be neglected, as scatter would result in a increasing cavity loss with increasing cavity length, due to a smaller solid angle. The absorption of the corning substrate and a-Si:H film can be determined from the slopes using Eq. (1). Typical absorption coefficients of 0.01 up to 0.02 cm^{-1} of the Corning 7059 have been found. The a-Si:H absorption per pass (αd) as function of the a-Si:H thickness d together with DBP results on the same samples are presented in Fig. 3. The DBP absorption is one order lower than the CRD absorption, showing that not every sub gap absorption results in a lift of an electron in to the conduction band. Assuming a homogeneous dangling bond distribution in the bulk absorption versus thickness dependence should have slope 1. Fig. 3 shows that CRD results converge to a slope 1 at large thickness. However at small thickness ($\leq$ 1 micron) the CRD results show an additional absorption in contrast to the DBP technique, which shows a slope 1 dependence over the entire thickness range. The additional absorption is due to surface defects and therefore it is concluded that DBP is less sensitive for surface defects as also reported by Smith et al. [9].

In Fig. 4 the obtained rms roughness $W(d)$ from *in situ* ellipsometry (RCE) and AFM analyses on the same samples is presented. Assuming a homogeneous distribution in the bulk and surface region over thickness $W(d)$ the CRD data is fitted with $\alpha d = \alpha_{bulk} d + \alpha_{surf} W(d)$. From this fit we obtained absorption coefficients of $\alpha_{bulk} = 31$ cm^{-1} and $\alpha_{surf} = (5 \pm 1) \times 10^3$ cm^{-1}. If we assume a db absorption cross section of $\sigma_{DB} = 1.1 \times 10^{-15}$ cm^2 (deduced from the empirical constant of Jackson et al. [13]), we obtain a surface db density of 1.0×10^{12} up to 1.4×10^{12} cm^{-2} in the same order as values reported in literature [14]. This corresponds to a

defect surface coverage of 10^{-3}. Note that this is a lower estimate since samples exposed to air will be passivated by oxidation on the defect sites.

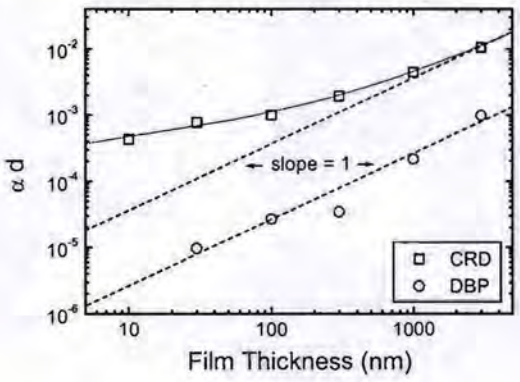

Fig. 3 The measured a-Si:H sub gap absorption per pass versus the film thickness. The solid line is a fit of $\alpha d = \alpha_{bulk} d + \alpha_{surf} W(d)$.

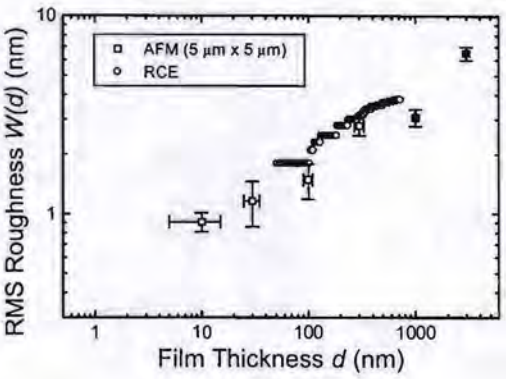

Fig. 4 The measured rms roughness obtained by AFM (squares) and RCE (circles) versus the a-Si:H film thickness.

A *mirror-prism(suprasil)-mirror* cavity configuration has been used for *in situ* measurements as shown in Fig. 5. The injected 1.17 eV light pulse incidents perpendicular on the two prism surfaces, on which the a-Si:H film is deposited, and has a total internal reflection at the prism's backside. The deposition starts by removing the shutter in front of the prism substrate.

Preliminary results for the initial a-Si:H growth at 5 Å/s and 200 °C are shown in Fig. 6. At t = 0 s the shutter is opened and the sub gap absorption increases until the plasma is turned off (after 40 s). In this time a thin film of approximately 20 nm has been deposited, meaning the initial defect evolution has been measured. In Fig. 6 two measurements performed at the same conditions are presented, showing the reproduction at 5 Å/s. At a growth rate of 2 Å/s the initial deposition shows some hysteresis due to the prism cleaning procedure. An effective a-Si:H absorption coefficient of $\alpha = 1.6 \times 10^4$ cm^{-1} is obtained. Assuming again a db absorption cross section of $\sigma_{DB} = 1.1 \times 10^{-15}$ cm^2 this corresponds to a surface defect density of 3×10^{13} cm^{-2} or in other words a db surface coverage of 0.03. During and after the deposition the surface db density (vacuum condition) is 30 times higher than the density obtained from the *ex situ* measurements, meaning that the surface defect disappear in time. Possible mechanisms are defect relaxation or passivation of surface defects by native oxide.

Conclusions

The CRD absorption technique enables us to measure the surface defects during deposition. *Ex situ* measurements show a surface defect density in atmosphere environment of approximately 1×10^{12} cm^{-2}. During deposition the surface density is 3×10^{13} cm^{-2} in agreement with values obtained with *in situ* ESR [14].

Acknowledgement

The authors thank Olivier de Barrilec for his experimental efforts. D.C. Schram is thanked for discussions. Paul Böcker and Johan Hoefnagels are acknowledged for the construction of the CRD software package. We acknowledge the technical assistance of Ries

van de Sande, Jo Jansen, Herman de Jong and Bertus Hüsken. This work was supported by NOVEM, TDO and FOM.

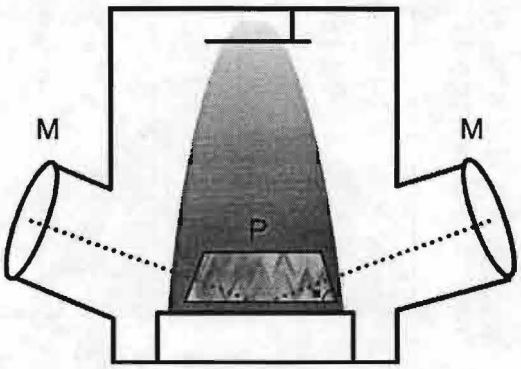

Fig. 5 Schematic representation of the in situ CRD set up, M cavity mirrors and P prism. Real prism dimension: height 5.36 mm and length 15.5 mm. Laser pulse incident on back surface is 70°.

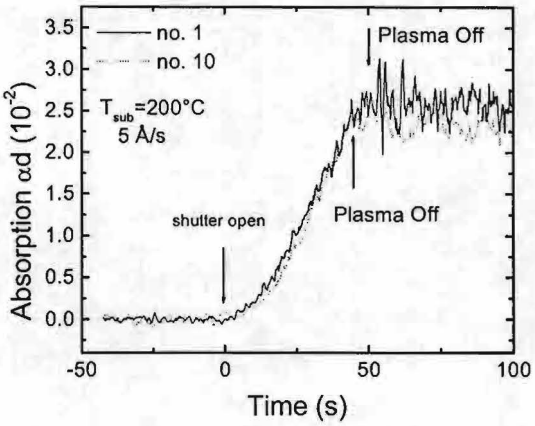

Fig. 6. Example of in situ sub gap measurement at 5 Å/s and 200 °C.

References

[1] A. Matsuda, K. Nomoto, Y. Takeuchi, A. Suzuki, A. Yuuki, J. Perrin, Surf. Sci. **22**, 50 (1990), J.L. Guizot, K. Nomoto, A. Matsuda, Surf. Sci. **244**, 22 (1991)

[2] J.R. Doyle, D.A. Doughty, A. Gallagher, J. Appl. Phys. **68**, 4375 (1990), J.R. Doyle, D.A. Doughty, A. Gallagher, J. Appl. Phys. **71**, 4727 (1997), J.R. Doyle, D.A. Doughty, A. Gallagher, J. Appl. Phys. **71**, 4771 (1992)

[3] J. Perrin, Y. Takeda, N. Hitano, Y. Takeuchi, A. Matsuda, Surf. Sci. **210**, 114 (1989), J. Perrin, Mshiritani, P. Kae-Nune, H. Videlot, J. Jolly, J. Guillon, J. Vac. Sci. Technol A **16**, 278 (1998)

[4] M.C.M. van de Sanden, W.M.M. Kessels, A.H.M. Smets, B.A. Korevaar, R.J. Severens and D.C. Schram, Mat. Res. Soc. Symp. Proc. **557**, 13 (1999)

[5] S. Yamasaki, Mat. Res. Soc. Symp. Proc. **609**, A1.1.1 (2000)

[6] L. Ley, p. 113-138 in *Properties of amorphous Silicon and its alloys*, editor T. Searle, Short Run Press, London (1998)

[7] M. Vanecek, J. Kocka, J Stuchlik, Z. Kozisek, O. Stika, and A. Triska, Sol. Energy Mat. **8**, 411 (1983)

[8] S. Lee, S. Kumar, C.R. Wronski and N. Maley, J. Non-Cryst. Solids **114**, 316 (1989)

[9] Z.E. Smith, V. Chu, K. Shepard, S. Aljishi, D. Slobodin, J. Kolodzey, and S. Wagner, Appl. Phys. Lett. **50**, 1521 (1987)

[10] F. Leblanc, Y. Maeda, K. Onisawa and T. Minemura, Phys. Rev. B **50**, 14613 (1994)

[11] A. O'Keefe and D.A.G. Deacon, Rev. Sci. Instrum. **59**, 2544 (1988)

[12] G. Meijer, M.G.H. Boogaarts, R.T. Jongma, D.H. Parker and A.M. Wodtke, Chem. Phys. Lett. **217**, 112 (1994)

[13] W.B. Jackson and N.M. Amer, Phys. Rev. B **25**, 5559 (1982)

[14] S. Yamasaki, U.K. Das, T. Umeda, J. Isoya and K. Tanaka, J. of Non-Cryst. Sol. **266-269**, 529 (2000)

The effect of spatial distribution of ion energies and current density on the adhesion and structure of Cu coatings deposited by planar magnetron sputtering

S.S. Alimov, V.V. Bobkov, R.I. Starovoitov, V.N. Andreyev
Kharkov National University, 31 Kurchatov ave., 61108, Kharkov
UKRAINE

In this contribution homemade planar magnetron sputtering device have been investigated by means of five-electrode energy analyzer. Spatial distribution of energy spectra of ions sputtered from target and plasma species are presented.
Chemical composition and surface profile of deposited Cu coatings was studied by Secondary Ion Mass Spectrometry and by Scanning Electron Microscopy respectively. Adhesion properties was measured also.
Results obtained from coatings investigation are compared with data from energy analyzer. It is concluded that properties of deposited coatings (especially adhesion) strongly influenced by ion current distribution and energy of deposited ions.